UNIVERZA V LJUBLJANI

FAKULTETA ZA MATEMATIKO IN FIZIKO

DOKTORSKA DISERTACIJA

Tara Nanut

2017

Tara Nanut

MEASUREMENT OF RADIATIVE D^0 MESON DECAYS WITH THE BELLE DETECTOR

Doctoral thesis

LJUBLJANA, 2017

UNIVERZA V LJUBLJANI
FAKULTETA ZA MATEMATIKO IN FIZIKO
ODDELEK ZA FIZIKO

Tara Nanut

MERITEV RADIATIVNIH RAZPADOV MEZONA D^0 Z DETEKTORJEM BELLE

Doktorska disertacija

MENTOR: doc. dr. Anže Zupanc

Ljubljana, 2017

IZJAVA O AVTORSTVU

Spodaj podpisana Tara Nanut, avtorica doktorske disertacije (v nadaljevanju: pisnega zaključnega dela študija) z naslovom:

Meritev radiativnih razpadov mezona D^0 z detektorjem Belle

izjavljam,

- da sem pisno zaključno delo študija izdelala samostojno pod mentorstvom doc. dr. Anžeta Zupanca,

- da je tiskana oblika pisnega zaključnega dela študija istovetna elektronski obliki,

- da sem pridobila vsa potrebna dovoljenja za uporabo podatkov in avtorskih del v pisnem zaključnem delu študija in jih jasno označila,

- da soglašam, da se elektronska oblika pisnega zaključnega dela študija uporabi za preverjanje podobnosti vsebine z drugimi deli s programsko opremo za preverjanje podobnosti vsebine, ki je povezana s študijskim informacijskim sistemom fakultete,

- da na UL neodplačno, neizključno, prostorsko in časovno neomejeno prenašam pravico shranitve avtorskega dela v elektronski obliki, pravico reproduciranja ter pravico dajanja pisnega zaključnega dela študija na voljo javnosti na svetovnem spletu preko Repozitorija UL,

- da dovoljujem objavo svojih osebnih podatkov, ki so navedeni v pisnem zaključnem delu študija in tej izjavi, skupaj z objavo pisnega zaključnega dela študija.

Ljubljana, 3.2.2017

Tara Nanut

IZVLEČEK

V delu je predstavljena meritev razvejitvenega razmerja in asimetrije CP v radiativnih razpadih mezona D^0, $D^0 \to V\gamma$, kjer je $V = \phi, \overline{K}^{*0}, \rho^0$. Meritev temelji na vzorcu 943 fb^{-1} podatkov, zbranih z detektorjem Belle na asimetričnem trkalniku e^+e^- KEKB. Gre za prvo meritev asimetrije CP v teh razpadih. Izmerjena razvejitvena razmerja so $\mathcal{B}r\left(D^0 \to \phi\gamma\right) = (2.76 \pm 0.19 \pm 0.10) \times 10^{-5}$, $\mathcal{B}r\left(D^0 \to \overline{K}^{*0}\gamma\right) = (4.66 \pm 0.21 \pm 0.21) \times 10^{-4}$ in $\mathcal{B}r\left(D^0 \to \rho^0\gamma\right) = (1.77 \pm 0.30 \pm 0.07) \times 10^{-5}$. V pričujoči analizi so bili razpadi $D^0 \to \rho^0\gamma$ prvič opaženi. Izmerjene vrednost asimetrij CP so $\mathcal{A}_{CP}\left(D^0 \to \phi\gamma\right) = -0.094 \pm 0.066 \pm 0.001$, $\mathcal{A}_{CP}\left(D^0 \to \overline{K}^{*0}\gamma\right) = -0.003 \pm 0.020 \pm 0.000$ in $\mathcal{A}_{CP}\left(D^0 \to \rho^0\gamma\right) = +0.056 \pm 0.152 \pm 0.006$. Rezultati ne kažejo kršitve simetrije CP.

Ključne besede:
detektor Belle, kršitev simetrije CP, radiativni razpadi mezona D^0

PACS:
11.30.Er, 13.20.Fc, 13.25.Ft

ABSTRACT

We present the measurement of the branching fraction and CP asymmetry in radiative charm decays $D^0 \to V\gamma$, where $V = \phi, \overline{K}^{*0}, \rho^0$. The measurement is based on 943 fb^{-1} of data, collected with the Belle detector at the KEKB asymmetric-energy e^+e^- collider. This is the first measurement of CP asymmetry in these decays. We obtain the branching fractions of $\mathcal{B}r\left(D^0 \to \phi\gamma\right) = (2.76 \pm 0.19 \pm 0.10) \times 10^{-5}$, $\mathcal{B}r\left(D^0 \to \overline{K}^{*0}\gamma\right) = (4.66 \pm 0.21 \pm 0.21) \times 10^{-4}$ and $\mathcal{B}r\left(D^0 \to \rho^0\gamma\right) = (1.77 \pm 0.30 \pm 0.07) \times 10^{-5}$. This is the first observation of the decay $D^0 \to \rho^0\gamma$. The obtained CP asymmetries, $\mathcal{A}_{CP}\left(D^0 \to \phi\gamma\right) = -0.094 \pm 0.066 \pm 0.001$, $\mathcal{A}_{CP}\left(D^0 \to \overline{K}^{*0}\gamma\right) = -0.003 \pm 0.020 \pm 0.000$ and $\mathcal{A}_{CP}\left(D^0 \to \rho^0\gamma\right) = +0.056 \pm 0.152 \pm 0.006$, are consistent with no CP violation.

Keywords:
the Belle detector, CP violation, radiative decays of D^0 mesons

PACS:
11.30.Er, 13.20.Fc, 13.25.Ft

ZAHVALA

Anže, Marko, hvala.

CONTENTS

INTRODUCTION

The Standard Model is a relativistic quantum field theory that describes the fundamental particles and interactions between them. It is based on the gauge symmetry group $SU(3)_C \times SU(2)_L \times U(1)_Y$, under which it is invariant.

The elementary particles can be split in two major groups: the spin $1/2$ constituents of matter, and the force carriers with integer spin. The Standard Model describes three out of four elementary interactions: the strong, weak, and electromagnetic force. The strong force, which is described by the $SU(3)$ group, is mediated by 8 gluons that carry colour charge. The weak force is mediated by the weak bosons $W^\pm$ and Z^0, while the carrier of the electromagnetic force is the photon γ. The electromagnetic and weak force can be described with a unified theory as the electroweak force under the gauge group $SU(2) \times U(1)$, where $SU(2)$ represents the weak isospin and $U(1)$ the weak hyper-charge. The symmetry of this group is spontaneously broken via the Higgs mechanism, which results in weak bosons acquiring mass and the existence of the also massive Higgs boson.

The fermions can be further divided based on the interactions that they couple to. The particles that carry colour charge and thus feel the strong force are quarks, and particles that do not are called leptons. All particles couple to the weak force, and quarks and charged leptons also to the electromagnetic force. The Standard Model is composed of 6 elementary quarks and 6 elementary leptons, arranged in three families:

$$\begin{pmatrix} \nu_e & u \\ e^- & d \end{pmatrix} \quad , \begin{pmatrix} \nu_\mu & c \\ \mu^- & s \end{pmatrix} \quad , \begin{pmatrix} \nu_\tau & t \\ \tau^- & b \end{pmatrix} \quad . \tag{1}$$

The analogous particles, belonging to different generations, differ in mass, while having the same charge, spin, and other quantum numbers. This leads to similar physical behaviour, hence the division in generations. Each particle has also a corresponding anti-particle, which has the same mass but opposite internal quantum numbers. Quarks further combine to form hadrons. Most commonly, hadrons are either baryons, consisting of three quarks, or mesons, consisting of a quark and anti-quark. All baryonic matter is composed of particles from the first generation, whereas hadrons that are composed of particles from the second and third generation are short-lived.

The Standard Model is an extremely well established theory, verified to a strikingly high degree of precision in certain aspects. It has successfully predicted a wide spectrum of new particles and processes, which have been subsequently confirmed by experiments. In the large majority of cases, the level of matching between theory

and experiment is good, while the rare discrepancies have not yet been measured with high enough precision.

Despite the great success of the Standard Model, there are several aspects which indicate its incompleteness. Some of the main shortcomings of the Standard Model are the fact that it does not incorporate the fourth elementary force, gravity; that it treats neutrinos as massless, while the experimentally confirmed process of neutrino oscillations requires them to have a mass, albeit small; that it does not provide a candidate for dark matter or explain dark energy; that the level of CP asymmetry in the Standard Model is not sufficient to describe the observed matter-antimatter asymmetry in the Universe. These weaknesses lead us to believe that the Standard Model is not the elementary description of Nature, but merely a low-energy limit of an underlying, more fundamental mechanism. The search for processes and particles beyond the Standard Model, commonly denoted as New Physics, has been the main focus of high energy physics in the last years.

In experimental terms, there are two main approaches to the search for New Physics:

THE ENERGY FRONTIER This approach is based on achieving higher particle collision energies, in order to reach the threshold for production of new, heavy particles. The current leader in this field is the Large Hadron Collider at CERN, exploring energies at the TeV scale.

THE INTENSITY FRONTIER The Intensity Frontier is a complementary approach, exploring lower energies at high precision. The aim is to measure deviations from the Standard Model predictions in known processes, to which New Physics processes could contribute.

An example of an Intensity Frontier experiment are B-factories, such as the Belle Experiment, on which the work of this thesis is based.

PHYSICS MOTIVATION

2.1 CP VIOLATION

Symmetries are an important concept in physics. Noether's theorem states that for every symmetry of the Lagrangian, there exists a corresponding conservation law and conserved quantity [1]. Two important discrete symmetries in the Standard Model are:

C SYMMETRY   Symmetry under charge conjugation, which inverts the internal quantum numbers like charge and flavour, thus transforming a particle into its anti-particle:

$$C \left| \psi(q) \right\rangle = \left| \psi(-q) \right\rangle \quad , \tag{2}$$

where q denotes internal quantum numbers. Quantities like mass and spin remain invariant.

P SYMMETRY Symmetry under parity transformation, i.e. reversal of spatial coordinates:

$$P \left| \psi(\mathbf{r}) \right\rangle = \left| \psi(-\mathbf{r}) \right\rangle \quad . \tag{3}$$

It has been long believed that C and P are exact symmetries of Nature and conserved individually. They are indeed conserved by both the strong and electromagnetic interaction, but in 1957 it was confirmed by experiments that both are violated in weak interactions, thus being only approximate symmetries of the Standard Model [2, 3]. The combination of the two, CP symmetry, still seemed to be conserved, however. This was believed until 1964, when CP violation was discovered in decays of neutral kaons, for which a Nobel prize was awarded to Cronin and Fitch [4]. This discovery lead to a long series of studies of CP violation, first in the kaon system, followed by B, and eventually D, system. CP violation in B meson systems was discovered in 2001 at B-factory experiments Belle and BaBar [5, 6], proving the mechanism of CP violation proposed by Kobayashi and Maskawa [7] by a large number of measurements at the two experiments. A Nobel prize was awarded to the two theorists.

2.1.1 *CKM Matrix*

At the time of the discovery of CP violation in neutral kaon systems, only the existence of the 3 lightest quarks was experimentally confirmed, though Glashow,

Iliopoulus and Maiani introduced the hypothesis of a fourth, c quark [8]. In a four-quark model, e.g. the u quark couples via weak interaction to d', a superposition of down-type quarks:

$$d' = \cos(\theta_C)d + \sin(\theta_C)s \quad , \tag{4}$$

where θ_C is the Cabibbo angle. The mixing matrix thus rotates the mass eigenstates of down-type quarks to eigenstates of the weak interaction:

$$\begin{bmatrix} d' \\ s' \end{bmatrix} = \begin{bmatrix} V_{ud} & V_{us} \\ V_{cd} & V_{cs} \end{bmatrix} \begin{bmatrix} d \\ s \end{bmatrix} = \begin{bmatrix} \cos(\theta_C) & \sin(\theta_C) \\ -\sin(\theta_C) & \cos(\theta_C) \end{bmatrix} \begin{bmatrix} d \\ s \end{bmatrix} \quad . \tag{5}$$

The matrix elements are related to the relative probability for transition between up- and down-type quarks, e.g. $|V_{ij}|^2$ represents the probability for a transition between the i and j quark.

In this four-quark model, CP violation cannot be explained, as the 2×2 mixing matrix has only one free parameter, the Cabibbo angle. Kobayashi and Maskawa extended the theory to include an additional generation of quarks. In a 6 quark picture, the mixing matrix, denoted as the Cabibbo-Kobayashi-Maskawa (CKM) matrix $\mathbf{V}_{\text{CKM}}$, rotates the mass eigenstates as follows:

$$\begin{bmatrix} d' \\ s' \\ b' \end{bmatrix} = \begin{bmatrix} V_{ud} & V_{us} & V_{ub} \\ V_{cd} & V_{cs} & V_{cb} \\ V_{td} & V_{ts} & V_{tb} \end{bmatrix} \begin{bmatrix} d \\ s \\ b \end{bmatrix} \quad . \tag{6}$$

The CKM matrix is unitary by construction. A 3×3 unitary matrix can be parametrised in terms of three real mixing angles and one complex phase. By comparing the charged current weak interaction Lagrangian and its CP-conjugated counterpart, it follows that they are identical only if $V_{ij} = V_{ij}^*$, i.e. if the elements of the mixing matrix are real. The complex phase in the CKM matrix thus introduces CP violation into the Standard Model.

The elements of the CKM matrix are free parameters of the Standard Model and thus need to be determined experimentally. Figure 1 shows the magnitudes of the individual elements. A strong hierarchical structure can be observed, with the diagonal elements being close to unity and the off-diagonal elements being much smaller in value.

A common parametrisation of the CKM matrix is the Wolfenstein parametrisation, which is an expansion in terms of $|V_{us}| = \lambda$. Up to the order of λ^3, it reads

$$V_{\text{CKM}} = \begin{bmatrix} 1 - \lambda^2/2 & \lambda & A\lambda^3(\rho - i\eta) \\ -\lambda & 1 - \lambda^2/2 & A\lambda^2 \\ A\lambda^3(1 - \rho - i\eta) & -A\lambda^2 & 1 \end{bmatrix} + \mathcal{O}(\lambda^4) \quad , \tag{7}$$

where real parameters A, ρ and η are assumed to be of order unity. In this parametrisation up to the order of λ^3, CP violation enters in the terms $\rho - i\eta$. However, the complex phase features also in higher orders of λ, so it must be kept in mind that in general, also other elements of the the matrix are complex when developed to a high enough order.
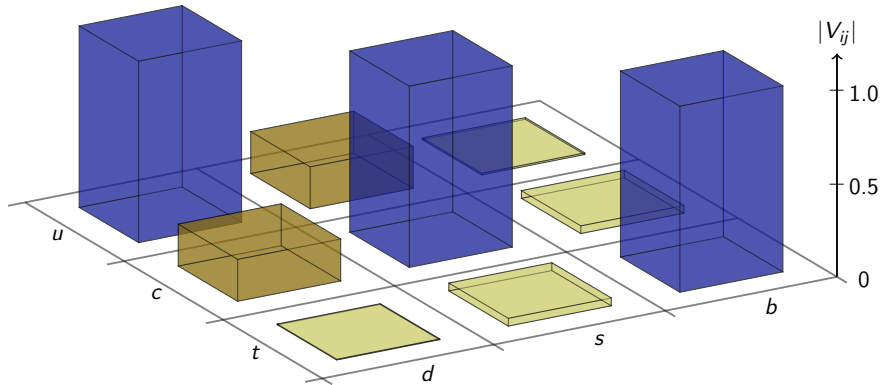
Figure 1: Magnitudes of the CKM elements.

As already mentioned in Chapter 1, the CP violation, as predicted by the Kobayashi-Maskawa mechanism, is not sufficient to explain the observed asymmetry between matter and anti-matter in the Universe. It is strongly believed that there must exist additional sources that generate CP violation. The search for CP asymmetry is thus one of the most prominent fields in which New Physics searches are conducted, with the aim of finding values of CP asymmetry that significantly supersede the Standard Model predictions, thus indicating new sources of CP violation.

A major emphasis of the present thesis will be the search for CP violation in radiative decays of the neutral charm meson, $D^0 \to V\gamma$, where V denotes a vector meson. The remainder of this chapter will thus first examine in more details CP violation in neutral meson systems in general, followed by a particular look into the charm sector and finally $D^0 \to V\gamma$ decays.

2.1.2 *CP Asymmetry in Neutral Meson Systems*

A measure of CP violation is the CP asymmetry $\mathcal{A}_{CP}$. Let us denote a general neutral meson P^0 and its anti-particle $\overline{P}^0$. The time-integrated CP asymmetry for a decay to a final state f is

$$\mathcal{A}_{CP} = \frac{\Gamma(P^0 \to f) - \Gamma(\overline{P}^0 \to \overline{f})}{\Gamma(P^0 \to f) + \Gamma(\overline{P}^0 \to \overline{f})} \quad . \tag{8}$$

There are three types of effects that can generate CP violation in neutral meson systems, and the consequential asymmetries: direct CP violation (generates a_{dir}), CP violation in mixing (generates a_{mix}), and mixing-induced CP violation, in which case the interference between the previous two sources leads to CP violation (generates a_{int}). $\mathcal{A}_{CP}$ can therefore be written as

$$\mathcal{A}_{CP} = a_{\mathrm{dir}} + a_{\mathrm{mix}} + a_{\mathrm{int}} \quad . \tag{9}$$

To be able to evaluate Equation 8 and consider the three sources of CP violation, it is necessary to first examine the time evolution in the neutral meson systems, from where decay rates can be obtained.

At $t = 0$, pure flavour eigenstates $|P^0\rangle$ and $|\overline{P}^0\rangle$ are produced. In time, they will evolve as a linear combination:

$$|P(t)\rangle = a(t) |P^0\rangle + b(t) |\overline{P}^0\rangle \quad . \tag{10}$$

The time evolution of the coefficients is described with the Schrödinger equation

$$i\frac{d}{dt}\begin{bmatrix} a(t) \\ b(t) \end{bmatrix} = \mathcal{H}_{\text{eff}} \begin{bmatrix} a(t) \\ b(t) \end{bmatrix} \quad , \tag{11}$$

where $\mathcal{H}_{\text{eff}}$ is the effective Hamiltionian and can be written as a linear combination of the matrix $\mathbf{M}$, representing the mass of the meson, and the matrix $\mathbf{\Gamma}$, representing the decay width:

$$\mathcal{H}_{\text{eff}} = \mathbf{M} - \frac{i}{2}\mathbf{\Gamma} = \begin{pmatrix} M_{11} & M_{12} \\ M_{21} & M_{22} \end{pmatrix} - \frac{i}{2}\begin{pmatrix} \Gamma_{11} & \Gamma_{12} \\ \Gamma_{21} & \Gamma_{22} \end{pmatrix} \quad . \tag{12}$$

Both $\mathbf{M}$ and $\mathbf{\Gamma}$ are Hermitian matrices, thus $M_{12} = M_{21}^*$, $M_{ii} = M_{ii}^*$, $\Gamma_{12} = \Gamma_{21}^*$, $\Gamma_{ii} = \Gamma_{ii}^*$, and $M_{11} = M_{22} = M$ and $\Gamma_{11} = \Gamma_{22} = \Gamma$.

The eigenstates of the effective Hamiltionian, which represent particles with a defined mass and lifetime (but different for the two), are

$$|P_1\rangle = p |P^0\rangle + q |\overline{P}^0\rangle \quad ,$$
$$|P_2\rangle = p |P^0\rangle - q |\overline{P}^0\rangle \quad .$$

The complex coefficients p and q satisfy the relation $|p|^2 + |q|^2 = 1$, and

$$\frac{q}{p} = \sqrt{\frac{M_{12}^* - \frac{i}{2}\Gamma_{12}^*}{M_{12} - \frac{i}{2}\Gamma_{12}}} \quad . \tag{13}$$

The time evolution of the mass eigenstates can be written as

$$|P_1(t)\rangle = e^{-i(m_1 - i\Gamma_1/2)t} |P_1(0)\rangle \quad ,$$
$$|P_2(t)\rangle = e^{-i(m_2 - i\Gamma_2/2)t} |P_2(0)\rangle \quad ,$$

where $m_{1,2}$ stand for the respective masses, and $\Gamma_{1,2}$ for the respective widths of the two mass eigenstates. The time evolution of the flavour eigenstates is

$$\left|P^0(t)\right\rangle = \frac{1}{2p}(|P_1(t)\rangle + |P_2(t)\rangle) =$$
$$= \left(|P^0\rangle \cosh\left(\frac{ix+y}{2}\Gamma t\right) - \frac{q}{p}|\overline{P}^0\rangle \sinh\left(\frac{ix+y}{2}\Gamma t\right) \right) e^{(-im - \Gamma/2)t} \quad ,$$
$$\left|\overline{P}^0(t)\right\rangle = \frac{1}{2q}(|P_1(t)\rangle - |P_2(t)\rangle) =$$
$$= \left(|\overline{P}^0\rangle \cosh\left(\frac{ix+y}{2}\Gamma t\right) - \frac{p}{q}|P^0\rangle \sinh\left(\frac{ix+y}{2}\Gamma t\right) \right) e^{(-im - \Gamma/2)t} \quad ,$$

where we have introduced dimensionless mixing parameters

$$\Gamma = \frac{\Gamma_1 + \Gamma_2}{2}$$

$$x = \frac{m_1 - m_2}{\Gamma} \quad ,$$

$$y = \frac{\Gamma_1 - \Gamma_2}{2\Gamma} \quad .$$

We define the instantaneous decay amplitudes for flavour eigenstates

$$\mathcal{A}_f = \langle f | \mathcal{H} | P^0 \rangle \quad ,$$

$$\overline{\mathcal{A}}_f = \langle f | \mathcal{H} | \overline{P}^0 \rangle \quad ,$$

$$\mathcal{A}_{\overline{f}} = \langle \overline{f} | \mathcal{H} | P^0 \rangle \quad ,$$

$$\overline{\mathcal{A}}_{\overline{f}} = \langle \overline{f} | \mathcal{H} | \overline{P}^0 \rangle \quad ,$$

where $\mathcal{H}$ represents the interaction potential that is responsible for the decay. We also define additional complex parameters $\lambda_f = \frac{q}{p} \frac{\overline{\mathcal{A}}_f}{\mathcal{A}_f}$ and $\lambda_{\overline{f}} = \frac{q}{p} \frac{\overline{\mathcal{A}}_{\overline{f}}}{\mathcal{A}_{\overline{f}}}$.

The decay rates can be obtained as the square of the time-dependent decay amplitudes: $\Gamma(P^0(t) \to f) = |\langle f | \mathcal{H} | P^0(t) \rangle|^2$. This gives us

$$\Gamma(P^0(t) \to f) = |\mathcal{A}_f|^2 e^{-\Gamma t} \left(\frac{1 + |\lambda_f|^2}{2} \cosh(y\Gamma t) - Re(\lambda_f) \sinh(y\Gamma t) + \right.$$
$$\left. + \frac{1 - |\lambda_f|^2}{2} \cos(x\Gamma t) + Im(\lambda_f) \sin(y\Gamma t) \right) \quad ,$$

$$\Gamma(\overline{P}^0(t) \to \overline{f}) = |\overline{\mathcal{A}}_{\overline{f}}|^2 e^{-\Gamma t} \left(\frac{1 + |\lambda_{\overline{f}}^{-1}|^2}{2} \cosh(y\Gamma t) - Re(\lambda_{\overline{f}}^{-1}) \sinh(y\Gamma t) + \right.$$
$$\left. + \frac{1 - |\lambda_{\overline{f}}^{-1}|^2}{2} \cos(x\Gamma t) + Im(\lambda_{\overline{f}}^{-1}) \sin(y\Gamma t) \right) \quad ,$$

$$\Gamma(P^0(t) \to \overline{f}) = |\overline{\mathcal{A}}_{\overline{f}}|^2 |\frac{q}{p}|^2 e^{-\Gamma t} \left(\frac{1 + |\lambda_{\overline{f}}^{-1}|^2}{2} \cosh(y\Gamma t) - Re(\lambda_{\overline{f}}^{-1}) \sinh(y\Gamma t) - \right.$$
$$\left. - \frac{1 - |\lambda_{\overline{f}}^{-1}|^2}{2} \cos(x\Gamma t) - Im(\lambda_{\overline{f}}^{-1}) \sin(y\Gamma t) \right) \quad ,$$

$$\Gamma(\overline{P}^0(t) \to f) = |\mathcal{A}_f|^2 |\frac{q}{p}|^2 e^{-\Gamma t} \left(\frac{1 + |\lambda_f|^2}{2} \cosh(y\Gamma t) - Re(\lambda_f) \sinh(y\Gamma t) - \right.$$
$$\left. - \frac{1 - |\lambda_f|^2}{2} \cos(x\Gamma t) - Im(\lambda_f) \sin(y\Gamma t) \right) \quad .$$

Having obtained the decay rates, it is possible to evaluate the asymmetries, arising from different sources of *CP* violation, from Equation 8.

2.1.2.1   *Direct CP Violation*

Direct CP violation, or CP violation in decays, arises from different amplitudes (and hence decay rates) for particles and anti-particles, i.e. if $|\overline{A}_{\overline{f}}/A_f| \neq 1$. The related asymmetry is

$$a_{\mathrm{dir}} = \frac{|A_f|^2 - |\overline{A}_{\overline{f}}|^2}{|A_f|^2 + |\overline{A}_{\overline{f}}|^2} \quad . \tag{14}$$

2.1.2.2   *CP Violation in Mixing*

Even if $|\overline{A}_{\overline{f}}| = |A_f|$, an asymmetry term will arise in flavour specific decays, i.e. in decays where $\overline{A}_f$ and $A_{\overline{f}}$ are 0:

$$a_{\mathrm{mix}} = \frac{1 - |p/q|^4}{1 + |p/q|^4} \quad , \tag{15}$$

which will be non-zero if $|p/q| \neq 1$. It can be noted that a_{mix} does not depend on a specific decay mode.

2.1.2.3   *Mixing-induced CP Violation*

Mixing-induced CP violation arises in flavour non-specific decays from interference between a decay without mixing and a decay with mixing, i.e. $P^0 \to f$ and $P^0 \to \overline{P}^0 \to f$. This term is non-zero if $\mathrm{Im}(\lambda_f) = \mathrm{Im}\left(\frac{q}{p}\frac{\overline{A}_f}{\mathcal{A}_f}\right) \neq 0$, even if there is no CP violation in decay or mixing ($|\overline{A}_{\overline{f}}| = |A_f|$ and $|p/q| = 1$).

CP violation in mixing and interference between mixing and decay are jointly denoted as indirect CP violation: $a_{\mathrm{ind}} = a_{\mathrm{mix}} + a_{\mathrm{int}}$. It can be commonly characterised with the requirement $p/q \neq 1$, where $p/q = |p/q|e^{i\phi}$. CP violation in mixing is obtained if $|p/q| \neq 1$, whereas the condition $\phi \neq 0$ (or π) signifies the occurence of mixing-induced CP violation. As both are independent of the specific decay mode, indirect CP violation will be universal for all decays of a specific neutral meson, e.g. D^0. The world-average values for $|p/q|$ and ϕ for D^0 mesons are $|p/q| = 0.89^{+0.08}_{-0.07}$ and $\phi = -12.9^{+9.9°}_{-8.7}$, giving $a_{\mathrm{ind}} = (-0.032 \pm 0.026)\%$ [9].

2.2   CHARM PHYSICS

The existence of the c, or charm, quark was predicted by Glashow, Iliopoulus and Maiani in 1970 as a needed constituent for the GIM mechanism, which explains the suppression of flavour-changing neutral currents. Its existence was confirmed in 1974 with the discovery of the J/Ψ particle, a meson composed of a charm and anti-charm quark [10, 11]. However, charm physics long remained a fairly neglected field of study, since the processes and observables that could be used as a probe for New Physics are on a lower scale than e.g. their counterparts in B meson systems. As an example, the first evidence of mixing in $D^0 - \overline{D}^0$ systems, which occurs through intermediate down type quarks (in contrast with mixing in K and B systems), dates to 2007, and the first single measurement to have a significance greater than 5σ dates to 2012 [12].

In the past years, charm physics has been gaining interest, as improved experimental conditions allow us to reach higher levels of precisions, unveiling the possibility of observing New Physics phenomena in the charm sector.

An additional reason for lesser attention being dedicated to charm physics is that it is a very challenging field also from a theoretical point of view. Weak decays of charm hadrons often include contributions involving the strong interaction. The short-distance contributions, which occur on the M_W scale, can be calculated perturbatively. On the other hand, the long-distance contributions, occurring on the strong interaction scale, do not allow for perturbative calculations. In rare processes, the long-distance contributions can become prominent or even dominant, making them theoretically much more challenging to predict. This hinders the searches for New Physics, as they require precise prediction for Standard Model contributions to be able to identify possible deviations due to New Physics. If relatively very large, long-distance contributions can shadow the Standard Model and New Physics effects to the point of losing the experimental sensitivity to observing them.

2.2.1 *CP Violation in the Charm Sector*

In the Standard Model, CP violation in the charm sector is expected to be very small. This is due to the fact that only the first two generations of quarks are relevant in charm hadron processes. The quarks that participate in the loops are down-type, and for the case of the intermediate b quark, the associated CKM matrix elements V_{cb} and V_{ub} are both very small (see Figure 1), while the mass of the b quark itself is also not that large (in contrast to the B system, where the t quark contribution is substantial due to its large mass and larger CKM elements). CP violation arises from the complex phase in the CKM matrix. As can be seen from the Wolfenstein parametrisation of the CKM matrix, the elements corresponding to the first two generations are real to the order of λ^2. The complex phase enters only at the order of λ^4, yielding a prediction for CP asymmetries in the Standard Model of the order of 10^{-3}. Studies of CP violation in charm decays have gained focus in the recent years, as experimentally achievable precisions approached a few 10^{-3}. To this date, no observation of CP violation in charm decays has been made.

An experimental overview of measured CP asymmetries in the charm sector is shown in Table 1.

2.2.2 *Radiative Charm Decays $D^0 \to V\gamma$*

Radiative decays of a D^0 meson to a vector meson and a photon take place under the joint occurrence of the weak and electromagnetic interaction. These are rare decays, dominated by the non-perturbative long-distance contributions. Theoretical calculations of branching fractions are thus challenging, and experimental measurements of these decays are welcome as a probe of the QCD-based calculations. The short distance-contributions are estimated to be of the order 10^{-8} [14]. The long-distance contributions have been computed by different authors using different

	$\mathcal{A}_{CP}$	Measured by
$D^0 \to \pi^+\pi^-$	0.0005 ± 0.0015	Belle, LHCb, BaBar, CLEO, FOCUS, E791
$D^0 \to \pi^0\pi^0$	-0.0003 ± 0.0064	Belle, CLEO
$D^0 \to K^0_S\pi^0$	-0.0020 ± 0.0017	Belle, CLEO
$D^0 \to K^0_S\eta$	$0.0054\pm0.0051\pm0.0016$	Belle
$D^0 \to K^0_S\eta'$	$0.0098\pm0.0067\pm0.0014$	Belle
$D^0 \to K^0_S K^0_S$	-0.23 ± 0.19	CLEO
$D^0 \to K^-K^-$	-0.0016 ± 0.0012	LHCb, Belle, CDF, BaBar, CLEO, FOCUS, E791
$D^0 \to \pi^+\pi^-\pi^0$	0.0032 ± 0.0042	BaBar, Belle, CLEO
$D^0 \to K^-\pi^+\pi^0$	0.0009 ± 0.0050	CLEO-c, CLEO
$D^0 \to K^+\pi^-\pi^0$	-0.0014 ± 0.0517	Belle, CLEO
$D^0 \to K^0_S\pi^+\pi^-$	-0.0008 ± 0.0077	CDF, CLEO
$D^0 \to K^-K^+\pi^0$	$-0.0100\pm0.0167\pm0.0025$	BaBar
$D^0 \to K^+\pi^-\pi^+\pi^-$	-0.018 ± 0.044	Belle
$D^0 \to K^+K^-\pi^+\pi^-$	$-0.082\pm0.056\pm0.047$	FOCUS

Table 1: Overview of experimental results for CP asymmetries in the charm sector [13].

	Burdman $et.\,al.$ [17]	Fajfer $et.\,al.$ [18]	Fajfer [19]
$\mathcal{B}r\left(D^0 \to \phi\gamma\right)$ $[10^{-5}]$	0.9-2.1	0.4-1.9	2.8-4.1
$\mathcal{B}r\left(D^0 \to \overline{K}^{*0}\gamma\right)$ $[10^{-5}]$	7-12	6-36	28-49
$\mathcal{B}r\left(D^0 \to \rho^0\gamma\right)$ $[10^{-5}]$	0.6-1	0.1-1	0.31

Table 2: Theoretical predictions of branching fractions of radiative charm decays.
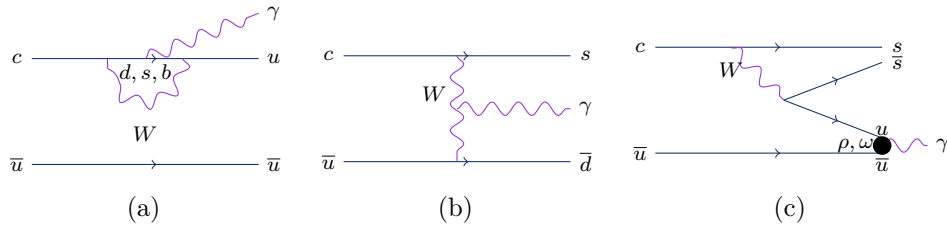
Figure 2: Some examples of Feynman diagrams for $D^0 \to V\gamma$ decays [17].

approaches, such as vector meson dominance, or a model of charm mesons as heavy mesons accompanied by hidden symmetry approach for the vector mesons. The theoretical predictions for the branching fractions of radiative $D^0 \to V\gamma$ decays, where $V = \phi, \overline{K}^{*0}, \rho^0$, are summarised in Table 2. For the ρ^0 mode, recent papers on $\mathcal{A}_{CP}$ use the branching fraction of $\mathcal{O}(10^{-5})$ in their calculations [15, 16], though the details of the calculation of these values are not stated, as they are not the main topic.

Figure 2 shows some examples of Feynman diagrams for short-distance contributions of the decays $D^0 \to V\gamma$. The decay $D^0 \to \overline{K}^{*0}\gamma$ is Cabibbo favoured, as can be seen from Figure 2b, whereas the other two modes are Cabibbo suppressed.

On the experimental side, the CLEO II Collaboration conducted a search in 1998 for $D^0 \to V\gamma$ decays, where $V = \phi, \overline{K}^{*0}, \rho^0$ and ω. Due to limited statistics, they were unable to observe any of the decay modes, resulting in setting the upper limits for the branching fractions [20]. The first observation of a radiative D^0 decay was made by the Belle Collaboration in 2004 [21], where they measured the decay $D^0 \to \phi\gamma$. In 2008, the BaBar collaboration reported an observation and branching fraction measurement of both the decays $D^0 \to \phi\gamma$ and $D^0 \to \overline{K}^{*0}\gamma$ [22]. Since 2008, no updated analysis of decays $D^0 \to V\gamma$ has been published. The world-average values of the branching fractions for decays $D^0 \to V\gamma$ decays, where $V = \phi, \overline{K}^{*0}, \rho^0$, are listed in Table 49. For the unobserved ρ^0 mode, only the upper limit is stated.

Theoretical calculations show that for $V = \phi, \rho^0$, sizeable CP asymmetry can be expected in Standard Model extensions with chromomagnetic dipole operators [15, 16]. The asymemtry could be expected to reach an order of magnitude above the Standard Model predictions of $\mathcal{O}(10^{-3})$. A measurement of $\mathcal{A}_{CP}$ significantly above $\mathcal{O}(10^{-3})$ would thus indicate New Physics. Furthermore, the experimental value can be used

	$\mathcal{B}r[10^{-5}]$
$\phi\gamma$	2.70 ± 0.35
$\overline{K}^{*0}\gamma$	$32.7\ \pm 3.4$
$\rho^0\gamma$	< 24 at 90% C.L.

Table 3: World-average values of branching fractions of radiative charm decays [23].

as a probe for testing chromomagnetic dipole operators contributions, which are not easily measured. Being Cabibbo favoured, the expectation for $\mathcal{A}_{CP}$ in tke $\overline{K}^{*0}$ mode is lesser, as Standard Model predicts a practically negligible CP violation in Cabibbo favoured decays, where the complex term enters only at the order of λ^6 in the Wolfenstein parametrisation.

The aim of the analysis, presented in this thesis, is to measure the branching fraction and CP asymmetry in radiative decays $D^0 \to V\gamma$, where $V = \phi, \overline{K}^{*0}, \rho^0$, on the full data set, collected by the Belle experiment. We will measure the time-integrated CP asymmetry, which includes both direct and indirect CP violation. As stated above, indirect CP asymmetry is universal for all D^0 mesons. Therefore, direct CP asymmetry can in principle be extracted from time-integrated measurements, provided that the indirect CP asymmetry is known.

Throughout this thesis, units are used in which $\hbar = c = 1$.

EXPERIMENTAL SETUP

The here presented analysis is based on data collected with the Belle detector at the KEKB asymmetric e^+e^- collider. The experiment was hosted at the High Energy Accelerator Research Organisation (KEK) in Tsukuba, Japan. The experiment ran from 1999 - 2010, collecting data at and near the $\Upsilon(4S)$ resonance. This chapter briefly describes the KEKB accelerator and the Belle detector. A detailed description is available in Reference [24] for the KEKB accelerator and in Reference [25] for the Belle detector.

3.1 KEKB ACCELERATOR

KEKB is an asymmetric e^+e^- collider, composed of two separate rings with a circumference of about 3 km. Electrons and positrons are first accelerated to the nominal energies in a linear accelerator (LINAC), then injected into the respective rings: the high energy ring (HER) for electrons and low energy ring (LER) for positrons. The beams collide at the single interaction point (IP) at an angle of 22 mrad. The energy of the electron beam is E_{HER}=8.0 GeV and the energy of the positron beam is E_{LER}=3.5 GeV, giving a combined centre-of-mass (CM) energy corresponding to the mass of the $\Upsilon(4S)$ resonance:

$$E_{\mathrm{CM}} = 2\sqrt{E_{\mathrm{HER}} \cdot E_{\mathrm{LER}}} = 10.58\,\mathrm{GeV} \quad . \tag{16}$$

The $\Upsilon(4S)$ resonance is a bound state of $b\bar{b}$ quarks that decays predominantly to a pair of charged or neutral B mesons. Such a setup was chosen in accordance with the main goal of the experiment, which was to study CP violation in the system of B mesons. Other interactions that occur in e^+e^- collisions are Bhabha scattering, two-photon events, muon and tau pair production, and quark par production $q\bar{q}$, where $q = u, d, s, c$. The cross-sections for all interactions are listed in Table 4. In addition to the nominal CM energy, the experiment collected data also at energies corresponding to the $\Upsilon(nS)$ resonances, where n = 1, 2, 3, 5, and also at energies below the resonances.

The rate of particle collisions is described by the collision cross section and the luminosity parameter of the accelerator:

$$\frac{dN}{dt} = \mathcal{L}\sigma \quad . \tag{17}$$

KEKB achieved a peak luminosity of $2 \cdot 10^{-34}$ cm^{-2}s^{-1}, which surpassed the design luminosity by a factor of 2. The measure of the collected data is the integrated

Interaction type	$\sigma[\mathrm{nb}]$
$b\bar{b}$	1.1
$c\bar{c}$	1.3
$q\bar{q}\,(q\,\epsilon\,u,d,s)$	2.1
$\tau^+\tau^-$	0.93
Bhabha scattering	37.8
$\gamma\gamma$	11.1

Table 4: Cross-sections for various interaction types in e^+e^- collisions at $E_{\mathrm{CM}} = 10.58$ GeV. The value of the cross-section for Bhabha scattering is given for the acceptance region of the Belle detector ($2.55° < \theta < 159.94°$).

luminosity $\mathcal{L}_{int} = \int \mathcal{L}dt$. The total integrated luminosity, collected by the KEKB accelerator, is slightly more than 1 ab^{-1}.

3.2 BELLE DETECTOR

The Belle detector is a large-solid-angle magnetic spectrometer, positioned around the IP. The configuration and sub-detectors are depicted in Figure 93. Decay vertices are reconstructed by the Silicon vertex detector (SVD). Momentum of charged particles is measured by the Central drift chamber (CDC). Particle identification in different momentum regimes is provided by the CDC, the Aerogel Cherenkov counter (ACC) and Time-of-flight counter (TOF). The Electromagnetic calorimeter (ECL) measures the energy of electromagnetic showers. All above-mentioned sub-detectors are positioned within a superconducting solenoid magnet, producing a magnetic field of 1.5 T. The solenoid axis coincides with the positron axis. Muons and K_L particles are detected with the outermost sub-detector (KLM).

The coordinate system, originating at the IP, is defined so that the z axis is pointing in the opposite direction of the positron beam, the horizontal x axis is pointing toward the outside of the ring, and the y axis is vertical. The angle θ is the polar angle to the z-axis. The Belle detector covers the polar angle between $17° < \theta < 150°$, corresponding to 93% of the solid angle.

3.2.1 *Silicon Vertex Detector*

The SVD measures the vertices of decaying particles with a precision of ≈ 100 μm. It is positioned immediately outside the beam pipe, as distance from the IP directly reflects on the resolution due to multiple Coulomb scattering.

The SVD is composed of layers of Double-Sided Silicon Detectors (DSSD). Two different SVD configurations were used during the experiment, denoted as SVD1 and SVD2. SVD1 is composed of three layers, positioned at distances 30, 45.5 and 60 mm from the IP. It covers a polar angle between $23° < \theta < 139°$. SVD1 was in operation from the beginning of the experiment until 2003, when it was replaced by the SVD2, which remained in place until the end of data taking. SVD2 is composed of four layers, positioned at distances 20, 43.5, 70 and 80 mm from the IP. It increases the coverage of the polar angle to match that of the CDC. Due to the increased number of layers and reduced distance of the first layer from the IP, the impact parameter resolution is greatly improved in SVD2. The resolution of the impact parameter as a function of the pseudo-momentum is shown in Figure 4 for both configurations. The pseudo-momentum is defined as $p\beta \sin^{5/2}(\theta)$ for the z direction, and $p\beta \sin^{3/2}(\theta)$ for the plane, perpendicular to the z direction. β denotes v/c.

3.2.2 *Central Drift Chamber*

The CDC measures the tracks of charged particles in a magnetic field and determines their momentum. It is a multi-wire drift chamber, filled with 50% - 50% helium-ethane mixture. The low-Z gas reduces the degradation of momentum resolution due to multiple Coulomb scattering. The CDC occupies the space between 103.5 mm and 874 mm in the radial direction. The angular coverage is $17° < \theta < 150°$. The position
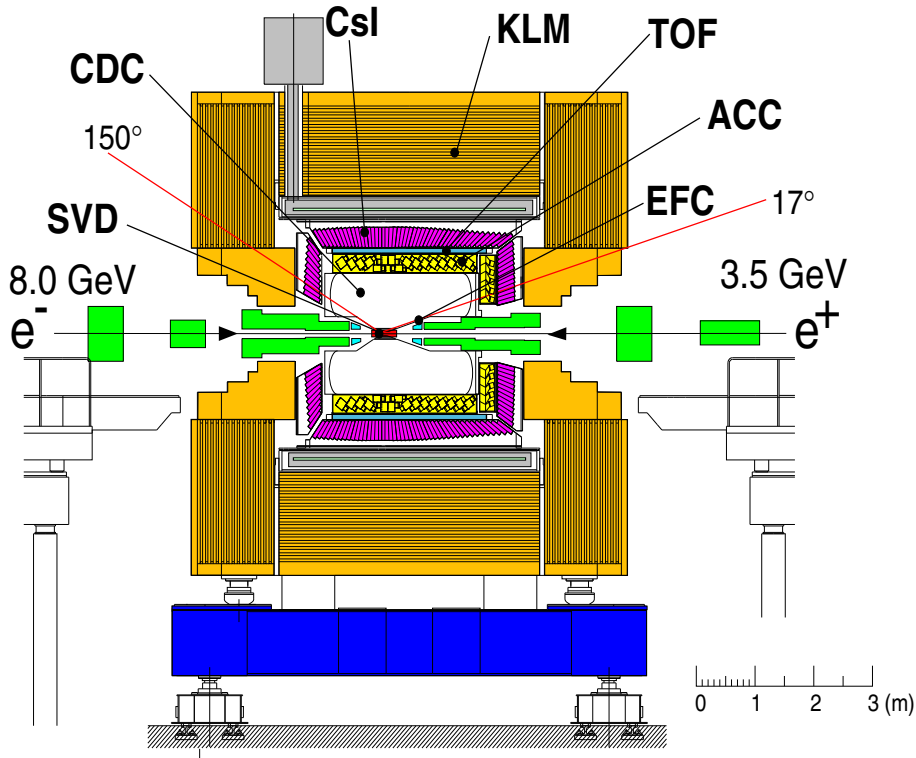
Figure 3: The Belle spectrometer [25].
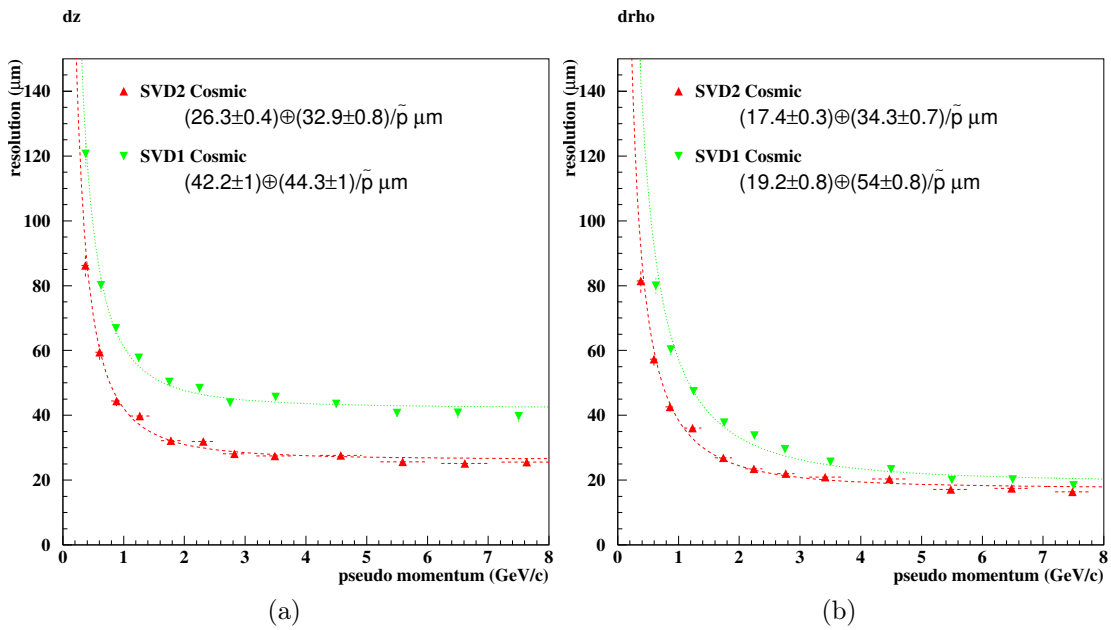
Figure 4: Impact parameter resolutions of SVD1 and SVD2 in the z direction (a) and in the plane, perpendicular to the z direction (b) [25].
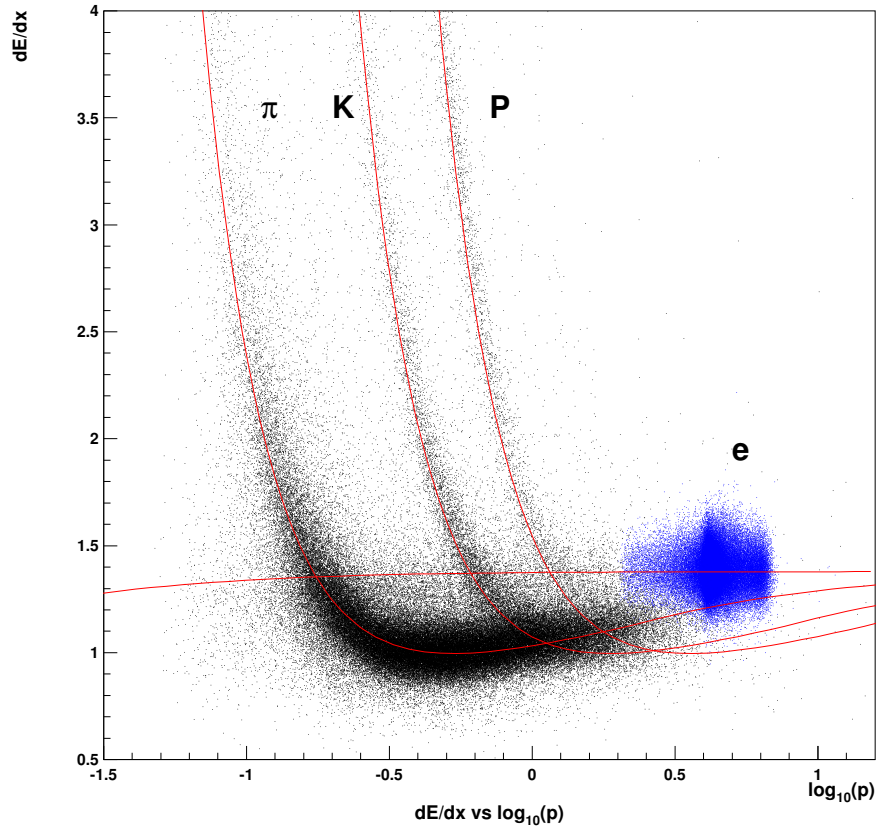
Figure 5: Measured dE/dx as a function of particle momentum [25]. The red lines show the expected distribution for different types of particles.

of a particle hit is determined from the time difference between the passage of the particle, which triggers a scintillation counter, and the detection of the pulse on the sense wire. An algorithm sorts hits into helical tracks and extracts the transverse momentum $p_T = \sqrt{p_x^2 + p_y^2}$ and p_z. From the fitted parameters of the track, p_x and p_y can be calculated for an arbitrary position on the track. The resolution of the transverse momentum can be expressed as

$$\frac{\sigma_{p_T}}{p_T} = (0.201 \pm 0.003)\% p_T \oplus (0.290 \pm 0.006)\%/\beta \quad , \tag{18}$$

where p_T is in units of GeV. This gives an uncertainty between 0.3% and 1.1% for particles with 0.6 GeV $< p_T < 5$ GeV.

Besides momentum measurements, the CDC also provides particle identification in the low-momentum regime through measurements of specific ionisation. The amplitude of the pulse on the wire is proportional to the energy loss $-dE/dx$, which is a function of the velocity of the particle. Figure 5 shows the momentum dependence of energy loss for different particles. The CDC enables a separation between pions and kaons up to 3σ for particles with momentum less than 0.8 GeV.

K/π Separation vs. Momentum

$$\text{SigSep} = (\mu_\pi - \mu_K)/\text{sqrt}(\sigma_\pi^2 + \sigma_K^2)$$
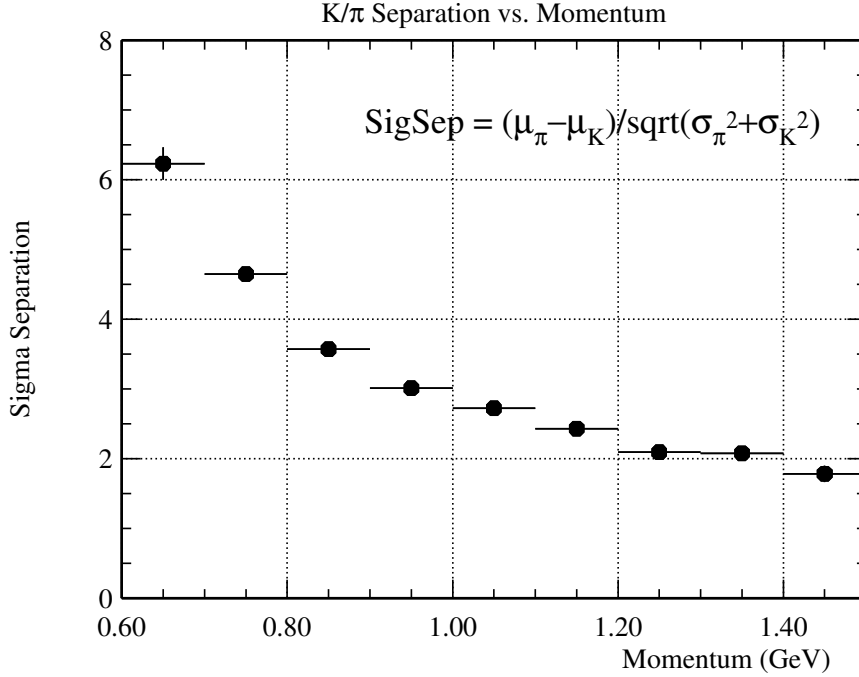
Figure 6: K/π separation power of TOF in units of standard deviation [25].

3.2.3   *Time-of-flight Counter*

The TOF provides particle identification in the momentum region between $0.8 < p < 1.2$ GeV. It consists of modules of fast plastic scintillator, concentrically arranged around the z axis at the radius 1.2 m. It covers the polar angle between $34° < \theta < 120°$. The scintillating photons are detected with fine mesh photo multipliers that are attached to the scintillators. The time interval between the e^+e^- collisions and the passage of the particle through the TOF is measured with a resolution of about 100 ps. The mass m of charged particles is then obtained as

$$m = p\sqrt{\frac{t^2}{l^2} - 1} \quad , \tag{19}$$

where t is the time measured by the TOF, p is the momentum measured by the CDC and SVD and l is the helix length from the IP to the TOF module. The separation between pions and kaons in terms of σ as a function of momentum is shown in Figure 6.

Additionally, the TOF is equpped with thin Trigger Scintillation Counters that provide additional trigger input.

3.2.4 *Aerogel Cherenkov Counter*

The ACC provides particle identification in the high-momentum regime, for $1.2 < p < 3.5$ GeV. It consists of Cherenkov treshold counters with silica aerogel radiators, covering the polar angle between $17° < \theta < 127°$. Charged paricles passing through a medium with a refractive index n emit Cherenkov radiation if their velocity exceeds the velocity of light in the medium:

$$\beta_{\text{treshold}} = \frac{1}{n} \quad . \tag{20}$$

The refractive indices in the ACC are between 1.01 and 1.03, depending on the polar angle, so that pions in the momentum region of interest emit Cherenkov light, while kaons do not. Cherenkov photons are collected with fine mesh photomultipliers attached to the aerogel. The kaon identification efficiency is 80% or more, with a pion fake rate below 10%.

3.2.5 *Electromagnetic Calorimeter*

The ECL provides energy and position measurements for photons and complementary particle identification for electrons, mainly separating them from pions. It consists of a highly segmented array of CsI(Tl) crystals, in which electrons and photons produce electromagnetic showers due to bremsstrahlung and pair production. The crystals are of the shape of a truncated pyramid pointing inward. The barrel crystals have a front-face cross-section of 55×55 mm and a rear-face cross-section of 65×65 mm. The dimension of the end-cap crystals have large variations, from 44.5 to 82 mm. The geometry of the crystals ensures that about 80% of the deposited energy is contained within the original crystal in which the shower starts, giving good energy resolution, while still providing good position resolution. The barrel section has an inner radius of 1.25 m, while the end-caps are positioned at -1.0 and 2.0 m from the IP in the z direction. Such a setup provides polar angle coverage between $17° < \theta < 150°$. Photons are detected with silicon photodiodes. The energy resolution, calibrated with Bhabha events, is shown in Figure 7. The average resolution is about 1.7%. It is given by

$$\frac{\sigma_E}{E} = \frac{0.0066(\%)}{E} \oplus \frac{1.53(\%)}{E^{1/4}} \oplus 1.18\% \quad , \tag{21}$$

where E is in units of GeV. The position resolution in mm is

$$\sigma_x = 0.27 + \frac{3.4}{\sqrt{E}} + \frac{1.8}{\sqrt[4]{E}} \quad . \tag{22}$$

Since hadrons and muons do not produce showers in the ECL and lose only a small portion of their energy by means of ionisation, the information from the ECL, compared with momentum measurements provided by the CDC enables the identification of electrons. The distribution of the deposited energy for different particles is shown in Figure 8. The probability of misidentifying an electron as a pion is approximately 5% for momenta less than 1 GeV, and less than 1% for momenta above 2 GeV.
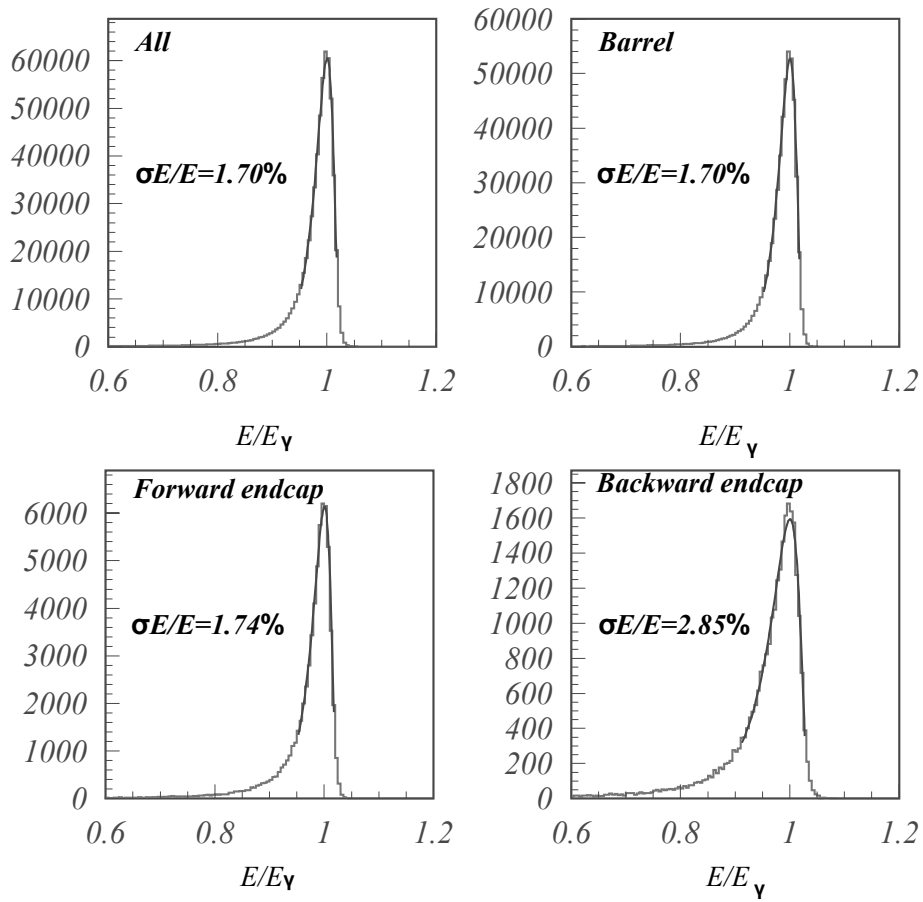
Figure 7: Energy resolution for overall, barrel, forward and backward end-cap calorimeters [25].
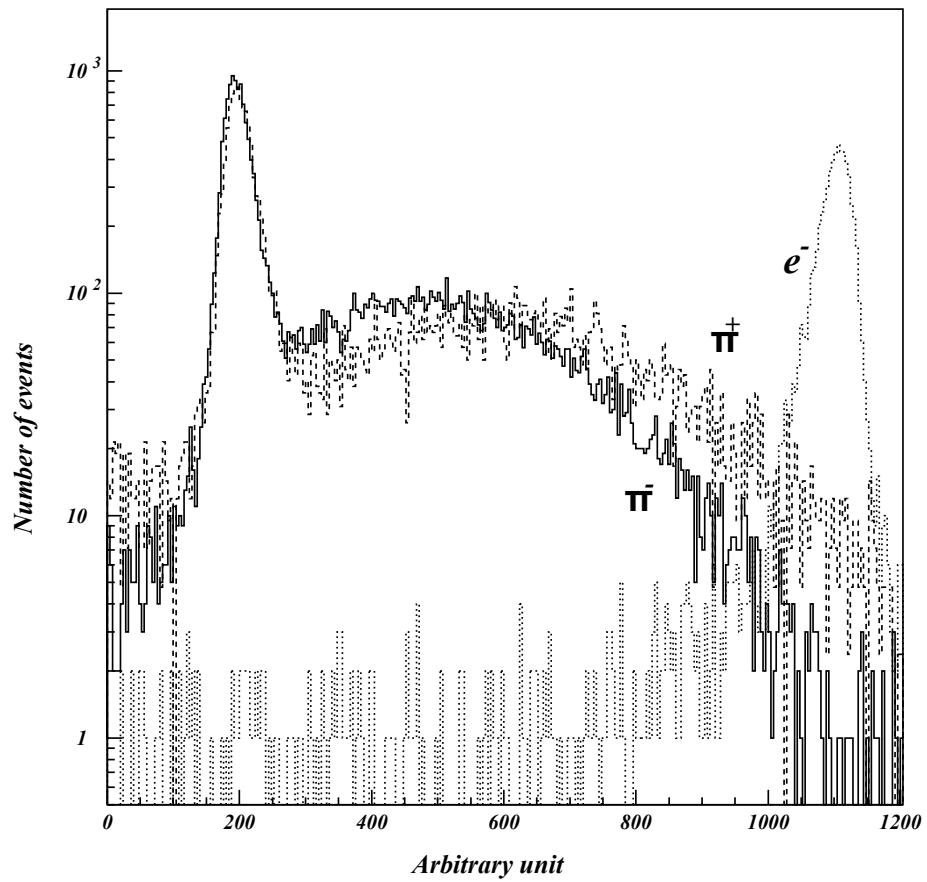
Figure 8: Deposited energy in the ECL by e^-, π^+ and π^- at a momentum of 1 GeV/c [25].
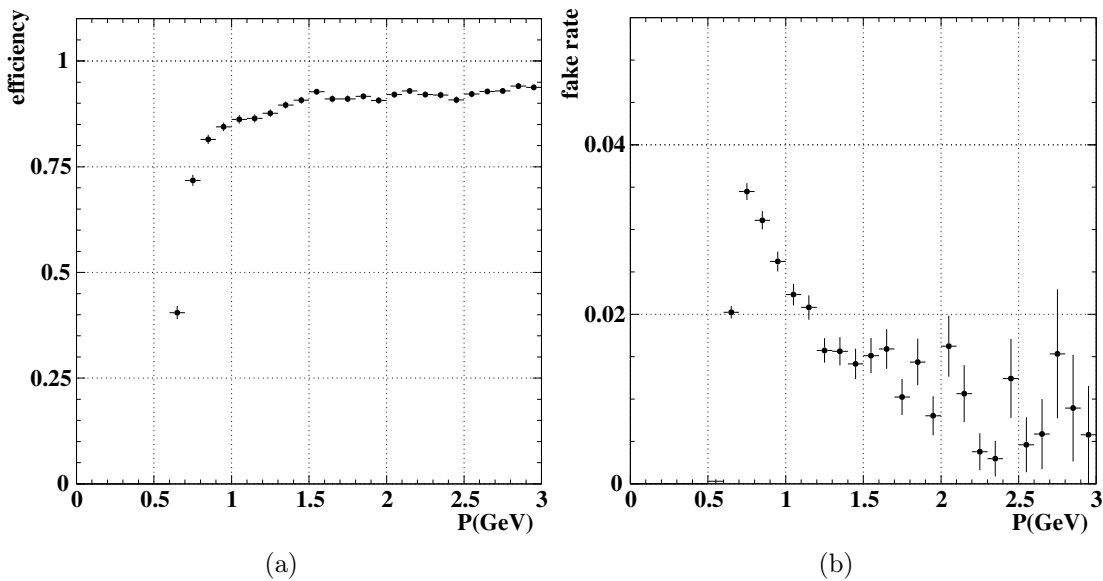
Figure 9: Muon efficiency (a) and fake rate (b) as a function of momentum [25].

3.2.6 K_L and Muon Detector

The KLM provides the detection and identification of K_L particles and muons in a wide momentum range, for $p > 600$ MeV. It consists of interchanging layers of glass resistive-plate chambers (RPCs) that detect charged particles and thick iron layers. The RPC modules consist of parallel plate electrodes, filled with gas. A charged particle passing the gas gap intiates a local discharge of the plates, which in turn induce signal to record the time and location of ionisation. The setup covers the polar angle between $20° < \theta < 155°$. K_L particles produce a shower of ionising particles in the iron plates that are detected with the RPCs. The flight direction of the K_L particles can be inferred from the location of the shower. They are distinguished from muons by the absence of a track in the CDC. Muons are distinguished from other charged particles, electrons and hadrons, as they penetrate much further in the KLM due to lesser bremsstrahlung energy losses and the fact that they do not interact strongly. The efficiency of muon identification for momenta above 1.5 GeV is greater than 90%, while the false positive rate is below 5%, as is shown in Figure 9.

3.2.7   Trigger and Data Acquisition

The purpose of the trigger system is to reduce the rate of data by immediately eliminating events that are not of interest, so that the amount of stored data is within the 500 Hz event limit of the data acquisition system (DAQ) and the efficiency for physics processes of interest is maximised. Only events that pass the trigger criteria are transfered by the DAQ to the data storage system. The trigger system comprises three stages: a Level 1 (L1) hardware trigger, a Level 3 (L3) software trigger and an offline Level 4 (L4) trigger. The system is described in detail in Reference [25].
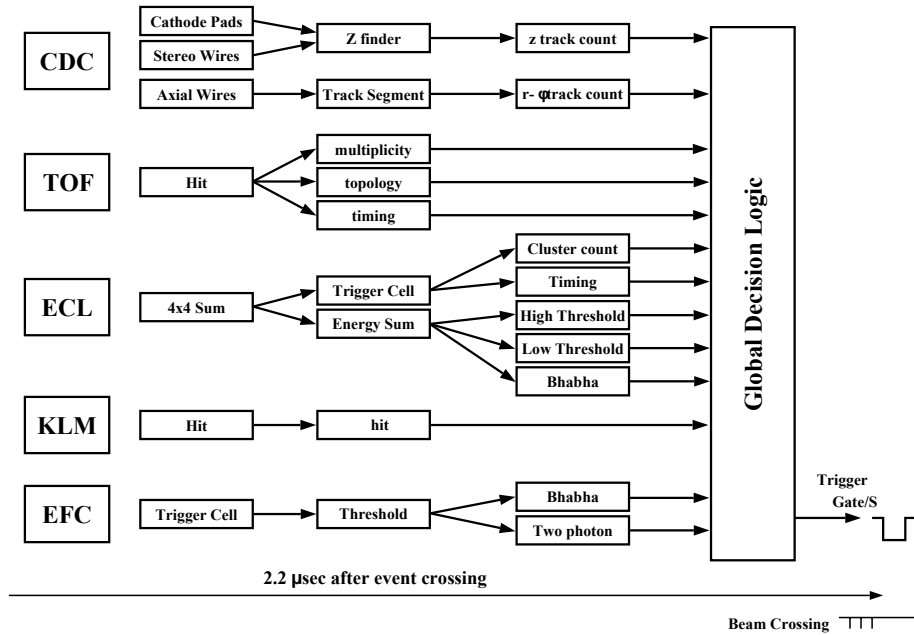
Figure 10: Schematics of the L1 trigger system [25].

The L1 trigger collects information from individual sub-detectors and feeds it into a central trigger system called the Global Decision Logic (GDL). A schematic overview of the L1 trigger is shown in Figure 10. In general, the sub-detector triggers work on two principles: whether a hit (or track) is detected, or by the measured energies. The information from the sub-detector triggers reaches the GLD withing 1.85 μs after the collision, and the final trigger signal is provided within 2.2 μs. The combined efficiency is greater than 99.5% for hadronic events.

The L3 trigger performs a fast reconstruction and rejects all events with no tracks with the impact parameter satisfying the condition $|dz| < 5.0$ cm, and for which the total energy deposit in the ECL less than 3 GeV. The L3 trigger reduces the event rate by 50%, with a 99% efficiency for hadronic events.

The L4 is an offline trigger that decides whether an event is appropriate for full reconstruction just before the Data Summary Tape (DST) production. Being offline, it enables a more advanced reconstruction than the L3 trigger. Events must satisfy the following conditions to pass: there must be at least one track with the transverse momentum $p_T > 300$ MeV, impact parameters must satisfy $|dr| < 1.0$ cm and $|dz| < 4.0$ cm, and the total energy deposit in the ECL must be greater than 4 GeV. Approximately 78% of triggered events are rejected, while keeping an almost full efficiency for hadronic events. Unlike the lower level triggers, the rejected data is not discarded.

Events that pass the L4 trigger are fully reconstructed and stored to the DST. The raw data is transformed into physical objects (particle identification information, helix parameters, momentum 4-vectors...). Events are classified into categories, e.g. hadronic, Bhabha, μ pair, etc.

3.2.8 *Particle Identification*

Several of the above described subdetectors are capable of providing information about the identity of particles. Each subdetector provides a probability for a particle to be of a certain type. Information from several subdetectors can be combined into a final likelihood.

Information about charged particle identification, e.g. pions and kaons, is obtained by combining information from the CDC, TOF and ACC. The likelihood for a particle to be of type f is obtained by multiplying the likelihoods from the subdetectors:

$$\mathcal{L}_f = \mathcal{L}_f^{\mathrm{CDC}} \cdot \mathcal{L}_f^{\mathrm{TOF}} \cdot \mathcal{L}_f^{\mathrm{ACC}} \quad . \tag{23}$$

The joint information from the three subdetectors provides a 3σ separation between kaons and pions for momenta up to 3.5 GeV.

SELECTION AND RECONSTRUCTION OF SIGNAL EVENTS

We are studying the decay of the D^0 meson in three signal channels: $\phi\gamma$, $\overline{K}^{*0}\gamma$ and $\rho^0\gamma$. Each vector meson is reconstructed in one chosen decay mode to a pair of oppositely charged hadrons. The exact decay chains used in the analysis are

$$
\begin{aligned}
D^{*+} &\to D^0\pi_s^+ \quad, \\
D^0 &\to \phi\gamma \to K^+K^-\gamma \quad, \\
D^0 &\to \overline{K}^{*0}\gamma \to K^-\pi^+\gamma \quad, \\
D^0 &\to \rho^0\gamma \to \pi^+\pi^-\gamma \quad.
\end{aligned}
$$

In order to study the CP asymmetry it is necessary to separate the D^0s and $\overline{D}^0$s in the sample. The flavour of the D^0 meson cannot be unambiguously determined solely from the decay products, especially for the ϕ and ρ^0 channels, as the final state is self-conjugate (it could be done to a certain precision level for the $\overline{K}^{*0}$ decay mode, where the ratio of the suppressed $K^+\pi^-$ decay compared to the favoured $K^-\pi^+$ decay is less than 1%). In order to provide the necessary tag on the neutral meson flavour, we restrict ourselves to D^0s coming from decays $D^{*+} \to D^0\pi_s^+$, and determine the flavour of the D^0 based on the charge of the slow pion. The decay $D^{*+} \to D^0\pi_s^+$ is a suitable choice for this task, with the branching fraction of 67.7% and the cross-section for $e^+e^- \to c\bar{c} \to D^{*+}X$, X is anything, of 597 pb [26] being sufficiently high to ensure a significant statistics of the D^0 sample. In addition, this condition enables us to set a constraint on the mass difference between the D^0 and the D^{*+} (optionally also subtracting the mass of the slow pion), and thus reducing the combinatorial background by a significant amount. This channel provides an exceptionally good background suppression due to the fact that the typical momentum of the pion in the decay $D^{*+} \to D^0\pi_s^+$ is very low (hence the subscript s, standing for "slow"), which enables the measurement of its momentum to a very high degree of precision. The resolution of the reconstructed D^{*+} will thus be almost exclusively governed by the uncertainties of the D^0. When looking at the mass difference $\Delta m = m(D^{*+}) - m(D^0)$, these uncertainties will in large part subtract, leaving the Δm distribution with a resolution about an order of magnitude better than the resolution of the invariant mass of the D^0 and enabling a very tight constraint on Δm, thus eliminating a large amount of background. The difference in resolutions between $m(D^0)$ and Δm can be seen e.g. in Figures 11a and 11c for the ρ^0 mode.

The ρ^0 decay mode requires a special consideration, as there is another radiative decay, $D^0 \to \omega\gamma$, that decays to the same final state ($\omega \to \pi^+\pi^-$). Coupled with the fact that their nominal masses lie very close ($m_{\rho^0} = 775$ MeV, $m_\omega = 782$ MeV), the mass distributions will overlap, making it an impossible task to clearly separate the two modes. Theoretical studies predict the branching fraction for the $D^0 \to V\gamma$ decay to be of the same order of magnitude for both modes [27]. However, while ρ^0 almost exclusively decays to a pair of charged pions, ω decays in this channel only in 1.5% of events. Assuming an equal branching fraction for radiative charm decays for both mesons, the ω mode becomes negligible in our analysis and we expect the result in the $\pi^+\pi^-\gamma$ channel to represent solely the ρ^0 mode. We will however study the invariant mass distribution of the charged pion pair, where we expect the ρ^0 contribution to exhibit a significantly wider shape than the ω, since the natural width of the ω resonance is much smaller than that of the ρ^0 resonance. An evaluation of the results in different bins of the $\pi^+\pi^-$ invariant mass can provide us with a clearer image of the fractions of ρ^0 and ω in our sample. This will be investigated, should we see a positive signal. Basing ourselves on theoretical predictions, we will therefore consider the $\pi^+\pi^-$ channel as arising solely from the ρ^0 mode during the main stage of our analysis, and estimate the systematic uncertainty of this assumption in the end. As the ρ^0 resonance is by far the broader one, any constraints regarding the mass distribution that will be applied are chosen according to this resonance, and completely cover also the narrower ω mode.

4.1   DATA SAMPLE

While most of the Belle data was collected at the $\Upsilon(4S)$ resonance, smaller data sets have been recorded also at different energies. The present analysis is based on data collected at the $\Upsilon(nS)$ resonances, where $n = 2, 3, 4, 5$, as well as data collected at energies just below the threshold of the resonances. The integrated luminosity of the total sample amounts to 943 fb^{-1}.

4.2   MONTE CARLO SIMULATION

The entire analysis procedure is developed and tested on Monte Carlo simulations. The Monte Carlo simulation is done in two steps: first, the decay process is generated with `EvtGen` [28], after which the detector response is simulated using `GEANT3` [29]. The final state radiation is described by `PHOTOS` [30].

There are two main categories of simulation that are used: dedicated Monte Carlo, which generates a specific event for the purpose of a detailed study, and generic Monte Carlo simulation. The latter simulates the general events in the detector based on the known branching fractions and cross-sections. The Belle Collaboration provides 6 streams of generic Monte Carlo, with each stream representing and equaling in luminosity the entire Belle data sample. We use all available 6 streams of generic Monte Carlo that match the intended data sample. As the signal decays are rare (in case of the ρ^0 mode, the branching fraction has not been measured yet), they
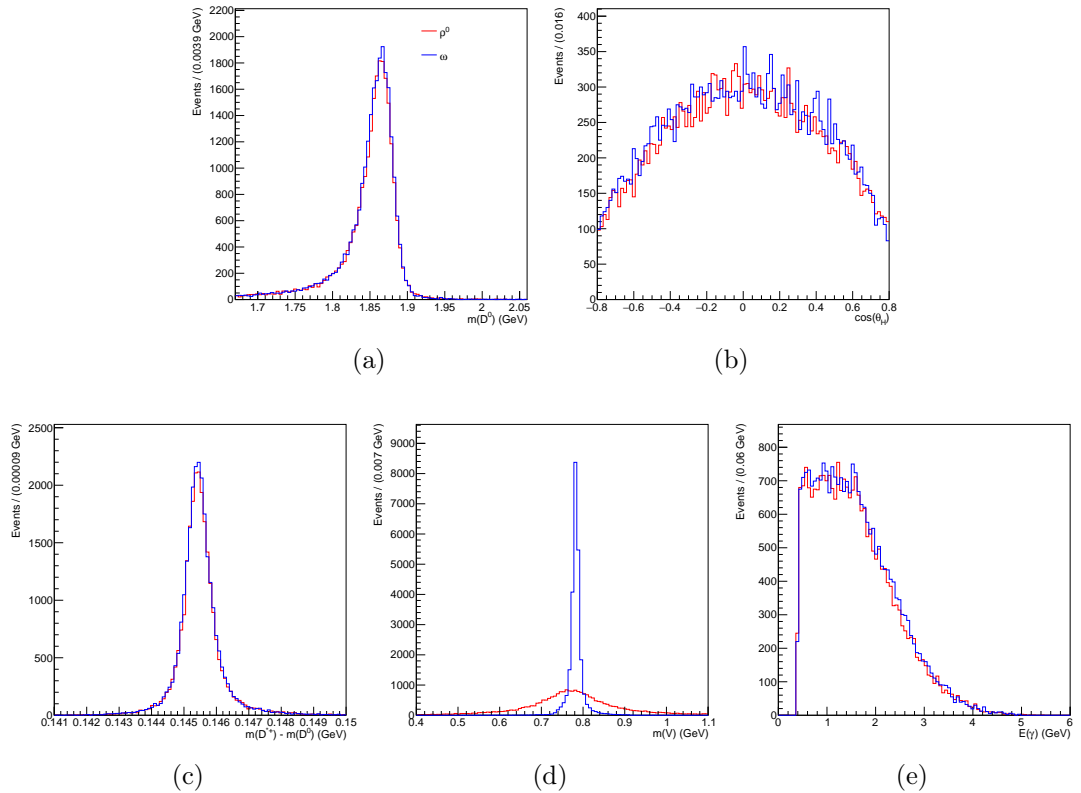
Figure 11: Comparison of $m(D^0)$, $\cos(\theta_H)$, Δm, $m(V)$ and $E(\gamma)$ distributions for the ρ^0 and ω decay mode.

are not included in the Belle generic Monte Carlo, which thus represents solely the background that is expected when reconstructing the signal decays on the data sample. For studying signal decays, dedicated signal Monte Carlo simulations are generated for each decay mode, comprising $2 \cdot 10^5$ events (10^5 events for each flavour of the D^0 meson).

As discussed earlier in this section, we expect the decay mode with final state particles $\pi^+\pi^-\gamma$ to represent predominantly the decay through the resonance ρ^0, with a small admixture of the ω resonance. Although we expect the contribution of ω to be minor, we cannot state this with absolute certainty, since both branching fractions have not been measured yet. We decide to use a joint signal Monte Carlo simulation for the $\pi^+\pi^-\gamma$ decay mode, comprising both resonances in equal measure. Such a decision is justified by checking for both modes the distributions in variables that we expect to use in our analysis. As can be seen in Figure 11, the distributions differ significantly in the mass of the reconstructed vector meson, a quantity that will not be used for the main purpose of the analysis (except for a mass width selection criteria, which will be based on the ρ^0 width and thus covers also the much narrower ω resonance), but can be used at the final stage of the analysis to investigate the exact fraction of the two decay modes in the $\pi^+\pi^-\gamma$ sample. All other distributions match, making the specific fraction of the two decay modes in the sample irrelevant for the purpose of the main analysis.

It is necessary to keep in mind that the simulation does not reproduce collected physical data perfectly in all aspects of all decays. Typically, the distributions on Monte Carlo will be narrower than distributions on real physical data, due to failure to include each and all factors that contribute to diminishing the resolution, especially in the second stage which simulates the detector response. Differences between the simulation and data that could have a significant impact on the analysis procedure and results must be carefully studied and accounted for. In certain cases, measures can be taken to correct these discrepancies and achieve agreement between Monte Carlo and data. When such corrections are not possible, a systematic error due to the discrepancy must be determined and assigned to the final result. Such cross-checks will be performed further into the analysis and suitable measures will be taken.

4.3 PRE-SELECTION

A relatively loose set of pre-selection criteria is applied during the reconstruction of signal decays in order to capture the grand majority of signal events and immediately discard events that in no aspect resemble signal decays.

The joint information from the CDC, ACC and TOF are combined into likelihood ratio for particle identification, from the likelihoods that the particle is either a kaon or a pion:

$$\mathcal{P}_{K/\pi} = \frac{\mathcal{L}_K}{\mathcal{L}_K + \mathcal{L}_\pi} \quad . \tag{24}$$

Particles with $\mathcal{P}_{K/\pi}$ exceeding (beneath) a chosen value are classified as kaons (pions).

For particles that are reconstructed from a combination of other particles (vector mesons, D^0, D^{*+}), we constrain the allowed deviation of the mass of the reconstructed particle from the nominal value [23], by requiring that the mass of the reconstructed particle lies in a certain window around the nominal mass. Similarly, the mass difference Δm is constrained to be below a certain value (the nominal value of Δm is 145.4 MeV [23]).

The centre-of mass (CMS) momentum of the D^0 is constrained to be above a chosen value. This in turn constrains the momentum of the D^{*+}, as the two are correlated.

The three candidate daughter particles of the D^0 (f^+, f^- and γ) are refitted to a common point of origin. Similarly, the reconstructed D^0 and the slow pion are refitted to a common vertex, with the added requirement that both originate in the e^+e^- interaction region. In both cases, an additional constraint on the mass window is imposed following the vertex fit. Such a step is necessary because during the refitting, the values of the momentum of the particles are changed in order to achieve the best vertex match. Consequentially, the invariant mass distribution becomes smeared at the edges of the chosen interval. A tighter mass window constraint is applied to eliminate this effect. In the case of the D^0, the cut is performed on the invariant mass, whereas for the D^{*+} the constraint is applied to the mass difference Δm, since the resolution of this distribution is by far better (as discussed previously).

The applied criteria are summarised in Table 5.

$\mathcal{P}_{K/\pi}$ (pions)	<0.9
$\mathcal{P}_{K/\pi}$ (kaons)	>0.1
mass window ϕ	± 20 MeV
mass window $\overline{K}{}^{*0}$	± 220 MeV
mass window ρ^0	± 245 MeV
mass window D^0	± 225 MeV
$p_{\text{CMS}}(D^0)$	> 2 GeV
p-value of D^0 vertex fit	>0.001
mass window after D^0 vertex fit	$1.665 \text{ GeV} < m(D^0) < 2.065 \text{ GeV}$
mass window D^{*+}	± 200 MeV
p-value of D^{*+} vertex fit	>0.001
Δm after D^{*+} vertex fit	<160 MeV

Table 5: Pre-selection criteria during reconstruction.

4.4 DOMINANT BACKGROUND AND $\pi^0(\eta)$ VETO

As our signal decays are rare, we expect a significant amount of background in our reconstructed data sample. The bulk of the background is expected to come from D^0 decays to $f^+f^-\pi^0$ (or, to a lesser amount, η) instead of a photon, with the $\pi^0(\eta)$ subsequently decaying to a pair of photons. In such cases, the final state particles are the same as in our signal decays, with one additional photon that can easily be missed in the reconstruction, especially if it is of low energy or the two clusters are merged in the ECL. The energy of the lost photon is limited by the allowed D^0 invariant mass range, however this constraint is quite loose, since also sidebands in $m(D^0)$ are needed in order to better parametrise the background further into the analysis.

In decays of a $\pi^0(\eta)$, the opening angle between the two daughter photons decreases with the increasing momentum of the particle. In decays of a highly energetic $\pi^0(\eta)$, the angle can become so small that the two clusters in the ECL will overlap. In an extreme case, the algorithm identifies them as one cluster. However, also if the centres of the showers are far enough apart and the clusters are be correctly recognised as two separate events, the overlapping area will typically be attributed to the larger cluster, resulting in an incorrect determination of the deposited energy. A schematic diagram of the energy deposit in the ECL is shown in Figure 12a. Events with a merged cluster can be removed to a high degree with a cut on the variable E_9/E_{25}. This is the ratio between the energy deposited in the 3×3 array of ECL crystals, and the energy deposited in the enclosing 5×5 array of ECL crystals. The electromagnetic showers caused by photons are generally very focused and the corresponding value of the variable E_9/E_{25} is close to 1, while for merged clusters this ratio will be smaller. Merged clusters can thus be rejected by requiring that the ratio exceeds a certain

(a)   (b)
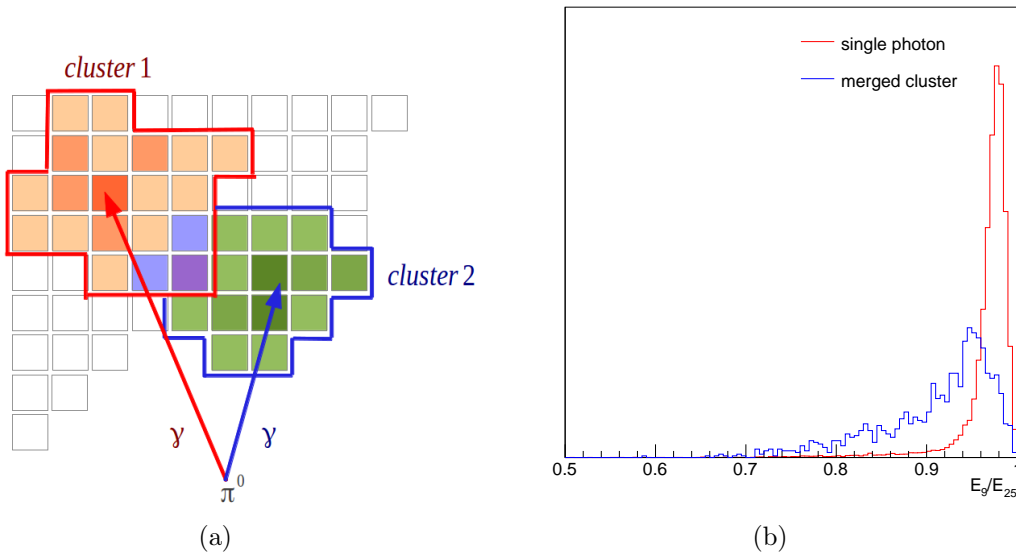
Figure 12: The left plots shows a schematic view of two overlapping clusters in the ECL, caused by a highly energetic π^0. The right plot shows a comparison of the E_9/E_{25} distributions for single photons and for merged clusters.

value. A schematic comparison of the E_9/E_{25} distributions for single photons and for merged clusters is shown in Figure 12b.

The invariant mass of the reconstructed D^0 in these dominant background decays will lie close to the D^0 nominal mass, with the value decreasing as the energy of the lost photon increases. The reconstructed $m(D^0)$ distribution of π^0-type decays will peak at a slightly lower value that the nominal D^0 mass, but still overlap with the signal distribution peak, and exhibit an enhanced left hand tail corresponding to the missing energy of the lost photon. This is demonstrated in Figure 13. All described features can be observed. The peak of the $m(D^0)$ distribution of η-type decays will be shifted toward lower values due to the greater mass of the η, which reflects in a greater energy of the missed photon. The peak of such decays will thus decouple from the signal peak, but still remain in the chosen $m(D^0)$ interval (see Figure 13). Due to greater missing mass and smaller branching fraction, the η-type decays are expected to contribute a lesser amount of background than the π^0-type decays.

The decays in question can be of the type $D^0 \to V\pi^0(\eta)$, where the vector meson is the same as in the signal decays, or a completely different decay chain resulting in the same charged final state particles and a $\pi^0(\eta)$ instead of a single photon, eg. $D^0 \to K^-\rho^+(\to \pi^+\pi^0)$. As the branching ratio of these decays can easily supersede that of our signal decays by one or more orders of magnitude (e.g. $\mathcal{B}r(D^0 \to \overline{K}^{*0}(\to K^-\pi^+)\pi^0)$=1.88%, $\mathcal{B}r(D^0 \to K^-\rho^+) = 10.8\%$, compared to $\mathcal{B}r(D^0 \to \overline{K}^{*0}\gamma) = \mathcal{O}(10^{-4})$), they represent a formidable source of background and a strategy is needed to reduce these contributions - a $\pi^0(\eta)$ veto, which determines the probability of a photon to be coming from a $\pi^0(\eta)$ decay. Based on this probability, a selection criterion is chosen to remove most efficiently as large a portion of events of this
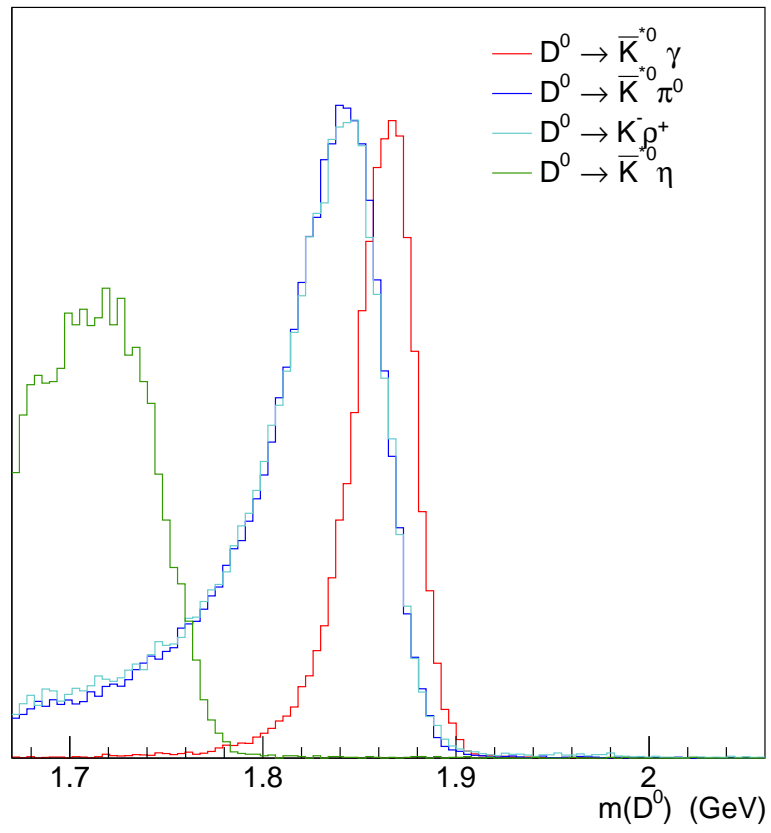
Figure 13: Schematic comparison between the $m(D^0)$ distributions of signal, two π^0-type background modes and an η-type mode for the $\overline{K}^{*0}$ channel.

background type as possible, while minimising the loss of signal events. Several possibilities were explored in order to achieve the most suitable veto.

4.4.1   Mass Veto

A simple mass veto calculates for each photon the invariant mass in combination with another photon (doing this for all other photons in the event). If both photons come in fact from a $\pi^0(\eta)$ decay, this value will yield the mass of the $\pi^0(\eta)$. To each photon the combination that lies closest to the $\pi^0(\eta)$ nominal mass is assigned, resulting in a distribution that peaks at the $\pi^0(\eta)$ mass if decays with a $\pi^0(\eta) \to \gamma\gamma$ are present in the data sample.

An additional possibility is imposing a constraint on the energy of the second photon while calculating the diphoton invariant mass. There is considerably more noise at low energies, hence the chance of a random combination of two photons yielding an invariant mass value close to the π^0 mass decreases with a demand for a minimal required energy. The above mentioned calculation is thus performed with different requirements on the energy of the second photon, assigning to each photon several different diphoton mass variables. Figure 14 shows the distribution of the diphoton invariant mass for signal and for π^0-type backgrounds for four different energy constraints on the second photon in the ρ^0 channel (it is assumed that the distributions are similar for the other two signal modes): 30 MeV, 75 MeV, 100 MeV and 150 MeV. It is obvious that the constraints of 75 MeV or higher, efficiently eliminate the peak at the π^0 mass in signal from random combinations, however the distributions for π^0 backgrounds reveal that stricter requirements also fail to account for some true $\pi^0 \to \gamma\gamma$ decays. All four variables are retained for further evaluation. The analogous plots for the η background are shown in Figure 15. In this case, even the 150 MeV constraint is not able to entirely suppress the random η combinations. It is plausible to assume the η mass veto will be less efficient compared to the π^0 mass veto.

4.4.2   Energy Asymmetry

As it was mentioned above, the photon noise level drastically increases towards low energies. Therefore, when combining two photons, a lot of chance combinations of the invariant mass incidentally lying close to the π^0 mass will include one of the low-energy photons. Background will thus have a peak at a high values of the energy asymmetry, making it a candidate variable to distinguish between signal and background. Similarly to the simple mass veto, the energy asymmetry variable is saved for each photon, for four different minimal energy requirements of the second photon: 30, 75, 100, 150 MeV.

(a) signal

(b) π^0-type backgrounds

Figure 14: Comparison between the diphoton invariant mass distributions with the π^0 hypothesis of signal (a) and all π^0-type background modes (b) for the ρ^0 channel.

(a) signal

(b) π^0-type backgrounds
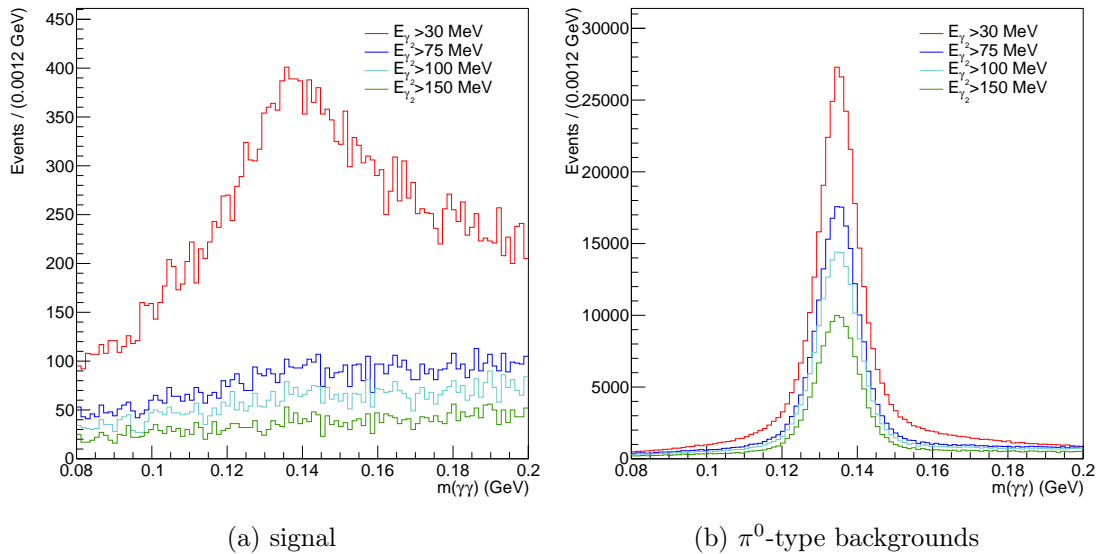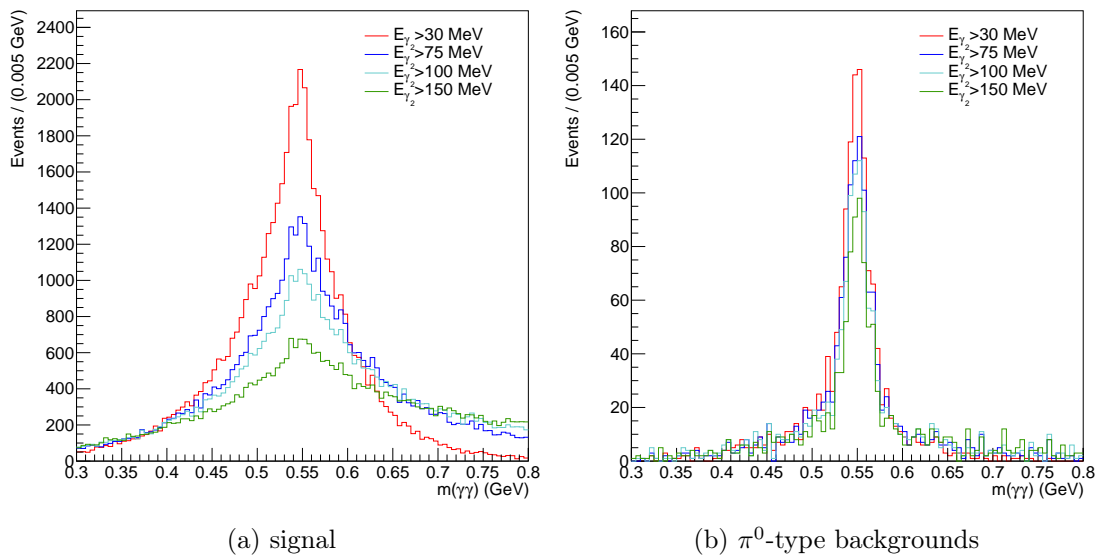
Figure 15: Comparison between the diphoton invariant mass distributions with the η hypothesis of signal (a) and all η-type background modes (b) for the ρ^0 channel.

4.4.3 *Standard Belle Veto*

There is a pre-existing π^0 (η) veto tool that has been in use in the Belle Collaboration [31]. The veto computes the probability for a photon to originate from a π^0 (η) decay by combining the photon with all other photons, as for the previously described mass veto. The final probability, which is the direct output of the veto tool, is based on the laboratory energy of the second photon, its polar angle and the diphoton mass. Photons arising from a π^0 (η) decay have the veto output variable close to 1, while values of the veto for photons that do not arise from a π^0 (η) peak at 0. The values of the Standard Belle veto for both π^0 and η are calculated and assigned to each candidate photon.

4.4.4 *Neural Network*

As we now have quite a large set of possible $\pi^0(\eta)$ veto variables, the possibility that a combination of certain variables could yield the most efficient veto must be considered. For the purpose of investigating this, the `NeuroBayes` neural network tool is chosen [32]. The tool's output is a single variable to distinguish between signal and background. The variable ranges between [-1,1] and peaks at 1 for events likely to be signal, while the value approaches -1 with increasing probability of events to belong to background.

For our analysis, an additional Monte Carlo simulation of decays $D^0 \to V\pi^0(\eta)$ is generated to represent the background sample, while half of the signal Monte Carlo is used as the signal sample. For all further analysis, only the other, statistically independent half of the signal Monte Carlo is used. All the veto candidates are input into the `NeuroBayes` tool, and the neural network training is performed separately for π^0 and η. The tool returns the list of the input variables, ordered by separation power, and the correlation between them. It is clear that the improvement of the separation power with the addition of further variables quickly saturates. After the first 4 most prominent variables, further increasing the number of variables in the neural network yields negligible improvement. The 4 variables with greatest separation power are, according to `NeuroBayes`, in decreasing order: mass veto with 75 MeV cut on energy of the second photon, mass veto with 30 MeV cut on energy of the second photon, Standard Belle veto, energy asymmetry between the photons with 30 MeV cut on energy of the second photon. We repeat the neural network training with limited sets of only these variables, i.e. with the two most important, the most important three, and all four. Only these three samples are taken into final consideration.

4.4.5 *Final Selection*

The selection of the final veto is made based on a plot of efficiency vs. background rejection for the $\phi\gamma$ decay mode (it is assumed this procedure would yield equivalent results for all three signal modes). Figure 16a shows the efficiency vs. background rejection plot for different π^0 vetos: the neural network variable based on 2-4 most sig-
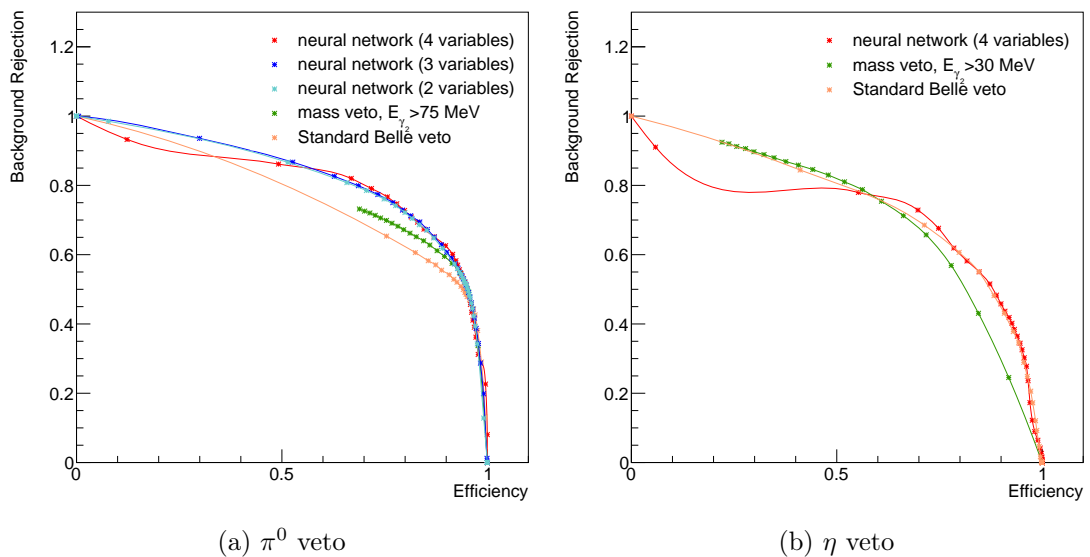
Figure 16: Plot of efficiency vs. background rejection for different π^0 vetos (a) and η vetos (b) for the ϕ mode.

nificant input variables, the single most significant veto as stated by the `NeuroBayes`' ordered list (mass veto with a requirement $E(\gamma_2) > 75$ MeV) and the Standard Belle veto. We observe that the neural network variables show a better performance than the single mass or Standard veto, however increasing the number of input variables in the neural network does not improve the performance significantly. We therefore decide on a neural network based on 2 variables (mass veto with $E(\gamma_2) > 75$ MeV and mass veto with $E(\gamma_2) > 30$ MeV) as the final choice for the π^0 veto.

After this selection is made, the neural network training is performed also for the other two signal decay modes, based on their own signal and background Monte Carlo simulations. Additionally, the neural network output variable is determined for each mode based also on the neural network training of the other two modes. For each signal mode, the distributions (for signal and background) of the three so obtained neural network variables are compared. It is revealed that the distributions are very similar regardless of which decay mode the neural network was trained on (see Figure 17). For simplicity sake, we therefore decide to use the neural network trained on the ρ^0 channel for all three signal decay modes.

When dealing with neural networks, one must take care that what is known as overtraining of the network does not occur. Overtraining describes a situation when the network training is too dependent on the very specific and localised shapes and characteristics of the input distributions, and will subsequently fail to perform optimally on an equivalent, but statistically independent sample. To check for overtraining, we run the neural network also on the half of the signal Monte Carlo on which the network was trained. The distribution of the output variable is compared between this sample and the statistically independent sample. In cases where the network is overtrained, the output of the sample on which the network was trained will be noticeably superior in distinguishing between signal

(a) signal
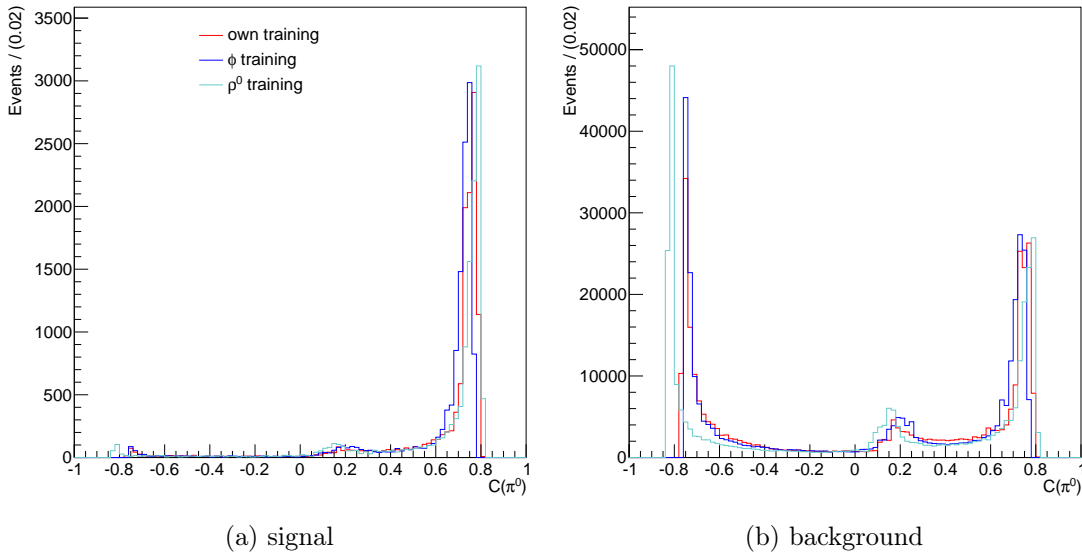
(b) background

Figure 17: Distribution of the neural network output variable for the three different trainings for signal (a) and generic Monte Carlo (b) for the $\overline{K}^{*0}$ channel.

and background than the output of an independent sample. The plots are shown in Figure 18 with the ϕ mode as the example. There are visible differences in the distribution on the independent sample and on the same sample on which the network was trained. The discrepancies are not so large as to incite immediate alarm, especially after disregarding some discrepancies that arise from a particular choice of binning. Information from Figure 16a, which is from an independent sample, suggests that the veto will perform well. A further evaluation of the efficiency of the veto will be performed subsequently for this and all other selection criteria, once they have been determined.

Figure 16 shows the same plot for the η veto. It can be seen that in this case, the Standard Belle veto by itself performs as well as the neural network variable. We therefore decide on the Standard veto variable as the η veto, as it is a simpler one than the neural network. We name the respective veto variables $C(\pi^0)$ and $K(\eta)$.

(a) signal   (b) background
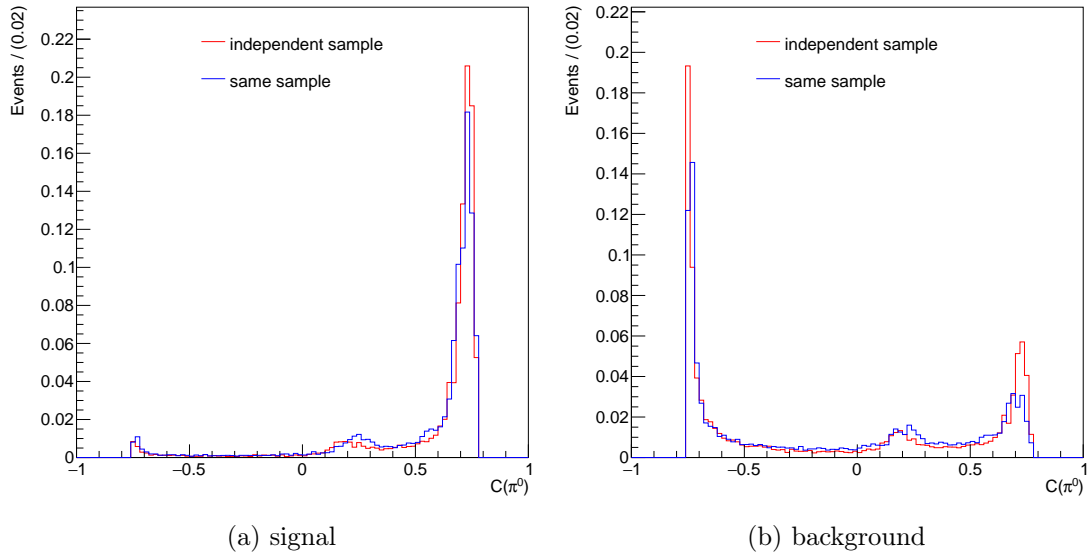
Figure 18: Distributions of the neural network output variable on the independent sample and on the same sample on which the network was trained in a check for overtraining, for signal (a) and background (b) of the ϕ channel.

4.5 SELECTION CRITERIA

When determining the selection criteria, the scope is to achieve the maximal possible figure of merit, i.e. the signal significance, defined as the ratio between the signal events and the statistical error of the sample, taken as the Poissonian error:

$$\text{F.O.M.} = \frac{N_{\text{sig}}}{\sqrt{N_{\text{sig}} + N_{\text{bkg}}}} \quad . \tag{25}$$

Several different variables were considered (some finally discarded, as it was revealed their contribution to the improvement of FOM is negligible), as well as two different approaches: a cut-based method, imposing a constraint on each variable, and a neural network based on the set of variables, with a final constraint on the single output variable. The final choice is a cut-based method with the following variables: total energy released in the decay $q = m(D^{*+}) - m(D^0) - m(\pi^+)$, mass of the vector meson, $m(V)$, centre-of-mass momentum of the D^{*+}, $p_{\text{CMS}}(D^{*+})$, π^0 veto neural network variable, $C(\pi^0)$, Standard Belle veto variable, $K(\eta)$, as the η veto, energy of the photon, $E(\gamma)$, and variable E_9/E_{25}.

An equivalent variable to q is the mass difference $\Delta m = m(D^{*+}) - m(D^0)$, which differs from q only by the constant value of the pion mass. Throughout this analysis the variable q is used, while Δm is only used for the relevant plots (but conveying the exact same information, as the plots are only shifted by a constant value with regard to q: $\Delta m = q + m(\pi^+)$).

Since the scope is to maximise the significance of signal events in the sample, the selection criteria are optimised in a signal window in which the grand majority of signal events is expected to lie. The signal window is chosen as an interval in the invariant mass of the D^0, namely $1.8 < m(D^0) < 1.9$ GeV, and in q and $m(V)$.

First, the q and $m(V)$ windows are optimised by varying the width of the window and in each step determining optimal constraints for all variables and calculating the FOM. The criterion which gives the maximal value of the FOM is chosen for both variables. Plots of Δm and $m(V)$ distributions for all three signal channels are shown in Figure 19. The optimal criteria for all other variables are determined by searching for the maximum of the FOM with the mass window criteria applied. The plots of signal and background distributions and the corresponding plots of FOM are shown in Figures 20 and 21 for the ϕ mode, Figures 22 and 23 for the $\overline{K}^{*0}$ mode and Figures 24 and 25 for the ρ^0 mode. The plots showing the signal and background distributions of $K(\eta)$ in all channels are set to a fixed maximum for a better visualisation, as the peak at zero for both signal and background is much higher than values in the rest of the bins. The starting value on the y axis in the corresponding plots of the FOM is lower in the $K(\eta)$ plots than on plots of other variables. This is due to the fact that in some events, this veto variable cannot be determined for various reasons (e.g. missing information). In such cases, the value is set to -999 and those events are excluded from the FOM calculation and the corresponding plots.

As the variables are not completely independent from one another, a set of criteria that maximise the FOM separately for each variable may not yield the maximum FOM when imposed all together. Hence, after each individual requirement has been determined, they are subjected to another process of optimisation taking the individual optimal constraints as a starting entry, until the maximum FOM is achieved based on the whole set of selection criteria. We observe that for some variables, the values of the optimal selection criterion for all three signal modes are very similar. It is therefore decided that a uniform criterion is chosen for a variable for all three signal channels, if it proves that such a choice does not affect the FOM significantly. In all of these cases, the criterion of the ρ^0 channel is the one that works best for all three modes. For some variables such a generalisation is not possible and different constraints are used.

We check for each criterion separately the efficiency in background reduction and signal loss, while all other selection criteria are applied. The q and $m(V)$ requirements are henceforth counted with the other selection criteria and are applied to all further used data samples. The mass window in D^0 in which the selection criteria were determined is not applied, as a wider mass window is used to enable a better parametrisation of background. The results are summarised in Table 6. It is obvious that the contribution of the η veto to further reducing background is negligible. It is therefore decided to remove it from the set of selection criteria. We check that after discarding the η veto, the relative values of signal and background loss for other variables listed in Table 6 change for a maximum of 0.1%. It can be seen that the π^0 veto does an effective job in removing background, as it is the variable with the individually second greatest background rejection. This confirms that the veto is suitable for its purposes.

The final selection criteria are summarised in Table 7.

	ϕ		$\overline{K}^{*0}$		ρ^0		
	B	S	B	S	B	S	[%]
q	88.2	19.1	80.0	19.7	91.3	20.5	
$m(V)$	24.4	5.3	60.8	17.9	59.2	9.1	
$p_{\text{CMS}}(D^{*+})$	21.9	7.7	1.6	0.6	56.8	22.3	
$C(\pi^0)$	60.3	14.6	61.5	15.2	55.6	12.9	
$K(\eta)$	0.3	0.1	0.2	0.09	0.2	0.07	
$E(\gamma)$	19.0	6.1	12.6	5.5	15.3	4.5	
E_9/E_{25}	20.1	5.3	11.4	4.5	17.6	4.5	

Table 6: Relative background (column "B") and signal (column "S") loss for each selection criterion separately, while others are applied.

	ϕ	$\overline{K}^{*0}$	ρ^0	all
q				< 0.6 MeV
$m(V)$	< 11 MeV	< 60 MeV	< 150 MeV	
$p_{\text{CMS}}(D^{*+})$	> 2.42 GeV	> 2.17 GeV	> 2.72 GeV	
$C(\pi^0)$				> 0.47
$E(\gamma)$				> 0.55 GeV
E_9/E_{25}				> 0.94

Table 7: Selection criteria for the three signal decay modes.
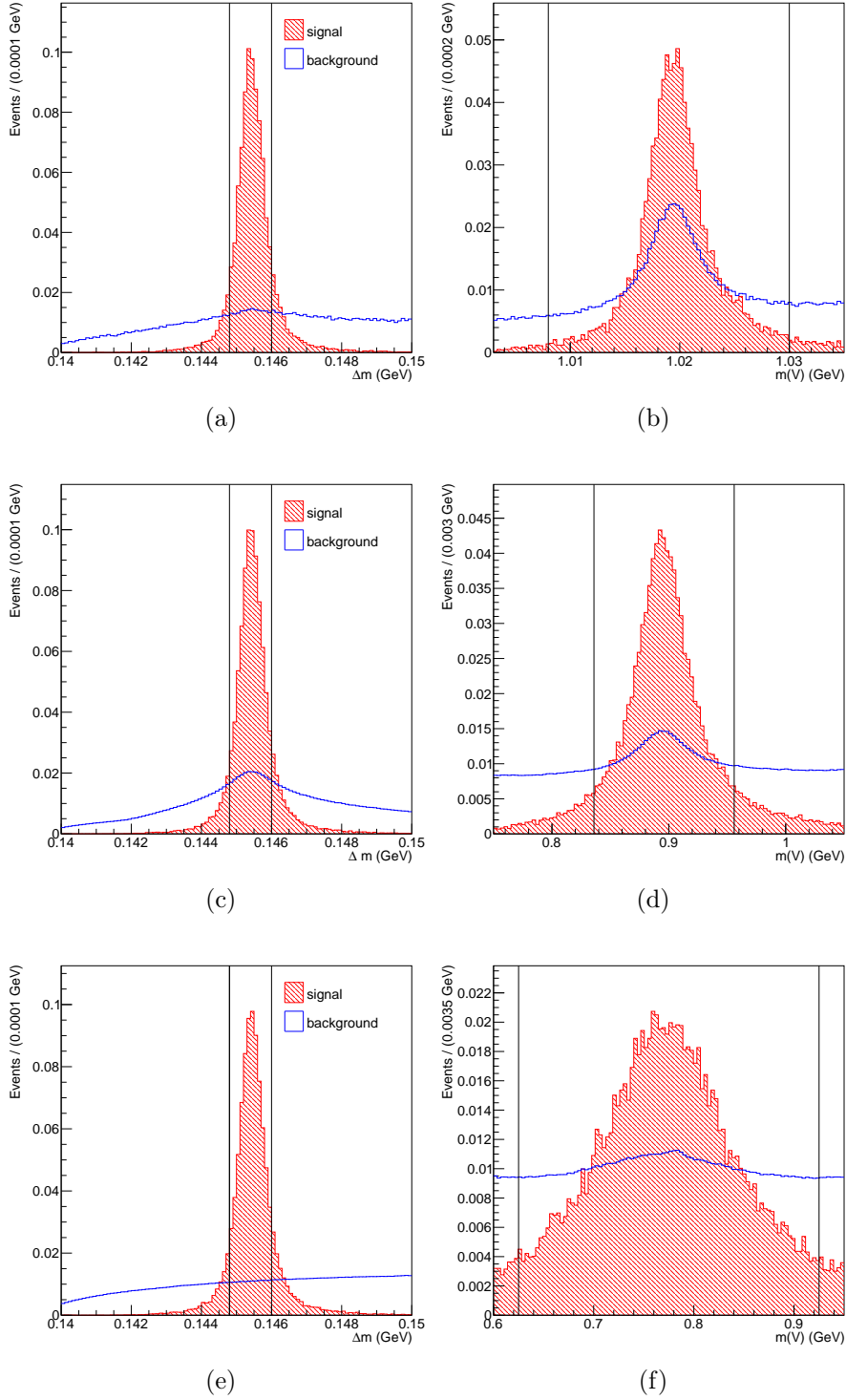
Figure 19: Normalised distributions of signal and background of Δm (left) and $m(V)$ (right) of the ϕ (top), $\overline{K}^{*0}$ (middle) and ρ^0 channel. The vertical lines indicate the signal window.
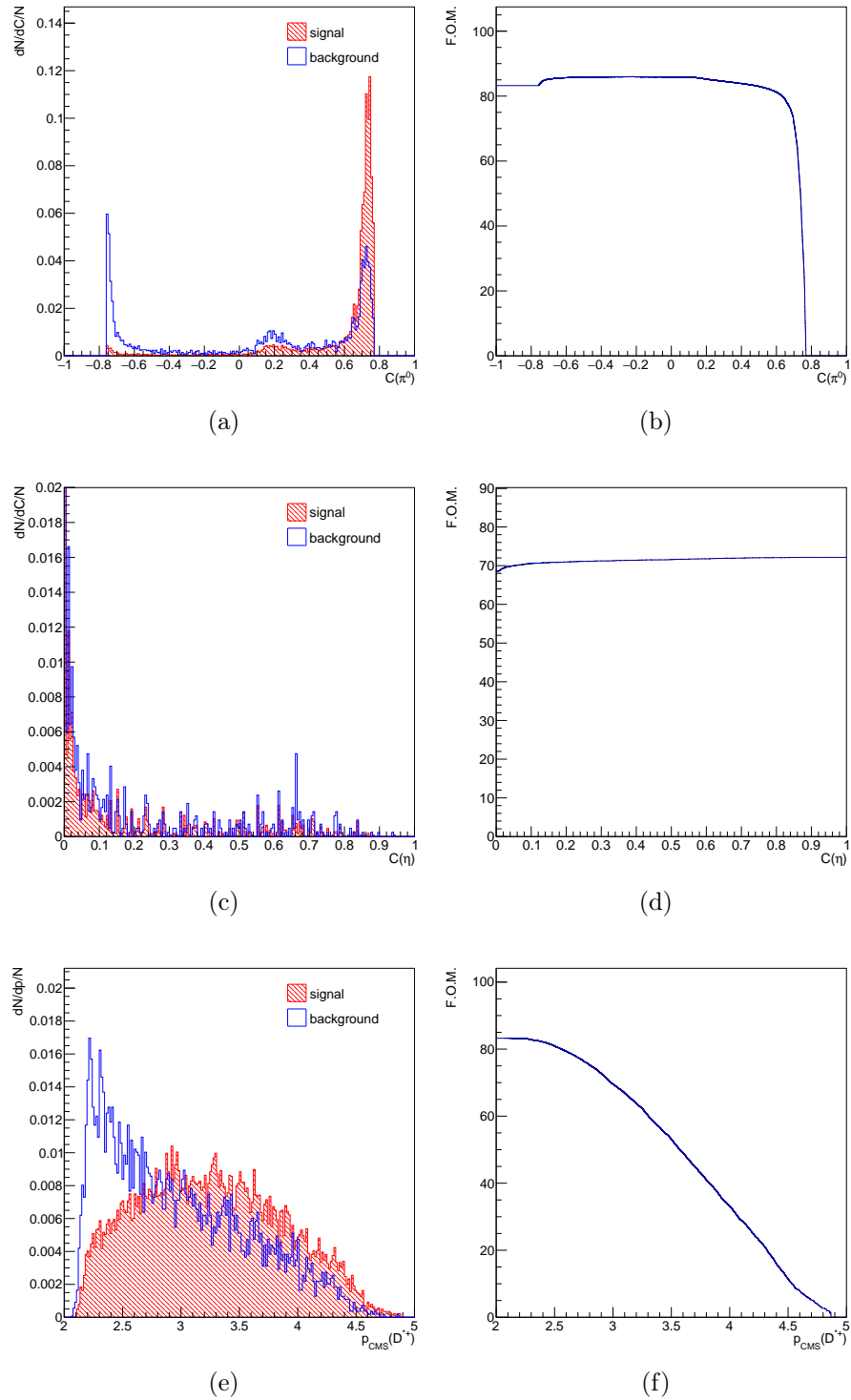
Figure 20: Normalised distributions of signal and background (left) and the befitting plots of the FOM (right) for $C(\pi^0)$ (top), $K(\eta)$ (middle) and $p_{\mathrm{CMS}}(D^{*+})$ (bottom) of the ϕ channel.
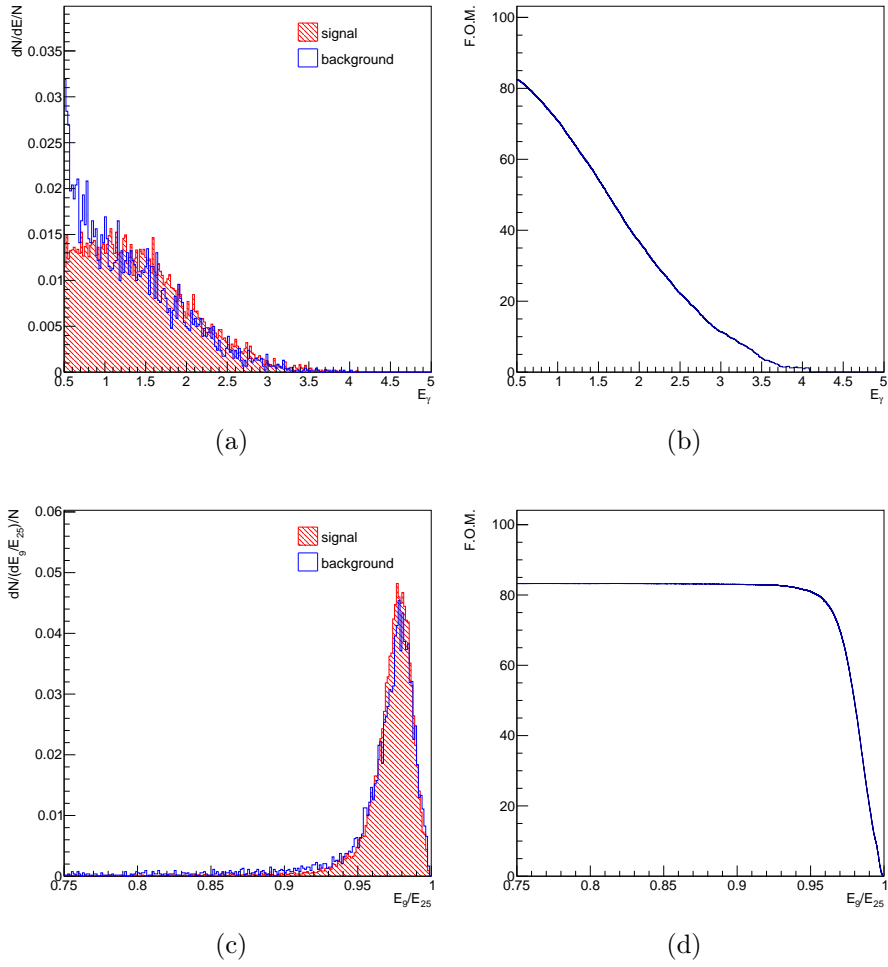
Figure 21: Normalised distributions of signal and background (left) and the befitting plots of the FOM (right) for $E(\gamma)$ (top) and E_9/E_{25} (bottom) of the ϕ channel.
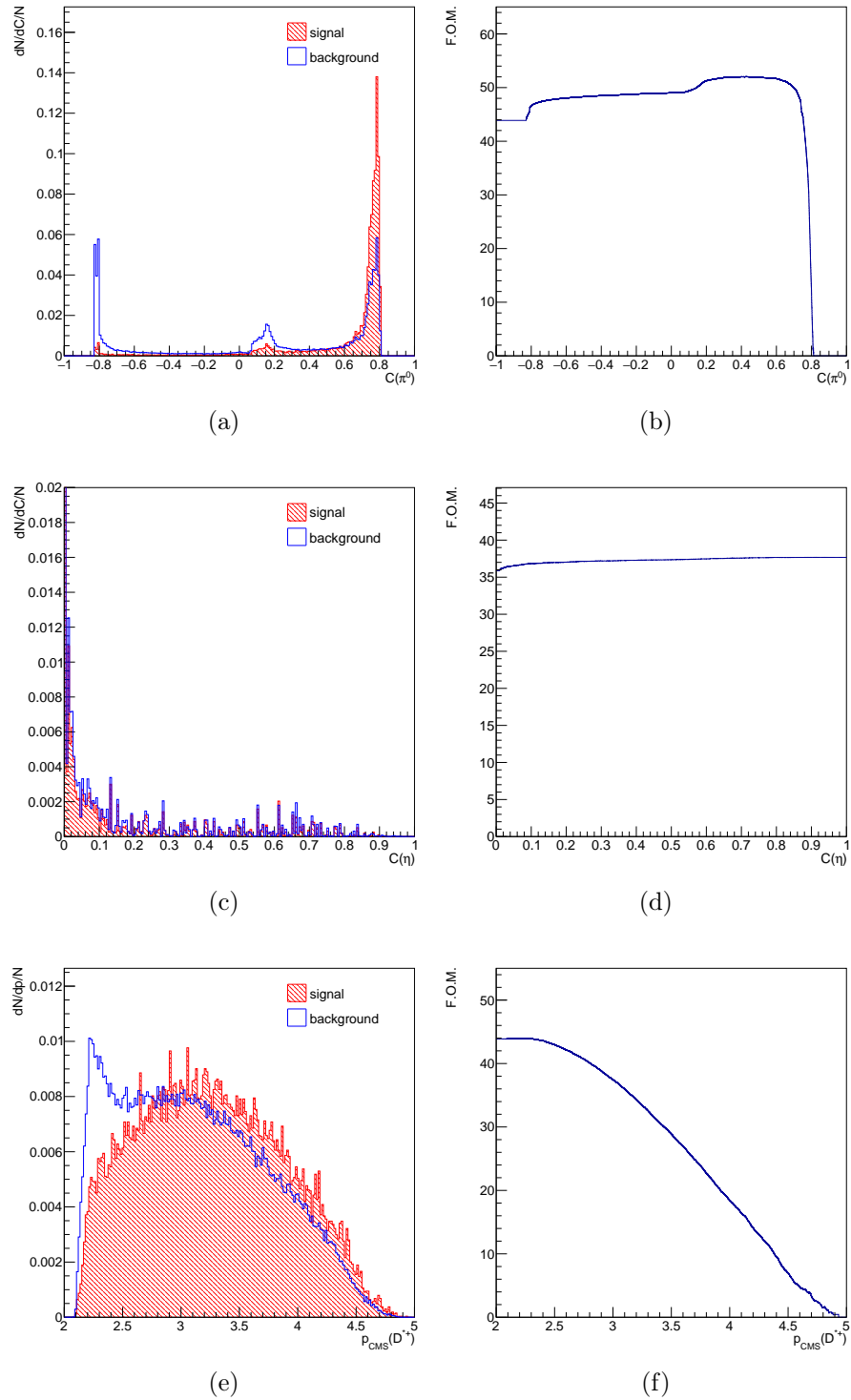
Figure 22: Normalised distributions of signal and background (left) and the befitting plots of the FOM (right) for $C(\pi^0)$ (top), $K(\eta)$ (middle) and $p_{CMS}(D^{*+})$ (bottom) of the $\overline{K}^{*0}$ channel.
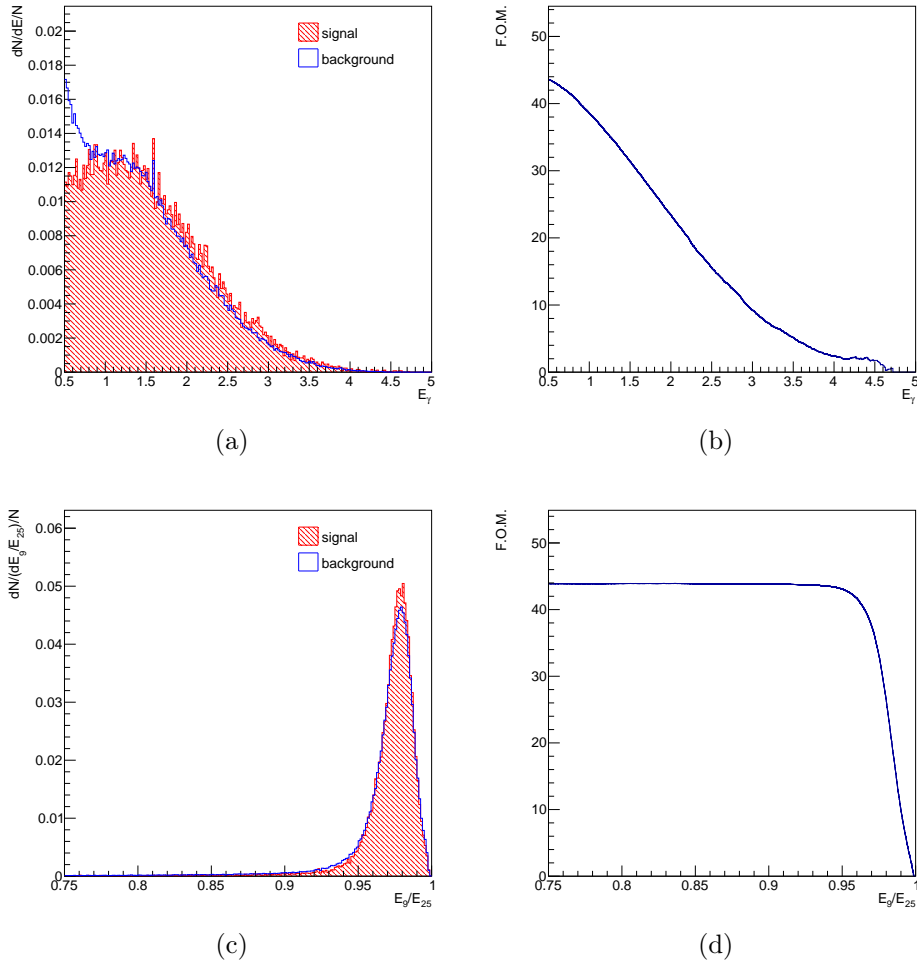
Figure 23: Normalised distributions of signal and background (left) and the befitting plots of the FOM (right) for $E(\gamma)$ (top) and E_9/E_{25} (bottom) of the $\overline{K}^{*0}$ channel.
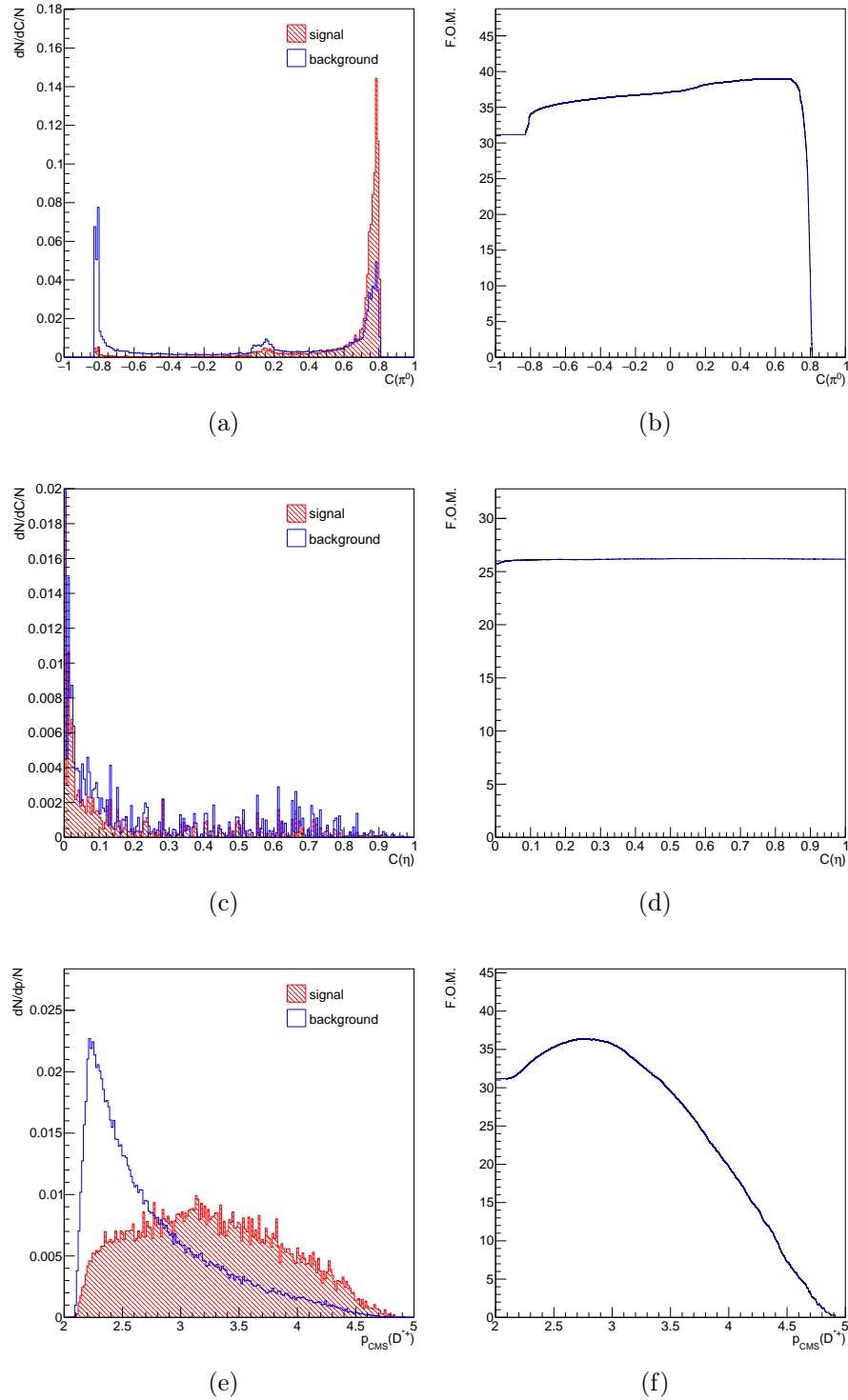
Figure 24: Normalised distributions of signal and background (left) and the befitting plots of the FOM (right) for $C(\pi^0)$ (top), $K(\eta)$ (middle) and $p_{CMS}(D^{*+})$ (bottom) of the ρ^0 channel.
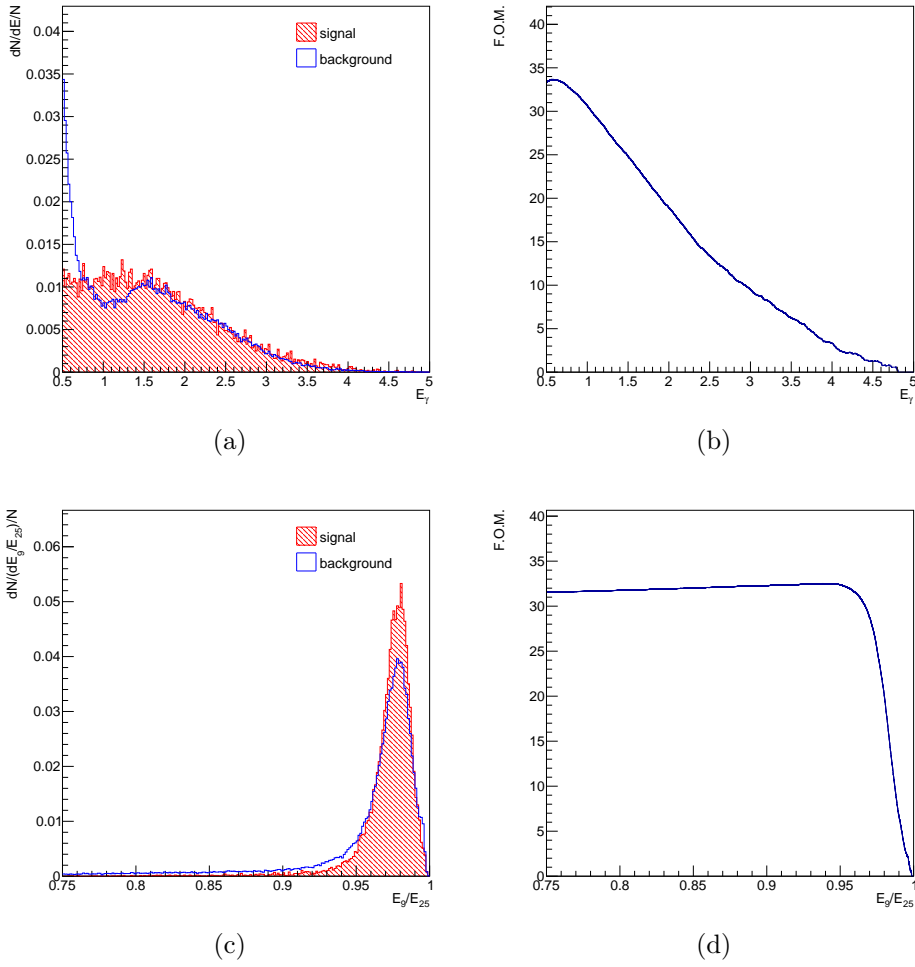
Figure 25: Normalised distributions of signal and background (left) and the befitting plots of the FOM (right) for $E(\gamma)$ (top) and E_9/E_{25} (bottom) of the ρ^0 channel.

4.6 MULTIPLE CANDIDATES

It is necessary to investigate the multiplicity of events in the reconstructed data sample to determine whether a best candidate selection should be implemented. Multiple candidates are obtained e.g. if a correctly reconstructed D^0 is paired with two different slow pions and thus creating two different D^{*+} candidates. Multiplicity is expected to be low after the application of selection criteria, where a very strict cut on q is imposed. The multiplicity plots for all three signal modes are shown in Figure 26. Multiplicity is plotted for signal Monte Carlo, and background as determined on generic Monte Carlo. A multiplicity of 2 occurs in a maximum of 2% of cases. Multiplicities of 3 and 4 are negligibly small, whereas multiplicities greater than 4 do not occur. We check for cases with multiplicity greater than 1 whether the D^0 mesons come from the same D^{*+} mother. This does not hold, meaning that the extra events fall under combinatorial background. We are confident that no double counting occurs during our analysis and thus decide that a best candidate selection is not necessary. It will be further checked in the final data sample if the Monte Carlo distributions of multiplicity represent well the distributions in data.
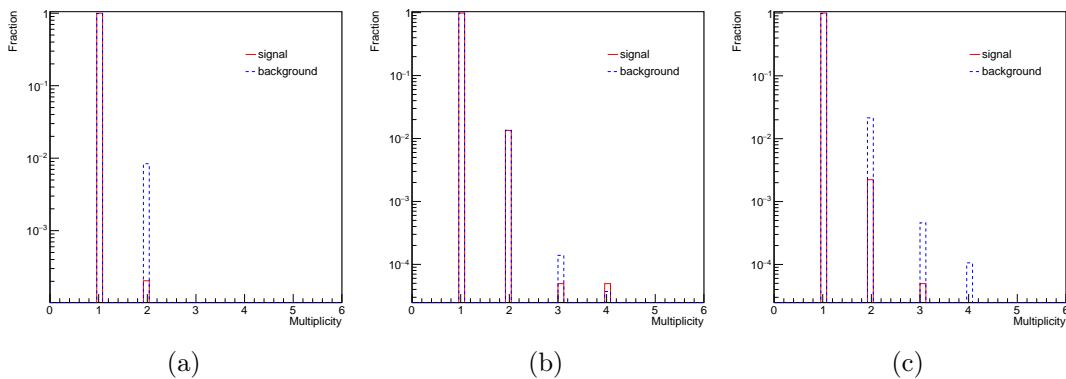
Figure 26: Multiplicity of both signal Monte Carlo and generic Monte Carlo (background) samples for the ϕ (a), $\overline{K}^{*0}$ (b) and ρ^0 (c) mode in the logarithmic scale for the y-axis.

4.7 EFFICIENCY

The final efficiency is calculated on signal Monte Carlo. The reconstructed data sample is (albeit to a low degree) polluted with incorrectly reconstructed events. These are events where a final state particle is misidentified (the reconstructed pion is actually a kaon or vice-versa), or combinatorial background where the D^0 and D^{*+} are incorrectly reconstructed. Only correctly reconstructed events, as determined from Monte Carlo truth, are subjected to the efficiency calculation. It is given by the number of correctly reconstructed events after the application of all selection criteria (N_{rec}) compared to the total number of events generated (N_{gen}):

$$\varepsilon = \frac{N_{\text{rec}}}{N_{\text{gen}}} \quad . \tag{26}$$

The ρ^0 mode demands special consideration regarding the efficiency. The signal Monte Carlo that is used for this mode is comprised of equal parts of the ρ^0 and ω resonances, as discussed in Section 4.2. The ρ^0 resonance is however much broader than ω. Considering the value of the selection criterion regarding the width of the vector meson, it can be expected that a considerably larger fraction of ω events than ρ^0 events will pass the cut. Therefore, the efficiencies of the two modes would differ, with the efficiency of ω being larger than that of ρ^0. We thus calculate both the efficiency of the combined Monte Carlo sample, as this is the sample that is used for developing and testing the analysis procedure, and the separate efficiency for the ρ^0 mode only, which should be used on data if verified that the $\pi^+\pi^-\gamma$ sample is composed of almost exclusively the ρ^0 mode as predicted.

The efficiencies for all modes are listed in Table 8. All values are close to 10%.

	Efficiency
$\phi\gamma$	9.7%
$\overline{K}^{*0}\gamma$	10.2%
$\rho^0\gamma$	9.0%
$\omega\gamma$	11.2%

Table 8: Efficiency after the application of selection criteria for the three signal decay modes. Also stated is the efficiency of the pure $\omega\gamma$ mode.

4.8 CALIBRATION OF THE π^0 VETO EFFICIENCY

The π^0 veto is a vital aspect of the analysis, as it reduces the most dangerous source of background, namely decays with the photon originating from a π^0 decay. It is necessary to check whether the applied veto, a constraint on the neural network variable, behaves similarly on Monte Carlo and data. For this cross-check, we use as a calibration channel the decay $D^0 \to K_S^0 \pi^0$. The argument for this choice is this channel being very clean with regard to background, meaning that the amount of combinatorial background will be small and no other specific decays significantly pollute the reconstructed sample. Plots of the Δm and $m(D^0)$ distributions on generic Monte Carlo are shown in Figure 27. The same relevant pre-selection criteria as for the signal modes have been applied during reconstruction. On the Δm plot, the signal window in this variable is indicated. Only the corresponding events are shown in the $m(D^0)$ plot. It can be seen that the amount of background is indeed very low, especially after the cut on Δm is imposed.

The decay $D^0 \to K_S^0 \pi^0$ is reconstructed on data and generic Monte Carlo. One of the daughter photons of the π^0 is chosen, and the other is explicitly discarded. Then, the mass vetos that are used for the final π^0 veto are determined for the chosen photon, pairing it with all other photons except the other true daughter, which was excluded. All these pairs of photons do not come from the same π^0 mother (since the other true daughter was explicitly discarded), however in some cases the diphoton invariant mass can by happenstance match the mass of a π^0. In such cases, the decay can be discarded by the π^0 veto, albeit wrongly. We wish to check whether the efficiency of the veto, namely the amount of such wrongly discarded events, is the same on data and Monte Carlo simulations,

The data and Monte Carlo samples are passed through the neural network to obtain the final veto variable. For both samples the following ratio is calculated:

$$R = \frac{N(\text{selection} + \text{veto})}{N(\text{selection})} \quad , \tag{27}$$

where "selection" denotes the selection criteria without the constraint on the veto variable. The applied selection criteria are the same as for the signal modes, with the $p_{\text{CMS}}(D^{*+})$ requirement being the one belonging to the ϕ mode, as it represents the middle value of the three, and the mass window around the nominal mass of the K_S^0 set to 9 MeV. All pre-selection and selection criteria are listed in Table 9.
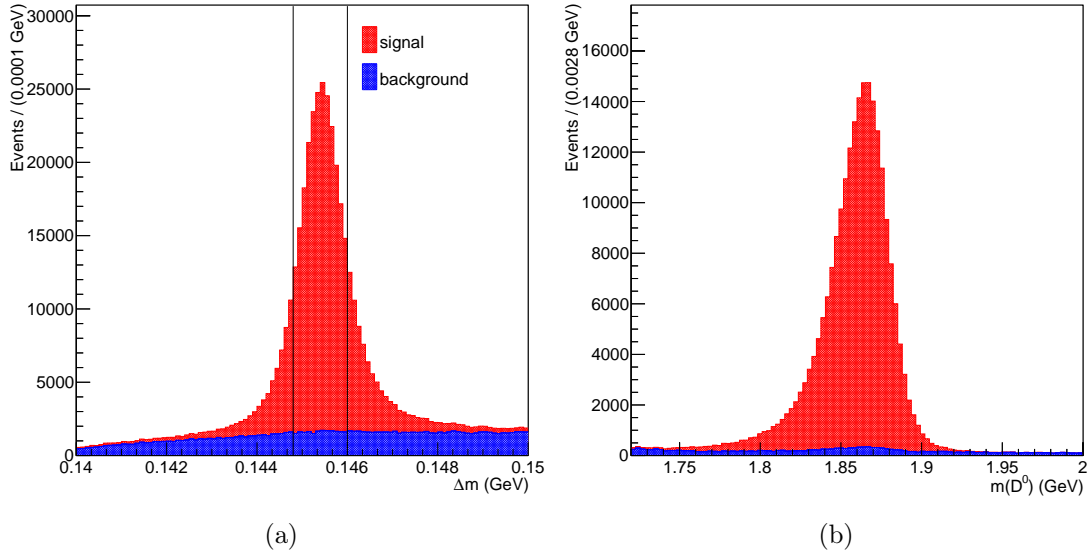
Figure 27: Distributions in Δm (a) and $m(D^0)$ (b) of the decay $D^0 \to K_S^0 \pi^0$ on generic
Monte Carlo. The D^0 mass is plotted in the indicated Δm signal window.

The number $N(\text{selection})$ represents the number of events that pass the selection
criteria without any constraint on the π^0 veto variable, and $N(\text{selection} + \text{veto})$ is
the number of events that pass the selection with the requirement on the π^0 veto
included. The rest of the events are discarded by the veto, however erroneously, as
the two photons did not come from a common π^0 mother.
We then compare the calculated R on data and Monte Carlo:

$$\frac{R(\text{MC})}{R(\text{data})} = 1.003 \pm 0.004 \quad , \tag{28}$$

where the error is statistical. The obtained number shows great accordance between
the performance of the veto on data and Monte Carlo. It is consistent with 1 within
the margin of error. We therefore conclude that no bias or error will ensue from this
source.

$\mathcal{P}_{K/\pi}$ (pions)	< 0.9	
$\mathcal{P}_{K/\pi}$ (kaons)	> 0.1	
$p_{\mathrm{CMS}}(D^0)$	> 2	GeV
q	< 0.6	MeV
$m(K_S^0)$	< 9	MeV
$p_{\mathrm{CMS}}(D^{*+})$	> 2.42	GeV
$\mathrm{C}(\pi^0)$	> 0.47	
$E(\gamma)$	> 0.55	GeV
E_9/E_{25}	> 0.94	

Table 9: Pre-selection and selection criteria for the control channel $D^0 \rightarrow K_S^0 \pi^0$. The photon-specific cuts ($\mathrm{C}(\pi^0)$, $E(\gamma)$, E_9/E_{25}) are applied to the first daughter photon of the π^0.

4.9 FINAL DATA SAMPLE

Running the reconstruction on the generic Monte Carlo gives us the expected background in the analysed sample. As our signal decays are rare, they are not included in the generic Monte Carlo of the Belle Collaboration at all. Therefore, they are subsequently added to the generic Monte Carlo data in the amount corresponding to the branching fraction of the signal decays and luminosity of the background sample. For the ϕ and $\overline{K}^{*0}$ modes, the world-average value of the branching fraction is taken. The branching fraction for the ρ^0 mode is not known, and the current established upper limit is of the order of 10^{-4}, however theory predicts it to be lower. For the analysis on Monte Carlo, we use as input value of a similar value as for the ϕ mode: $3 \cdot 10^{-5}$. A linearity test will be performed further into the analysis to validate the performance also for different values of the branching fraction, higher and lower.

One stream of generic Monte Carlo with the corresponding admixture of signal gives us the expected data sample that will be obtained from running the reconstruction on Belle data. Histograms are plotted in Figure 28, showing the expected set of reconstructed data for each of the signal modes in $m(D^0)$. Signal Monte Carlo is added to one stream of generic Monte Carlo, which is roughly divided into three categories: the π^0-type background, comprising decays with a correctly identified D^0 and the photon coming from a π^0, the η-type background, comprising all events with a correctly identified D^0 and the photon coming from an η, and combinatorial background, which contains the rest of events.

(a) ϕ mode
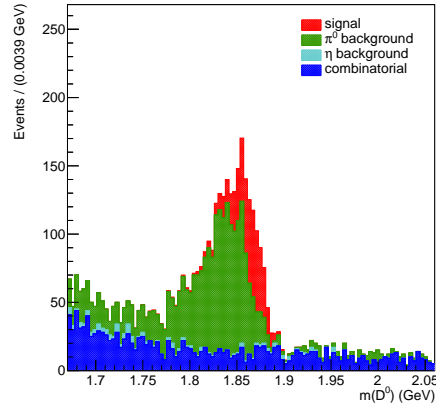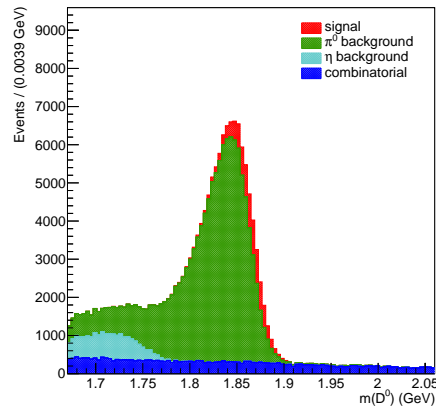
(b) $\overline{K}^{*0}$ mode
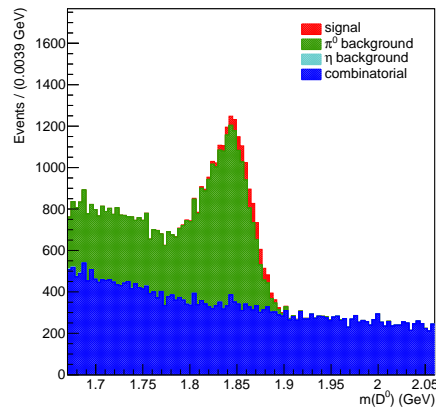
(c) ρ^0 mode

Figure 28: Expected data set in $m(D^0)$ after all selection criteria for the ϕ (top), $\overline{K}^{*0}$ (middle) and ρ^0 (bottom) mode, containing one stream of generic Monte Carlo, divided into three background categories, and the appropriate amount of signal events.

ANALYSIS METHOD

The information that is extracted from data is the signal yield N_{sig}. It is in turn related to the branching fraction as

$$N_{\text{sig}} = N(D^0) \cdot \mathcal{B}r(D^0 \to V\gamma) \cdot \mathcal{B}r(V \to f_1 f_2) \cdot \varepsilon \quad , \tag{29}$$

where ε is the reconstruction efficiency. The number of D^0 mesons in the above equation is conditioned by the required origin from a D^{*+} decay:

$$N(D^0) = N(D^{*+}) \cdot \mathcal{B}r(D^{*+} \to D^0 \pi_s^+) \quad , \tag{30}$$

thus ε in Equation 29 represents the reconstruction efficiency for the whole chain of decays.

However, determining the inital number of generated D^{*+}s in the entire sample poses a problem, as the value of the cross section for e^+e^- into charm mesons through hadronisation of a $c\bar{c}$ pair $\sigma(e^+e^- \to D^{*+}X, X$ is anything) suffers from a large uncertainty of 12.5% [23]. This prevents us from being able to determine the number of D^{*+}s with the necessary accuracy. A solution to this problem is not measuring the absolute branching fraction, but instead normalising it to a decay channel with a well known branching fraction. The branching fraction calculation then translates to

$$\mathcal{B}r_{\text{sig}} = \mathcal{B}r_{\text{norm}} \cdot \frac{N_{\text{sig}}}{N_{\text{norm}}} \cdot \frac{\varepsilon_{\text{norm}}}{\varepsilon_{\text{sig}}} \quad . \tag{31}$$

where N_{sig} and N_{norm} are the yields of the signal and normalisation modes as extracted with the analysis procedure, and ε_{sig} and $\varepsilon_{\text{norm}}$ are the respective reconstruction efficiencies. For the branching fraction of the normalisation mode, the world average value is taken [23].
A welcome additional feature of a relative calculation is the fact that all systematic uncertainties that are common to both the signal and normalisation mode cancel out, increasing the precision of the final result.

The time-integrated CP asymmetry of a decay to a final state f is defined as

$$\mathcal{A}_{CP} = \frac{\Gamma(D^0 \to f) - \Gamma(\overline{D}^0 \to \overline{f})}{\Gamma(D^0 \to f) + \Gamma(\overline{D}^0 \to \overline{f})} \quad , \tag{32}$$

however the quantity that is determined from the measurement, i.e. from the respective yields, is the raw asymmetry

$$A_{\text{raw}} = \frac{N_f - \overline{N}_f}{N_f + \overline{N}_f} \quad . \tag{33}$$

Apart from the physical CP violation, two other sources of asymmetry contribute to the measured value of A_{raw}. With the well supported assumption that all asymmetries are small, it can be written in the first order of expansion:

$$A_{\mathrm{raw}} = \mathcal{A}_{CP} + A_{\mathrm{FB}} + A_{\varepsilon}^{\pi_s} + A_{\varepsilon}^{f^+ f^-} \quad . \tag{34}$$

The forward-backward asymmetry A_{FB} is the asymmetry in production of D^{*+} and D^{*-}. It arises from the $\gamma - Z^0$ interference and other higher order QED effects in the process $e^+ e^- \to c\bar{c}$. The second one of these additional asymmetries is detector-induced and is due to different reconstruction efficiencies of positively and negatively charged particles. This in turn arises from different cross-sections for interaction of particles and antiparticles with the detector material. For self-conjugate final states, as is the case in the decays of ϕ and ρ^0 mesons, the asymmetry $A_{\varepsilon}^{f^+ f^-}$ is 0. The only remaining source of asymmetry in this regard is then the slow pion from the D^{*+} decay. In the $\overline{K}^{*0}$ channel, also the asymmetry between positively and negatively charged kaons and pions contributes.

Both the forward-backward asymmetry and the detector-induced asymmetry can be eliminated through a relative measurement of $\mathcal{A}_{CP}$, rather than calculating them separately. Choosing a normalisation mode with the same charm mesons (meaning also the D^0s that feature in the normalisation channel must be required to originate from a D^{*+} decay) and the same final state particles gives

$$A_{\mathrm{raw}}^{\mathrm{sig}} = \mathcal{A}_{CP}^{\mathrm{sig}} + A_{\mathrm{FB}} + A_{\varepsilon}^{\pi_s} + A_{\varepsilon}^{f^+ f^-} \quad ,$$
$$A_{\mathrm{raw}}^{\mathrm{norm}} = \mathcal{A}_{CP}^{\mathrm{norm}} + A_{\mathrm{FB}} + A_{\varepsilon}^{\pi_s} + A_{\varepsilon}^{f^+ f^-} \quad ,$$

from where $\mathcal{A}_{CP}$ of the signal mode can be extracted:

$$\mathcal{A}_{CP}^{\mathrm{sig}} = (A_{\mathrm{raw}}^{\mathrm{sig}} - A_{\mathrm{raw}}^{\mathrm{norm}}) + \mathcal{A}_{CP}^{\mathrm{norm}} \quad , \tag{35}$$

an additional requirement for the normalisation mode thus being a well-measured value of the CP asymmetry.

In accordance with the above discussion, the following normalisation modes are selected:

$$D^0 \to K^+ K^- \text{ for the } \phi \text{ mode} \quad ,$$
$$D^0 \to K^- \pi^+ \text{ for the } \overline{K}^{*0} \text{ mode} \quad ,$$
$$D^0 \to \pi^+ \pi^- \text{ for the } \rho^0 \text{ mode} \quad .$$

The CP asymmetry of the normalisation modes $K^+ K^-$ and $\pi^+ \pi^-$ has been measured in a previous Belle analysis [33] and $\mathcal{A}_{CP}$ in the $K^- \pi^+$ mode has been measured by CLEO [34]. Since the branching fraction for these modes is significantly higher than that of our signal decays, the systematic uncertainties that are brought by the introduction of normalisation modes are expected to be small or negligible in comparison to the statistical uncertainties related to the signal modes.

SIGNAL EXTRACTION

The signal yield and $\mathcal{A}_{CP}$ will be extracted through a simultaneous fit to D^0 and $\overline{D}^0$ data samples.

6.1 SELECTION OF FIT VARIABLES

To extract the signal events from the reconstructed sample, we decide on a 2-dimensional fitting procedure in the following variables: mass of the reconstructed D^0 meson $m(D^0)$ and cosine of the helicity angle $\cos(\theta_H)$.

The invariant mass of the D^0 is an obvious first chose for a fit variable. However, there will be a substantial amount of peaking background from decays with the photon originating from a π^0 decay. As explained in Section 4.4, such decays exhibit a $m(D^0)$ distribution very similar to that of signal decays, with the two peaks actually overlapping. The separation power to extract signal can thus be enhanced, and the corresponding statistical uncertainty reduced, by introducing a second fit variable, chosen as such that signal and background decays differ significantly in the second variable. A well-suited quantity to satisfy this requirement is the cosine of the helicity angle. The helicity angle is defined as the angle between the mother particle (D^0) and daughter particle (one of the charged final state particles) of the vector meson, measured in the vector meson rest frame. A sketch is depicted in Figure 29.

According to the conservation of angular momentum laws, the distribution of signal events in the cosine of the helicity angle is

$$\frac{\mathrm{dN}}{\mathrm{dcos}(\theta_H)} = \sin^2(\theta_H) = 1 - \cos^2(\theta_H) \quad .$$
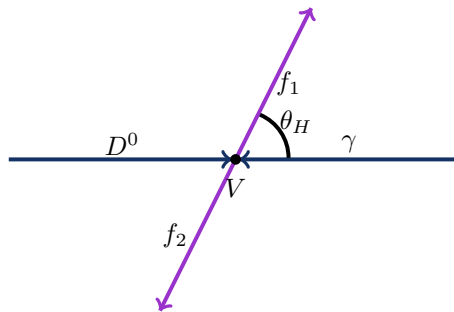
Figure 29: Definition of the helicity angle.

For decays $D^0 \to V\pi^0(\to \gamma\gamma)$, which represent a large contribution to dominant π^0-type decays, this distribution is proportional to $\cos^2(\theta_H)$, a clearly distinct shape compared to that of the signal events. When reconstructing such a decay as $D^0 \to V\gamma$, thus missing one photon, the distribution still obeys $\cos^2(\theta_H)$ in a good approximation. The same is valid for decays $D^0 \to V\eta(\to \gamma\gamma)$. In other decays that mimic our signal decay because of an identical set of charged final state particles, those do not in truth come from the intermediate vector meson resonance, so it is not trivial to predict what results will arise from a $\cos(\theta_H)$ calculation as defined for signal decays. We expect distributions corresponding to those decays to take a variety of shapes, but for all of them to distinctly differ from the signal distribution. A study of these distributions on Monte Carlo is in agreement with such predictions.

One must be careful when calculating the helicity angle to correctly treat the D^0 and $\overline{D}^0$ modes. For the charge conjugated mode, the helicity angle must be calculated with regard to the oppositely charged daughter particle as for the nominal decay. Such a reflection might be intuitive when the two charged particles in the final state are of a different identity, as is the case of the $\overline{K}^{*0}$ decay mode, where the helicity angle is calculated either using the pion or kaon. It is less obvious when dealing with decays that are self-conjugate (such are the ϕ and ρ^0 decay modes). In this case, the tag on the flavour of the D^0 meson is not provided during the reconstruction, as the set of particles from which it is reconstructed is the same for both decays, making it impossible to separate between the reconstructed D^0 and $\overline{D}^0$ based on the daughter particles. Therefore it is necessary to include the slow pion charge in the helicity angle calculation in order to ensure that the kaon (ϕ case) or pion (ρ^0 case) used is of opposite charge in the D^0 and $\overline{D}^0$ decays.

In the $\overline{K}^{*0}$ and ρ^0 mode, there are other decays beside $D^0 \to V\pi^0(\eta)$ whose $\cos(\theta_H)$ distribution peaks at values approaching ± 1. As the signal distribution approaches 0 in this regions, it is decided to reduce the range of the $\cos(\theta_H)$ variable for the fit, since such a cut significantly decreases the amount of background while keeping most of the signal events. The reduced range is set to $|\cos(\theta_H)| < 0.8$ for the $\overline{K}^{*0}$ and ρ^0 modes. For the ϕ mode, as this resonance is much narrower and the amount of background is much smaller compared to the other two signal channels, it is deemed that such a constraint is not necessary.

The additional constraint on the helicity angle brings the efficiencies of the $\overline{K}^{*0}$ and ρ^0 modes down to 9.6% and 8.5%, respectively (see Table 8).

6.2   BACKGROUND CATEGORIES

The background present in the reconstructed data sample arises from different sources. The first coarse-grained division can be made into two main categories: the physical background and combinatorial background. The combinatorial background comprises all events where a set of particles in the event completely by chance satisfies the pre-selection and selection criteria and thus passes the reconstruction. The single odds for such a coincidence are of course extremely low, however given the huge statistics of the whole data sample such random combinations still amount to form a significant contribution. Combinatorial background distributions typically exhibit

no distinct shape and can be generally described with flat functions or low-level polynomials.

Physical background arises from specific decays which exhibit enough similarities with signal decays to pass the reconstruction and selection criteria despite small deviations and irregularities. These events consist of other decays of the D^0 meson with the same charged final state particles. The dominant background source for our signal decays, as has been discussed at length in Section 4.4, are events where the photon originates from a $\pi^0(\eta)$, either through the same vector resonance or a different decay chain, be it through another resonance or a non-resonant decay. Another possibility is that the D^0 decays into solely charged decay products and the photon is emitted as final state radiation. Such events are rare and their relative contribution is small, however since there are no missed particles in the reconstruction of the D^0, the invariant mass distribution will exactly mimic the signal distribution. A similar sub-category of physical background are events where the photon originates from a decay of a charged ρ meson into a charged pion and a photon. These decays again exactly mimic the signal decay with no missing particles (this type of background is only relevant in the $\overline{K}^{*0}$ and ρ^0 modes, as the ϕ mode does not contain pions in the final state). Fortunately, the branching fraction for a radiative $\rho^\pm$ decay is very small ($\mathcal{O}(10^{-4})$), and thus such decays represent only a marginal fraction of background. An additional source of background can be represented by decays where pions and kaons are incorrectly identified.

For the 2-dimensional fit, signal and background are parameterised separately. The individual probability density functions (PDFs) are determined on the Monte Carlo simulations, signal Monte Carlo being used for parameterising signal and generic Monte Carlo for background. Because the ratio between specific decays that constitute the physical background in the Monte Carlo might not be completely accurate compared to data, as a consequence the shape of the background as a whole on Monte Carlo might not equal that of data. It is therefore necessary to split the physical background into separate contributions and fit them individually, subsequently allowing their individual fractions in the final fit to float. However, especially for the $\overline{K}^{*0}$ and ρ^0 modes, the number of specific decays constituting the physical background can quickly rise to a large number, and with that rises the number of free parameters, thus endangering the stability of the final fit. An adequate balance must be found between allowing as many free parameters as possible, thus reducing the reliance on Monte Carlo, while still ensuring the stability of the fit. It is therefore decided to fix the yields in the fit of some components with a low number of events. This still enables us to later adjust the number for the fit on data, if it is estimated that we can expect a different yield than on Monte Carlo.

Only the main physical background decays are extracted, to not swell up the number of free parameters of the final fit above a reasonable limit. Therefore, especially in the $\overline{K}^{*0}$ and ρ^0 modes, some additional physical decays can remain in the combinatorial background, when estimated that further division into individual decays would no longer benefit the procedure as a whole. Some of these decays share common properties (e.g. the D^0 is reconstructed from the majority of its daughter

	fraction of background [%]
$\phi\pi^0$	47.6
"remaining"	6.1
combinatorial	46.3

Table 10: Background categories for the ϕ mode, and the fraction of events each background represents on Monte Carlo.

	fraction of background [%]
$\overline{K}^{*0}\pi^0$	24.9
$K^-\pi^+\eta$	5.1
$K^-\pi^+\pi^0$	3.4
$K^-\pi^+\eta$	1.3
$K^-\rho^+$	45.3
$K_0^*(1430)^-\pi^+$	1.3
$K^{*-}\pi^+$	0.3
$K^-\rho^+(\to \pi^+\gamma)$	0.1
$K^-\pi^+$ FSR	0.1
"remaining"	0.3
combinatorial	17.9

Table 11: Background categories for the $\overline{K}^{*0}$ mode, and the fraction of events each background represents on Monte Carlo.

particles) and therefore exhibit distinct common shapes in the fit variables. They are thus subtracted as one category, named "remaining" background.

The final set of background categories for each signal mode is listed in Tables 10, 11 and 12. Also listed is the fraction of events each background represents. It must be noted that the stated fractions correspond to the Monte Carlo simulation. As explained above, the relative fractions on data might differ.

	fraction of background [%]
$\rho^0\pi^0$	7.9
$\rho^+\pi^-$	10.6
$\rho^-\pi^+$	11.1
$K^-\rho^+$	7.4
$\rho(\to \pi\gamma)\pi$	0.1
$\pi^+\pi^-$ FSR	0.1
"remaining"	3.9
combinatorial	58.9

Table 12: Background categories for the ρ^0 mode, and the fraction of events each background represents on Monte Carlo.

6.3 CALIBRATION OF π^0 AND η TYPE BACKGROUNDS

Since the PDF shapes are determined on the Monte Carlo simulation, it is vital to ensure that the simulation matches the data as well as can be achieved. Events of the π^0 and η background types represent a major portion of all analysed candidates, as is evident from Figure 28. Discrepancies between Monte Carlo and data distributions of said decays could have a significant impact on the quality of the extraction of signal events. A cross-check is performed to analyse such possible discrepancies and take suitable measures to improve the parametrisation of said events accordingly.

Since it is impossible to clearly separate the π^0 and η type backgrounds of the signal modes on data, a control channel must be chosen for this cross-check, which enables the identification of π^0 and η type backgrounds in the distribution of fit variables $m(D^0)$ and $\cos(\theta_H)$. A suitable calibration mode is the decay $D^0 \to K_S^0\pi^0$. As already explained in Section 4.8, the $D^0 \to K_S^0\pi^0$ channel is very clean in terms of signal-to-background ratio. The analogous decay to our signal decay modes, $D^0 \to K_S^0\gamma$, is a forbidden decay. Therefore, if reconstructing the forbidden decay $D^0 \to K_S^0\gamma$, the events in the obtained sample will almost solely come from the $D^0 \to K_S^0\pi^0$ decay, with a smaller contribution of $D^0 \to K_S^0\eta$ decays and a relatively low combinatorial background component. This enables us to directly study the distribution of $D^0 \to X\pi^0(\eta)$ decays, obtained when reconstructing a $D^0 \to X\gamma$ decay.

We thus perform a reconstruction of decays $D^0 \to K_S^0\gamma$ on the Monte Carlo simulation and on data, with the applicable pre-selection criteria being the same as for the signal decay modes reconstruction. The samples are passed through the neural network to obtain the π^0 veto variable. The same set of selection criteria as for the signal modes is applied. Since the requirement on $p_{\mathrm{CMS}}(D^{*+})$ is slightly different for the three signal modes, the constraint of the ϕ mode is selected, as it is the middle value of the three. The mass window around the nominal mass of the K_S is set to 9 MeV.

Figure 30 shows the comparison between the normalised distributions of Monte
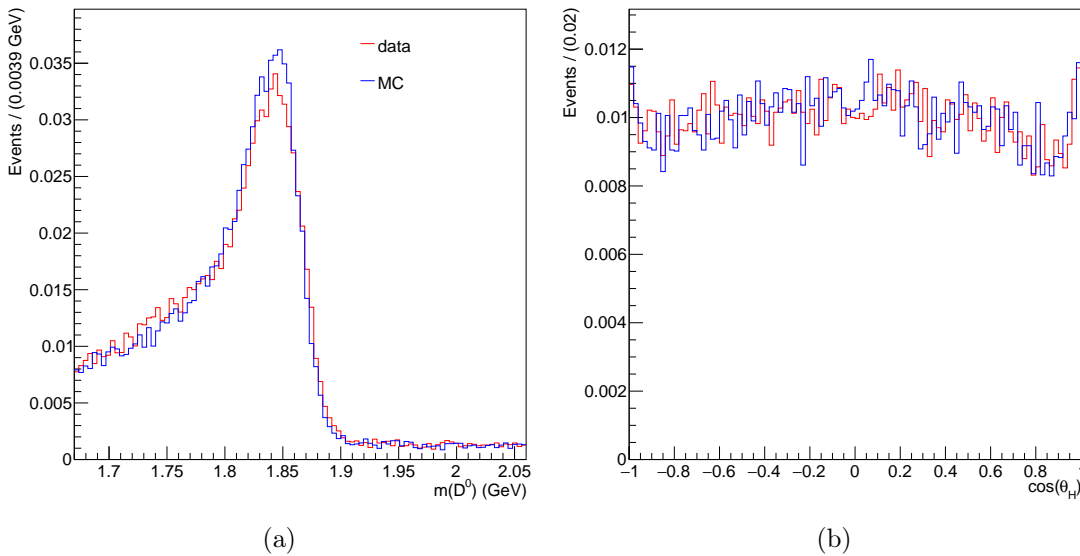
Figure 30: Comparison of normalised Monte Carlo and data distributions in $m(D^0)$ (a) and $\cos(\theta_H)$ (b) for the reconstructed $D^0 \to K_S^0 \gamma$ decay.

Carlo and data samples in the variables $m(D^0)$ and $\cos(\theta_H)$. In $\cos(\theta_H)$, the Monte Carlo and data distributions match. This is not the case in $m(D^0)$, where the data distribution is visibly broader. A function describing the shape, determined on Monte Carlo, would thus not fit the data sample precisely. Background events being incorrectly described would impact the power of signal recognition of the fit. To correct for this discrepancy and avoid any ensuing liabilities, steps are taken to modify the $m(D^0)$ distribution on Monte Carlo and bring it closer to the data distribution.

The procedure is developed on the calibration channel. Firstly, three categories are identified: the π^0 background, belonging to $D^0 \to K_S^0 \pi^0$ decays, the η background from $D^0 \to K_S^0 \eta$ decays, and combinatorial background, which covers the rest of events. We then construct several samples by taking the values of $m(D^0)$ of the π^0 and η distributions and numerically convolving them with a Gaussian with a specific width σ. Each value of $m(D^0)$ is replaced with a random value from a Gaussian distribution with the mean being the original value of $m(D^0)$, and a certain width. The procedure is repeated with different widths, σ ranging from 0 to 14 MeV, with a step of 0.1 MeV. 140 samples are thus obtained. The mean of the distribution is not smeared, as it will instead be allowed to float in the subsequent fit.

For each value of the smearing σ, a master PDF is constructed (we denote as master PDF the composite PDF, which describes the entire data sample and is composed of PDFs of individual categories that make up the sample). The combinatorial background PDF, a second order Chebyshev polynomial, is determined on Monte Carlo. The same combinatorial PDF is used in all subsamples and it is assumed it will also describe the data distribution well. For the π^0 and η components, a

histogrammed PDF based on the corresponding smeared sample is determined in each step. The master PDF is constructed as a sum of the three PDFs:

$$f_{\text{master}} = N_1 \cdot f_{\text{comb}} + N_2 \cdot f_{\pi^0} + N_3 \cdot f_\eta =$$
$$= N_1 \cdot T_2(m) + N_2 \cdot f_{\pi^0}^{\text{histo}}(m, o) + N_3 \cdot f_\eta^{\text{histo}}(m, o) \quad ,$$

where m denotes the variable $m(D^0)$, and the free parameters are the yields N_i of the three components, and a common offset o for the two histogrammed PDFs, which allows the mean of the two PDFs to float by a common value. All the so constructed master PDFs, corresponding to each value of the smearing σ, are fitted to data using a χ^2 fit and the value of χ^2 is calculated in each step. A chosen representative set of those fits is shown in Figure 31, with the corresponding binned pull distributions being drawn below each plot. The pull of each bin i is defined as the difference between the value of the fit function N^{fit} and the actual number of events N^{bin} in the bin, divided by the Poissonian error of the number of events:

$$\text{pull}_i = \frac{N_i^{\text{fit}} - N_i^{\text{bin}}}{\sqrt{N_i^{\text{bin}}}} \quad . \tag{36}$$

It can be observed that the starting PDF, obtained from the non-smeared Monte Carlo sample (but still allowing the mean of the π^0 and η components to float), fits data poorly, however the matching gradually improves with the increasing width until a certain point. Further increasing of the width causes the PDF to again deviate from the data distribution. The results are summarised on the graph in Figure 32, which shows for each σ the χ^2 value of the fit. The conclusions that can be drawn from the observation of the individual fit plots are clearly visible in this graph: the χ^2 value of the fit, starting at about 1.5, decreases with increasing σ until reaching a minimum for σ between 6 and 8 MeV. In this minimum, the values of χ^2 range between 1 and 1.2. For larger σ, the χ^2 rapidly increases, reaching 2.8 for the maximum applied smearing. It can be clearly concluded that applying a smearing corresponding to the minimum of the χ^2 distribution to the Monte Carlo sample results in a satisfactory matching between the Monte Carlo and data distributions. The minimum of the χ^2 distribution is broad, including all values of σ between 6 and 8 MeV, with statistical fluctuations preventing a more precise determination of the minimum. It is decided that on data, the fit will be performed three separate times, each time with PDFs for the π^0 (η) backgrounds obtained from Monte Carlo distributions smeared by 6, 7, and 8 MeV, respectively. The fit obtained with the 7 MeV Monte Carlo sample will be taken as the nominal fit, while the results of the fits obtained with 6 and 8 MeV samples will be used to determine the corresponding systematic error. To ensure that signal extraction works well in all cases, the 8 MeV sample is used for further analysis on Monte Carlo, as it is the largest value and the signal and π^0 background peaks overlap most in this case.

For all three signal modes' Monte Carlo simulations, events corresponding to backgrounds of the π^0 and η type are smeared with the obtained σ, effectively replacing the values of $m(D^0)$ with a new set of values. For other categories, the values of $m(D^0)$ are left unmodified. From this point on, the modified Monte Carlo
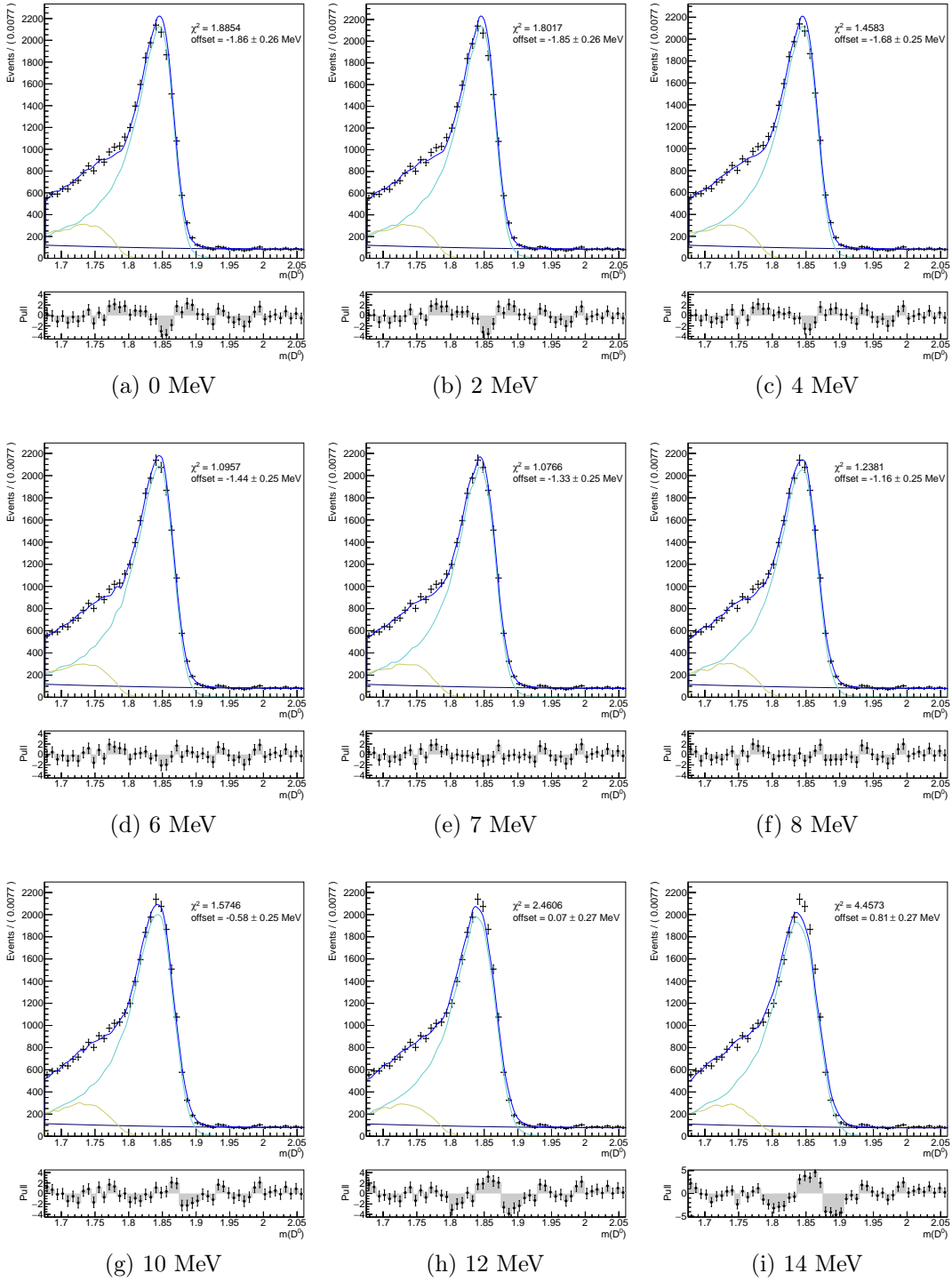
Figure 31: Fit of data with PDFs determined on smeared Monte Carlo samples, for different values of σ, on the K_S^0 calibration mode. On each plot the χ^2 and offset values are stated.
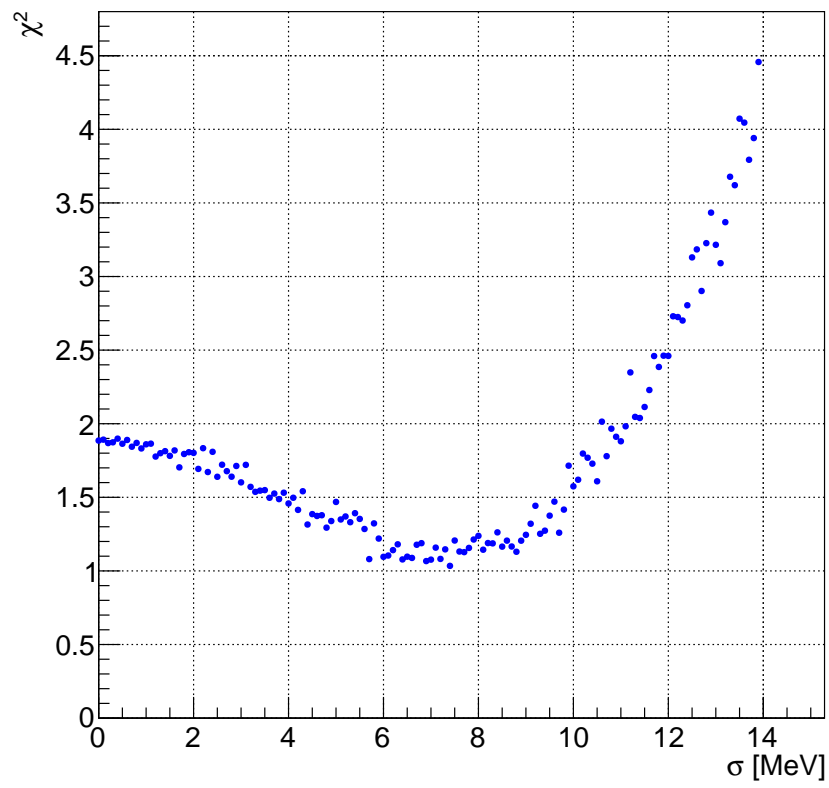
Figure 32: χ^2 values of the fit on data for different values of the smearing σ on the K_S^0 calibration mode.

samples, smeared by $\sigma = 8$ MeV, are used for all purposes of the analysis. For the future fit on data, the offset of the mean peak of the PDF values that corresponds to the chosen σ for smearing can be easily applied.

We have also considered a smearing with a separate width and separate offset for the π^0 and η components, as well as combinations of single and separate values. It was estimated that a common σ and offset yield the best performance.

6.4   CALIBRATION OF SIGNAL MODES

In the above section, it has been investigated and discovered that the Monte Carlo simulation does not accurately describe the $m(D^0)$ distribution of the π^0-type backgrounds. A solution was applied that consisted of smearing the Monte Carlo distributions to achieve matching with data. It stands to reason that a similar problem could occur in the signal modes and the PDF that has been determined on Monte Carlo would not describe the data distribution well, resulting in a bias in the extraction of the signal yield on data. Not having the possibility to investigate this for signal modes similarly to the procedure that was used for the π^0-type backgrounds, we are presented with two options: devise a method to determine the systematic uncertainty due to possible discrepancies between data and Monte Carlo, or have the width and mean of the signal PDF as free parameters of the fit. The latter option is the more favourable one, however it has the drawback that additional free parameters in the signal PDF will negatively impact the power of signal recognition, increasing the statistical error of the yield.

For the calibration of the dominant background, a uniform smearing factor was applied to all π^0 and η-type decays. This was supported by the reasoning that since the kinematics is the same for all decays of this type, it can be assumed that the discrepancy between Monte Carlo and data will be the same as well. Similarly, it stands to reason that the offset and width scale factor determined on one of the signal channels should be appropriate also for the other two channels. By using a $m(D^0)$ signal PDF with free parameters only on one of the signal channels, the obtained modification parameters can be directly applied to the PDFs of the other two signal modes, avoiding an increased statistical error on the yield in these two channels. The $\overline{K}^{*0}$ channel has a branching fraction an order of magnitude larger than the ϕ channel, and, as suggested by theoretical predictions, the branching fraction of the ρ^0 channel can be expected to be similar to that of ϕ or smaller. The $\overline{K}^{*0}$ channel thus has the largest statistics, implying that the statistical error of the correction factors could be smallest in this channel. The branching fraction of this mode has already been measured, and since it is a Cabibbo favoured decay, no significant CP asymmetry is expected compared to the other two modes, meaning that achieving better precision on the other two signal modes is is of greater importance. It is therefore decided to use a $m(D^0)$ signal PDF with free parameters for the $\overline{K}^{*0}$ mode, and subsequently apply the obtained modification parameters on the PDFs of the ϕ and ρ^0 mode.

The first step in the parametrisation process is to fit the distributions of the two variables that will constitute the final 2-dimensional fit: invariant mass $m(D^0)$ and $\cos(\theta_H)$, individually for signal and all background categories. Five streams of generic Monte Carlo are used to parametrise the background components, while signal PDFs are determined on signal Monte Carlo (only correctly reconstructed decays are used). The mass range that is chosen for the fit is $1.67 < m(D^0) < 2.06$ GeV. Although the signal distribution is expected to be narrower based on the signal Monte Carlo, a wider mass range is chosen to enable a better recognition of the background components, which in turn improves the recognition of signal. The range of $\cos(\theta_H)$ is left full for the ϕ mode and reduced to $|\cos(\theta_H)| < 0.8$ for the $\overline{K}^{*0}$ and ρ^0 modes (reasons for this choice have been explained in Section 6.1).

Some of the background categories have very little events outside the main peak, especially in the $m(D^0)$ distributions. They are therefore fitted in a reduced range, as the few events in the sidebands otherwise require an additional flat function that complicates the fit unnecessarily. However, such a simplification is not suitable in cases where a greater number of categories have matching distributions and the sum of omitted events from all categories would amount to a non-negligible contribution.

When more than one PDF is needed to describe a category, they are summed together using recursively parametrised coefficients in the following manner:

$$c_1 \cdot PDF_1 + (1 - c_1)(c_2 \cdot PDF_2 + (1 - c_2)(c_3 \cdot PDF_3 + ...)) \quad , \tag{37}$$

where $c_n = 1$ for a sum of n PDFs. Each of the coefficient ranges between 0 and 1 and it holds that $c_1 + (1 - c_1)c_2 + (1 - c_1)(1 - c_2)c_3 + ... = 1$.

We perform an unbinned maximum likelihood fit. The quality of the fit is assessed by inspecting the binned distribution of the pull.

6.5.1   Fits in $m(D^0)$

The main peak for signal and π^0-type decays is fitted with either a single Crystal-Ball function [35] wherever possible, or a combination of a Crystal-Ball or logarithmic Gaussian function [36] with an additional Gaussian or logarithmic Gaussian. In the $\overline{K}^{*0}$ mode, a wide Gaussian is added, as limiting the fit range proves an unsuitable measure.

The Crystal-Ball function is a combination of a main Gaussian function and a power-law tail below a certain treshold:

$$f_{\mathrm{CB}}(m, m_0, \sigma, a, n) = \begin{cases} \dfrac{(\frac{n}{|a|})e^{-\frac{1}{2}a^2}}{\left((\frac{n}{|a|}) - |a| - m\right)^2} & , \quad m < -|a| \\ \exp\left(-\frac{1}{2}(\frac{m - m_0}{\sigma})^2\right) & , \quad m > -|a| \end{cases} \tag{38}$$

where m_0 is the peak position of the Gaussian, σ is the width of the Gaussian, and n and a are the tail parameters. The logarithmic Gaussian is a Gaussian with an

extra tail parameter that skews it into an asymmetric shape, with a long tail on one side and a short tail on the other. It is defined as

$$f_{\text{logG}}(m, m_0, \sigma, n) = A \exp\left(-\frac{1}{2}(\ln^2(1 + \lambda n(m - m_0))/n^2 + n^2)\right) \qquad (39)$$

where $\lambda = \sinh(n\sqrt{\ln 4})/(\sigma n \sqrt{\ln 4})$.

The $m(D^0)$ distribution of the combinatorial background is fitted with a second order Chebyshev polynomial ($\overline{K}^{*0}$ and ρ^0 modes) or an exponential function (ϕ mode). To reduce dependence on Monte Carlo, the parameters of this PDF will be left floating in the final 2-dimensional fit, if proven that such a measure does not compromise the stability of the fit or significantly increase the statistical error on the signal yield.

6.5.2   Fits in $\cos(\theta_H)$

The signal shape is parametrised as $1\text{-}\cos^2(\theta_H)$ with no free parameters for all three signal modes. The $D^0 \to V\pi^0$ decay, which follows closely a $\cos^2(\theta_H)$ distribution, is parametrised as such with no free parameters for the ϕ mode. In the $\overline{K}^{*0}$ and ρ^0 channel, the shape somewhat deviates from $\cos^2(\theta_H)$ and is fitted with a second order polynomial for ρ^0 and a second order Chebyshev polynomial in $\overline{K}^{*0}$. As for the other physical background decays, they take a variety of shapes and are fitted as required.

The combinatorial background is fitted with a polynomial or Chebyshev polynomial, with an addition of Gaussians to account for any remaining peaks (when necessary).

6.5.3 ϕ Mode

An analysis of background sources in the ϕ channel reveals two peaks over the combinatorial background in the distribution of $m(D^0)$. One is the typical π^0-type peak, belonging to the $D^0 \to \phi\pi^0$ decay, and is parametrised separately as one of the background components (Figure 33b). The other peak is located at a lower value of the D^0 invariant mass (Figure 33c) and comprises decays such as $D^0 \to \phi\eta, D^0 \to \phi K_S^0(\to \pi^0\pi^0)$ and others. None of the components present in this peak is significantly represented, and they do not overlap with the signal peak, so they are classified as one joint category with the following criteria: the reconstructed D^0 is and actual D^0 and the reconstructed V meson is in fact a ϕ, while the criterion for the $\phi\pi^0$ background does not hold.

Individual components of the ϕ mode and the PDFs used to fit them are summarised in Table 13. Figure 33 shows the fits in $m(D^0)$ of all categories. The fitted PDF is depicted with the bold blue line. A pull distribution is plotted below each fit to show the accordance of the fit with the Monte Carlo data. The analogous plots in $\cos(\theta_H)$ are shown in Figure 34. It can be seen that the fit describes the simulated data well in all cases.

	$m(D^0)$	$\cos(\theta_H)$	NDF
$\phi\gamma$	Crystal-Ball	$1\text{-}\cos^2(\theta_H)$	1
$\phi\pi^0$	Crystal-Ball	$\cos^2(\theta_H)$	1
"remaining"	Gaussian	2nd order Chebyshev	1
combinatorial	exponential	2nd order Chebyshev	1+1

Table 13: Categories for the ϕ mode, and the respective PDFs used for 1-dimensional fits. NDF refers to the number of free parameters in the 2-dimensional fit (including also free yields).

(a) $D^0 \rightarrow \phi\gamma$

(b) $D^0 \rightarrow \phi\pi^0$

(c) "remaining"
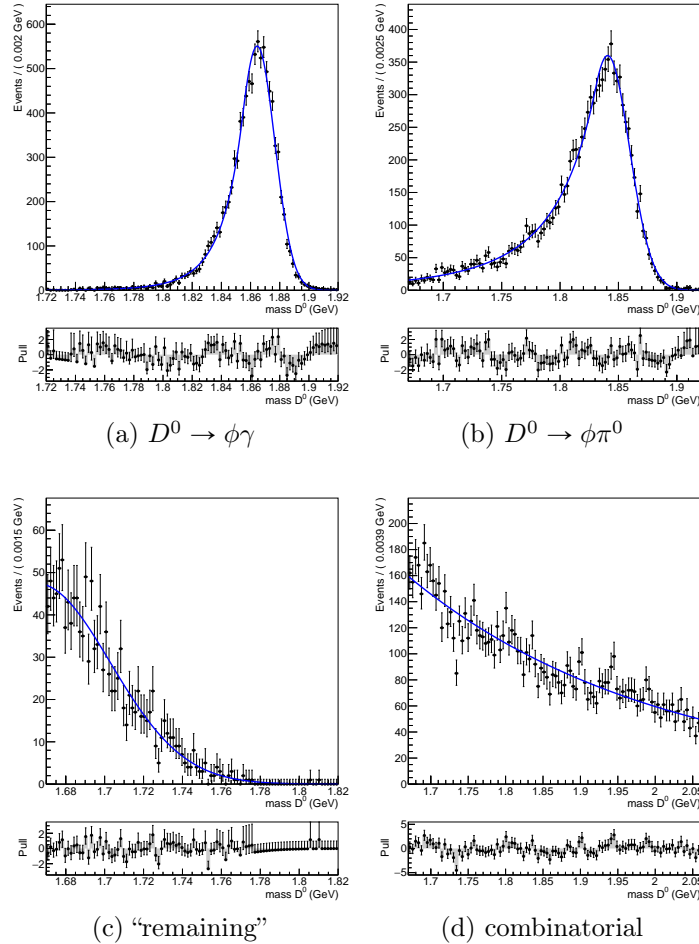
(d) combinatorial

Figure 33: 1-dimensional fits in $m(D^0)$ of all the categories in the ϕ mode. The χ^2/NDF of the fit, where NDF is the number of degrees of freedom, is 1.3 for signal, 1.2 for $\phi\pi^0$, 0.7 for the category "remaining" background and 1.4 for combinatorial background.

(a) $D^0 \to \phi\gamma$

(b) $D^0 \to \phi\pi^0$

(c) "remaining"
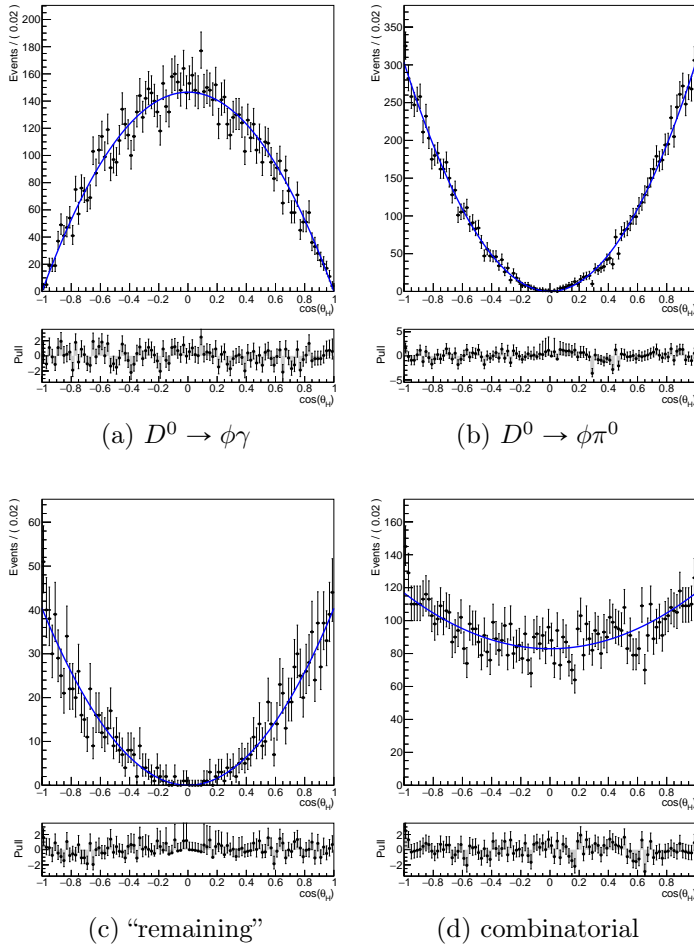
(d) combinatorial

Figure 34: 1-dimensional fits of $\cos(\theta_H)$ of all the categories in the ϕ mode. The χ^2/NDF of the fit is 1.1 for signal, 0.9 for $\phi\pi^0$, 0.7 for the category "remaining" background and 0.9 for combinatorial background.

	$m(D^0)$	$\cos(\theta_H)$	NDF
$\overline{K}^{*0}\gamma$	Crystal-Ball + 2 Gaussians	$1\text{-}\cos^2(\theta_H)$	1+2
$\overline{K}^{*0}\pi^0$	2 log. Gaussians + Gaussian	3rd order Chebyshev	1
$K^-\pi^+\eta$	log. Gaussian + Gaussian	3rd order Chebyshev	1
$K^-\pi^+\pi^0$	Crystal-Ball + 2 Gaussians	2nd order Chebyshev	1
$K^-\pi^+\eta$	log. Gaussian + Gaussian	$K^-\pi^+\pi^0$ PDF	1
$K^-\rho^+$	2 log. Gaussians + Gaussian	log. Gaussian + Gaussian + Bifurcated Gaussian	1
$K_0^*(1430)^-\pi^+$	$\overline{K}^{*0}\pi^0$ PDF	3rd order Chebyshev + Gaussian	/
$K^{*-}\pi^+$	$\overline{K}^{*0}\pi^0$ PDF	log. Gaussian	/
$K^-\rho^+(\to \pi^+\gamma)$	signal PDF	Crystal-Ball + Gaussian	/
$K^-\pi^+$ FSR	signal PDF	3rd order Chebyshev	/
"remaining"	log. Gaussian + Gaussian	3rd order Chebyshev	/
combinatorial	2nd order Chebyshev	3rd order Chebyshev	1+2

Table 14: Categories for the $\overline{K}^{*0}$ mode, and the respective PDFs used for 1-dimensional fits. NDF refers to the number of free parameters in the 2-dimensional fit (including also free yields).

6.5.4 $\overline{K}^{*0}$ Mode

The $\overline{K}^{*0}$ signal mode comprises the largest number of different background decay channels. In the $m(D^0)$ distribution, the background comprises two main peaks: a very prominent π^0-type peak and a considerably smaller η-type peak. The π^0-type peak is composed of two main contributions, decays $D^0 \to K^-\rho^+(\to \pi^+\pi^0)$ and $D^0 \to \overline{K}^{*0}\pi^0$, with smaller admixtures of decays (in descending order of contribution) $D^0 \to K^-\pi^+\pi^0$ (non-resonant), $D^0 \to K_0^*(1430)^-(\to K^-\pi^0)\pi^+$, $D^0 \to K^{*-}(\to K^-\pi^0)\pi^+$, $D^0 \to K^-\rho^+(\to \pi^+\gamma)$ and $D^0 \to K^-\pi^+$ with the photon emitted as final state radiation. The yields of the last four components are fixed in the final fit. The η-type peak contains $D^0 \to \overline{K}^{*0}\eta$, non-resonant decay $D^0 \to K^-\pi^+\eta$ and the majority of events of the joint "remaining" category of other decays where the D^0 (and D^{*+}) are correctly reconstructed from the majority of their daughter particles. The latter category contains very few events and its yield is fixed in the final fit.

Individual components of the $\overline{K}^{*0}$ mode and the PDFs used to fit them are summarised in Table 14. Figures 35 and 36 show the fits in $m(D^0)$ of all categories. The fitted PDF is depicted with the bold blue line. If more than one function is used for the fit, the individual components are shown with coloured dashed lines. A pull distribution is plotted below each fit to show the accordance of the fit with the Monte Carlo data. The analogous plots in $\cos(\theta_H)$ are shown in Figures 37 and 38. It can be seen that the fit describes the simulated data well in all cases.
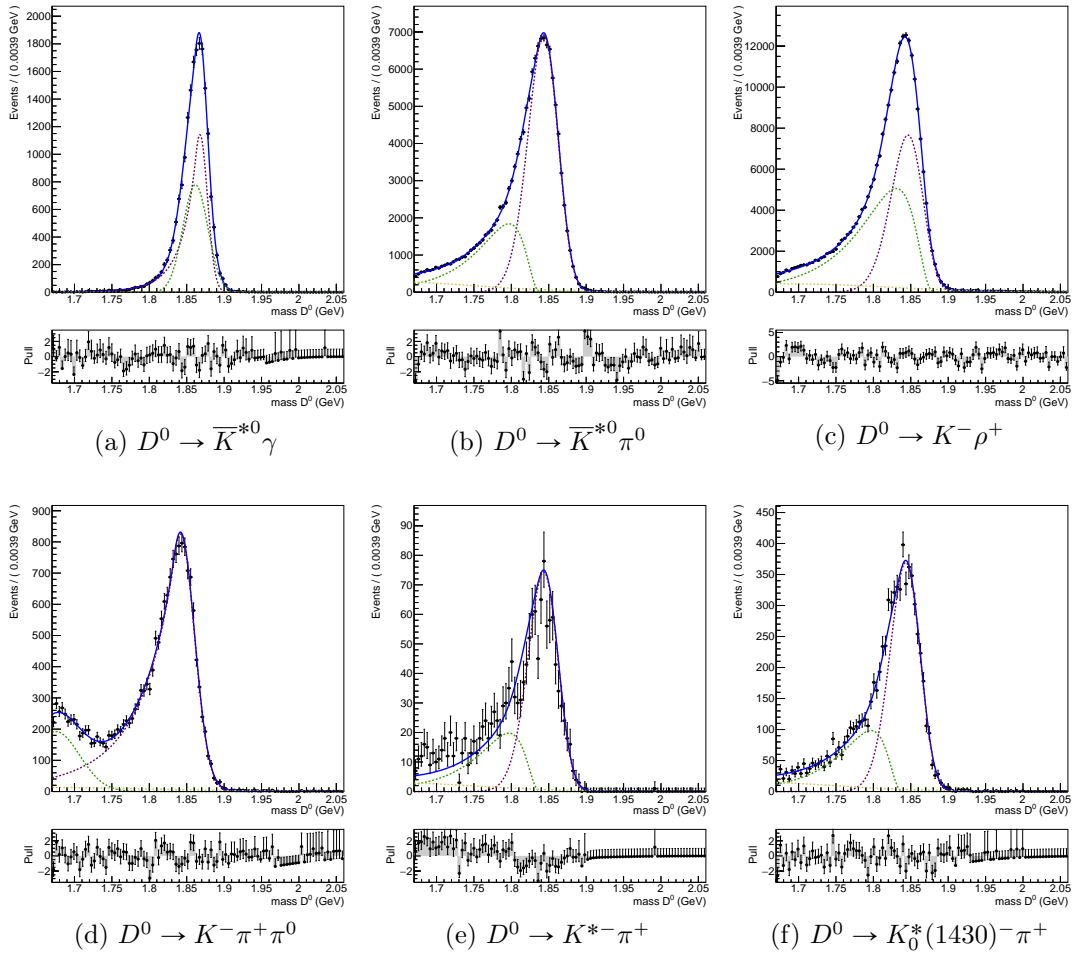
Figure 35: 1-dimensional fits in $m(D^0)$ of half of categories in the $\overline{K}^{*0}$ mode. The χ^2/NDF of the fit is 0.8 for signal, 1.6 for $\overline{K}^{*0}\pi^0$, 1.8 for $K^-\rho^+$, 1.0 for $K^-\pi^+\pi^0$, 1.1 for $K^{*-}\pi^+$ and 1.0 for $K_0^*(1430)^-\pi^+$.
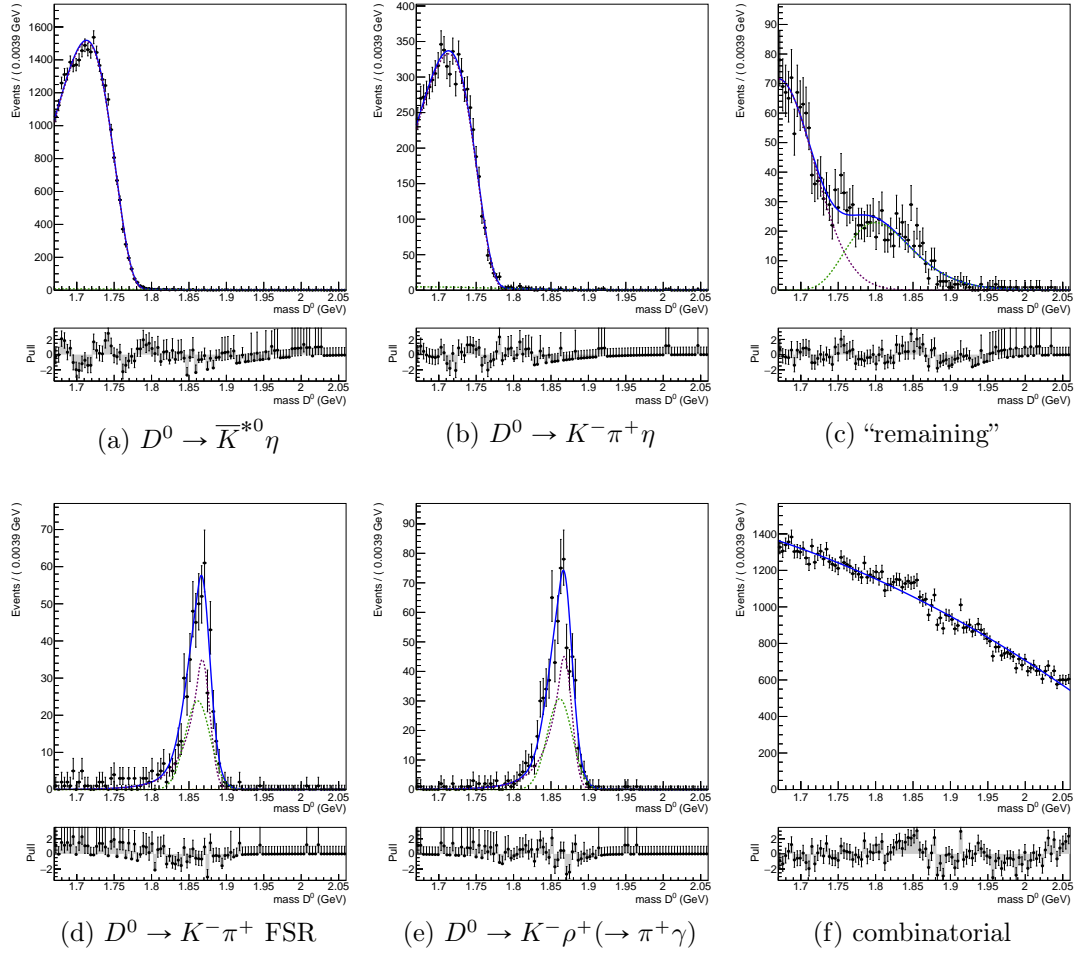
Figure 36: 1-dimensional fits in $m(D^0)$ of half of categories in the $\overline{K}^{*0}$ mode. The χ^2/NDF of the fit is 1.1 for $\overline{K}^{*0}\eta$, 0.6 for $K^-\pi^+\eta$, 0.8 for the "remaining" category, 1.0 for $K^-\pi^+$ FSR, 1.1 for $K^-\rho^+(\to \pi^+\gamma)$ and 1.6 for the combinatorial background.

(a) $D^0 \to \overline{K}^{*0}\gamma$

(b) $D^0 \to \overline{K}^{*0}\pi^0$

(c) $D^0 \to K^-\rho^+$

(d) $D^0 \to K^-\pi^+\pi^0$

(e) $D^0 \to K^{*-}\pi^+$

(f) $D^0 \to K^-\pi^+\eta$

Figure 37: 1-dimensional fits of $\cos(\theta_H)$ of half of categories in the $\overline{K}^{*0}$ mode. The χ^2/NDF of the fit is 1.0 for signal, 1.2 for $\overline{K}^{*0}\pi^0$, 1.8 for $K^-\rho^+$, 0.9 for $K^-\pi^+\pi^0$, 1.1 for $K^{*-}\pi^+$ and 0.7 for $K_0^*(1430)^-\pi^+$.

(a) $D^0 \to \overline{K}^{*0}\eta$

(b) $D^0 \to K_0^*(1430)^-\pi^+$

(c) "remaining"

(d) $D^0 \to K^-\pi^+$ FSR

(e) $D^0 \to K^-\rho^+(\to \pi^+\gamma)$
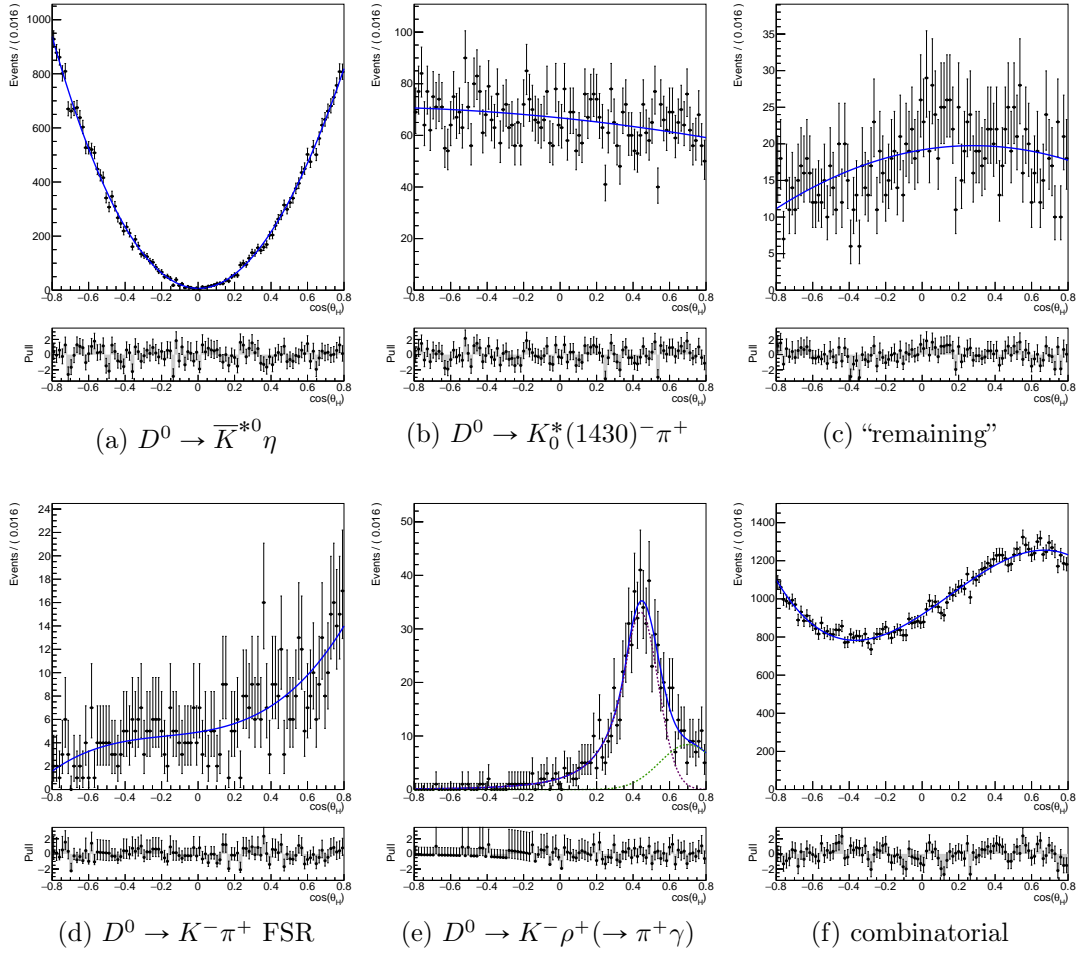
(f) combinatorial

Figure 38: 1-dimensional fits of $\cos(\theta_H)$ of half of categories in the $\overline{K}^{*0}$ mode. The χ^2/NDF of the fit is 0.9 for $\overline{K}^{*0}\eta$, 1.1 for $K^-\pi^+\eta$, 1.0 for the "remaining" category, 0.7 for $K^-\pi^+$ FSR, 0.5 for $K^-\rho^+(\to \pi^+\gamma)$ and 1.1 for the combinatorial background.

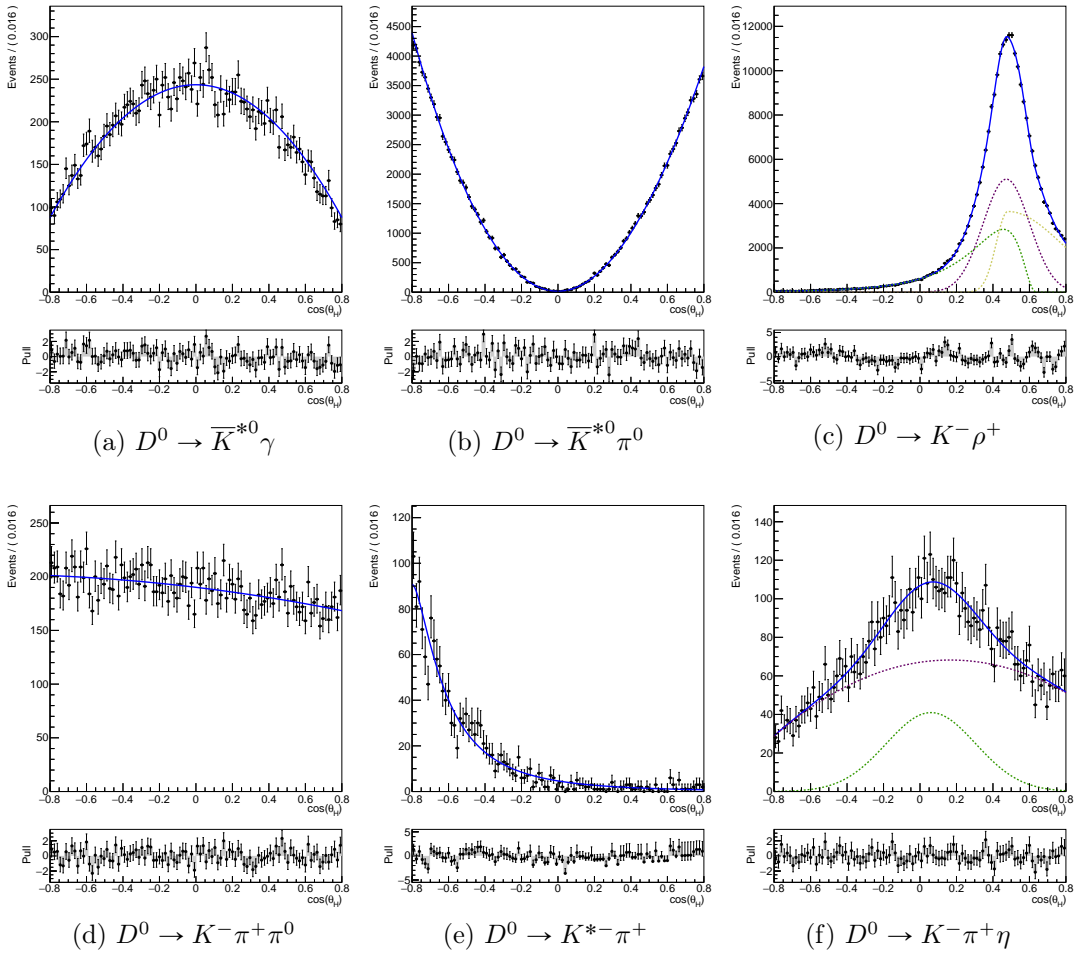As discussed in Section 6.4, it was decided that the mean and width of the signal $m(D^0)$ PDF in the $\overline{K}^{*0}$ mode should be free parameters of the 2-dimensional fit, in order to reduce reliance on Monte Carlo. The $m(D^0)$ distribution is described with a Crystal-Ball and a Gaussian, with an additional broad Gaussian that describes the tails. The smearing that was applied for the π^0-type background is of the order of several MeV. A discrepancy between simulation and data in the signal modes of a similar order of magnitude would not significantly affect the broad Gaussian, which is therefore left unmodified. The Crystal-Ball and Gaussian that describe the main peak are rewritten so that the mean and width of each become a function of a parameter common to both. Both means are redefined to add a common offset, and the widths are redefined to being multiplied with a common weight:

$$\text{mean}_{\text{CB}} \longrightarrow \text{mean}_{\text{CB}} + \text{offset}$$
$$\text{mean}_{\text{G}} \longrightarrow \text{mean}_{\text{G}} + \text{offset}$$
$$\sigma_{\text{CB}} \longrightarrow \sigma_{\text{CB}} \cdot \text{weight}$$
$$\sigma_{\text{G}} \longrightarrow \sigma_{\text{G}} \cdot \text{weight} \quad .$$

The offset and weight obtained from the fit on physical data in the $\overline{K}^{*0}$ channel will be applied to the $m(D^0)$ PDFs of the ϕ and ρ^0 mode at the later stage of fitting the data. For the following analysis on Monte Carlo, the respective PDFs will be left unchanged.

6.5.5 ρ^0 Mode

There are three main decays constituting the π^0-peak in $m(D^0)$ in the ρ mode: $D^0 \to \rho^+(\to \pi^+\pi^0)\pi^-, D^0 \to \rho^-(\to \pi^-\pi^0)\pi^+$ and $D^0 \to \rho^0(\to \pi^+\pi^-)\pi^0$. Decays where the photon is emitted as final state radiation or through a radiative decay of a charged ρ meson have very small yields and are fixed in the final fit.

The low-mass peak in $m(D^0)$ is composed of the decay $D^0 \to K^-\rho^+$, where the kaon is misidentified as a pion and thus the calculation of the D^0 invariant mass is shifted toward lower values due to a larger kaon mass in confront to the pion mass (Figure 39g), and a joint "remaining" component of all other decays where the D^0 is reconstructed from the majority of its daughter particles (Figure 39h).

The combinatorial background in the ρ^0 channel is substantial, amounting to more than half of all the background, due to the large width of the ρ^0 resonance and subsequently a very loose constraint in that regard. Its distribution in $m(D^0)$ is a smooth slope with no additional peaking shapes. In $\cos(\theta_H)$, the distribution is not smooth, but comprises two symmetrical peaks, fitted with a Gaussian each over a polynomial.

Individual components of the ρ^0 mode and the PDFs used to fit them are summarised in Table 15. Figure 39 shows the fits in $m(D^0)$ of all categories. The fitted PDF is depicted with the bold blue line. If more than one function is used for the fit, the individual components are shown with coloured dashed lines. A pull distribution is plotted below each fit to show the accordance of the fit with the Monte Carlo data.

	$m(D^0)$	$\cos(\theta_H)$	NDF
$\rho^0\gamma$	Crystal-Ball	1-$\cos^2(\theta_H)$	1
$\rho^0\pi^0$	Crystal-Ball	2nd order polynomial	1
$\rho^+\pi^-$	Crystal-Ball	2 Gaussians	1
$\rho^-\pi^+$	Crystal-Ball	2 Gaussians	1
$K^-\rho^+$	log. Gaussian + Gaussian	2 Gaussians	1
$\rho(\to \pi\gamma)\pi$	Crystal-Ball	2 Gaussian	/
$\pi^+\pi^-$ FSR	$\rho(\to \pi\gamma)\pi$ PDF	2nd order Chebyshev	/
"remaining"	Gaussian	2 Gaussians + exponential	1
combinatorial	2nd order Chebyshev	4th order polynomial + 2 Gaussians	1+2

Table 15: Categories for the ρ^0 mode, and the respective PDFs used for 1-dimensional fits. NDF refers to the number of free parameters in the 2-dimensional fit (including also free yields).

The analogous plots in $\cos(\theta_H)$ are shown in Figure 40. It can be seen that the fit describes the simulated data well in all cases.

(a) $D^0 \to \rho^0 \gamma$

(b) $D^0 \to \rho^0 \pi^0$

(c) $D^0 \to \rho^+ \pi^-$

(d) $D^0 \to \rho^- \pi^+$

(e) $D^0 \to \pi^- \rho^+ (\to \pi^+ \gamma)$

(f) $D^0 \to \pi^+ \pi^-$ FSR

(g) $D^0 \to K^- \rho^+$

(h) "remaining"
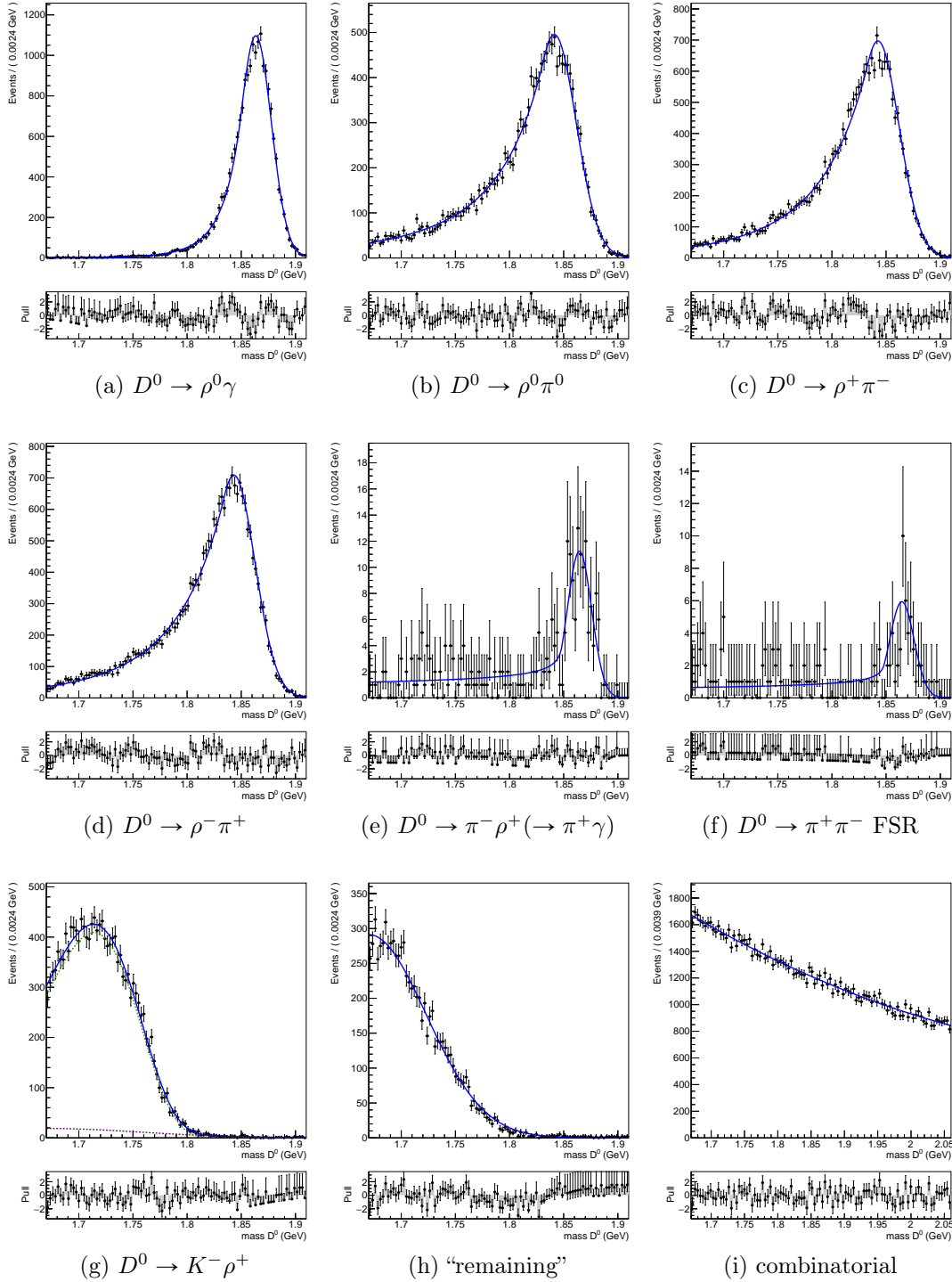
(i) combinatorial

Figure 39: 1-dimensional fits in $m(D^0)$ of all categories in the ρ^0 mode. The χ^2/NDF of the fit is 1.4 for signal, 1.3 for $\rho^0 \pi^0$, 1.7 for $\rho\pi$, 0.8 for $\pi^- \rho^+ (\to \pi^+ \gamma)$, 0.6 for $\pi^+ \pi^-$ FSR, 1.0 for $K^- \rho^+$, 1.4 for the "remaining" category and 1.0 for combinatorial background.

(a) $D^0 \to \rho^0 \gamma$

(b) $D^0 \to \rho^0 \pi^0$

(c) $D^0 \to \rho^+ \pi^-$

(d) $D^0 \to \rho^- \pi^+$

(e) $D^0 \to \pi^- \rho^+ (\to \pi^+ \gamma)$

(f) $D^0 \to \pi^+ \pi^-$ FSR

(g) $D^0 \to K^- \rho^+$

(h) "remaining"

(i) combinatorial

Figure 40: 1-dimensional fits of $\cos(\theta_H)$ of all categories in the ρ^0 mode. The χ^2/NDF of the fit is 1.3 for signal, 1.2 for $\rho^0 \pi^0$, 1.6 for $D^0 \to \rho \pi$, 1.5 for $\overline{D}^0 \to \rho \pi$, 0.6 for $\pi^- \rho^+ (\to \pi^+ \gamma)$, 0.6 for $\pi^+ \pi^-$ FSR, 1.0 for $K^- \rho^+$, 1.0 for the "remaining" category and 1.0 for combinatorial background.
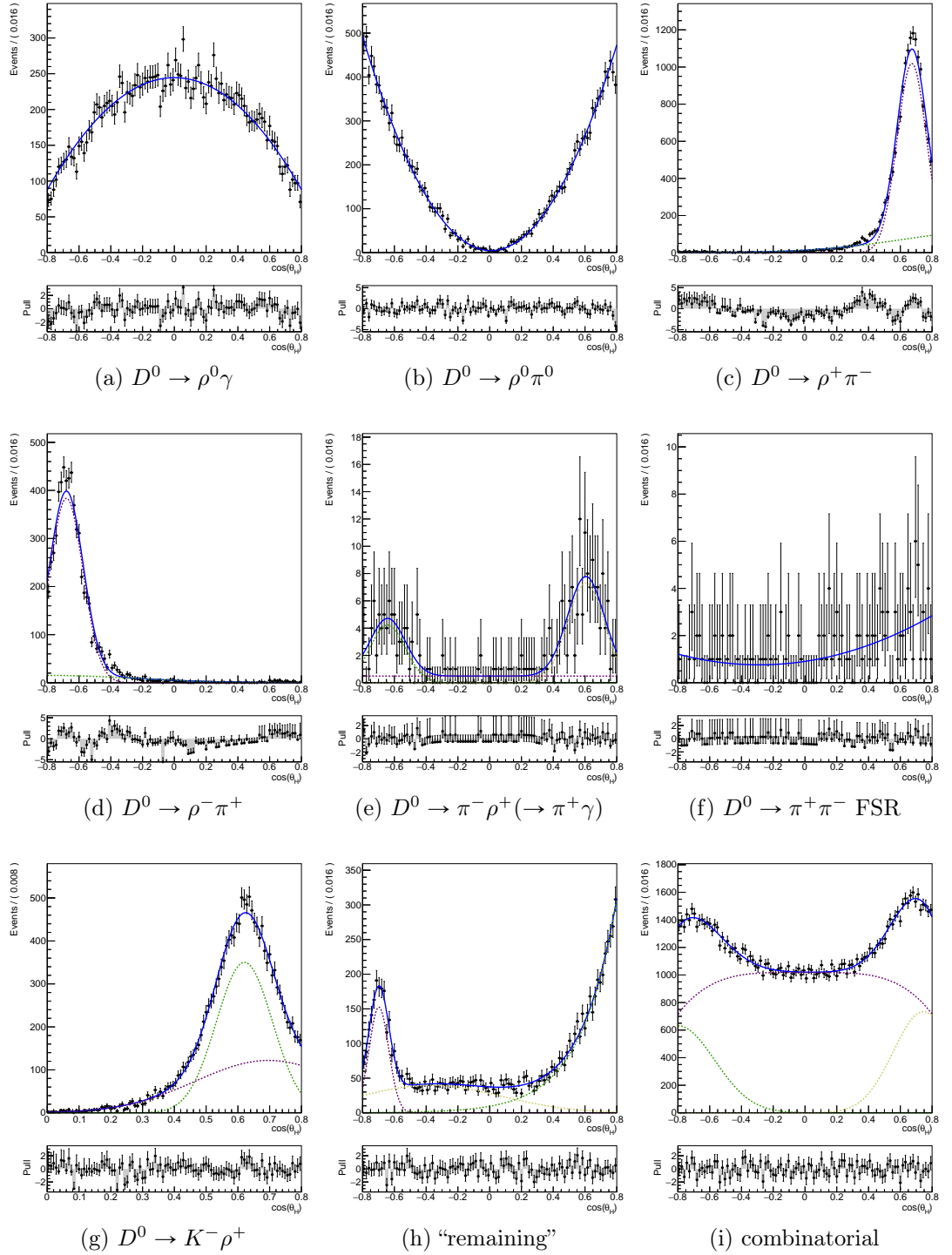
6.6   2-DIMENSIONAL FIT

6.6.1   *Correlation Test*

Since a 2-dimensional fit is performed, it is necessary to check the level of correlation between the two fit variables. Ideally, the variables would not be correlated at all. However, often only a small correlation between variables is present, and in such cases the 2-dimensional fit can still prove to be a reliable method. If the correlation is sufficiently small, the variables can be treated as uncorrelated, while any possible consequences that affect the final result can be attributed to the systematic error.

To test for correlation between $m(D^0)$ and $\cos(\theta_H)$ the correlation analysis tool CAT [37] is used. The tool identifies any dependence in the data set by performing a hypothesis test for two variables being independent. It returns the significance of the correlation this corresponds to in units of standard deviation σ.

For all three signal modes, the tools is run on all categories separately. Signal Monte Carlo is used to check for correlation in signal distributions. In all three signal modes, the correlation between $m(D^0)$ and $\cos(\theta_H)$ for signal is found to have less than 1σ significance. Figures 41, 42 and 46 show the distributions of $m(D^0)$ in bins of $\cos(\theta_H)$ and $\cos(\theta_H)$ in bins of $m(D^0)$. The bins in one variable, in which the other variable is plotted, are not equidistant, their number and spacing being determined by the tool to ensure equivalent statistics between bins. Plots under the diagonal show the difference between bins i and j. This distribution should be flat if no correlation is present. Plots above the diagonal represent the pulls of bins i and j. With no correlations these should exhibit a Gaussian shape with width 1.

Correlations are checked also for all background categories on 5 streams of generic Monte Carlo. In the ϕ mode, no significant correlations seem to be present. Special attention is dedicated only to categories where the correlation has a significance greater than 5σ, which occurs in the $\overline{K}^{*0}$ and ρ^0 modes. In the $\overline{K}^{*0}$ mode, these categories are the combinatorial, π^0 and $K^-\rho^+$ backgrounds, i.e. all categories with the highest number of events in this mode. The corresponding plots are shown in Figures 43, 44 and 45. Since 5 streams of generic Monte Carlo have been used for this check, it must be present in mind that the final data sample will contain approximately 5 times less statistics, which implies also the significance of correlations will be scaled accordingly. In the combinatorial background, no further categories can be identified that would comprise a significant number of events and could be further extracted from the combinatorial background. As for the π^0 and $K^-\rho^+$ categories, it can be seen that differences appear in the $m(D^0)$ distribution in a form of an additional small peak at low values of $m(D^0)$ appearing in certain bins, while the main shape of the distribution remains the same. For the π^0 background, these bins are in the middle, whereas for the $K^-\rho^+$ category this feature appears in the most negative bins of $\cos(\theta_H)$. In both cases, this is the region with the least amount of events. As the π^0 and $K^-\rho^+$ categories represent 80% of events from the three categories that show a significant correlation (with the combinatiorial background representing the remaining 20%), and the correlations manifest in a specific, parametrisable form, we proceed with the task of describing the correlations in $m(D^0)$ in bins of $\cos(\theta_H)$

Figure 41: Invariant D^0 mass in bins of $\cos(\theta_H)$ (a) and $\cos(\theta_H)$ in bins of $m(D^0)$ (b) for the signal ϕ mode as taken from the output of the `CAT` correlation tool. Plots under the diagonal show the difference between bins and plots above the diagonal represent the pulls.

for these two categories. The procedure along with the results is reported in the following chapter.

In the ρ^0 mode, the problematic categories are the $K^-\rho^+$, which is the fourth background category in terms of the number of events, "remaining" background with half as many events as $K^-\rho^+$ and the category with the radiative ρ decay, $\rho(\to \pi\gamma)\pi$, which is one of the least populated categories. While this category exhibits a great correlation, it also features large statistical fluctuations, and keeping in mind that the final physical data set will only feature about 20% of the present statistics, the statistical fluctuations become comparable to the correlation between the fit variables. This is not the case for the "remaining" background category, which also shows large correlations, but has a significantly higher number of events. However, as is the case in the combinatorial background of the $\overline{K}^{*0}$ channel, no subcategories are identified that could be further extracted. The corresponding plots are shown in Figures 47, 48 and 49.

In summary, in the $\overline{K}^{*0}$ and ρ^0 mode, a certain level of correlation is present in some background categories. Some of these will be immediately accounted for, as described in the following chapter. Since the planned 2-dimensional fit treats the two variables as completely uncorrelated, it will be necessary to verify that the remaining neglected correlations do not affect the performance of the fit. The projections of the fit to each variable in bins of the other variable will be examined for all three signal modes, to ensure the fit works well in all regions.

(a)

(b)

Figure 42: Invariant D^0 mass in bins of $\cos(\theta_H)$ (a) and $\cos(\theta_H)$ in bins of $m(D^0)$ (b) for the signal $\overline{K}^{*0}$ mode as taken from the output of the `CAT` correlation tool. Plots under the diagonal show the difference between bins and plots above the diagonal represent the pulls.

(a)

(b)
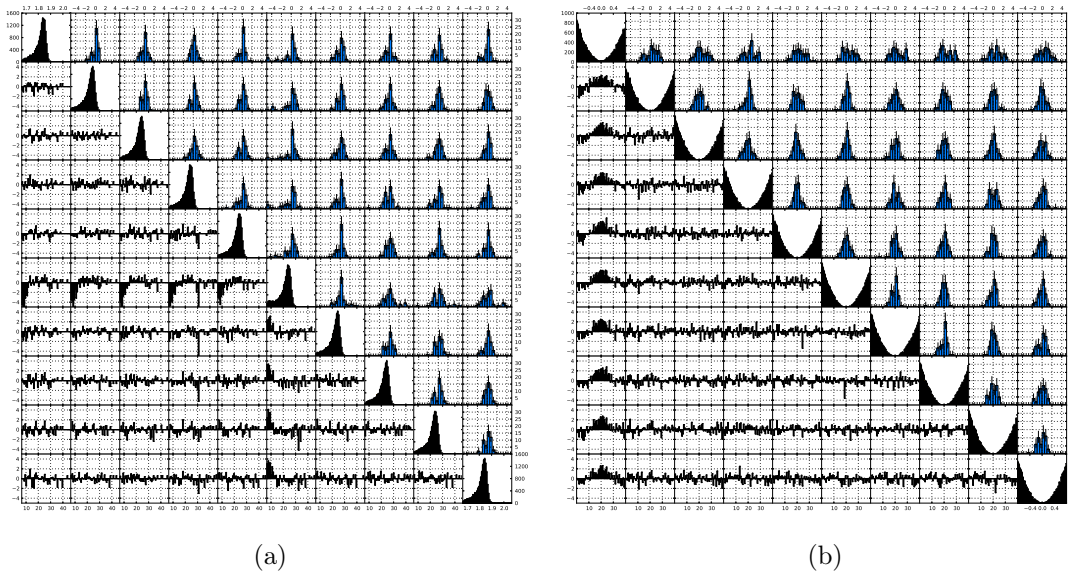
Figure 43: Invariant D^0 mass in bins of $\cos(\theta_H)$ (a) and $\cos(\theta_H)$ in bins of $m(D^0)$ (b) for the π^0 background of the $\overline{K}^{*0}$ mode as taken from the output of the `CAT` correlation tool. Plots under the diagonal show the difference between bins and plots above the diagonal represent the pulls.
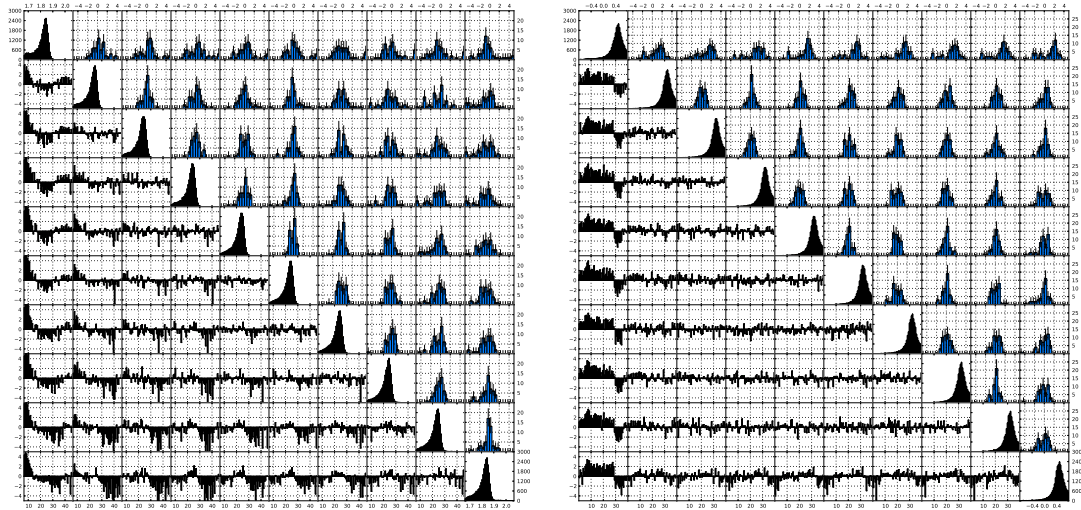
Figure 44: Invariant D^0 mass in bins of $\cos(\theta_H)$ (a) and $\cos(\theta_H)$ in bins of $m(D^0)$ (b) for the $K^-\rho^+$ background of the $\overline{K}^{*0}$ mode as taken from the output of the CAT correlation tool. Plots under the diagonal show the difference between bins and plots above the diagonal represent the pulls.
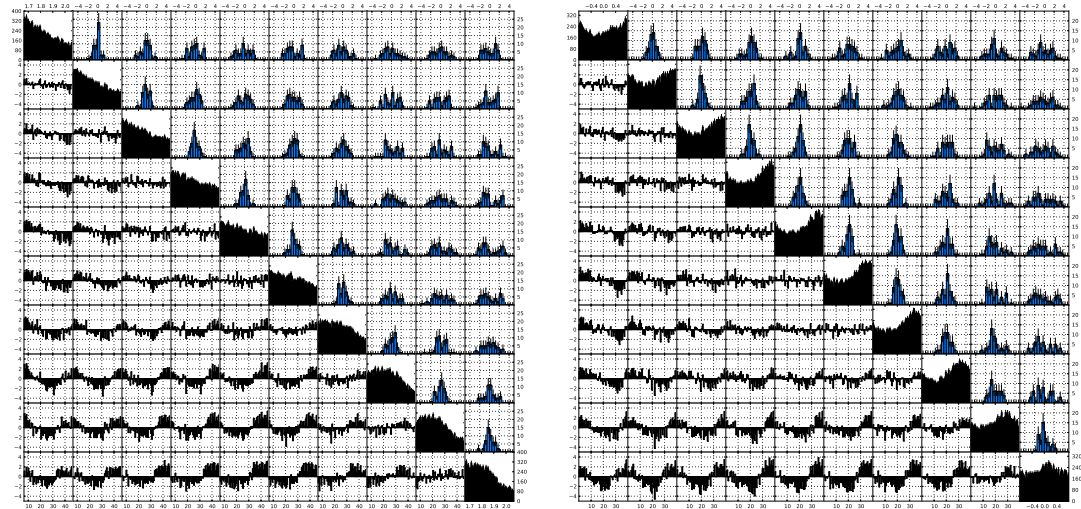
Figure 45: Invariant D^0 mass in bins of $\cos(\theta_H)$ (a) and $\cos(\theta_H)$ in bins of $m(D^0)$ (b) for the combinatorial background of the $\overline{K}^{*0}$ mode as taken from the output of the CAT correlation tool. Plots under the diagonal show the difference between bins and plots above the diagonal represent the pulls.

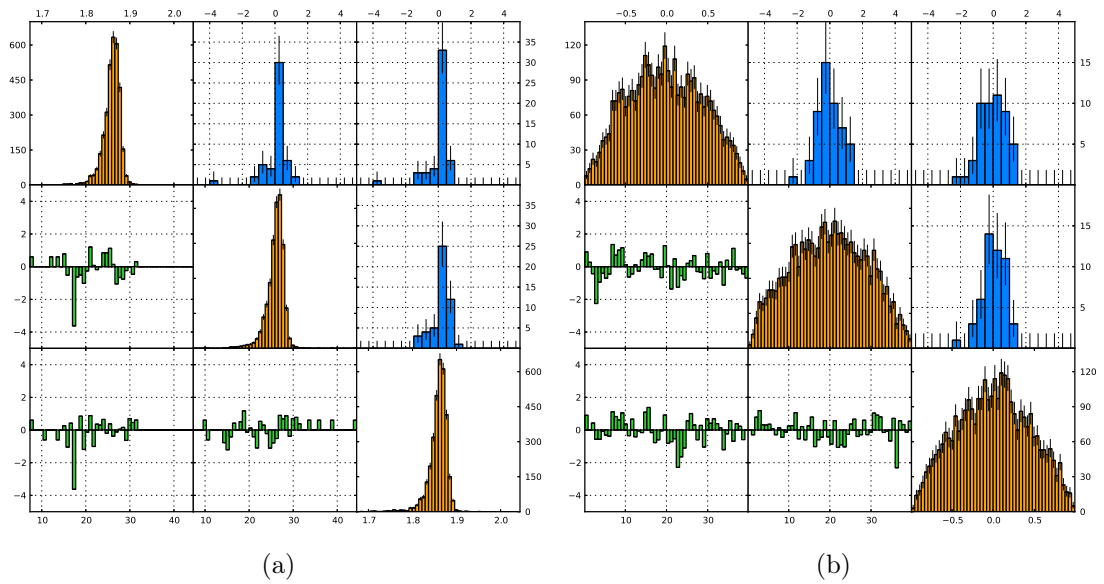(a)   (b)
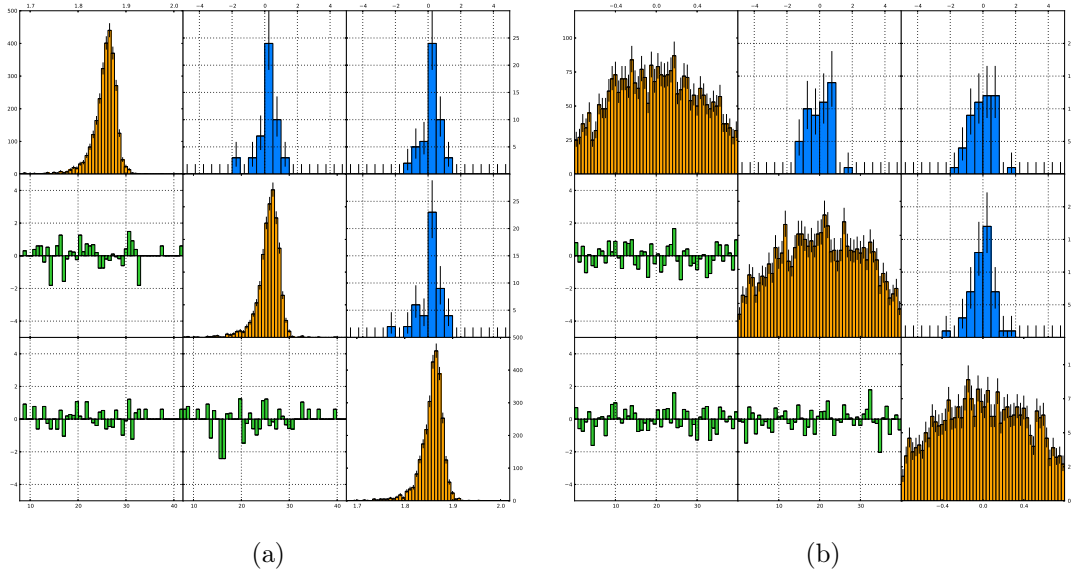
Figure 46: Invariant D^0 mass in bins of $\cos(\theta_H)$ (a) and $\cos(\theta_H)$ in bins of $m(D^0)$ (b) for the signal ρ^0 mode as taken from the output of the `CAT` correlation tool. Plots under the diagonal show the difference between bins and plots above the diagonal represent the pulls.

(a)   (b)
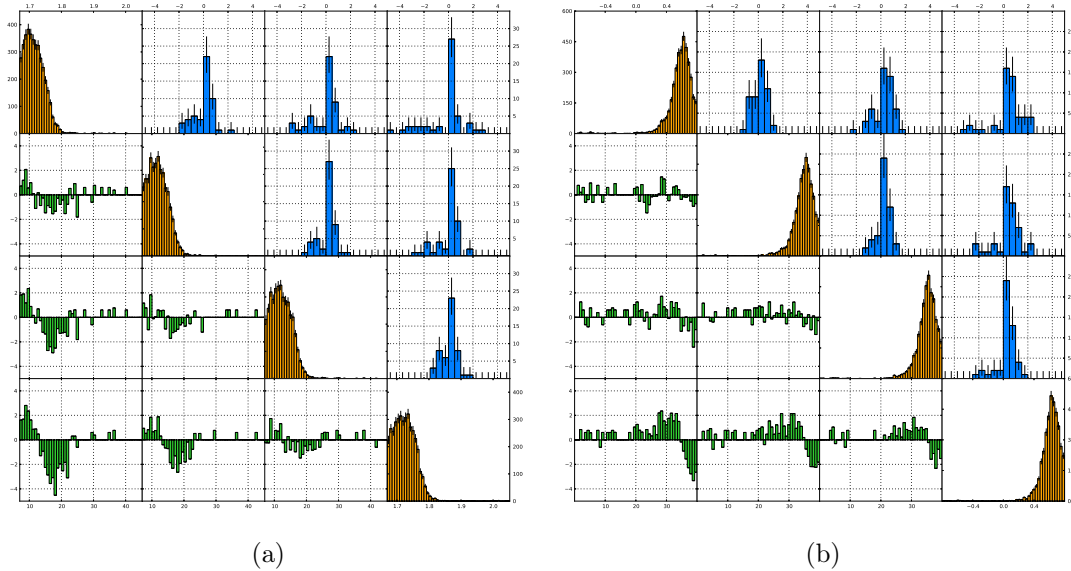
Figure 47: Invariant D^0 mass in bins of $\cos(\theta_H)$ (a) and $\cos(\theta_H)$ in bins of $m(D^0)$ (b) for the $K^-\rho^+$ background of the ρ^0 mode as taken from the output of the `CAT` correlation tool. Plots under the diagonal show the difference between bins and plots above the diagonal represent the pulls.

(a)

(b)
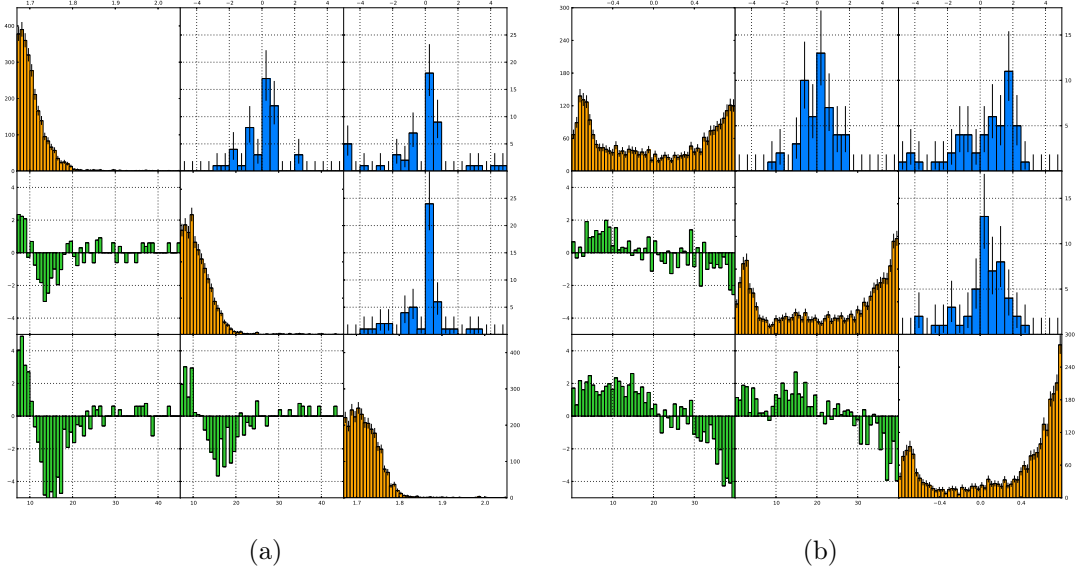
Figure 48: Invariant D^0 mass in bins of $\cos(\theta_H)$ (a) and $\cos(\theta_H)$ in bins of $m(D^0)$ (b) for the "remaining" background of the ρ^0 mode as taken from the output of the CAT correlation tool. Plots under the diagonal show the difference between bins and plots above the diagonal represent the pulls.

(a)

(b)
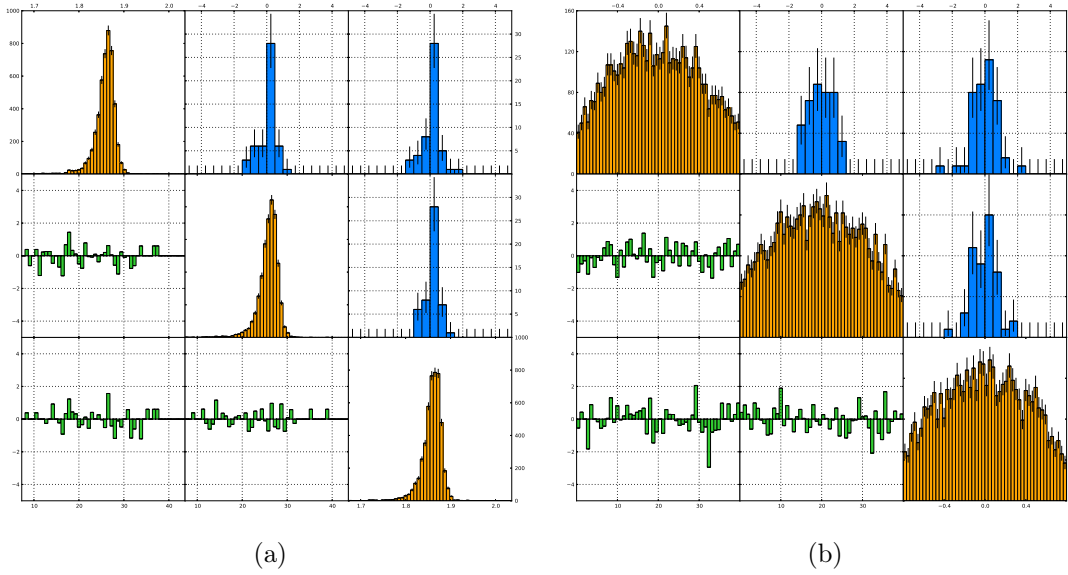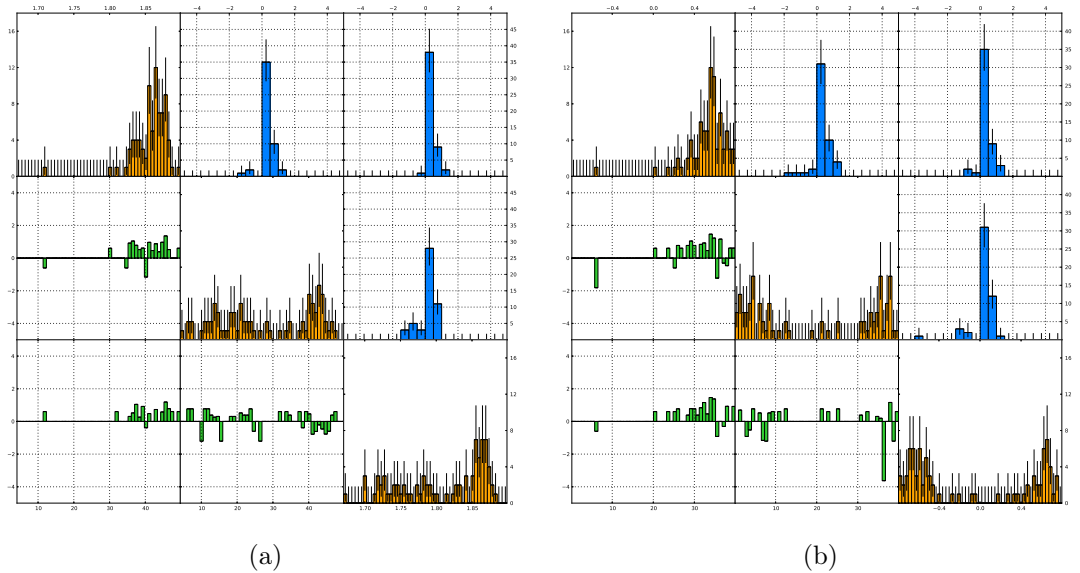
Figure 49: Invariant D^0 mass in bins of $\cos(\theta_H)$ (a) and $\cos(\theta_H)$ in bins of $m(D^0)$ (b) for the $\rho(\to \pi\gamma)\pi$ background of the ρ^0 mode as taken from the output of the CAT correlation tool. Plots under the diagonal show the difference between bins and plots above the diagonal represent the pulls.
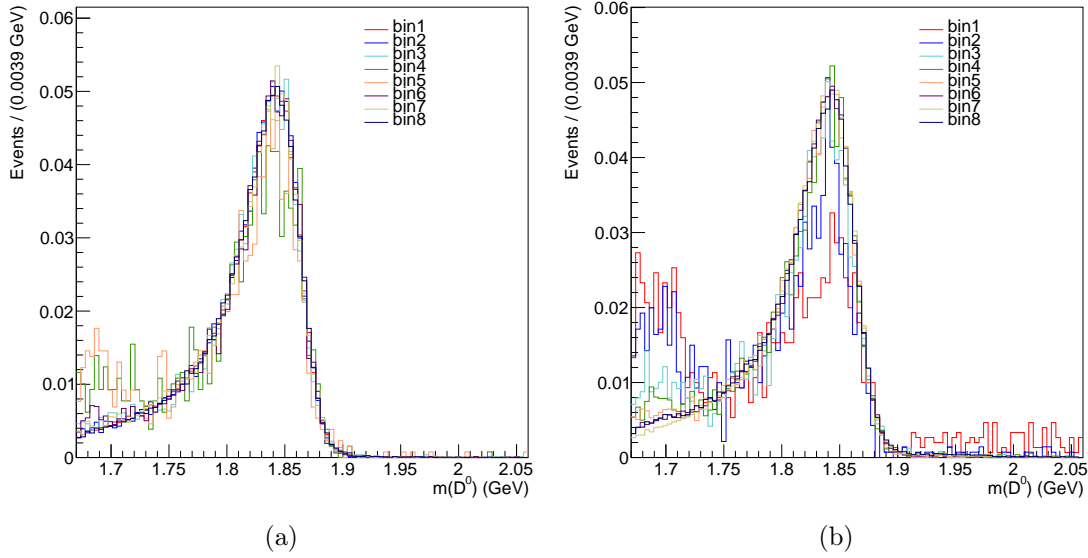
Figure 50: Normalised histograms of $m(D^0)$ in 8 equal bins of width 0.2 in $\cos(\theta_H)$ for the π^0 background (a) and the $K^-\rho^+$ background (b).

6.6.1.1   *Correlations in the $\overline{K}^{*0}$ Mode*

To gain a better insight in the features of the correlations in the π^0 and $K^-\rho^+$ backgrounds, $m(D^0)$ is plotted in 8 equal bins of width 0.2 in $\cos(\theta_H)$, ranging from -0.8 to 0.8. The normalised plots are shown in Figure 50 for both categories. The observation based on the output of the CAT tool is confirmed - the correlations consist of an additional peak appearing in certain bins at lower values of $m(D^0)$. In the π^0 category, the additional peak seems to be fairly limited to bins 3 and 4, corresponding to -0.2<$\cos(\theta_H)$ <0.2. In the $K^-\rho^+$ category, the additional peak is most prominent in the most negative bins of $\cos(\theta_H)$ and gradually receding with increasing $\cos(\theta_H)$. It might seem that bins 1 and 2 exhibit greater discrepancies also in the main peak, however large statistical fluctuations in those bins must be present in mind, since it is clear from Figure 37c that the distribution is essentially zero in this region.

To describe the main peak shape, the same 1-dimensional PDF comprising two logarithmic Gaussians and one Gaussian that was determined for the overall $m(D^0)$ in Section 6.5 is used. A Gaussian is added to describe the additional peak at lower $m(D^0)$ and once determined, its parameters are fixed. The four PDFs are added with recursive coefficients (see Equation 37) to form an overall PDF. The ordering of the PDFs is done so that the additional PDF that describes correlation is in the first place, and thus the first coefficient c_1 directly represents the fraction of this additional PDF - in bins where there is no additional peak, coefficient c_1 is zero. The mass distribution is fitted in all 8 bins of $\cos(\theta_H)$ separately, with the three coefficients being the free parameters of the fit. The results are shown in Figure 51 for both background categories. The coefficient c_1, corresponding to the additional PDF describing correlations, is the violet coloured one. For the π^0 category, it is immediately visible that the additional peak arises in the central bins of $\cos(\theta_H)$, while the recursive coefficients corresponding to the remaining PDFs remain fairly
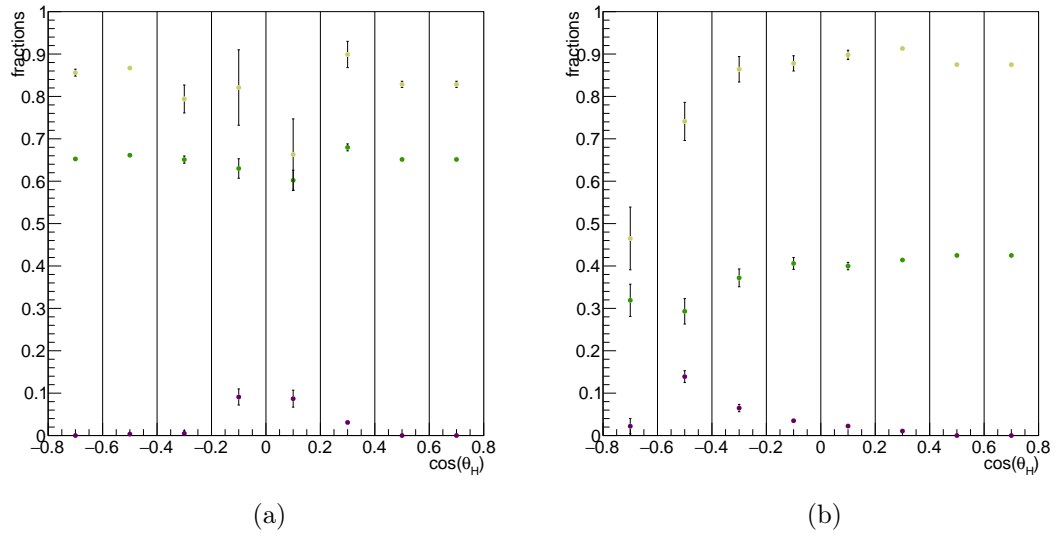
Figure 51: Recursive fractions of individual PDFs describing the $m(D^0)$ distribution in bins of $\cos(\theta_H)$ for the π^0 background (a) and the $K^-\rho^+$ background (b). The violet markers correspond to the coefficient that directly represents the fraction of the additional PDF that describes correlations between $m(D^0)$ and $\cos(\theta_H)$.

constant. For the $K^-\rho^+$ background, the additional PDF is present in the left-hand bins and the recursive coefficients corresponding to the remaining PDFs are also fairly constant with the exception of the first two bins. Since, as it was already discussed earlier, these bins contain an extremely low number of events, it is deemed this discrepancy is unreliable and misleading, as a few events can be easily misinterpreted and absorbed in the fit. It is therefore decided that for both categories, the fraction of the remaining PDFs (green and yellow in Figure 51) can be fixed to an average value. For the π^0 category, the average is taken from all 8 bins, while for the $K^-\rho^+$ category the first two bins are excluded from this calcuation. The fit is repeated with the coefficient corresponding to the additional peak PDF being the only free parameter. The results are plotted in Figure 52 for both the π^0 and the $K^-\rho^+$ category. The graphs are fitted to continuously describe the fraction of the added PDF as a function of the cosine of the helicity angle. The distribution of the fraction in the π^0 category is fitted with a single Gaussian, while for the distribution of the fraction in the $K^-\rho^+$ category two Gaussians are used. The fits are shown in Figure 53. This dependence is then added to the overall PDF describing the distribution in $m(D^0)$ for the π^0 and $K^-\rho^+$ backgrounds. The PDF describing the additional peak is added in the first place of the overall PDF, and instead of a constant coefficient corresponding to the fraction of this PDF the single Gaussian (π^0) or double Gaussian ($K^-\rho^+$) from Figure 53 is used. In this way, the fraction of the additional PDF is a function of $\cos(\theta_H)$.

(a)   (b)
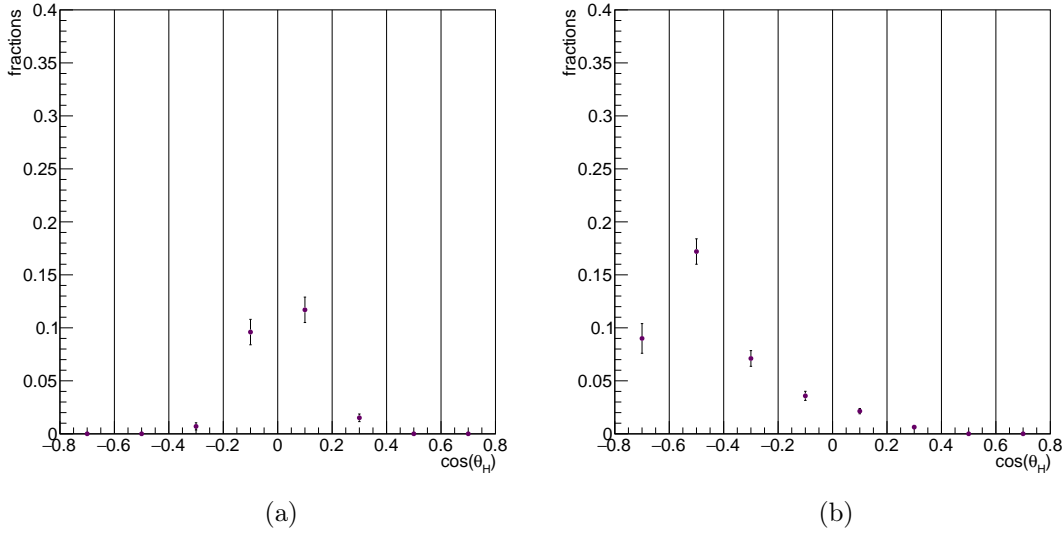
Figure 52: Fraction of the additional PDF in $m(D^0)$ that describes correlations between $m(D^0)$ and $\cos(\theta_H)$ in bins of $\cos(\theta_H)$ for the π^0 background (a) and the $K^-\rho^+$ background (b). The other recursive coefficients are fixed.

(a)   (b)
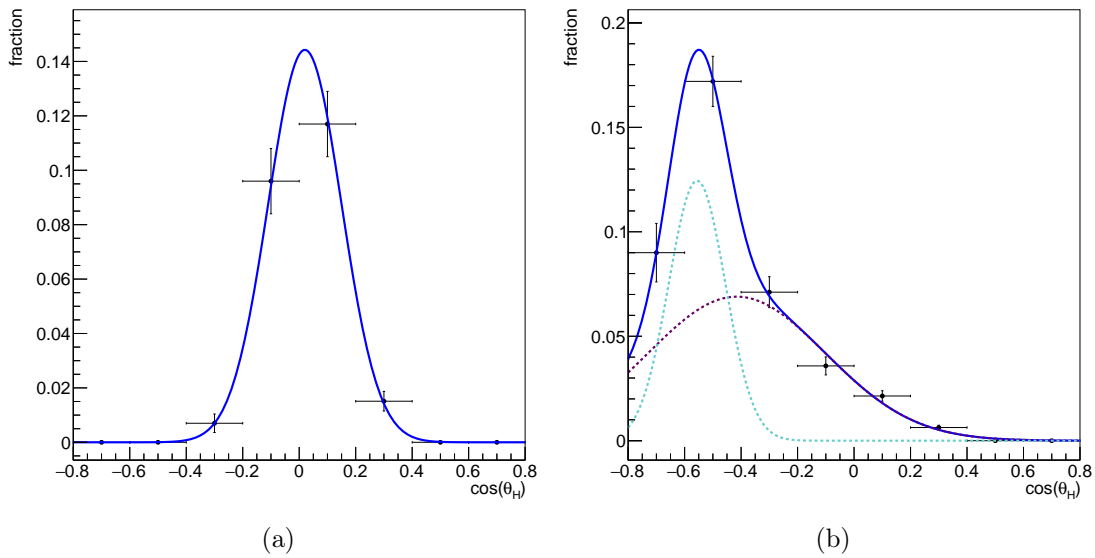
Figure 53: Fit of the fraction of the additional PDF in $m(D^0)$ that describes correlations between $m(D^0)$ and $\cos(\theta_H)$ in bins of $\cos(\theta_H)$ for the π^0 background (a) and the $K^-\rho^+$ background (b).

6.6.2 *Constructing the 2-dimensional PDF*

The 1-dimensional parametrisation was performed on 5 streams of the Belle generic Monte Carlo simulation. The 2-dimensional fit is performed on the 6th, statistically independent stream of generic Monte Carlo, to which signal events are added according to the expected yield, extrapolated to the luminosity of the data sample, 943 fb^{-1}. For each category (signal and all individual background components) a 2-dimensional PDF is constructed by multiplying the respective 1-dimensional PDFs for $m(D^0)$ and $\cos(\theta_H)$:

$$f_i(m(D^0), \cos(\theta_H)) = g_i(m(D^0)) \cdot h_i(\cos(\theta_H)) \quad . \tag{40}$$

The $m(D^0)$ and $\cos(\theta_H)$ PDFs are independent of one another, except in the two cases, described in the previous chapter, where correlations are taken into account by constructing a PDF for $m(D^0)$, which contains a parameter that is a function of $\cos(\theta_H)$.

All product PDFs f_i are then summed into a final master PDF of the form

$$c_1 \cdot f_1 + c_2 \cdot f_2 + ...c_n \cdot f_n \quad . \tag{41}$$

All 1-dimensional PDFs are normalised, therefore the coefficients c_i represent the yields of the corresponding PDFs and Σc_i is the total expected number of events.

For the $\mathcal{A}_{CP}$ calculation it is necessary to extract the separate signal yields for both flavours of the D^0 meson (Equation 33). Instead of fitting the D^0 and $\overline{D}^0$ samples completely separately and then calculating A_{raw}, we decide on a simultaneous fit of both samples as this enables the fit to directly extract the common parameters and subsequently achieve greater precision. The data sample is split in two based on the charge of the slow pion.

The master two-dimensional PDF is constructed separately for each sample, using the same 2-dimensional PDFs for background components which are symmetrical with regard to the D^0 flavour. The coefficients of each master PDF now represent the yield of the individual components in each sample. Instead of extracting them as they are, they are parametrised as functions of the total yield of a component (combined yield of the D^0 and $\overline{D}^0$ sample) and the asymmetry between the two yields. For each category, the yields of the D^0 and $\overline{D}^0$ sample (N_+ and N_-) are related to the total yield (N) and the raw asymmetry of the component in question as follows:

$$N_+ = \frac{1}{2}N(1 + A_{\mathrm{raw}}) \quad , \tag{42}$$

$$N_- = \frac{1}{2}N(1 - A_{\mathrm{raw}}) \quad . \tag{43}$$

Using such a parametrisation, the simultaneous fit is able to directly return for each component the total yield and asymmetry, regardless of the fact that two separate samples are being fitted, without additional calculations being needed. We perform an unbinned extended maximum likelihood fit. The quality of the fit is assessed by inspecting the distribution of the pull.

For components, for which it was decided to fix the yields, the values are fixed to the average number of events in the 5 streams that were used to determine the

1-dimensional PDFs. This value represents the expected value of the yield. The asymmetry of these categories is also fixed.

Compared to the basic 2-dimensional fit, the simultaneous fit has a near to doubled number of free parameters, as we have for each component in addition to the yield also the raw asymmetry. The effect of this increase is greatest in the $\overline{K}^{*0}$ mode, which has the largest number of categories, and seriously compromises the stability of the fit. The number of free parameters can be reduced using the following reasoning: all physical background categories with free yields and asymmetries are Cabibbo favoured decays, thus in the Standard model the physical CP asymmetry $\mathcal{A}_{CP}$ is expected to be zero. The raw asymmetry, however, can be non-zero due to reconstruction asymmetries, described in Chapter 5, but can be expected to be the same for all decays with the same final state particles. A single free asymmetry parameter is thus assigned to all remaining background categories of the π^0-type ($\overline{K}^{*0}\,\pi^0$, non-resonant $K^-\pi^+\pi^0$, $K^-\rho^+$), and a separate one for all η-type backgrounds ($\overline{K}^{*0}\,\eta$, non-resonant $K^-\pi^+\eta$). In the other two signal modes, a similar reduction of the number of asymmetry parameters is not necessary.

6.6.3   *Random π_s*

It can occur that a correctly reconstructed D^0 is combined with a true pion, but the two particles do not originate from a $D^{*+} \to D^0\pi_s^+$ decay. These are thus events where the D^0 is correctly identified but the D^{*+} is not. Such events are called random slow pions. It is possible that this incorrect pion is also of the wrong charge. It is necessary to check the efficiency of tagging the flavour of the D^0 based on the charge of the slow pion, and asses the impact and consequences of wrongly tagged events. Even if random slow pion events are true events of signal or peaking background type, the flavour of the D^0 remains unknown, hence these events represent a problem in the analysis for the purpose of calculating the CP asymmetry. The D^0 is correctly reconstructed, so these events will still peak in the $m(D^0)$ distribution and exhibit the same $\cos(\theta_H)$ distribution as the correctly tagged events of the same type, since the $\cos(\theta_H)$ definition refers to D^0 and its decay products, not involving D^{*+}. Some of these events will thus feature in the signal yield as extracted from the fit. Of these wrongly tagged charm mesons, it can be expected that some will be of the opposite flavour, meaning there will be a number of $\overline{D}^0$s in the extracted yield of the D^0s and vice-versa. The extracted yield of D^0s can be written as

$$N(D^0)^{\mathrm{fit}} = N(D^0)^{\mathrm{tag}} + N(D^0)^{\mathrm{wtag}}_{D^0} + N(D^0)^{\mathrm{wtag}}_{\overline{D}^0} \quad , \tag{44}$$

where in addition to the correctly tagged D^0s ($N(D^0)^{\mathrm{tag}}$) there will be a certain number of wrongly tagged D^0s, of which some will be of the correct flavour ($N(D^0)^{\mathrm{wtag}}_{D^0}$) and some of the opposite ($N(D^0)^{\mathrm{wtag}}_{\overline{D}^0}$). An analogous expression follows for the

extracted yield of $\overline{D}^0$s. It is necessary to evaluate the effect of the opposite flavour neutral charm mesons on the extracted asymmetry. Let us expand the three terms as

$$
\begin{aligned}
N(D^0)^{\text{tag}} &= N(D^{*+}) \cdot \mathcal{B}r(D^{*+}) \cdot \mathcal{B}r(D^0) \cdot \varepsilon \cdot \tfrac{1}{2}(1 + \mathcal{A}_{CP}) \quad, \\
N(D^0)^{\text{wtag}}_{D^0} &= N(D^{*+}) \cdot \mathcal{B}r(D^{*+}) \cdot \mathcal{B}r(D^0) \cdot \varepsilon' \cdot \tfrac{1}{2}(1 + \mathcal{A}_{CP}) \quad, \\
N(D^0)^{\text{wtag}}_{\overline{D}^0} &= N(D^{*-}) \cdot \mathcal{B}r(D^{*-}) \cdot \mathcal{B}r(D^0) \cdot \varepsilon'' \cdot \tfrac{1}{2}(1 - \mathcal{A}_{CP}) \quad,
\end{aligned}
\tag{45}
$$

and similarly

$$
\begin{aligned}
N(\overline{D}^0)^{\text{tag}} &= N(D^{*-}) \cdot \mathcal{B}r(D^{*-}) \cdot \mathcal{B}r(D^0) \cdot \varepsilon \cdot \tfrac{1}{2}(1 - \mathcal{A}_{CP}) \quad, \\
N(\overline{D}^0)^{\text{wtag}}_{\overline{D}^0} &= N(D^{*-}) \cdot \mathcal{B}r(D^{*-}) \cdot \mathcal{B}r(D^0) \cdot \varepsilon' \cdot \tfrac{1}{2}(1 - \mathcal{A}_{CP}) \quad, \\
N(\overline{D}^0)^{\text{wtag}}_{D^0} &= N(D^{*+}) \cdot \mathcal{B}r(D^{*+}) \cdot \mathcal{B}r(D^0) \cdot \varepsilon'' \cdot \tfrac{1}{2}(1 + \mathcal{A}_{CP}) \quad.
\end{aligned}
\tag{46}
$$

We have written the branching fraction of the neutral charm mesons of both flavours as a single average value with an additional asymmetry term. Since $D^{*+} \to D^0 \pi_s^+$ is a strong decay and no asymmetry is expected, let us assume $\mathcal{B}r(D^{*+}) = \mathcal{B}r(D^{*-})$ and also $N(D^{*+}) = N(D^{*-})$. Additionally, we assume for the purpose of this calculation that no other asymmetries are present. The raw asymmetry as defined in Equation 33 now becomes

$$
A_{\text{raw}} = \frac{N(D^0)^{\text{tag}} + N(D^0)^{\text{wtag}}_{D^0} + N(D^0)^{\text{wtag}}_{\overline{D}^0} - N(\overline{D}^0)^{\text{tag}} - N(\overline{D}^0)^{\text{wtag}}_{\overline{D}^0} - N(\overline{D}^0)^{\text{wtag}}_{D^0}}{N(D^0)^{\text{tag}} + N(D^0)^{\text{wtag}}_{D^0} + N(D^0)^{\text{wtag}}_{\overline{D}^0} + N(\overline{D}^0)^{\text{tag}} + N(\overline{D}^0)^{\text{wtag}}_{\overline{D}^0} + N(\overline{D}^0)^{\text{wtag}}_{D^0}} \quad.
\tag{47}
$$

Expanding the terms as above, the branching fractions and $N(D^{*\pm})$ cancel out, leaving

$$
A_{\text{raw}} = \mathcal{A}_{CP} \cdot \frac{\left(1 - \frac{\varepsilon''}{\varepsilon + \varepsilon'}\right)}{\left(1 + \frac{\varepsilon''}{\varepsilon + \varepsilon'}\right)} \quad.
\tag{48}
$$

If no wrong flavour events would be present, i.e. in the case $\varepsilon'' = 0$, it follows that the raw asymmetry becomes directly the CP asymmetry. Acknowledging $\varepsilon'' \neq 0$ but assuming $\varepsilon'' \ll \varepsilon + \varepsilon'$, we can expand the denominator and, keeping only linear terms, obtain

$$
A_{\text{raw}} = \mathcal{A}_{CP} \cdot \left(1 - 2\frac{\varepsilon''}{\varepsilon + \varepsilon'}\right) \quad.
\tag{49}
$$

The procedure for extracting the raw asymmetry will be reliable only in the case where $\frac{\varepsilon''}{\varepsilon + \varepsilon'} \ll 1$. It is necessary to prove this assumption holds before continuing with the analysis.

The signal Monte Carlo simulations are used for the purpose of evaluating the effect of random slow pions. Firstly, the sample is divided in two based on the charge of the slow pion as determined in the reconstruction. Then, the three terms from Equation 44 are extracted. Assuming $\mathcal{A}_{CP}$ is small, the fraction $\frac{\varepsilon''}{\varepsilon + \varepsilon'}$ is approximately equal to $N(D^0)^{\text{wtag}}_{\overline{D}^0} / (N(D^0)^{\text{tag}} + N(D^0)^{\text{wtag}}_{D^0})$, which should in term be equal to $N(\overline{D}^0)^{\text{wtag}}_{D^0} / (N(\overline{D}^0)^{\text{tag}} + N(\overline{D}^0)^{\text{wtag}}_{\overline{D}^0})$. The values are listed in Table 16 for both before and after the application of selection criteria, for all three signal modes. Values

	no selection		with selection criteria	
	D^0	$\overline{D}^0$	D^0	$\overline{D}^0$
ϕ mode	$(1.61\pm0.14)\%$	$(1.65\pm0.15)\%$	$(0.16\pm0.06)\%$	$(0.12\pm0.05)\%$
$\overline{K}^{*0}$ mode	$(0.43\pm0.04)\%$	$(0.40\pm0.04)\%$	$(0.01\pm0.01)\%$	0%
ρ^0 mode	$(1.49\pm0.08)\%$	$(1.54\pm0.09)\%$	$(0.03\pm0.02)\%$	$(0.06\pm0.03)\%$

Table 16: Fraction of wrong flavour neutral charm mesons in a sample with a certain tag (i.e. $\overline{D}^0$s in the sample tagged with π_s^+ and vice-versa), determined on the signal simulation, both before and after the application of selection criteria, for all three signal channels.

obtained from the D^0 and $\overline{D^0}$ sample indeed exhibit good matching in all cases. It can be observed that the number is low to start with and drops significantly lower when selection criteria are applied. This is mainly due to a strict cut on q, since for random slow pion events the D^0 and π_s are uncorrelated and the q distribution is broad. It follows from Equation 49 that the numbers in Table 16 represent half of the relative error on $\mathcal{A}_{CP}$. Given the fact that the expected $\mathcal{A}_{CP}$ itself is a small number, a relative error of the order of 0.1% or less becomes quite negligible in absolute terms. It is decided that no systematical uncertainty will be attributed to this source.

While the reconstruction and identification efficiency of the slow pion is good, it is nevertheless still possible to misidentify another particle as a pion (mostly electrons or positrons, either direct or from a converted photon), or for the reconstruction algorithm of the Monte Carlo truth to be unable to identify the particle at all. These events shall be dubbed false slow pions. In the majority of such cases also the D^0 and subsequently D^{*+} are wrongly reconstructed, meaning these events fall under the combinatorial background and thus do not pose a direct threat to the extraction of the asymmetry through signal yields. However, since these events are still divided in two based on the charge of the false slow pion, it is important to assert whether the distribution is completely symmetrical with regard to the division in question. All 6 streams of generic Monte Carlo are used for this check. Figure 54 shows the comparison of the distributions of false π_s charge in $m(D^0)$ and $\cos(\theta_H)$ for the two samples, as the ratio of histograms. For all three signal modes, no visible asymmetry is present between the two samples. It is concluded that false slow pions do not affect the analysis in any way.

6.6.4   *Cross-check on Other Streams*

A satisfactory performance of the fit on one stream of Monte Carlo, representing the equivalent of the physical data set, is nonetheless not a sufficient proof of the quality of the fit. Certain statistical fluctuations are to be expected. Similarly, a small inaccuracy in the fit results might not necessary indicate a definite flaw in the procedure. Ideally, the fit would be repeated on other equivalent but statistically

(a)

(b)

(c)

(d)

(e)

(f)
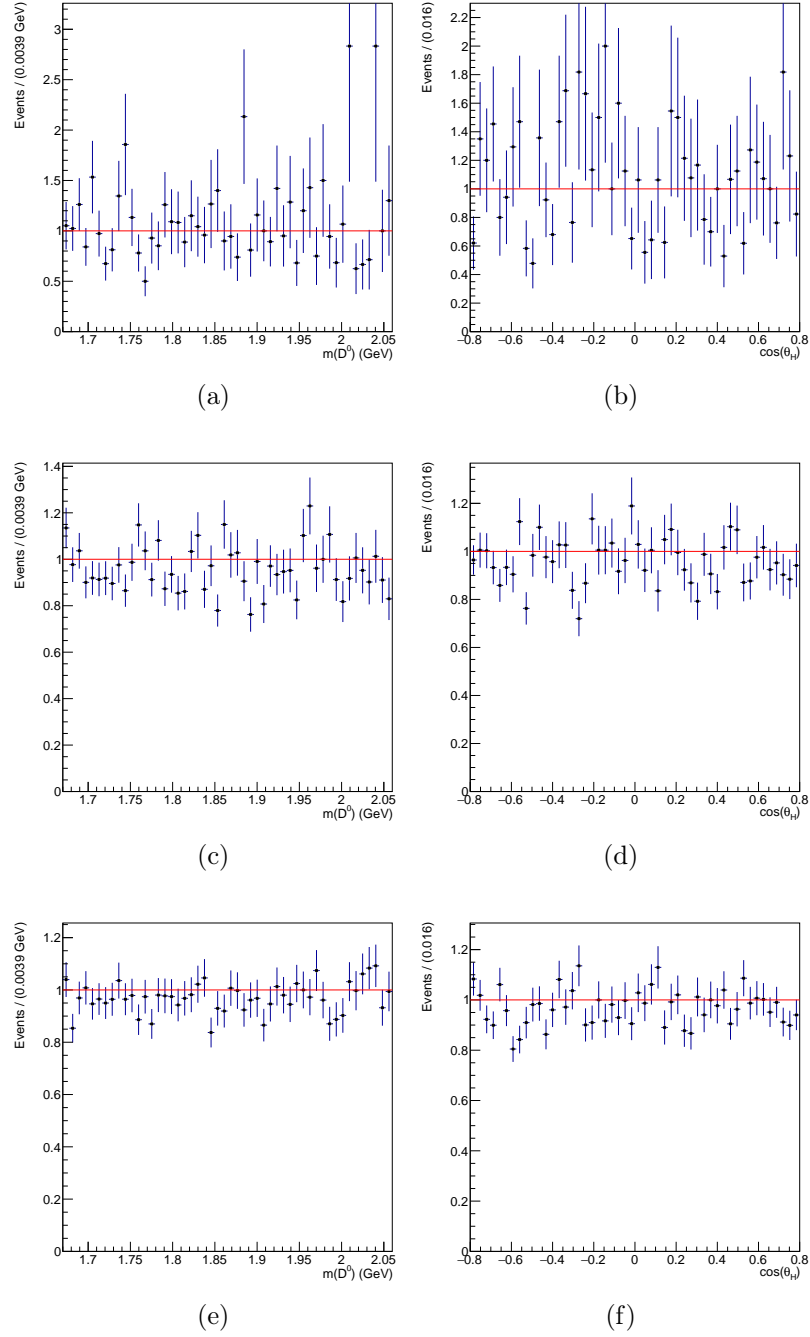
Figure 54: The ratio of distributions of false π_s in $m(D^0)$ (left) and $\cos(\theta_H)$ (right) of the two samples, differentiated by the charge of the false π_s, for all three signal modes: ϕ (top row), $\overline{K}^{*0}$ (middle row) and ρ^0 (bottom row).

independent simulations to assure the stability of the fit results and detect possible trends that indicate bias. Since the other 5 streams of the provided generic Monte Carlo have been used to determine the individual 1-dimensional PDFs, they are not completely independent. In an ideal case, the procedure could be repeated 6 times, leaving each time a different stream as independent and determining the 1-dimensional PDFs on the other 5 streams. Since all streams are equivalent, the semi-dependent streams are still suitable enough for such a cross-check. An additional small measure that can be taken to decrease the dependence is to repeat the smearing procedure for π^0 and η-type backgrounds using a different random seed, obtaining an equivalent but statistically different smearing. No similar issue is present for the signal events, for which signal Monte Carlo simulations are generated separately. Only a portion of signal Monte Carlo events is added to each stream of the generic Monte Carlo in order to create a data-equivalent set of events, supplying a sufficient amount of statistically independent signal events.

To verify that the performance of the fit has no dependence on the specific set of events in the data sample, the fit will be repeated separately on all 5 initial streams of the generic Monte Carlo, with a different random smearing for π^0 and η-type backgrounds and adding each time a different subset of events from the signal simulation. Results of this cross-check are stated in the following signal mode subchapters, respectively.

6.6.5 ϕ Mode

Figure 55 shows the simultaneous fit, projected to each of the fit variables, for both flavours of the reconstructed D^0. It can be seen that the fit describes the data sample well in all four cases, as is confirmed by the pull distributions plotted below the fit projections. Distributions in both variables are symmetrical with regard to the flavour of the D^0. The fitted yields are given in Table 17, along with the expected number of events. The expected number of events for background categories is taken to be the average number of events on 5 Monte Carlo streams, all independent from the stream on which the fit is performed. The expected number of signal events is equivalently obtained from 5 independent sets of signal Monte Carlo. Also listed in Table 17 is the value of the pull, obtained as the difference between the number of events as returned from the fit, and the expected number of events, divided by the error of the fitted yield:

$$\text{pull} = \frac{N_{\text{fit}} - N_{\text{expected}}}{\sigma} \quad . \tag{50}$$

An absolute value of the pull below 1 signifies that the fitted yield is consistent with the expected number of events within the margin of error on the fitted yield. Furthermore, a negative value of the pull implies that the fit is underestimating the number of events of the particular category, while a positive pull indicates that the fitted yield exceeds the expected number of events.

Table 17 also lists the values of the raw asymmetry, as returned by the fit, the respective expected values and the corresponding pulls.

	N_{fit}	N_{expected}	pull	$A_{\text{raw}}^{\text{fit}}$	$A_{\text{raw}}^{\text{expected}}$	pull
$\phi\gamma$	615 ± 36	573	**1.2**	-0.052 ± 0.057	-0.006	-0.8
$\phi\pi^0$	1813 ± 58	2021	$-\mathbf{3.6}$	0.054 ± 0.031	0.006	**1.6**
"remaining"	232 ± 34	263	-0.9	0.030 ± 0.120	-0.001	0.3
combinatorial	1957 ± 69	1882	**1.1**	-0.075 ± 0.032	0.007	$-\mathbf{2.6}$

Table 17: The first three columns give the yield, obtained from the fit, the expected yield and the corresponding pull for all components in the ϕ sample. The last three columns give the analogous values for A_{raw}. Values indicated in bold denote categories where the difference between the fitted and expected value exceeds the error on the fitted yield or asymmetry.

	stream 1	stream 2	stream 3	stream 4	stream 5
$\phi\gamma$	$-\mathbf{1.1}$	0.0	$-\mathbf{1.4}$	-0.9	0.6
$\phi\pi^0$	-1.0	$-\mathbf{1.4}$	$-\mathbf{1.7}$	0.0	-0.1
"remaining"	0.1	0.4	-0.2	0.1	-0.7
combinatorial	**2.4**	**1.4**	**2.0**	**1.3**	-0.2

Table 18: Pull values of the yield for the ϕ sample on the 5 semi-dependent streams of generic Monte Carlo, and a different subset of signal Monte Carlo events. Values indicated in bold denote categories where the difference between the fitted and expected value exceeds the error on the fitted yield.

In accordance to Section 6.6.4, the fit is repeated on the 5 semi-dependent streams. The obtained pulls for all categories are listed in Tables 18 and 19. Looking firstly at the pull of the signal yield and adding the value from Table 17, it can be concluded that no bias is present in the extraction of signal, as the pull takes both positive and negative values. In some cases the fitted yield deviates from the expected value for more than 1σ, however it is statistically expected that in some cases the absolute value of the pull will exceed 1. The "remaining" background category shows no bias as well. The combinatorial background shows a tendency to overestimate the yield, however it is clear that this does not affect the quality of signal extraction, and since the aim of the fit is to correctly extract the signal yield, this fact presents no issue for the analysis. As for A_{raw}, no bias seems to be present in any of the categories. We conclude that the performance of the 2-dimensional simultaneous fit in the ϕ channel is suitable.

6.6.6 $\overline{K}^{*0}$ Mode

Figure 56 shows the simultaneous fit, projected to each of the fit variables, for both flavours of the reconstructed D^0. It can be seen that the fit describes the data sample well in all four cases, as is confirmed by the pull distributions plotted below the
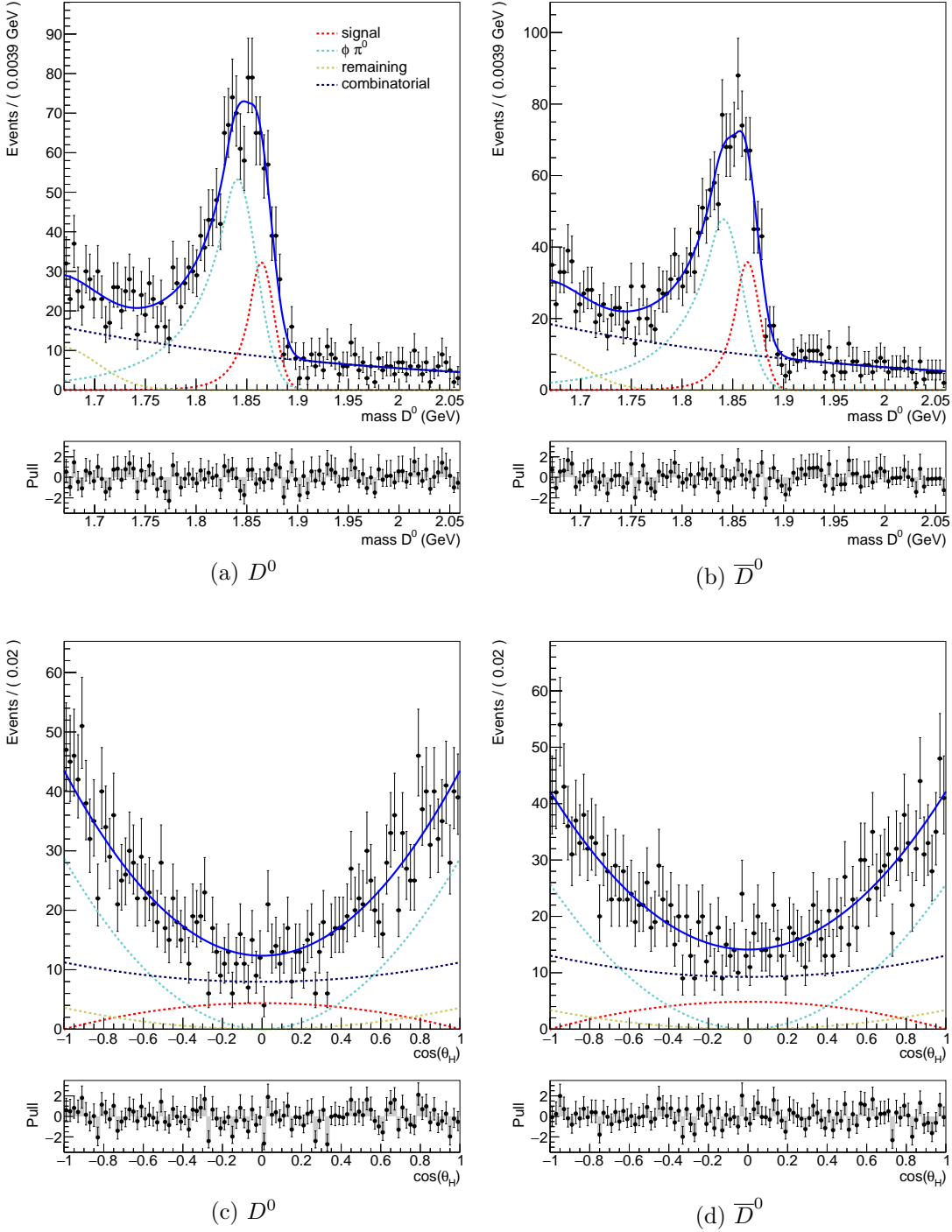
Figure 55: Simultaneous 2-dimensional fit in $m(D^0)$ (top) and $\cos(\theta_H)$ (bottom) of the ϕ mode for D^0 (left) and $\overline{D}^0$ (right). The χ^2/NDF of the $m(D^0)$ fit is 0.8 for D^0 and 0.8 for $\overline{D}^0$. The χ^2/NDF of the $\cos(\theta_H)$ fit is 1.1 for D^0 and 0.9 for $\overline{D}^0$.

	stream 1	stream 2	stream 3	stream 4	stream 5
$\phi\gamma$	0.6	0.5	0.6	0.1	**1.1**
$\phi\pi^0$	**−1.3**	−0.7	**1.2**	−0.6	−0.2
"remaining"	0.5	−0.3	−0.5	0.8	−0.6
combinatorial	0.7	−0.1	−0.1	**−1.1**	−0.7

Table 19: Pull values of A_{raw} for the ϕ sample on the 5 semi-dependent streams of generic Monte Carlo, and a different subset of signal Monte Carlo events. Values indicated in bold denote categories where the difference between the fitted and expected value exceeds the error on the fitted asymmetry.

fit projections. Distributions in both variables are symmetric with regard to the flavour of the D^0. The fitted yields, along with the expected number of events and the respective pulls are listed in Table 20. Table 20 also lists the values of the raw asymmetry, as returned by the fit, the expected values and the corresponding pulls. For all background modes of the π^0-type, as well as for all modes of the η-type for which a joint asymmetry parameter was used, also a joint pull value is calculated. For this purpose, the joint expected value of asymmetry is used, calculated as

$$\frac{\Sigma N_i^+ - \Sigma N_i^-}{\Sigma N_i^+ + \Sigma N_i^-} \quad , \tag{51}$$

where i runs over all background categories of the π^0 or η-type, respectively. The values of the pull of the yield and raw asymmetry on the 5 semi-dependent streams are listed in Tables 21 and 22, respectively. Looking at the pulls of the signal component for all 6 streams, it is concluded that no bias is present in the extraction of neither the yield or the raw asymmetry.

The returned offset of the $m(D^0)$ PDF is -0.00 ± 0.00, while the returned width correction factor is 1.018 ± 0.034. Both are consistent with their expected values, which are 0 and 1, respectively.

6.6.7 ρ^0 Mode

Figure 57 shows the simultaneous fit, projected to each of the fit variables, for both flavours of the reconstructed D^0. It can be seen that the fit describes the data sample well in all four cases, as is confirmed by the pull distributions plotted below the fit projections. The fitted yields, their corresponding expected values and the respective pulls are listed in Table 23, as are analogous values for the raw asymmetry.

It is noticed that the decays of D^0 to $\rho^+\pi^-$ and $\rho^-\pi^+$ have approximately the same number of events. However, the ratio of D^0 decays to these states should be about 2:1. It is revealed that there is an error in the Belle generic Monte Carlo simulation, where the branching fractions are reversed for the decay of the $\overline{D}^0$. Instead of

$$\mathcal{B}r(D^0 \rightarrow \rho^+\pi^-) = \mathcal{B}r(\overline{D}^0 \rightarrow \rho^-\pi^+) \quad \text{and}$$
$$\mathcal{B}r(D^0 \rightarrow \rho^-\pi^+) = \mathcal{B}r(\overline{D}^0 \rightarrow \rho^+\pi^-) \quad ,$$

(a) D^0

(b) $\overline{D}^0$

(c) D^0

(d) $\overline{D}^0$

Figure 56: Simultaneous 2-dimensional fit in $m(D^0)$ (top) and $\cos(\theta_H)$ (bottom) of the $\overline{K}^{*0}$ mode for D^0 (left) and $\overline{D}^0$ (right). The χ^2/NDF of the $m(D^0)$ fit is 1.4 for D^0 and 1.2 for $\overline{D}^0$. The χ^2/NDF of the $\cos(\theta_H)$ fit is 1.3 for D^0 and 1.3 for $\overline{D}^0$.

	N_{fit}	N_{expected}	pull	$A_{\text{raw}}^{\text{fit}}$	$A_{\text{raw}}^{\text{expected}}$	pull
$\overline{K}^{*0}\gamma$	9805 ± 417	9421	0.9	-0.037 ± 0.020	-0.010	$-\mathbf{1.3}$
$\overline{K}^{*0}\pi^0$	$28\,733 \pm 362$	$28\,473$	0.7			
$K^-\rho^+$	$52\,735 \pm 336$	$52\,430$	0.9	-0.010 ± 0.004	-0.003	$-\mathbf{1.7}$
$K^-\pi^+\pi^0$	3984 ± 849	4337	-0.4			
$\overline{K}^{*0}\eta$	6316 ± 195	6201	0.6	-0.040 ± 0.020	0.004	$-\mathbf{2.2}$
$K^-\pi^+\eta$	1763 ± 383	1554	0.5			
$K_0^*(1430)^-\pi^+$		$1503^{(*)}$			-0.001	
$K^{*-}\pi^+$		$306^{(*)}$			-0.003	
$K^-\rho^+(\to \pi^+\gamma)$		$167^{(*)}$			0.049	
$K^-\pi^+ FSR$		$112^{(*)}$			-0.007	
"remaining"		$359^{(*)}$			-0.009	
combinatorial	$18\,867 \pm 756$	$19\,172$	-0.4	-0.004 ± 0.012	-0.015	0.9

Table 20: The first three columns give the yield, obtained from the fit, the expected yield and the corresponding pull for all components in the $\overline{K}^{*0}$ sample. The last three columns give the analogous values for A_{raw}. The superscript $^{(*)}$ denotes the values that are fixed.

	stream 1	stream 2	stream 3	stream 4	stream 5
$\overline{K}^{*0}\gamma$	$-\mathbf{1.0}$	0.6	0.0	0.6	-0.3
$\overline{K}^{*0}\pi^0$	-0.8	-0.7	-0.8	0.8	$\mathbf{1.5}$
$K^-\rho^+$	$\mathbf{1.5}$	-0.4	-0.7	$\mathbf{2.6}$	$-\mathbf{3.0}$
$K^-\pi^+\pi^0$	0.0	0.2	0.5	-0.4	-0.2
$\overline{K}^{*0}\eta$	0.7	-0.1	0.3	0.0	-0.9
$K^-\pi^+\eta$	$-\mathbf{2.2}$	0.1	0.2	$\mathbf{1.4}$	0.6
combinatorial	$\mathbf{1.5}$	-0.5	-0.1	$-\mathbf{1.1}$	0.1

Table 21: Pull values of the yield for the $\overline{K}^{*0}$ sample on the 5 semi-dependent streams of generic Monte Carlo and a different subset of signal Monte Carlo events. Values indicated in bold denote categories where the difference between the fitted and expected value exceeds the error on the fitted asymmetry.

	stream 1	stream 2	stream 3	stream 4	stream 5
$\overline{K}^{*0}\gamma$	**−2.0**	0.2	0.1	**1.5**	**−1.1**
$\overline{K}^{*0}\pi^0$					
$K^-\rho^+$	**−1.4**	0.7	**−1.0**	0.7	0.4
$K^-\pi^+\pi^0$					
$\overline{K}^{*0}\eta$	**−1.1**	0.3	−0.9	**−2.4**	**−1.6**
$K^-\pi^+\eta$					
combinatorial	**2.5**	0.2	−0.2	**1.3**	**1.8**

Table 22: Pull values of A_{raw} for the $\overline{K}^{*0}$ sample on the 5 semi-dependent streams of generic Monte Carlo and a different subset of signal Monte Carlo events. Values indicated in bold denote categories where the difference between the fitted and expected value exceeds the error on the fitted asymmetry.

it holds

$$\mathcal{B}r(D^0 \to \rho^+\pi^-) = \mathcal{B}r(\overline{D}^0 \to \rho^+\pi^-) \quad \text{and}$$
$$\mathcal{B}r(D^0 \to \rho^-\pi^+) = \mathcal{B}r(\overline{D}^0 \to \rho^-\pi^+) \quad .$$

This error causes the $\cos(\theta_H)$ distributions of the D^0 and $\overline{D}^0$ samples in Monte Carlo to be the mirror images of one another, instead of exhibiting the exact same distribution, as if direct CP violation was present. This can be clearly observed in Figures 57c and 57d. This feature is correctly recognised by the fit, as the returned value of raw asymmetries for the two modes in question describes well the asymmetry in the simulated events.

The results of the fit for both the yield and the raw asymmetry on the independent stream, as well as on the 5 initial semi-dependent streams (Tables 24 and 25), indicate that the procedure is reliable and yields satisfactory results.

6.6.8 *Projection to Bins*

We examine the projection of the fit to each variable in different bins of the other variable in order to analyse possible effects of any remaining neglected correlations between the variables on the extraction of signal. The fit range of both variables is divided into 8 bins. The mass range, which is between 1.67 and 2.06 GeV for all three signal modes, is divided into 7 bins of 50 MeV and an 8th bin of 40 MeV. The range of $\cos(\theta_H)$ is divided into 8 equal bins of 0.25 for the ϕ mode and and 8 equal bins of 0.2 in the $\overline{K}^{*0}$ and ρ^0 mode, since the full range of the variable is [-1,1] for ϕ and [-0.8, 0.8] for $\overline{K}^{*0}$ and ρ^0. The fit is performed on a joint sample of both D^0 flavours. The projections of the fit to $m(D^0)$ in different bins of $\cos(\theta_H)$, and projections to $\cos(\theta_H)$ in bins of $m(D^0)$, are plotted in Figures 58, 59 and 60, for the ϕ, $\overline{K}^{*0}$ and ρ^0 mode, respectively. The corresponding pulls are drawn below each plot. It can be seen that the fit describes the simulated data well in all cases,
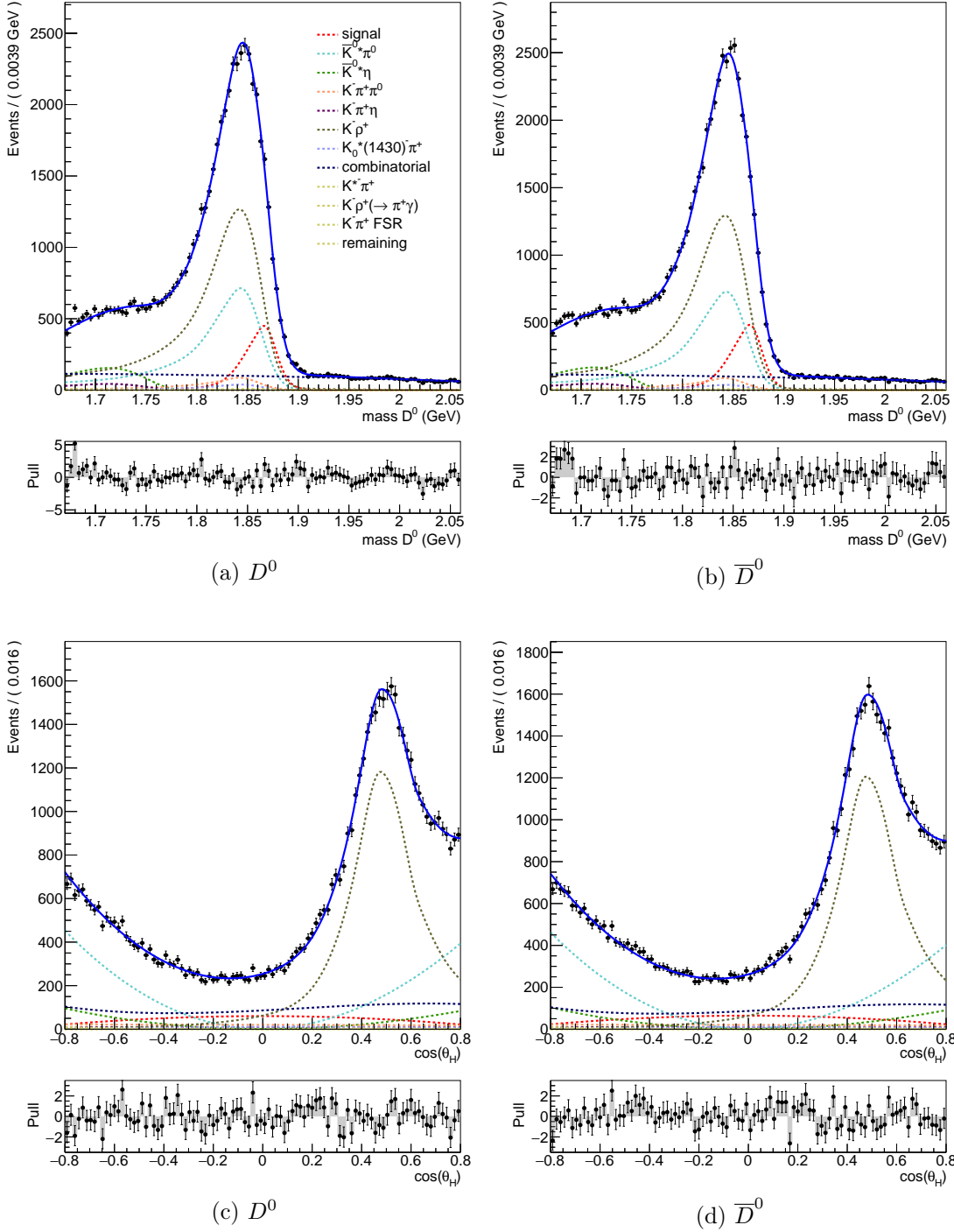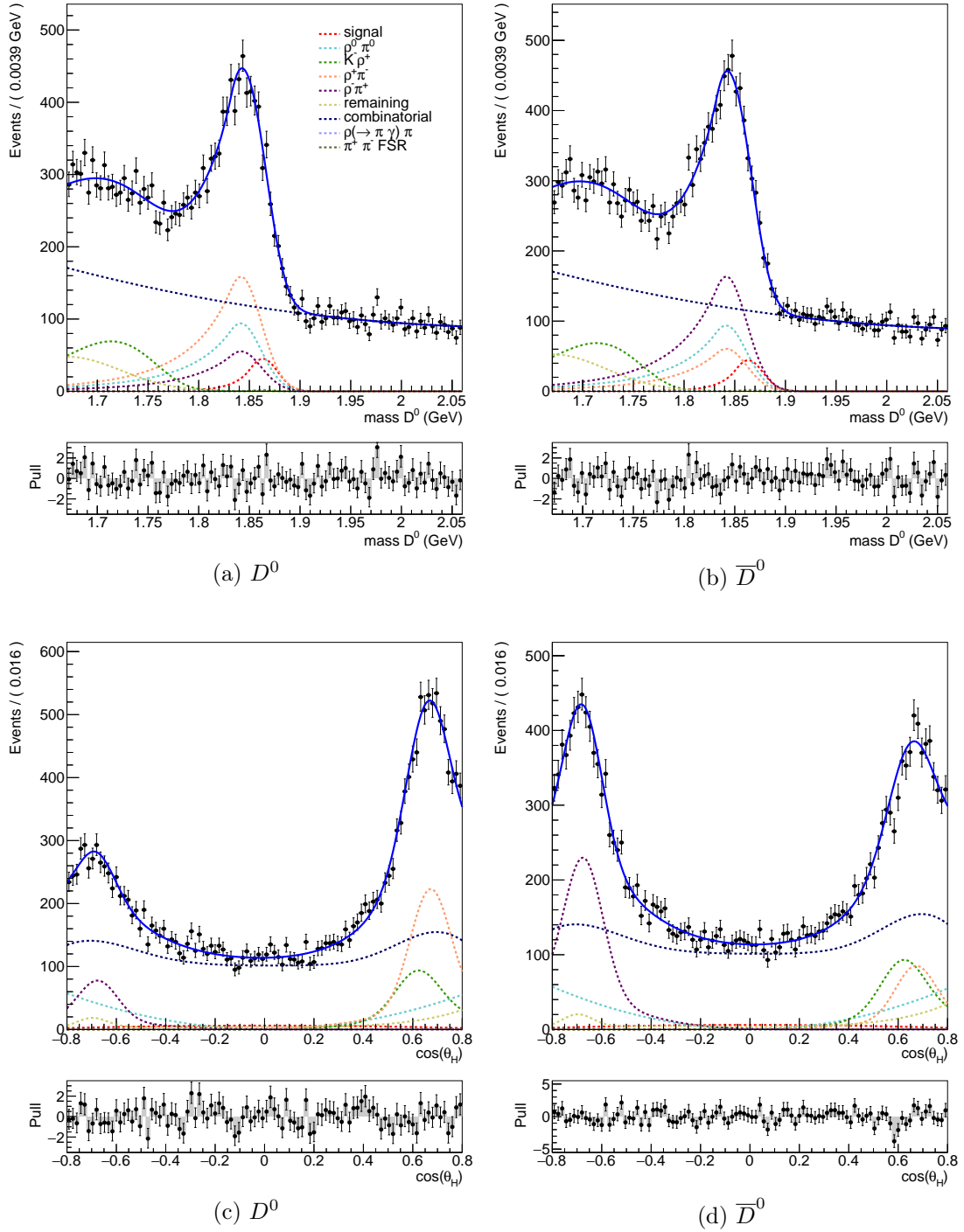
Figure 57: Simultaneous 2-dimensional fit in $m(D^0)$ (top) and $\cos(\theta_H)$ (bottom) of the ρ^0 mode for D^0 (left) and $\overline{D}^0$ (right). The χ^2/NDF of the $m(D^0)$ fit is 1.2 for D^0 and 1.1 for $\overline{D}^0$. The χ^2/NDF of the $\cos(\theta_H)$ fit is 1.2 for D^0 and 1.1 for $\overline{D}^0$.

	N_{fit}	N_{expected}	pull	A_{raw}	$A_{\text{raw}}^{\text{expected}}$	pull
$\rho^0\gamma$	960 ± 93	969	0.4	0.008 ± 0.093	-0.005	0.1
$\rho^0\pi^0$	3814 ± 367	3280	$\mathbf{1.4}$	0.002 ± 0.082	-0.001	0.0
$\rho^+\pi^-$	4349 ± 172	4459	-0.5	0.447 ± 0.043	0.431	0.4
$\rho^-\pi^+$	4342 ± 177	4538	$-\mathbf{1.1}$	-0.495 ± 0.041	-0.463	-0.8
$K^-\rho^+$	3083 ± 112	3098	0.2	0.003 ± 0.036	-0.013	0.4
$\rho(\to \pi\gamma)\pi$		$48^{(*)}$			-0.080	
$\pi^+\pi^-$ FSR		$26^{(*)}$			0.054	
"remaining"	1717 ± 215	1621	0.4	-0.048 ± 0.089	-0.007	-0.5
combinatorial	$23\,989 \pm 280$	$24\,126$	$-\mathbf{1.4}$	0.001 ± 0.095	-0.007	0.1

Table 23: The first three columns give the yield, obtained from the fit, the expected yield and the corresponding pull for all components in the ρ^0 sample. The last three columns give the analogous values for A_{raw}. The superscript $^{(*)}$ denotes the values that are fixed.

	stream 1	stream 2	stream 3	stream 4	stream 5
$\rho^0\gamma$	-0.5	0.4	0.6	$-\mathbf{1.1}$	-0.4
$\rho^0\pi^0$	$-\mathbf{1.8}$	$-\mathbf{2.6}$	-0.8	$-\mathbf{1.4}$	-0.9
$\rho^+\pi^-$	$\mathbf{2.4}$	$\mathbf{2.8}$	$\mathbf{1.7}$	$\mathbf{1.3}$	$\mathbf{2.2}$
$\rho^-\pi^+$	0.8	0.7	-0.1	$\mathbf{1.2}$	0.2
$K^-\rho^+$	$\mathbf{2.1}$	0.1	0.3	$\mathbf{3.1}$	$-\mathbf{1.0}$
"remaining"	$-\mathbf{3.3}$	$-\mathbf{1.6}$	$-\mathbf{1.3}$	$-\mathbf{2.0}$	$-\mathbf{1.6}$
combinatorial	$\mathbf{1.7}$	$\mathbf{1.6}$	0.2	0.3	$\mathbf{1.6}$

Table 24: Pull values of the yield for the ρ^0 sample on the 5 semi-dependent streams of generic Monte Carlo and a different subset of signal Monte Carlo events. Values indicated in bold denote categories where the difference between the fitted and expected value exceeds the error on the fitted asymmetry.

	stream 1	stream 2	stream 3	stream 4	stream 5
$\rho^0\gamma$	-0.5	$-\mathbf{1.1}$	0.2	$-\mathbf{2.0}$	0.4
$\rho^0\pi^0$	-0.8	-0.8	-0.1	0.2	-0.9
$\rho^+\pi^-$	-0.2	0.3	-0.8	-0.5	$\mathbf{1.2}$
$\rho^-\pi^+$	1.0	0.5	$\mathbf{1.1}$	0.2	-0.1
$K^-\rho^+$	0.0	-0.3	0.1	$\mathbf{2.0}$	0.1
"remaining"	0.2	-0.3	-0.1	0.0	-0.5
combinatorial	-0.4	$\mathbf{1.7}$	-0.7	0.0	-0.3

Table 25: Pull values of A_{raw} for the ρ^0 sample on the 5 semi-dependent streams of generic Monte Carlo and a different subset of signal Monte Carlo events. Values indicated in bold denote categories where the difference between the fitted and expected value exceeds the error on the fitted asymmetry.

leading to the conclusion that any remaining correlations between the fit variables did not compromise the fit.

In the $K^-\rho^+$ component of the $\overline{K}^{*0}$ mode the additional peak that describes correlations between $m(D^0)$ and $\cos(\theta_H)$ is clearly visible in bins 3,4,5, while being less prominent or absent in the other bins. For the $\overline{K}^{*0}\pi^0$ component, the variations in the distribution of $m(D^0)$ in different bins of $\cos(\theta_H)$ is not visible, as the additional peak appears in bins with a very low number of events.

Bins number 4 and 5 in each variable show the region where the fraction of signal events is highest and therefore provide also the role of signal-enhanced plots. The signal component can be clearly seen in all of the plots in question.
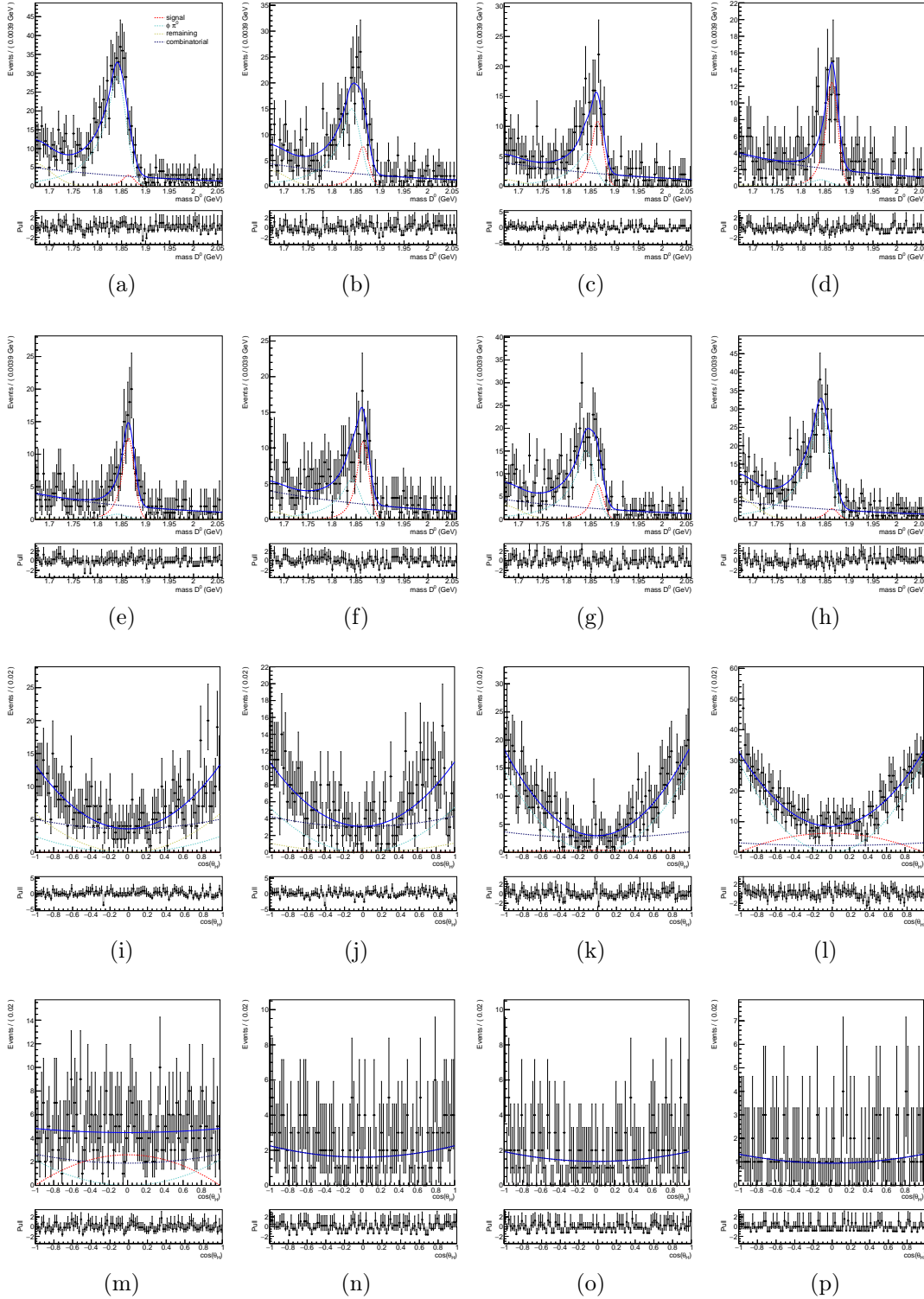
Figure 58: The top two rows show the projections of the fit to $m(D^0)$ in bins of $\cos(\theta_H)$ for the ϕ mode. The $\chi^2/$NDF of the fits is 0.7, 0.8, 1.0, 0.8, 0.7, 0.8, 1.0, 0.8 for bins 1, 2, 3, 4, 5, 6, 7 and 8, respectively. The bottow two rows show the projections of the fit to $\cos(\theta_H)$ in bins of $m(D^0)$. The $\chi^2/$NDF value of the fits are 0.9, 1.2, 0.6, 0.7, 1.0, 0.9, 0.8 and 0.6.
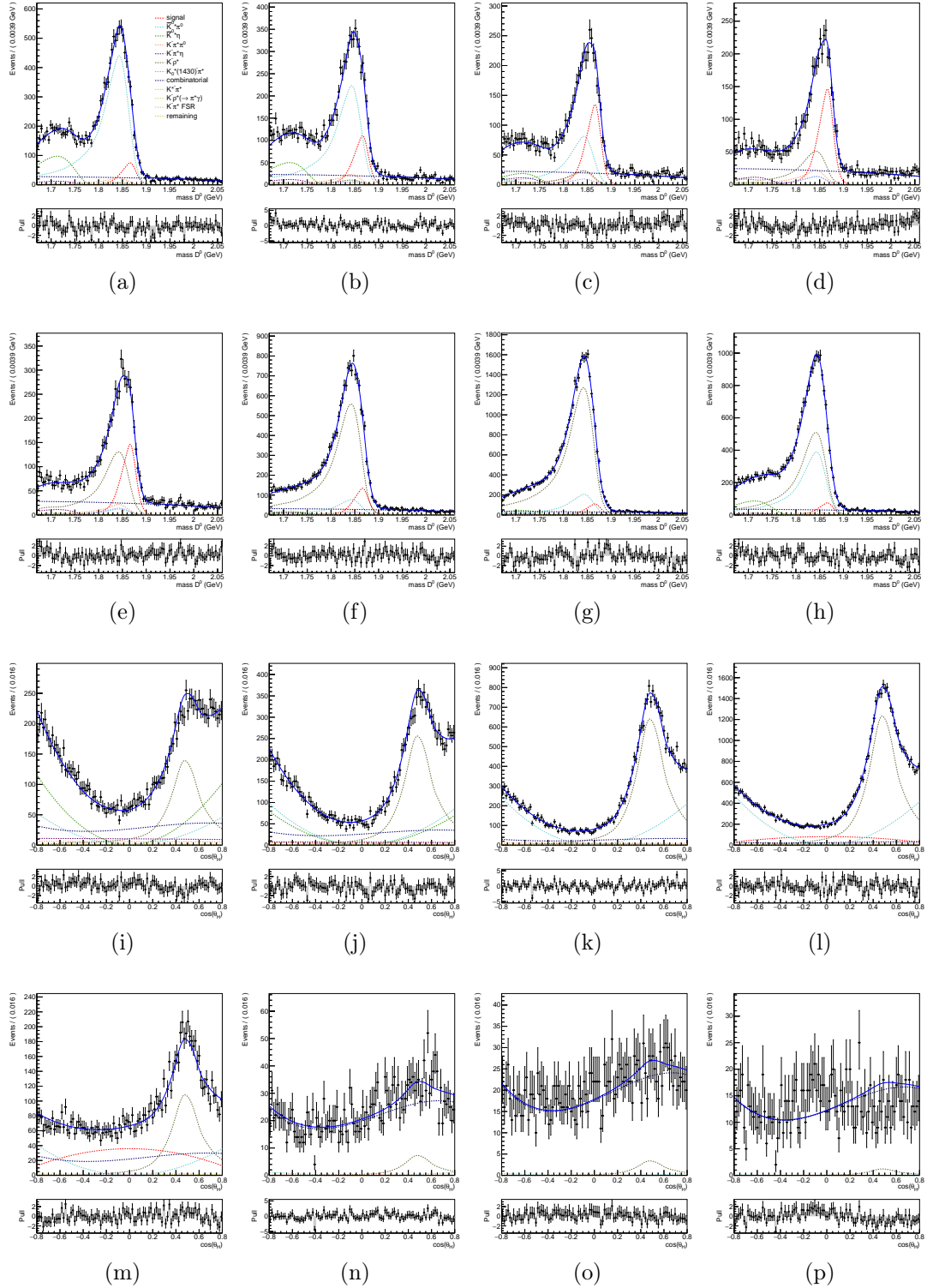
Figure 59: The top two rows show the projections of the fit to $m(D^0)$ in bins of $\cos(\theta_H)$ for the $\overline{K}^{*0}$ mode. The χ^2/NDF of the fita is 1.1, 1.1 , 1.3, 1.1, 1.3, 1.0, 1.5 and 1.3 for bins 1, 2, 3, 4, 5, 6, 7 and 8, respectively. The bottom two rows show the projections of the fit to $\cos(\theta_H)$ in bins of $m(D^0)$. The χ^2/NDF values of the fits are 1.0, 1.1, 1.2, 1.3, 1.0, 1.0, 1.2 and 1.1.

Figure 60: The top two rows show the projections of the fit to $m(D^0)$ in bins of $\cos(\theta_H)$ for the ρ^0 mode. The χ^2/NDF of the fits is 1.0, 1.1, 1.0, 0.9, 1.0, 0.9, 0.8 and 1.3 for bins 1, 2, 3, 4, 5, 6, 7 and 8, respectively. The bottom two rows show the projections of the fit to $\cos(\theta_H)$ in bins of $m(D^0)$. The χ^2/NDF values of the fits are 1.1, 1.1, 1.2, 1.5, 1.0, 0.9, 0.8 and 0.9.
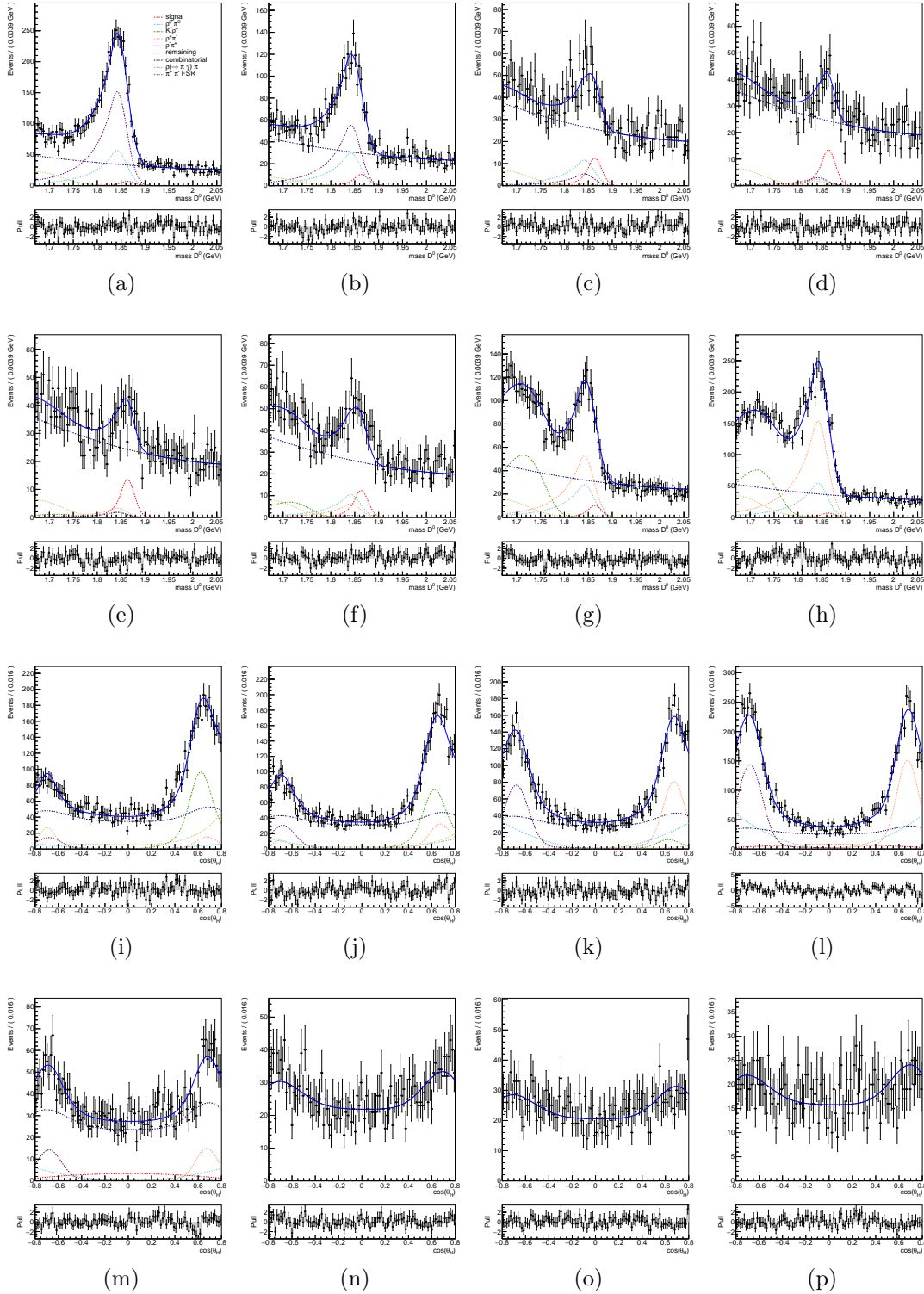
6.7 LINEARITY TEST

Linearity tests are used to analyse the performance of the simultaneous fit for different amounts of signal events. This test is especially important in the case of the ρ^0 channel, since the branching fraction of this decay has not yet been measured. It is therefore important to test the power and reliability of signal extraction in a broad range of signal events.

The linearity test is performed by repeating cycles of generating and fitting events. The 2-dimensional PDFs determined in Section 6.6 are used for both event generation and fitting. For each category, an input value of the number of events is provided. In each cycle, the amount of events generated for a category is randomly taken from a Poissonian distribution around the input value. The input number of events for background categories is the expected number of events on the data sample, determined from the fit on one Monte Carlo stream. The linearity test is performed for different input numbers of signal events, from less to more events than the expected number, which was used in the 2-dimensional fit. For the ϕ and $\overline{K}^{*0}$ modes, for which the branching fraction is known and therefore the calculated expected number of events is relatively reliable, the linearity test is performed with the expected number of signal events, half the expected number and twice the expected number of events. For the ρ^0 mode, where the branching fraction is unknown, the test is performed also with one tenth of expected events and 10 times the expected value.

One set of the linearity test consists of 100 cycles, each corresponding in luminosity to the full Belle data sample. The pull distribution of each set is fitted with a Gaussian. If no issues are present in the fit, the values of the fitted parameters should return a mean = 0 and σ = 1. The test is repeated 4 times for each fraction of signal events, since due to statistical fluctuations a single result can sometimes not be consistent with the expected value, even if the fit performs well. The results of the test are shown in Figure 61 for the ϕ mode, Figure 62 for the $\overline{K}^{*0}$ mode and Figure 63 for the ρ^0 mode, with the values of the fitted mean and σ of the pull distribution plotted for both the yield and the raw asymmetry of signal. The red lines indicate the expected values (0 for the mean and 1 for σ). For each fraction of signal events four results are shown, corresponding to four independent runs of the test. For the ϕ and $\overline{K}^{*0}$ modes, the results of the linearity test are satisfying, showing no bias is present in the fit. In the case of the ρ^0 mode, the results are satisfactory for all fractions of signal except the point corresponding to 10% of expected signal. In that case, it can be seen that while the mean of the pull distribution is consistent with zero for both the yield and A_{raw}, σ is biased toward lower values for A_{raw} and toward larger values for the yield. This would mean that the error on the yield is underestimated and the error on the raw asymmetry is overestimated. If the branching fraction of the ρ^0 mode would result to be an order of magnitude less than the value used in the Monte Carlo analysis, the fit procedure of the ρ^0 mode will have to be revisited.

Figure 61: Results of the linearity test for the ϕ mode. The mean and σ of the pull distribution are plotted for signal yield (a) and signal A_{raw} (b). The red lines indicate the expected values of mean and σ.

Figure 62: Results of the linearity test for the $\overline{K}^{*0}$ mode. The mean and σ of the pull distribution are plotted for signal yield (a) and signal A_{raw} (b). The red lines indicate the expected values of mean and σ.
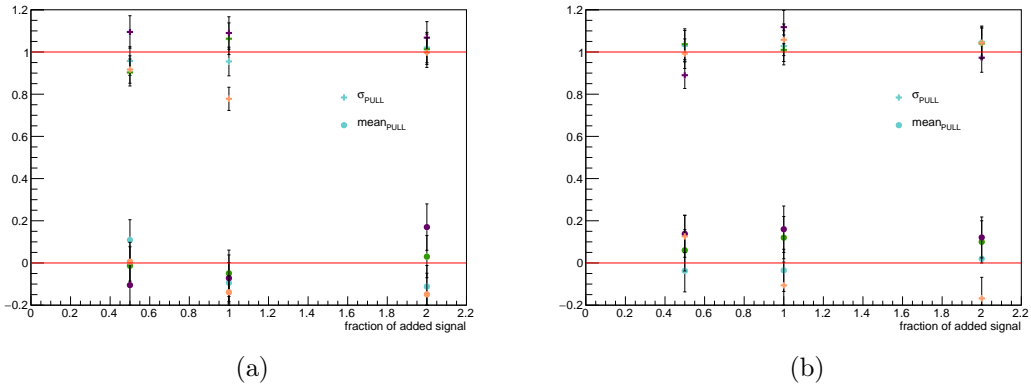

Figure 63: Results of the linearity test for the ρ^0 mode. The mean and σ of the pull distribution are plotted for signal yield (a) and signal A_{raw} (b). The red lines indicate the expected values of mean and σ.
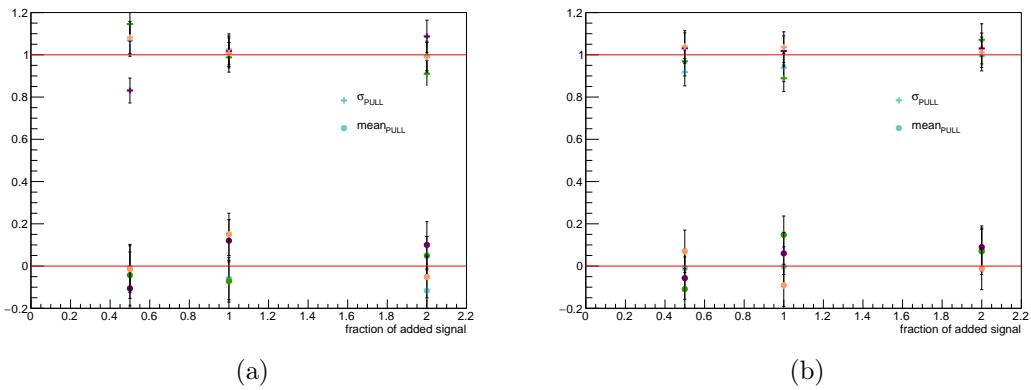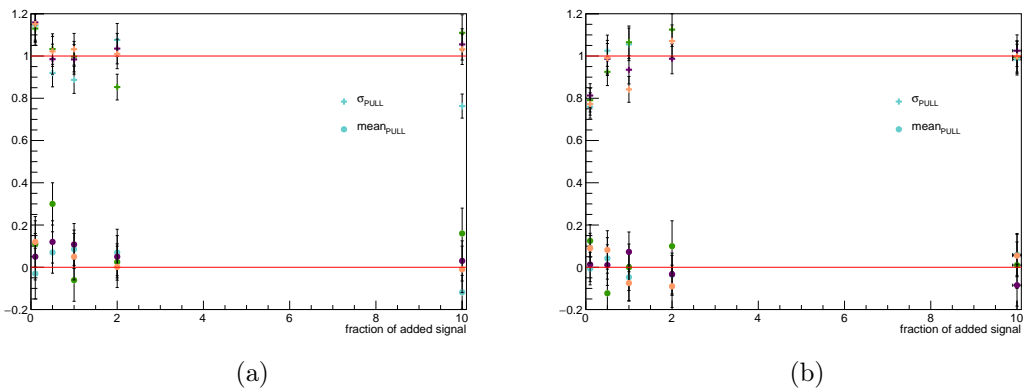
7

NORMALISATION MODES

Both branching fraction and CP asymmetry will be determined via a normalisation to modes, specifically chosen for this purpose. The chosen decay modes are $D^0 \to K^+ K^-$ for the ϕ mode, $D^0 \to K^- \pi^+$ for the $\overline{K}^{*0}$ mode and $D^0 \to \pi^+ \pi^-$ for the ρ^0 mode. The requirement that the D^0 meson comes from a decay $D^{*+} \to D^0 \pi_s^+$ is imposed.

All three chosen normalisation modes are reconstructed on the generic Monte Carlo simulation, and on data. The same pre-selection and selection criteria as for signal modes are used whenever applicable, in order for the related uncertainties to subtract. They are stated in Table 26.

The analysis of the normalisation modes is heavily based on the previous analysis of the same modes by the Belle Collaboration [33]. The decision is supported by the success of the aforementioned analysis and by the good statistics of the normalisation modes in comparisons to the signal modes. It can be expected that both the extracted yield and asymmetry of the normalisation modes be superior by far in terms of the uncertainty than the values corresponding to signal modes. The uncertainty of the final result will thus be mostly dominated by the uncertainties emerging from signal modes. Consequentially, it is not necessary to absolutely optimise the analysis of the normalisation modes, as the final result will not profit from further precision in this part.

To extract signal events, the analysis from Reference [33] used a counting method with background subtraction in the invariant mass of D^0 candidates, $m(D^0)$. The procedure is slightly modified for the present analysis, since looser particle identification criteria are applied due to referencing to signal modes, which results in some differences in the distributions. The core method of background subtraction remains the same: the number of background events in a chosen signal window in $m(D^0)$ is estimated directly from two symmetrical sidebands on each side of the signal window, whose joined width equals that of the signal window.

We define the fraction of background between the signal window and sidebands, determined on Monte Carlo, as

$$f = \left(\frac{N_{\mathrm{SW}}^{\mathrm{bkg}}}{N_{\mathrm{LSB}} + N_{\mathrm{USB}}} \right)_{\mathrm{MC}} , \qquad (52)$$

where $N_{\mathrm{SW}}^{\mathrm{bkg}}$ is the number of background events in the signal window and N_{LSB} and N_{USB} are the total number of events in the upper and lower sidebands, respectively.

	K^+K^-	$K^-\pi^+$	$\pi^+\pi^-$	all
$\mathcal{P}_{K/\pi}$ (pions)				<0.9
$\mathcal{P}_{K/\pi}$ (kaons)				>0.1
mass window D^0				± 225 MeV
$p_{CMS}(D^0)$				> 2 GeV
p-value of D^0 vertex fit				>0.001
mass window after D^0 vertex fit				1.765 GeV $< m(D^0) <$ 1.965 GeV
mass window D^{*+}				± 200 MeV
p-value of D^{*+} vertex fit				>0.001
Δm after D^{*+} vertex fit				<160 MeV
q				<0.6 MeV
$p_{CMS}(D^{*+})$	>2.42 GeV	>2.17 GeV	>2.72 GeV	

Table 26: Pre-selection and selection criteria for the three normalisation modes.

(a)   (b)   (c)
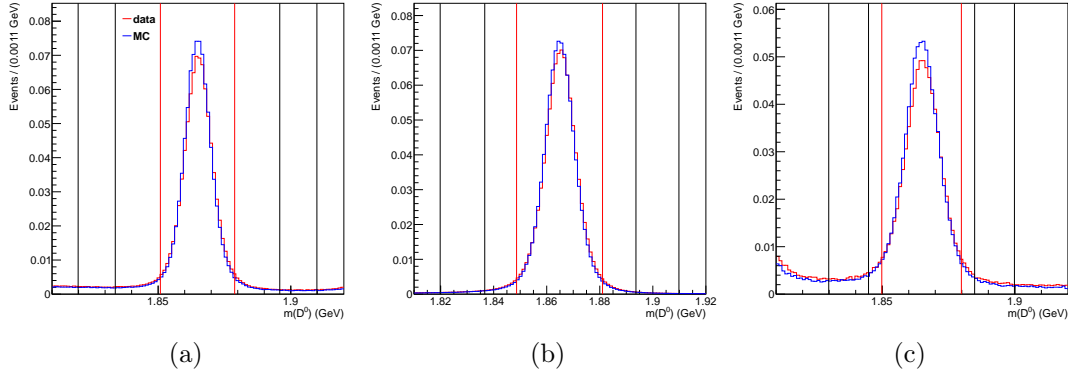
Figure 64: Distributions in $m(D^0)$ of the three normalisation modes: K^+K^- (a), $K^-\pi^+$ (b) and $\pi^+\pi^-$ (c) for both data and Monte Carlo. The signal window and sidebands used for background subtraction are marked on each plot with vertical red and black lines, respectively.

The same fraction will then be used on data to calculate the number of background events in the signal window by multiplying it with the sum of events in the sidebands:

$$(N_{\text{SW}}^{\text{bkg}})_{\text{DATA}} = f \cdot (N_{\text{LSB}} + N_{\text{USB}})_{\text{DATA}} \quad . \tag{53}$$

The signal window and sidebands are taken from Reference [33] and only slightly modified in the $\pi^+\pi^-$ mode due to differences in background amount and shape. The final values are listed in Table 27. The $m(D^0)$ distributions of all three normalisation modes with marked signal window and sidebands are shown in Figure 64, for both data and Monte Carlo. Some discrepancies between the two are immediately spotted, especially in the signal peak. This does not necessarily mean that the proposed signal extraction procedure is unsuitable. Further tests are conducted to establish whether the method is applicable.

Firstly, solely the distributions of background on data and Monte Carlo are compared. Since the background under the signal peak cannot be isolated on data,

	signal window	sidebands
K^+K^-	± 14 MeV	$\pm(31\ -45)$ MeV
$K^-\pi^+$	± 16.2 MeV	$\pm(28.8-45)$ MeV
$\pi^+\pi^-$	± 15 MeV	$\pm(20\ -35)$ MeV

Table 27: The signal window and sidebands of the normalisation modes.
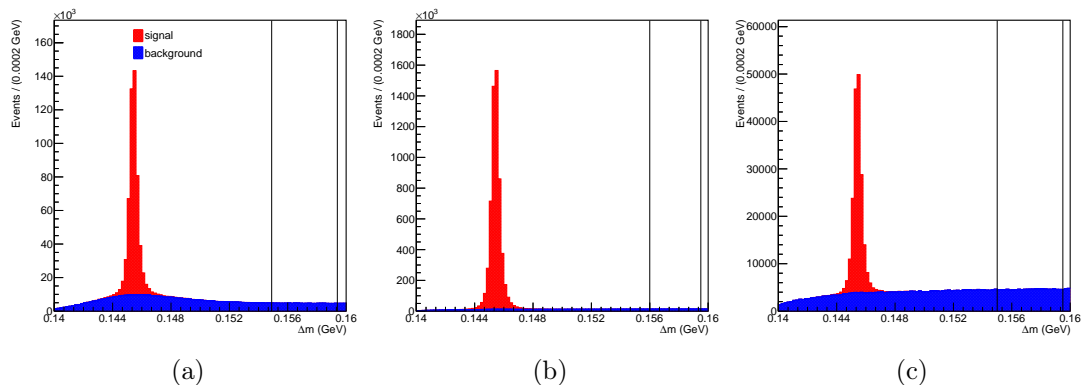
Figure 65: Distributions in Δm of the three normalisation modes: K^+K^- (a), $K^-\pi^+$ (b) and $\pi^+\pi^-$ (c), on Monte carlo. The sidebands used for the comparison between data and Monte Carlo are marked on each plot.

the comparison is done in a sideband of the mass difference $\Delta m = m(D^{*+}) - m(D^0)$. The Δm distributions on Monte Carlo with the marked sidebands are shown in Figure 65.

Figure 66 shows the normalised distributions of $m(D^0)$ in the Δm sidebands for Monte Carlo and data. The sidebands from Table 27 are also marked, since this is the region that interests us the most. Despite being plotted in a sideband, all three distributions still exhibit a prominent peak at the nominal D^0 mass. There is a certain fraction of signal events left in the sideband, however the bulk of the peak belongs to the random slow pion candidates. These are a background category where the D^0 is correctly reconstructed, but paired with an uncorrelated pion in a case where the combined invariant mass by chance falls in the allowed mass range of the D^{*+}. The properties and impact of this type of background have been discussed in Section 6.6.3. The background fraction as calculated in the procedure through Equation 52 does not include the random π_s^+ category, covering instead only the combinatorial fraction. It is clearly visible in Figure 66 that the random π_s^+ peak does not feature in the sidebands that are used for calculating f.

We thus remain interested only in the comparison of combinatorial background distributions. Examining Figure 66, the distributions visually seem to match, especially in the sidebands where f will be calculated. A virtual extrapolation to the combinatorial events under the peaking background does not give any indication that the distribution would not match in this region. For a further check of the accordance between Monte Carlo and data background shapes, the ratio of events in the lower

(a)   (b)   (c)
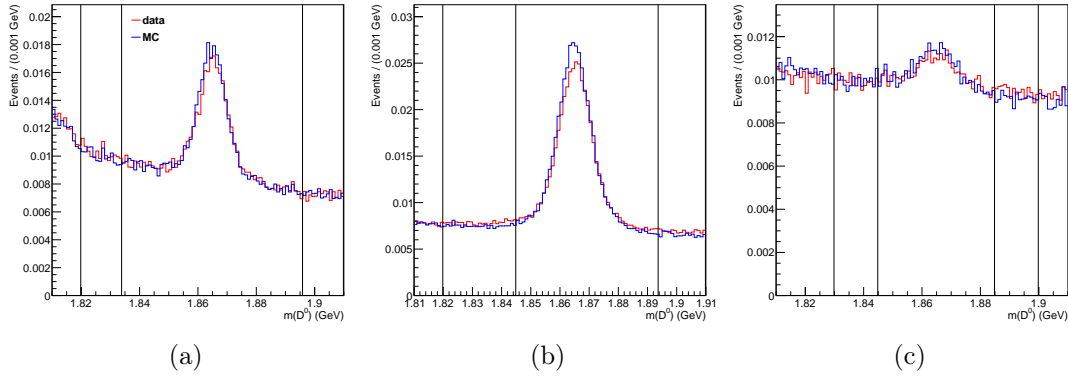
Figure 66: Distributions of $m(D^0)$ in the Δm sidebands for the three normalisation modes: K^+K^- (a), $K^-\pi^+$ (b) and $\pi^+\pi^-$ (c). The sidebands used for background subtraction are marked on each plot.

	R	pull
K^+K^-	1.054 ± 0.022	**2.45**
$K^-\pi^+$	0.990 ± 0.011	-0.9
$\pi^+\pi^-$	1.065 ± 0.021	**3.10**

Table 28: The quotients of the ratios of events in the lower and upper sideband on Monte Carlo and data, and their pulls for the hypothesis $R = 1$.

and upper sidebands is calculated for both data and Monte Carlo in the sideband of Δm and with the cut on $p_{\text{CMS}}(D^{*+})$ imposed. Then, the quotient of the ratios R is calculated as

$$R = \frac{\left(\frac{N_{\text{LSB}}}{N_{\text{USB}}}\right)_{\text{MC}}}{\left(\frac{N_{\text{LSB}}}{N_{\text{USB}}}\right)_{\text{DATA}}} \quad . \tag{54}$$

The values of R for all three normalisation modes are listed in Table 28, along with the pull, calculated assuming a hypothesis $R = 1$ as the expected value. R is consistent with the hypothesis in the $K^-\pi^+$ mode, while in the other two modes the obtained value of R is slightly larger than the expected 1. This will by accounted for in the systematic uncertainties, by assigning the uncertainty of 5.4% (6.5%) to the fraction of the $K^-\pi^+$ ($\pi^+\pi^-$) mode, and propagating it further.

Similarly as for signal events, the ratio of wrong flavour events compared to correct flavour events is calculated as $N(D^0)_{\overline{D}^0}^{\text{wtag}}/(N(D^0)^{\text{tag}} + N(D^0)_{D^0}^{\text{wtag}})$ (and analogously for the charge conjugated decays). The calculation is done for the signal window with selection criteria applied $(q, p_{\text{CMS}}(D^{*+}))$. The results are summarised in Table 29. It can be seen that the fraction of wrong flavour events is very low, less than 0.2%, in the conditions under which the signal yield of normalisation modes will be extracted. Based on these values, it is estimated that by simply absorbing the random π_s^+ background into signal events, the impact on the final result would be negligible. The random π_s^+ background is therefore not accounted for separately.

	D^0	$\overline{D}^0$
K^+K^-	$(0.09\pm0.02)\%$	$(0.07\pm0.02)\%$
$K^-\pi^+$	0%	0%
$\pi^+\pi^-$	$(0.06\pm0.02)\%$	$(0.08\pm0.02)\%$

Table 29: Fraction of wrong flavour neutral charm mesons in a sample with a certain tag (i.e. $\overline{D}^0$s in the sample tagged with π_s^+ and vice-versa), determined on the signal simulation of normalisation modes, in the signal window and with applied selection criteria.

7.1 DETERMINATION OF f

For the calculation of the fraction f three streams of generic Monte Carlo are used. The fraction is first calculated separately for the D^0 and $\overline{D}^0$ to check whether any asymmetries are present. The two obtained fractions are very similar, so a uniform fraction is used for both flavours. The final fractions are summarised in Table 30. It is immediately noticed that the fraction in the $K^-\pi^+$ channel substantially differs from the other two. This is due to the fact that after the application of selection criteria, this channel exhibits the highest ratio of signal-to-background, with signal amounting to 98% of all events (in the K^+K^- and $\pi^+\pi^-$ channels, this value is 59% and 37%, respectively). Consequentially, signal events represent also a major fraction of events in the mass sidebands, N_{LSB} and N_{USB}. In the $K^-\pi^+$ channel, signal events constitute 73% of events in this region, compared to 16% in K^+K^- and 35% in $\pi^+\pi^-$. This discrepancy in the fraction of the different normalisation modes does not represent an issue, as long as the corresponding fraction can be expected to be the same on data and Monte Carlo. This was verified by checking the distributions in Figure 66.

We check also the fractions, obtained on the other 3 independent streams of Monte Carlo, and compare them with f. All are found to be consistent with f within a 1% margin of error.

To test the performance of using the obtained fractions and Equation 52 to calculate the number of signal events, a comparison is done between the calculated signal yield and the true number of signal events for the three streams of generic Monte Carlo that were used for the determination of f. For each signal mode, we calculate the difference between the number of signal events, extracted using the fractions from

	f
K^+K^-	0.722 ± 0.005
$K^-\pi^+$	0.239 ± 0.001
$\pi^+\pi^-$	0.604 ± 0.005

Table 30: The background fractions f for all three normalisation modes.

Table 30, and the true number of signal events. It is found that there is a small bias in the extraction of the signal yield through this procedure. The relative bias of the extracted yield is 0.5%, 0.3% and 0.4%, for the K^+K^-, $K^-\pi^+$ and $\pi^+\pi^-$ modes, respectively. It will be attributed as a systematical error.

7.2 EXTRACTION OF THE RAW ASYMMETRY

Having obtained the background fraction through which it is possible to extract the signal yield, we now proceed to the calculation of the raw asymmetry of the normalisation modes on the three independent Monte Carlo streams as well as on the first three streams. A_{raw} is determined for each stream separately. The sample is divided in two based on the charge of the slow pion. The signal yields for samples of both flavours are calculated using sidebands and signal window from Table 27 and the fraction from Table 30. From both signal yields, A_{raw} is calculated through Equation 33. The obtained results are listed in Table 31, where streams 0-2 are the streams on which the fraction was determined and streams 3-5 are the completely independent streams. The true value of the asymmetry on each stream is also listed. It is obvious that the A_{raw} extraction procedure performs well.

	K^+K^-		$K^-\pi^+$		$\pi^+\pi^-$	
	A_{raw}	A_{true}	A_{raw}	A_{true}	A_{raw}	A_{true} $[\times 10^{-3}]$
stream0	-1.09 ± 1.60	-1.27	-5.87 ± 0.45	-5.92	0.71 ± 2.81	0.09
stream1	-1.98 ± 1.60	-2.25	-5.39 ± 0.45	-5.44	0.36 ± 2.81	-0.64
stream2	-2.32 ± 1.60	-2.54	-6.05 ± 0.45	-6.09	-3.60 ± 2.80	-2.81
stream3	-0.58 ± 1.60	-0.75	-6.11 ± 0.45	-6.06	2.42 ± 2.81	2.32
stream4	2.07 ± 1.60	2.05	-4.70 ± 0.45	-4.71	-3.03 ± 2.80	-3.23
stream5	-4.17 ± 1.60	-3.76	-5.75 ± 0.45	-5.85	-3.83 ± 2.80	-3.71

Table 31: Values of A_{raw} for all three normalisation channels, along with the true value of the asymmetry for each stream.

7.3 EFFICIENCY

The efficiency of the normalisation modes is required for the calculation of the branching fraction as in Equation 31. For the purpose of determining it, signal Monte Carlo simulations are generated for all three normalisation modes with the same tools as used for the signal Monte Carlo simulations for signal modes. During reconstruction, all applicable pre-selection criteria from the reconstruction of signal modes are used. The final efficiency is calculated applying the selection criteria on $p_{\mathrm{CMS}}(D^{*+})$ and Δm for the signal window as stated in Table 27, since the signal yield will be calculated in the signal window only. The obtained values are listed in Table 32.

	ε
K^+K^-	22.7%
$K^-\pi^+$	27.0%
$\pi^+\pi^-$	21.4%

Table 32: Efficiency after the application of selection criteria for the three normalisation modes.

EXTRACTION OF $\mathcal{A}_{CP}$ ON MONTE CARLO

Having obtained the raw asymmetry of both signal and normalisation modes, we now proceed to the calculation of the CP asymmetry by pairing the results belonging to the same Monte Carlo stream. In the Belle generic Monte Carlo, the input CP asymmetry is zero for all decays in question, signal and normalisation. The value $\mathcal{A}_{CP} = 0$ for the normalisation modes is therefore used for the following calculation. For the final analysis of real data, the world average values of $\mathcal{A}_{CP}$ will be used [13]. The values of the raw asymmetry on each stream of all three signal modes are summarised in Table 33. The completely independent stream is number 0.

For each stream, we calculate the value of $\mathcal{A}_{CP}$ using Equation 35 and the values of A_{raw} for the signal modes from Table 33, A_{raw} for the normalisation modes from Table 31 and putting $\mathcal{A}_{CP} = 0$ for the normalisation modes. The results are listed in Table 34. It is clear that the dominant term with regard to precision is the statistical uncertainty on the raw asymmetry of signal modes, as it is on average an order or magnitude larger than the other two terms. Since the input value of the CP asymmetry on Monte Carlo is 0 (there is no asymmetry) for all decay modes in question, the calculated values are expected to be 0 within the margin of error. This is true in all but 7 cases in Table 34, however all of them except one are within a 2σ deviation. Since this is a stochastic process, the measured values are normally distributed, and it is expected that in some of cases, deviations of more than 1σ will be observed. The obtained results are thus statistically expected and understandable. We conclude that the $\mathcal{A}_{CP}$ extraction procedure is suitable and performs well.

	ϕ	$\overline{K}^{*0}$	ρ^0
stream0	-5.2 ± 5.7	-3.7 ± 2.0	0.3 ± 9.0
stream1	3.5 ± 6.3	-5.0 ± 2.0	-5.5 ± 9.5
stream2	2.2 ± 6.0	-0.5 ± 1.9	-10.4 ± 8.8
stream3	3.5 ± 6.4	-0.8 ± 2.0	0.9 ± 8.7
stream4	-0.1 ± 6.3	1.8 ± 1.9	-20.4 ± 10.0
stream5	5.6 ± 5.8	-3.3 ± 2.0	3.2 ± 9.5

Table 33: Values of A_{raw} in % on each stream for all three signal modes.

	ϕ	$\overline{K}^{*0}$	ρ^0
stream0	-5.1 ± 5.9	-3.1 ± 2.1	0.2 ± 9.3
stream1	3.7 ± 6.5	-4.5 ± 2.1	-5.5 ± 9.8
stream2	2.4 ± 6.2	0.1 ± 2.0	-10.0 ± 9.1
stream3	3.6 ± 6.6	-0.2 ± 2.1	0.7 ± 9.0
stream4	-0.3 ± 6.5	2.3 ± 2.0	-20.1 ± 10.3
stream5	6.0 ± 6.0	-2.7 ± 2.1	3.6 ± 9.8

Table 34: Values of $\mathcal{A}_{CP}$ in % on each stream for all three signal modes.

FIT IN DATA

To asses the performance of the Monte Carlo based PDFs, we first perform a basic 2-dimensional fit in data. The fit is performed firstly in the $\overline{K}^{*0}$ channel to obtain the values of the offset and width scale factor of the signal $m(D^0)$ PDF, which will be used as fixed parameters for the fit in the ϕ and ρ^0 channels, as described in Section 6.5.4.

For the nominal fit, the PDFs obtained from the Monte Carlo sample smeared with a Gaussian of 7 MeV width are used for the π^0 and η-type background for the nominal fit. Samples with 6 MeV and 8 MeV smearing will be used to estimate the systematic uncertainty due to the choice of smearing value.

All yields of background categories in the $\overline{K}^{*0}$ and ρ^0 modes that are fixed, are scaled with the ratio between reconstructed signal events on simulation and data of the normalisation modes. If branching fractions that were used in the generic Monte Carlo do not match the latest world-average [23], the yields are adjusted accordingly.

9.1 $\overline{K}^{*0}$ MODE

The results of the 2-dimensional fit in data of the $\overline{K}^{*0}$ mode are shown in Figure 67. While the fit seems to describe the $m(D^0)$ data distribution quite well, an obvious discrepancy is immediately spotted in the $\cos(\theta_H)$ distribution. The fit function, which is based on Monte Carlo predictions, seems to described the $\cos(\theta_H)$ data distribution well for $\cos(\theta_H) < 0.7$, while in the region $\cos(\theta_H) > 0.7$ there is a significant deviation from the data distribution. The simulation predicts a shift in the derivative from negative to positive (turn from decreasing to increasing function) around $\cos(\theta_H) \approx 0.8$, which is confirmed by inspecting the full $\cos(\theta_H)$ range. In data, this trends seems to be shifted to a lower value of $\cos(\theta_H)$, with the function starting to increase already from $\cos(\theta_H) \approx 0.7$.

It is not immediately clear what feature causes this discreapancy between simulation and data. As discrepancies between the two have been known to occur in momentum distributions, we first compare the $\cos(\theta_H)$ distributions of Monte Carlo and data with a tighter constraint imposed on the CMS momentum of D^{*+}, requiring $p_{\mathrm{CMS}}(D^{*+}) > 3.0$ GeV. It is found that a tighter constraint on $p_{\mathrm{CMS}}(D^{*+})$ does not affect the position where the $\cos(\theta_H)$ distribution turns. We also investigate correlations between $p_{\mathrm{CMS}}(D^{*+})$ and $\cos(\theta_H)$, and find that there is no significant correlation between the two. As laboratory momentum has an influence on particle identification, we also investigate the $\cos(\theta_H)$ distribution with several tighter constraints applied to both

kaon and pion identification. We find that a variation in these constraints does not significantly alter the $\cos(\theta_H)$ distribution.

This leaves us with the presumption that the cause of the deviation is an inaccurate description of background contributions in Monte Carlo. The background contributions that exhibit a significantly increasing behaviour in this $\cos(\theta_H)$ range are the $\overline{K}^{*0}\pi^0$ and $\overline{K}^{*0}\eta$ categories, i.e. both categories with the true vector meson and a π^0 or η instead of a photon. For both categories, conservation of angular momentum dictates that the $\cos(\theta_H)$ distributions exhibit a $\cos^2(\theta_H)$ shape. While the decays are reconstructed not as such, but as a decay to the vector meson and one photon, it is unrealistic that the distributions would distort so much as to account for the observed rise in the data distribution of $\cos(\theta_H)$. This is confirmed by a quick examination of the $\cos(\theta_H)$ distribution in the ϕ and ρ^0 channels, where $V\pi^0$ decays also constitute a prominent background source. The observed trend is not present in either of the $\cos(\theta_H)$ distributions of the other two signal modes, confirming that the $V\pi^0$ and $V\eta$ backgrounds are not likely to be the sole cause of the discrepancy. We further investigate this issue by looking at the $\cos(\theta_H)$ distribution in sidebands of the mass of the vector meson. The sideband is characterised by the requirement that the difference between the reconstructed and nominal mass of $\overline{K}^{*0}$ is greater than 100 MeV. The corresponding plot of the normalised distribution is shown in Figure 68, together with the plot in the signal window of $m(V)$, for both data and Monte Carlo. All distributions are plotted in the full $\cos(\theta_H)$ range, to enable also a thorough examination of backgrounds that peak at ± 1.

There are several conclusions that can be drawn from Figure 68. The cause of the discrepancy seems to be an inaccurate description of the physical backgrounds, while the combinatorial background seems to be described well with a PDF with free parameters. There is a visible divergence in the peak belonging to the $K^-\rho^+$ category, starting at the value $\cos(\theta_H) \approx 0.6$, where the data distribution exhibits a significant rise, compared to the Monte Carlo distribution. This cannot, however, fully account for the observed shift in the turn of the whole $\cos(\theta_H)$ distribution. It seems that the observed discordance is a result of inaccurate description of several background categories, with different individual discrepancies that sum up to form the observed effect. Altogether, this examination sheds some light into this problematic discrepancy, but unfortunately it does not provide a definitive answer as to what is the cause of this feature and how to reliably correct for it. Adding a free linear term to the π^0 and η background PDFs proves an unsuitable action as it destabilises the fit, leading it into a physically unrealistic final state, while still not being able to achieve satisfactory matching between data and the fit function. As the fit seems to describe data well for lower values of $\cos(\theta_H)$, we opt to attempt a further reduction in the $\cos(\theta_H)$ range for the 2-dimensional fit instead.

9.1.1 *1-dimensional fit*

The discrepancy between data and simulation seems to arise in the range $\cos(\theta_H) > 0.7$. However, as the two fit variables are not completely uncorrelated, a change in the $\cos(\theta_H)$ range could also affect the $m(D^0)$ distribution. While the difference might

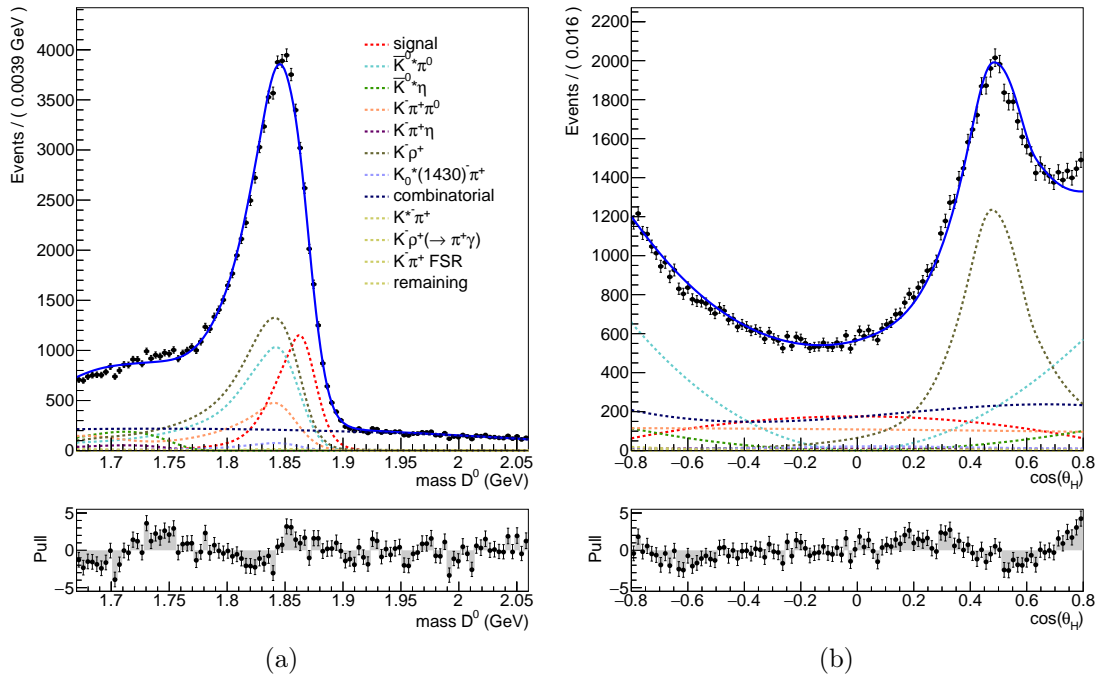Figure 67: 2-dimensional fit in $m(D^0)$ (a) and $\cos(\theta_H)$ (b) of the $\overline{K}^{*0}$ mode sample in data in the full $\cos(\theta_H)$ range. The χ^2/NDF of the fit is 2.5 for $m(D^0)$ and 2.3 for $\cos(\theta_H)$.
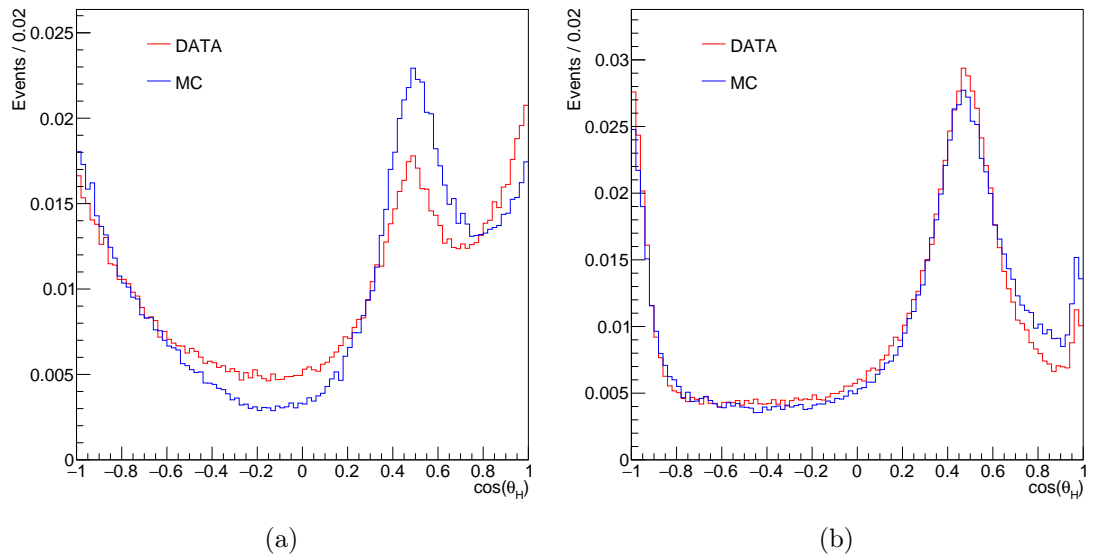

Figure 68: Distributions of $\cos(\theta_H)$ in the signal window (a) and sideband (b) of $m(V)$, with all other selection criteria applied, for both data and Monte Carlo.
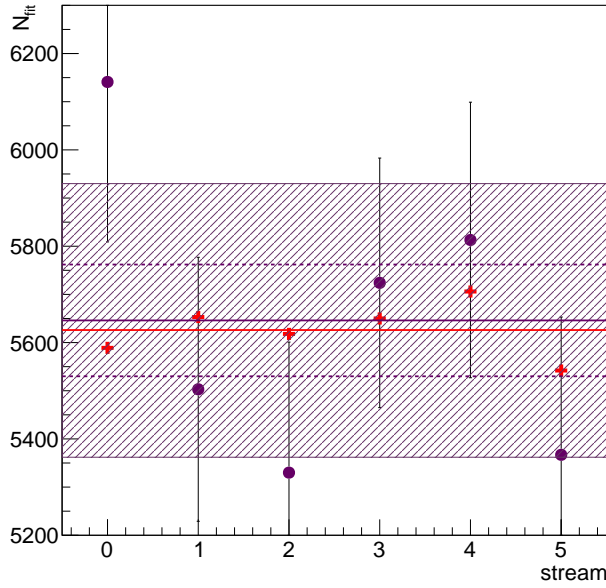
Figure 69: Plot of extracted signal yields (purple dots) with the respective errors, obtained from the 1-dimensional fit in $m(D^0)$ of the $\overline{K}^{*0}$ mode, for six Monte Carlo streams. The red crosses correspond to the true number of signal events in each stream, while the red line shows the average true number of signal events. The full purple line represents the average yield as extracted from the fit, with the dashed purple lines representing the error on the average yield. The entire shaded purple area corresponds to the average error.

be small and not visibly identifiable, the signal yield extraction could be sensitive to it. We therefore decide to first investigate 1-dimensional fits in $m(D^0)$ in different $\cos(\theta_H)$ ranges. We conserve the lower bound of -0.8, and consider upper bounds from 0.0 to 0.8 with a step of 0.2. This gives us five different $\cos(\theta_H)$ ranges. For each range, a Monte Carlo study is performed first.

Since all π^0-type backgrounds exhibit the same $m(D^0)$ distribution (see Figure 13), a 1-dimensional fit cannot distinguish between them. They are therefore fitted as one category. A slight exception is the non-resonant $K^-\pi^+\pi^0$ category, which has a smaller additional peak at lower values of $m(D^0)$, as can be seen in Figure 35d. The shape of the main peak is still the same as in the other π^0-type backgrounds, so it is absorbed in the joint category, while the small peak at lower $m(D^0)$ values is parametrised separately and the corresponding fraction is left as a free parameter of the fit. Similarly, both η-type categories are joint as one.

The $m(D^0)$ PDFs are separately determined for each $\cos(\theta_H)$ range, and the fit is performed on an independent Monte Carlo stream, as well as on the 5 semi-dependent streams. The extracted signal yield is compared to the true value. The results are presented in Figure 69. It can be seen that the average extracted signal yield on six streams closely matches the average true number of events. It is clear that the 1-dimensional fit is reliable and the signal extraction procedure works well on simulation.
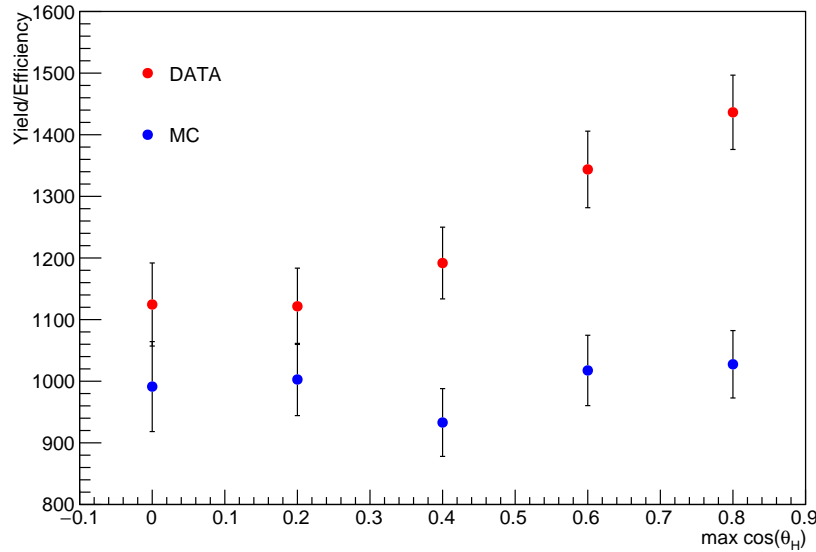
Figure 70: Values of the fraction between the extracted signal yield and effciency for 1-dimensional fits on data and Monte Carlo in the $\overline{K}^{*0}$ mode, for five different $\cos(\theta_H)$ ranges.

For each $\cos(\theta_H)$ range, the efficiency is determined from signal Monte Carlo. In the final equation from which the branching fraction is obtained (Equation 31), the quantity that comes from the fit on signal modes is the fraction of the signal yield over efficiency, $N_{\mathrm{sig}}/\varepsilon_{\mathrm{sig}}$. This quantity should prove to be constant regardless of the range of $\cos(\theta_H)$. The values of $N_{\mathrm{sig}}/\varepsilon_{\mathrm{sig}}$ for each of the $\cos(\theta_H)$ ranges, obtained from Monte Carlo, are plotted in Figure 70 with blue markers. As they are indeed consistent with one another, it can be concluded that the fit performs well regardless of the $\cos(\theta_H)$ range. The same procedure is then repeated for data. The results are plotted in Figure 70 with red markers. It can be observed that the value of $N_{\mathrm{sig}}/\varepsilon_{\mathrm{sig}}$ is constant within the error margins for $\cos(\theta_H)$ ranges with the maximum bound up to 0.4, while for larger ranges the value shows an increasing trend. It is concluded that the problematic upper $\cos(\theta_H)$ range in data affects also the 1-dimensional fit in $m(D^0)$ if included, making the extracted results unreliable. The fit performs well in a reduced range with the upper bound less than 0.4. It is therefore decided to reduce the range of $\cos(\theta_H)$ accordingly. Although no visible issues seem to arise in the lower region of the $\cos(\theta_H)$ distribution, all fits are repeated with the lower bound being moved to -0.6. The corresponding efficiencies are determined and the values of $N_{\mathrm{sig}}/\varepsilon_{\mathrm{sig}}$ compared to those obtained from the fits with the lower bound at -0.8. The results match for all ranges, proving that the lower region of the $\cos(\theta_H)$ distribution is not problematic. The chosen final range for the $\overline{K}^{*0}$ mode is $-0.8 < \cos(\theta_H) < 0.4$, with the corresponding efficiency of 7.8%.
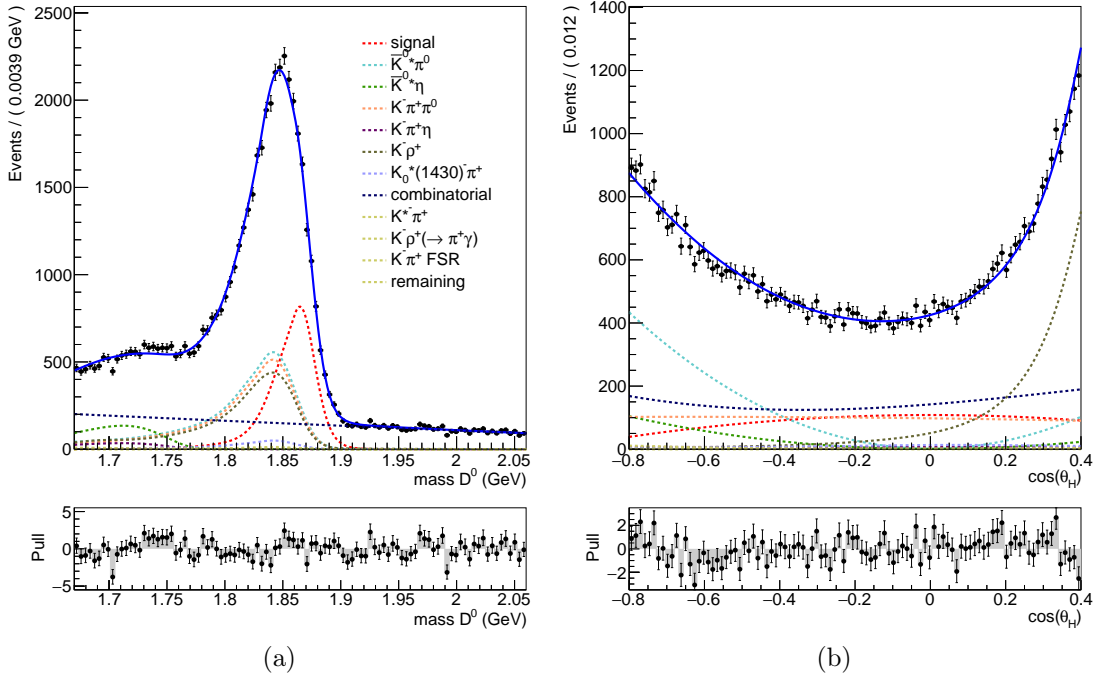
Figure 71: 2-dimensional fit in $m(D^0)$ (a) and $\cos(\theta_H)$ (b) of the $\overline{K}^{*0}$ mode sample in data in a reduced $\cos(\theta_H)$ range. The χ^2/NDF of the fit is 1.5 for $m(D^0)$ and 1.4 for $\cos(\theta_H)$.

9.1.2   *2-dimensional fit*

We now go back to the 2-dimensional fit in the reduced $\cos(\theta_H)$ range. The results are shown in Figure 71. It can be seen that the fit function matches the data well. The extracted signal yield is consistent with that obtained from the 1-dimensional fit, but with a smaller statistical error (relatively, the statistical error of the 2-dimensional fit is 9% smaller compared to the error of the 1-dimensional fit). As a final check, the fit is projected to each of the fit variables in several bins of the other, analogously to the projections to bins performed on Monte Carlo (Section 6.6.8). As the bin widths are preserved, the number of bins in projections to $m(D^0)$ is smaller, due to a reduced range in $\cos(\theta_H)$. The projections to $m(D^0)$ are shown in Figure 72, while projections to $\cos(\theta_H)$ are shown in Figure 73. In all cases, the fit function describes the data points well. We conclude that the 2-dimensional fit in the reduced $\cos(\theta_H)$ range is reliable and an appropriate method for signal extraction.

The obtained offset and width scale factor of the signal $m(D^0)$ PDF are -1.80 $\pm$ 0.66 MeV and 1.099 $\pm$ 0.033, respectively.
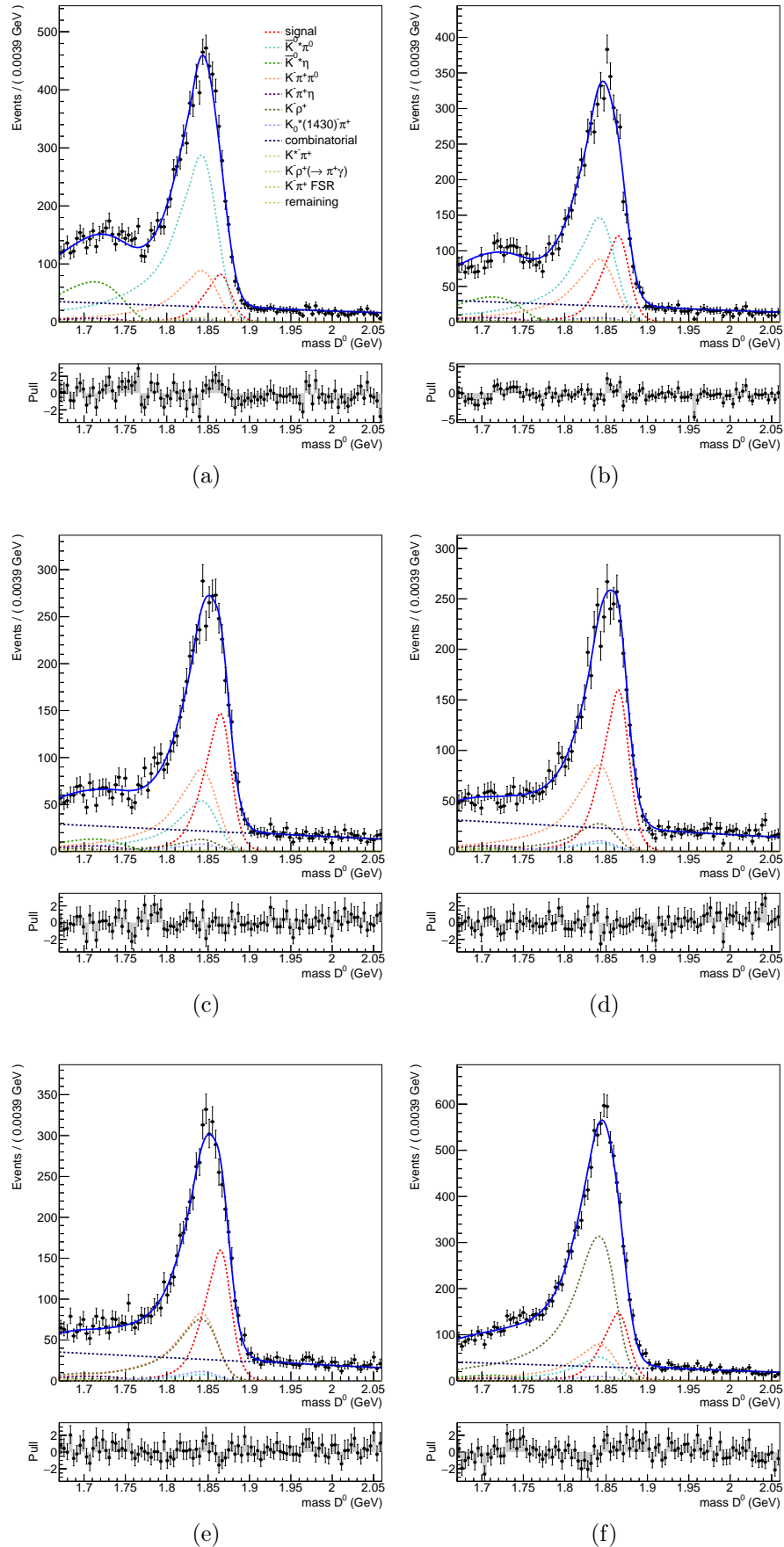
Figure 72: Projections of the fit to $m(D^0)$ in bins of $\cos(\theta_H)$ in data for the $\overline{K}^{*0}$ mode. The χ^2/NDF of the fits are 1.3, 1.4, 1.0, 1.0, 0.9 and 1.2 for bins 1, 2, 3, 4, 5 and 6, respectively.
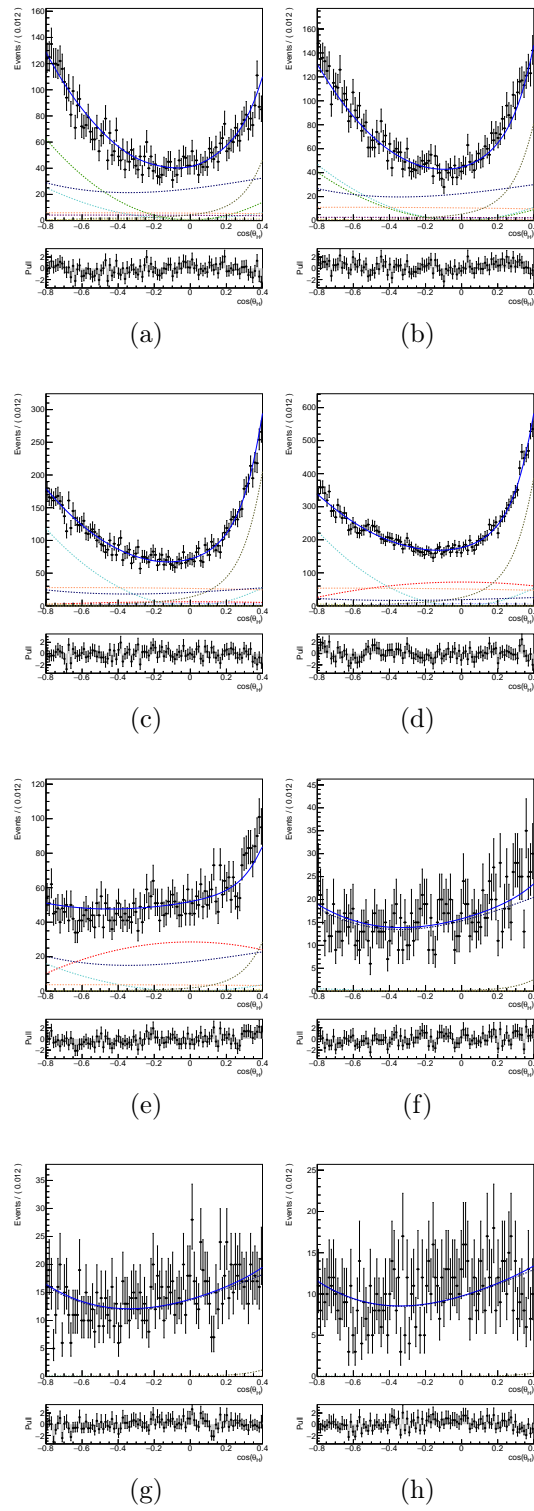
Figure 73: Projections of the fit to $\cos(\theta_H)$ in bins of $m(D^0)$ in data for the $\overline{K}^{*0}$ mode. The χ^2/NDF of the fits are 1.0, 1.1, 0.9, 1.0, 1.0, 1.1, 1.0 and 1.0 for bins 1 2, 3, 4, 5, 6, 7 and 8, respectively.

9.2 φ MODE

The results of the 2-dimensional fit in data of the ϕ mode are shown in Figure 74. The $m(D^0)$ PDF of the signal component is modified according to the offset and width scale factor, obtained from the fit on the $\overline{K}^{*0}$ mode. It can be seen that the fit matches the $m(D^0)$ distribution well, while in the projection to $\cos(\theta_H)$ a slope can be observed in the pull distribution, with the fit function being slightly above the data points in the left-hand part of the range and slightly below the data points on the right-hand side. It is most likely that the cause of the observed discrepancy is an innacurate description of the π^0 background contribution in Monte Carlo, which is most probably due to inteference with non-resonant $K^+K^-\pi^0$ decays. The total amplitude in multi-body decays is given by the coherent sum of amplitudes from resonant and non-resonant contributions and includes interference terms that cancel out if the integration is performed over the full phase space. In data sets where only a portion of phase space is used due to selection criteria, the interference terms do not neccessarily cancel out completely. This effect has already been observed in a previous Belle analysis [38]. In the present case, it can be corrected for with a modification of the $\phi\pi^0$ PDF, using a second-order Chebychev polynomial instead of a fixed $\cos^2(\theta_H)$ shape. The linear term of the polynomial is left as a free parameter of the fit in order to describe the observed slope. The addition of this free parameter does not affect the extracted signal yield, neither the central value nor the error. The results of the modified fit are shown in Figure 75 and it can be seen that the taken measure resolves the issue in the $\cos(\theta_H)$ distribution, while not affecting the power of signal extraction.

As a final check, the fit is projected to each of the fit variables in several bins of the other. The projections to $m(D^0)$ are shown in Figure 76, while projections to $\cos(\theta_H)$ are shown in Figure 77. In all cases, the fit function describes the data points well. We conclude that with the small modification in the $\phi\pi^0$ $m(D^0)$ PDF, the fit in data in the ϕ mode works well.
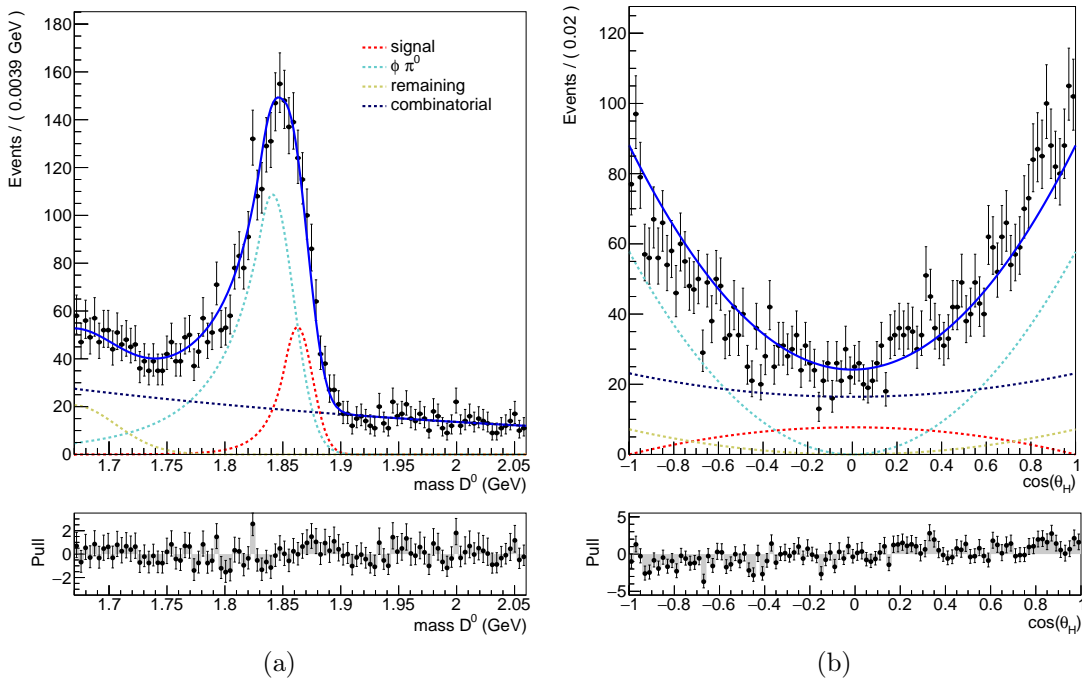
Figure 74: 2-dimensional fit in $m(D^0)$ (a) and $\cos(\theta_H)$ (b) of the ϕ mode sample in data. The χ^2/NDF of the fit is 0.7 for $m(D^0)$ and 1.7 for $\cos(\theta_H)$.

Figure 75: 2-dimensional fit in $m(D^0)$ (a) and $\cos(\theta_H)$ (b) of the ϕ mode sample in data, using the modified $\phi\pi^0$ $\cos(\theta_H)$ PDF. The χ^2/NDF of the fit is 0.7 for $m(D^0)$ and 1.1 for $\cos(\theta_H)$.
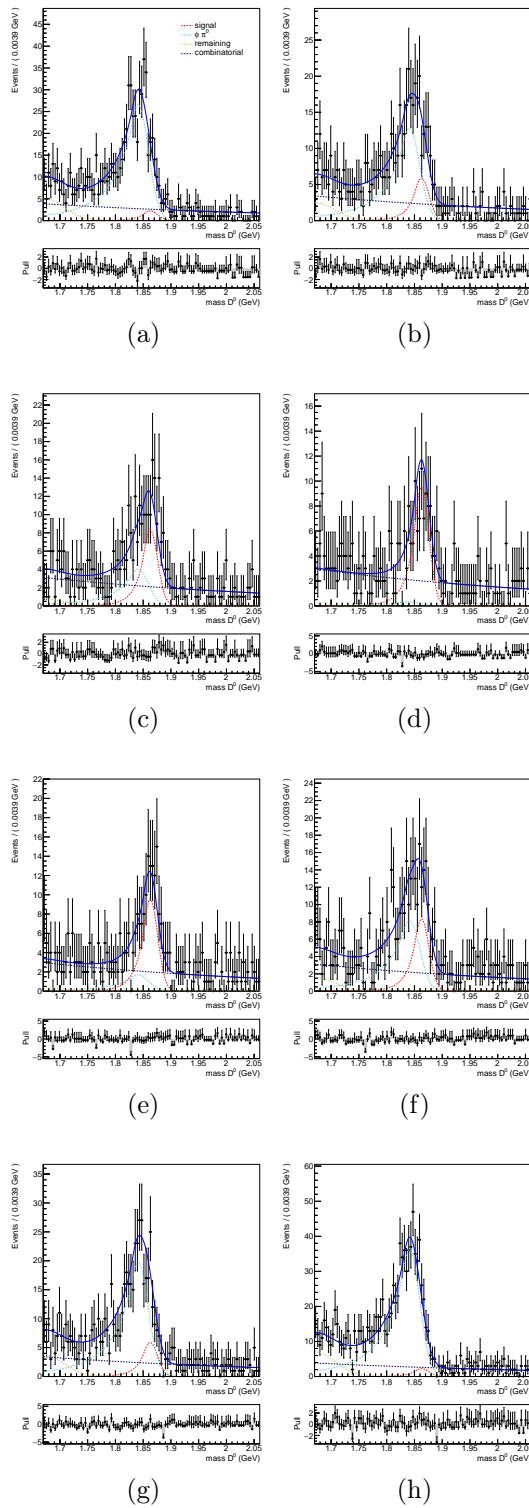
Figure 76: Projections of the fit to $m(D^0)$ in bins of $\cos(\theta_H)$ in data for the ϕ mode. The χ^2/NDF of the fits are 0.8, 0.7, 0.7, 0.8, 1.0, 0.8, 0.8 and 0.9 for bins 1, 2, 3, 4, 5, 6, 7 and 8, respectively.
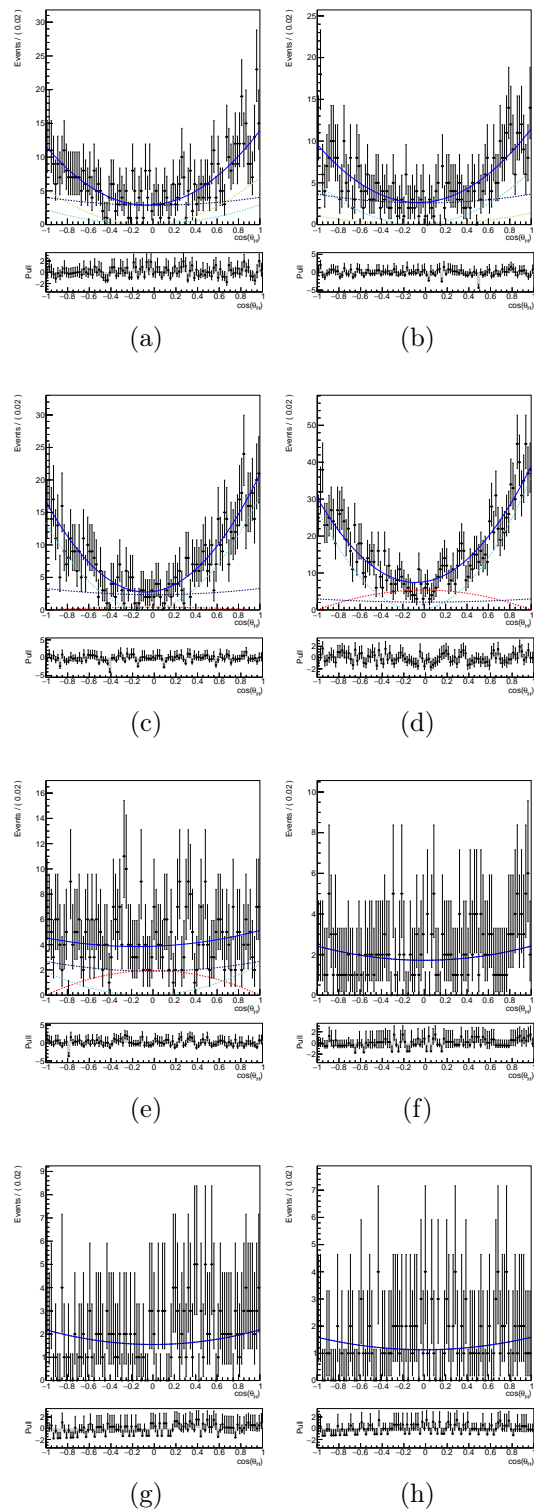
Figure 77: Projections of the fit to $\cos(\theta_H)$ in bins of $m(D^0)$ in data for the ϕ mode. The χ^2/NDF of the fits are 0.8, 0.9, 1.0, 0.8, 0.8, 0.6, 0.9, 0.7 for bins 1, 2, 3, 4, 5, 6, 7 and 8, respectively.

9.3 ρ^0 MODE

The results of the 2-dimensional fit in data of the ρ^0 mode are shown in Figure 78. The $m(D^0)$ PDF of the signal component is modified according to the offset and width scale factor, obtained from the fit on the $\overline{K}^{*0}$ mode. It can be seen that the fit matches the $m(D^0)$ distribution well. The fit to $\cos(\theta_H)$ also seems to match data fairly well, however the pull distribution indicates a slightly greater discrepancy in the far right hand-side region, above $\cos(\theta_H) > 0.5$, than in the rest of the range. Given the problems in the similar region in the $\overline{K}^{*0}$ mode, we decide it is best to use also a reduced $\cos(\theta_H)$ range for the ρ^0. For simplicity and consistency with the $\overline{K}^{*0}$ mode, the chosen reduced range is the same as in the $\overline{K}^{*0}$ mode, $-0.8 < \cos(\theta_H) < 0.4$. The corresponding efficiency is 6.8%. The fit results using the reduced range of $\cos(\theta_H)$ are shown in Figure 79. The fit matches data well in both variables.

It can be seen that the asymmetry that is present in the $\rho^+\pi^-$ and $\rho^-\pi^+$ modes in Monte Carlo due to wrong branching fractions in the generator, is not present in data, as is expected.

As a final check, the fit is projected to each of the fit variables in several bins of the other. As the bin widths from Section 6.6.8 are preserved, the number of bins in projections to $m(D^0)$ is smaller, due to a reduced range in $\cos(\theta_H)$. The projections to $m(D^0)$ are shown in Figure 80, while projections to $\cos(\theta_H)$ are shown in Figure 81. In all cases, the fit function describes the data points well.

As this is the first observation of the decay $D^0 \to \rho^0\gamma$, an additional signal enhanced plot is shown in Figure 82a, where the $m(D^0)$ distribution is plotted in an optimised $\cos(\theta_H)$ window of $-0.32 < \cos(\theta_H) < -0.32$. Figure 82 also includes a plot of the fit in the same window without the signal component, i.e. with the signal yield fixed to zero. It can be seen both from the plot and from the corresponding pull distribution that there is an excess that the background PDFs cannot describe in the precise spot where signal is expected.
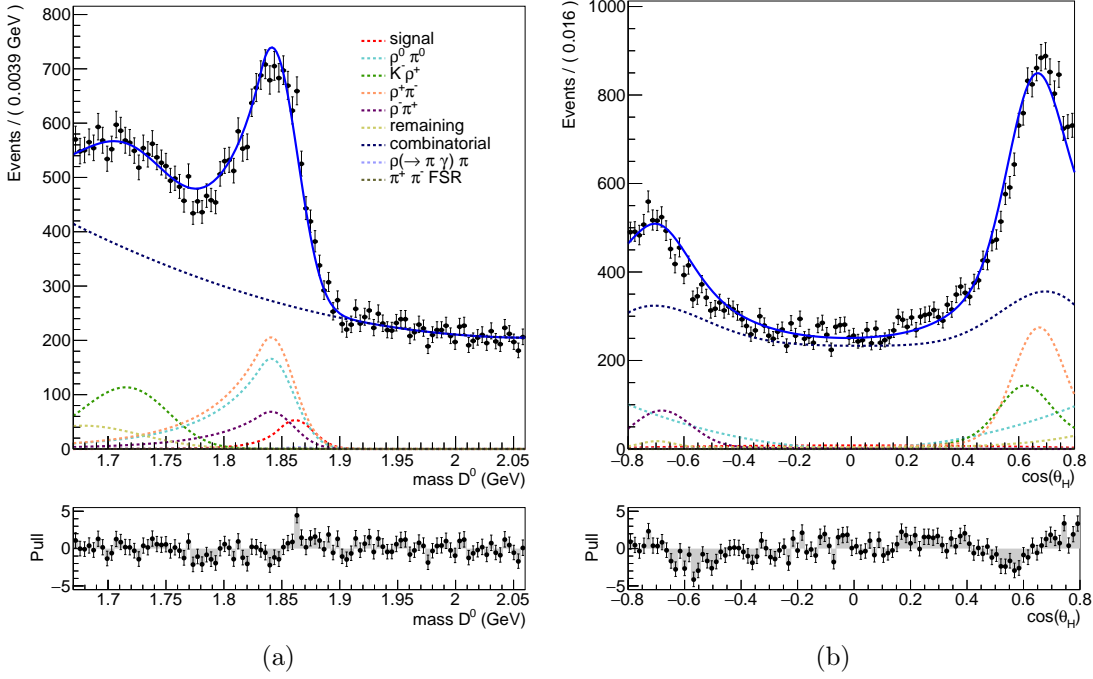
Figure 78: 2-dimensional fit in $m(D^0)$ (a) and $\cos(\theta_H)$ (b) of the ρ^0 mode sample in data in the full $\cos(\theta_H)$ range. The χ^2/NDF of the fit is 1.3 for $m(D^0)$ and 2.3 for $\cos(\theta_H)$.
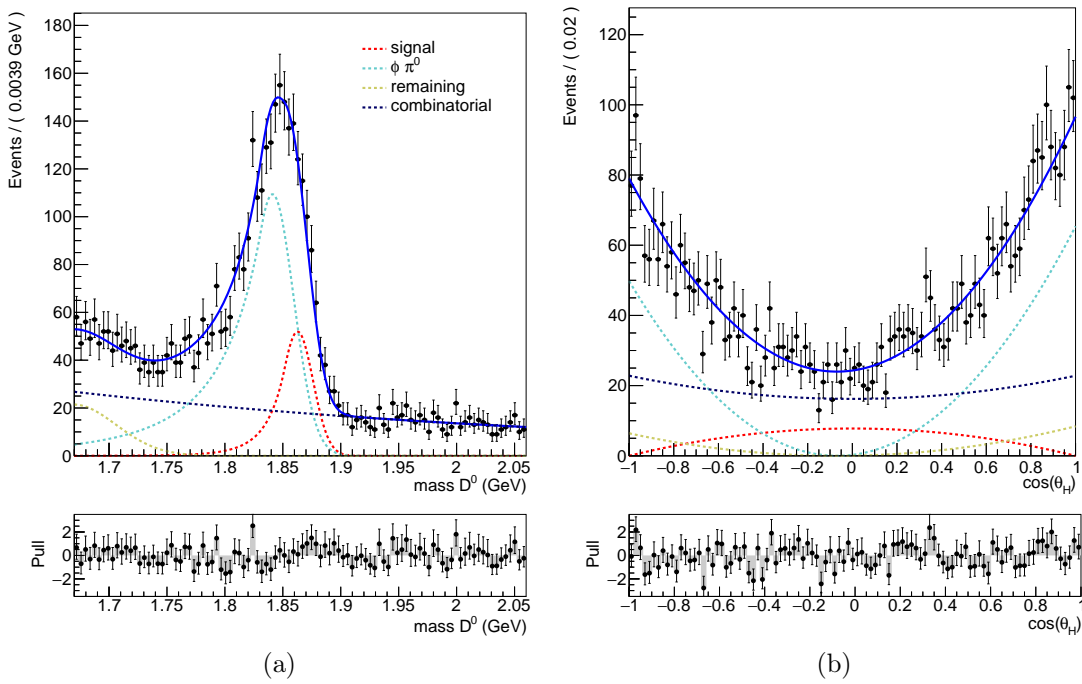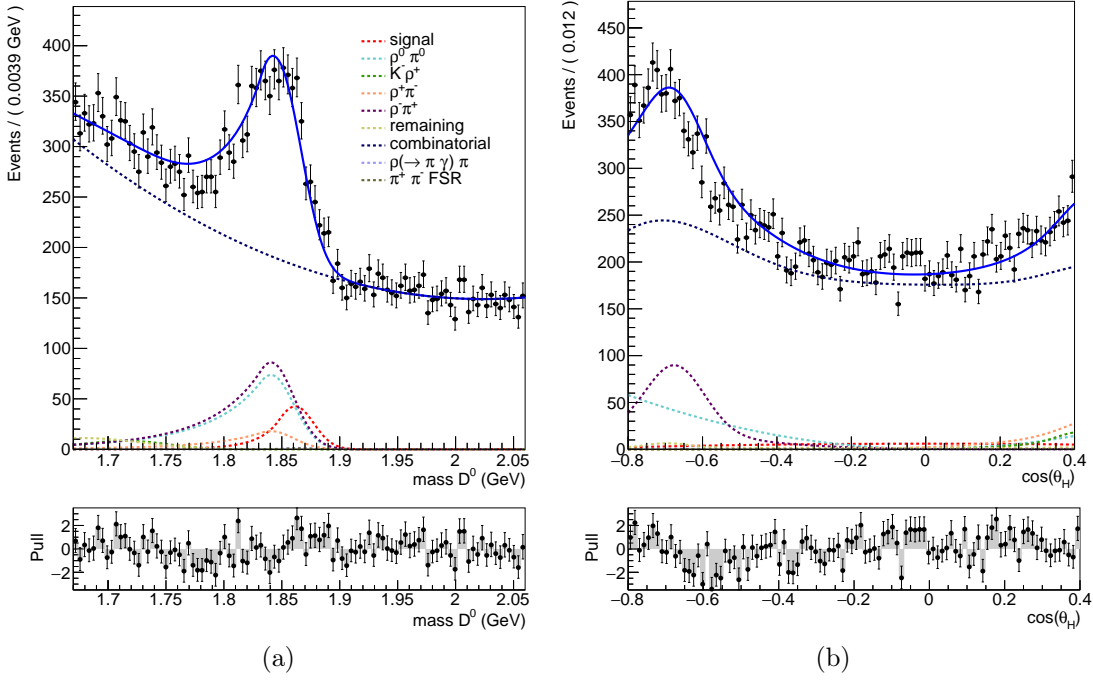

Figure 79: 2-dimensional fit in $m(D^0)$ (a) and $\cos(\theta_H)$ (b) of the ρ^0 mode sample in data in the reduced $\cos(\theta_H)$ range. The χ^2/NDF of the fit is 1.2 for $m(D^0)$ and 1.8 for $\cos(\theta_H)$.
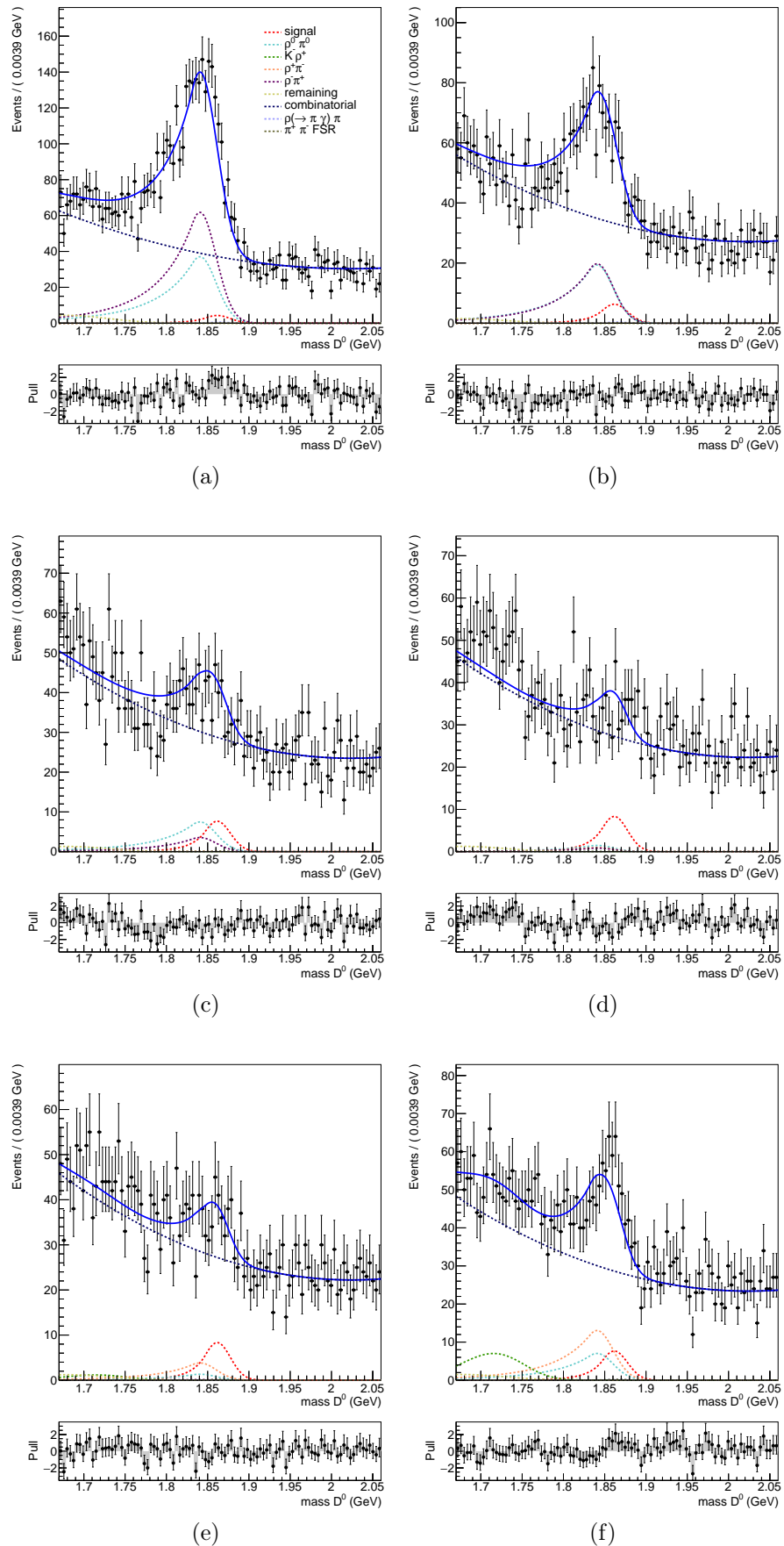
Figure 80: Projections of the fit to $m(D^0)$ in bins of $\cos(\theta_H)$ in data for the ρ^0 mode. The χ^2/NDF of the fits are 1.3, 1.0, 1.2, 1.3, 0.9 and 0.9 for bins 1, 2, 3, 4, 5 and 6, respectively.
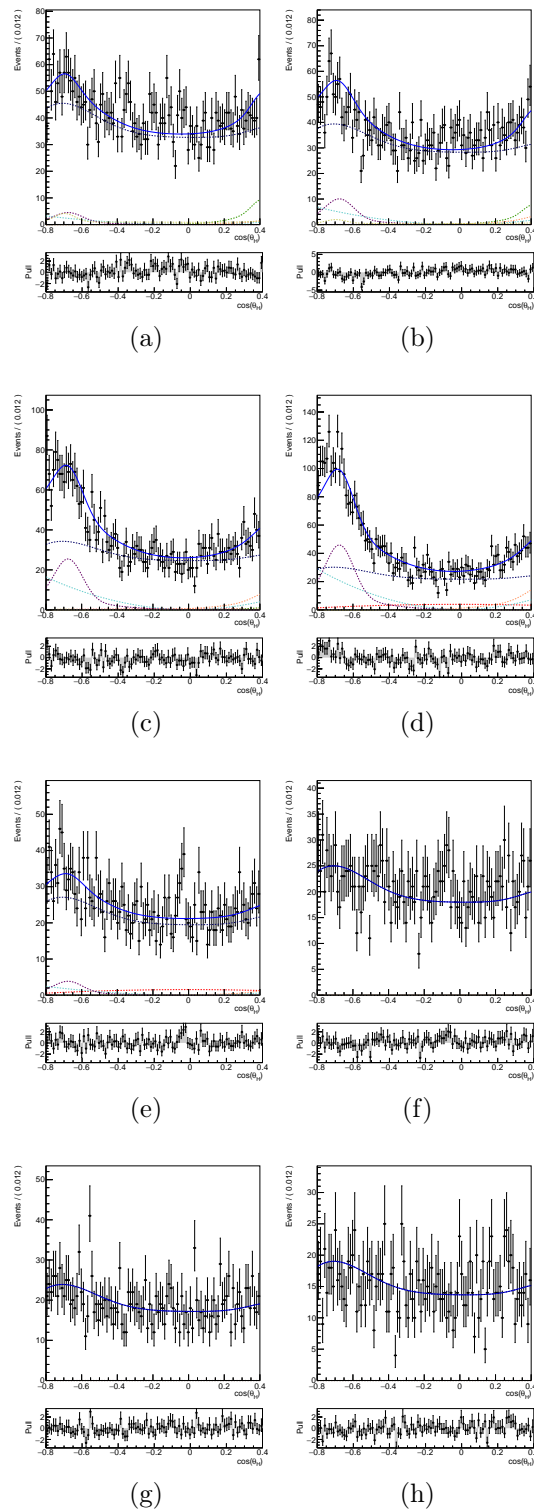
Figure 81: Projections of the fit to $\cos(\theta_H)$ in bins of $m(D^0)$ in data for the ρ^0 mode. The χ^2/NDF of the fits are 1.2, 1.3, 1.2, 1.3, 1.0, 1.0, 1.0 and 1.1 for bins 1, 2, 3, 4, 5, 6, 7 and 8, respectively.
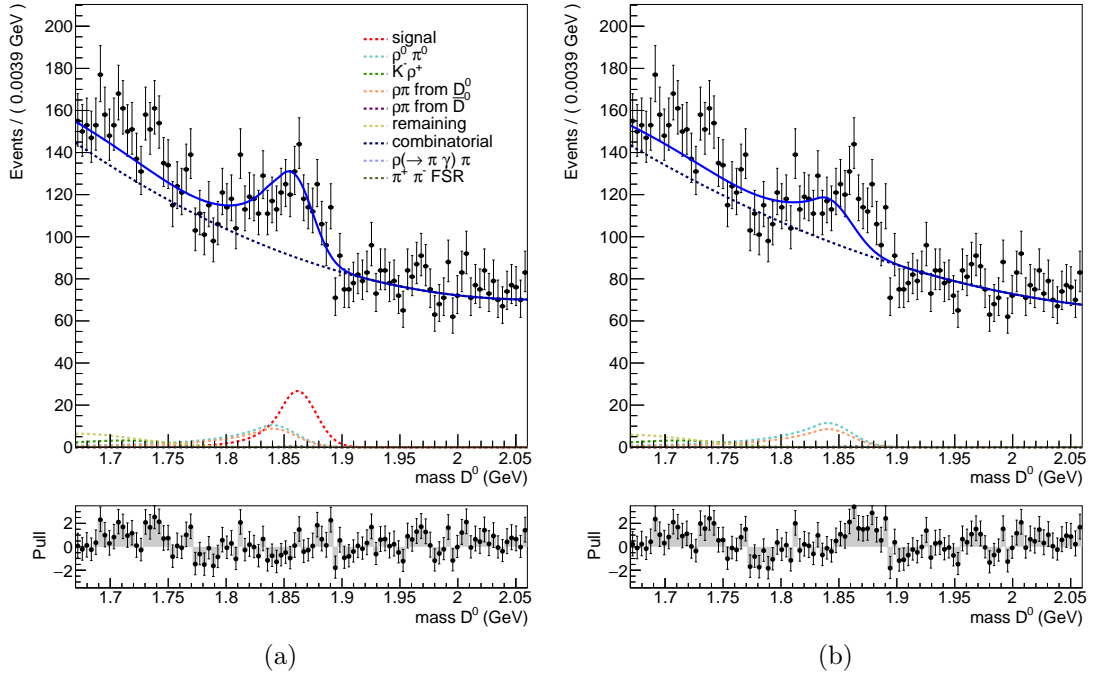
Figure 82: A signal enhanced plot of the $m(D^0)$ distribution of the ρ^0 mode in the window $-0.32 < \cos(\theta_H) < -0.32$, with the signal yield as a free parameter (a) and with the signal yield fixed to zero (b). The χ^2/NDF of the fit with the signal component is 1.2 and the χ^2/NDF of the fit without the signal component is 1.5.

9.4 SIMULTANEOUS FIT

Having tested the performance of the fit on data and taken the necessary measures to resolve or avoid any discrepancies between the simulation and data, we are now confident that the fit performs well and gives reliable results. We thus proceed with the simultaneous fit to obtain the final signal yield and raw asymmetry.

9.4.1 ϕ mode

The results of the 2-dimensional simultaneous fit in data of the ϕ mode are shown in Figure 94. It can be seen that the fit function matches the data points well, as is confirmed by the pull distributions plotted below the fit projections. The extracted signal yield is 524 ± 35 events, which is consistent with the result obtained from the basic 2-dimensional fit. The statistical error on the yield is consistent with the prediction from Monte Carlo, further confirming the stability of the fit in data. The extracted raw asymmetry is -0.0091 ± 0.0066. As the central value is almost 10%, it is visible also from the plots (Figure 94a). The statistical error is slightly larger than that predicted from simulation, which was just below 6%.

The full results of the fit, namely the extracted yield and raw asymmetry for all categories, are listed in Table 35.

Figure 83: Simultaneous 2-dimensional fit in $m(D^0)$ (top) and $\cos(\theta_H)$ (bottom) of the ϕ mode for D^0 (left) and $\overline{D}^0$ (right) in data. The χ^2/NDF of the $m(D^0)$ fit is 0.9 for D^0 and 0.8 for $\overline{D}^0$. The χ^2/NDF of the $\cos(\theta_H)$ fit is 0.8 for D^0 and 1.1 for $\overline{D}^0$.

	yield	A_{raw}
$\phi\gamma$	524 ± 35	-0.091 ± 0.066
$\phi\pi^0$	1923 ± 59	0.035 ± 0.030
"remaining"	241 ± 32	-0.186 ± 0.260
combinatorial	1859 ± 67	0.028 ± 0.033

Table 35: Results of the simultaneous 2-dimensional fit in data of the ϕ mode.

	yield	A_{raw}
$\overline{K}^{*0}\gamma$	9104 ± 396	-0.002 ± 0.020
$\overline{K}^{*0}\pi^0$	$10\,776 \pm 236$	
$K^-\pi^+\pi^0$	9892 ± 645	0.008 ± 0.009
$K^-\rho^+$	8960 ± 177	
$K_0^*(1430)^-\pi^+$	$956^{(*)}$	$0^{(*)}$
$K^{*-}\pi^+$	$248^{(*)}$	$0^{(*)}$
$\overline{K}^{*0}\eta$	2590 ± 120	0.023 ± 0.033
$K^-\pi^+\eta$	667 ± 333	
$K^-\rho^+(\to \pi^+\gamma)$	$62^{(*)}$	$0^{(*)}$
$K^-\pi^+$ FSR	$47^{(*)}$	$0^{(*)}$
"remaining"	$216^{(*)}$	$0^{(*)}$
combinatorial	$14\,514 \pm 555$	-0.008 ± 0.013

Table 36: Results of the simultaneous 2-dimensional fit in data of the $\overline{K}^{*0}$ mode. The superscript $^{(*)}$ denotes the values that are fixed in the fit.

9.4.2 $\overline{K}^{*0}$ mode

The results of the 2-dimensional simultaneous fit in data of the $\overline{K}^{*0}$ mode are shown in Figure 95. It can be seen that the fit function matches the data points well, as is confirmed by the pull distributions plotted below the fit projections. The extracted signal yield is 9104 ± 396 events, which is consistent with the result obtained from the basic 2-dimensional fit. The extracted raw asymmetry is -0.002 $\pm$ 0.020. The statistical error is consistent with the prediction from Monte Carlo.

The full results of the fit, namely the extracted yield and raw asymmetry for all categories, are listed in Table 36. The superscript $^{(*)}$ denotes the values that are fixed. All remaining π^0-type backgrounds have a joint asymmetry parameter, as do all η-type backgrounds. It can be observed that there is no discernible asymmetry in any of the categories.

Figure 84: Simultaneous 2-dimensional fit in $m(D^0)$ (top) and $\cos(\theta_H)$ (bottom) of the $\overline{K}^{*0}$ mode for D^0 (left) and $\overline{D}^0$ (right) in data. The χ^2/NDF of the $m(D^0)$ fit is 1.2 for D^0 and 1.4 for $\overline{D}^0$. The χ^2/NDF of the $\cos(\theta_H)$ fit is 1.4 for D^0 and 1.4 for $\overline{D}^0$.

	yield	A_{raw}
$\rho^0\gamma$	500 ± 85	0.064 ± 0.151
$\rho^0\pi^0$	1488 ± 247	0.082 ± 0.163
$\rho^+\pi^-$	1686 ± 187	-0.306 ± 0.181
$\rho^-\pi^+$	356 ± 64	0.028 ± 0.113
$K^-\rho^+$	174 ± 45	-0.123 ± 0.245
$\rho(\to \pi\gamma)\pi$	$19^{(*)}$	$0^{(*)}$
$\pi^+\pi^-$ FSR	$14^{(*)}$	$0^{(*)}$
"remaining"	209 ± 156	-0.433 ± 0.525
combinatorial	$19\,675 \pm 255$	-0.002 ± 0.010

Table 37: Results of the simultaneous 2-dimensional fit in data of the ρ^0 mode. The superscript $^{(*)}$ denotes the values that are fixed in the fit.

9.4.3 ρ^0 mode

The results of the 2-dimensional simultaneous fit in data of the ρ^0 mode are shown in Figure 96. It can be seen that the fit function matches the data points well, as is confirmed by the pull distributions plotted below the fit projections. The extracted signal yield is 500 ± 85 events, which is consistent with the result obtained from the basic 2-dimensional fit. The extracted raw asymmetry is 0.064 ± 0.151. The statistical error is greater than the Monte Carlo prediction, but it has to be kept in mind that the $\cos(\theta_H)$ range in data was subseqently reduced, thus reducing the absolute number of signal events.

The full results of the fit, namely the extracted yield and raw asymmetry for all categories, are listed in Table 37. The superscript $^{(*)}$ denotes the values that are fixed.
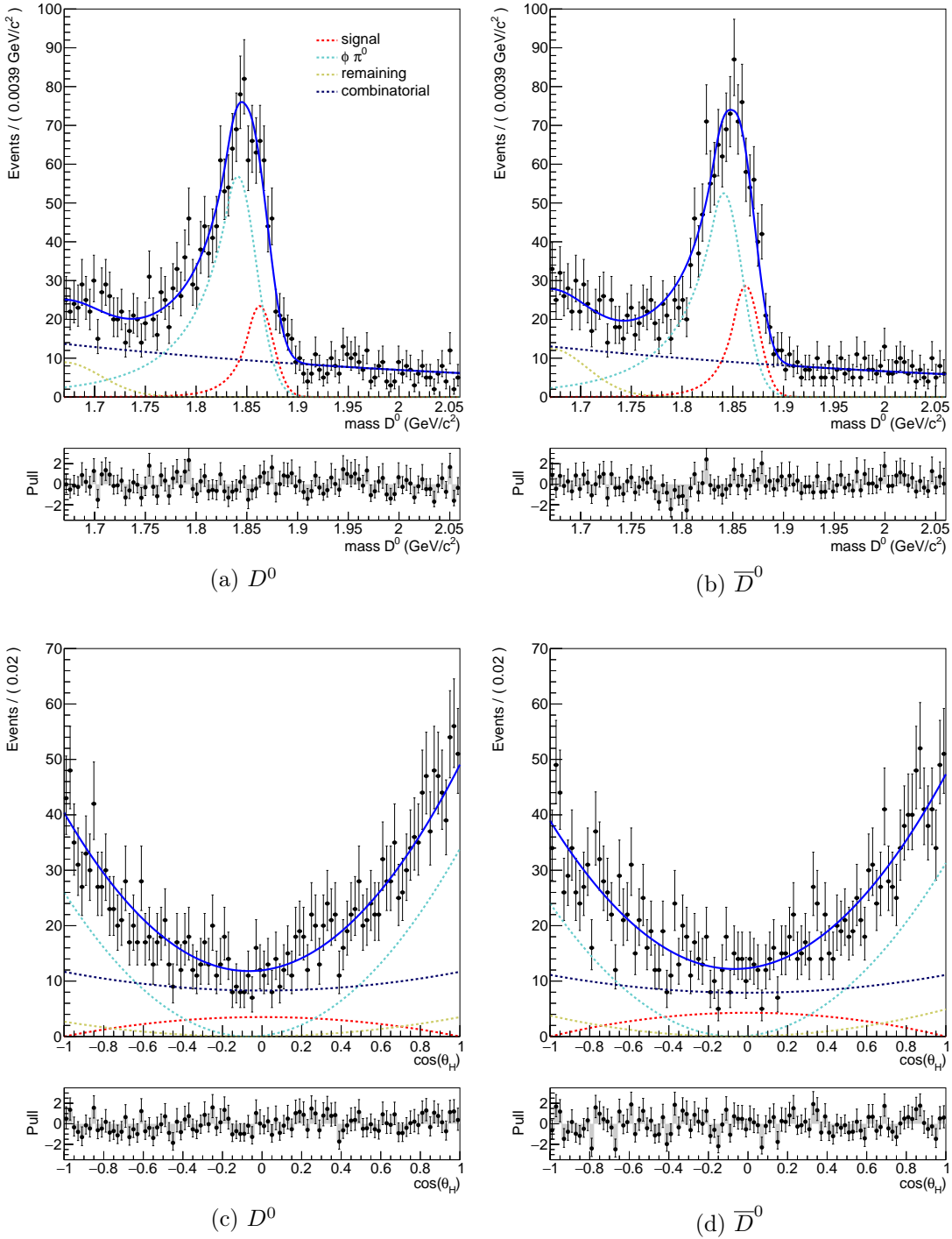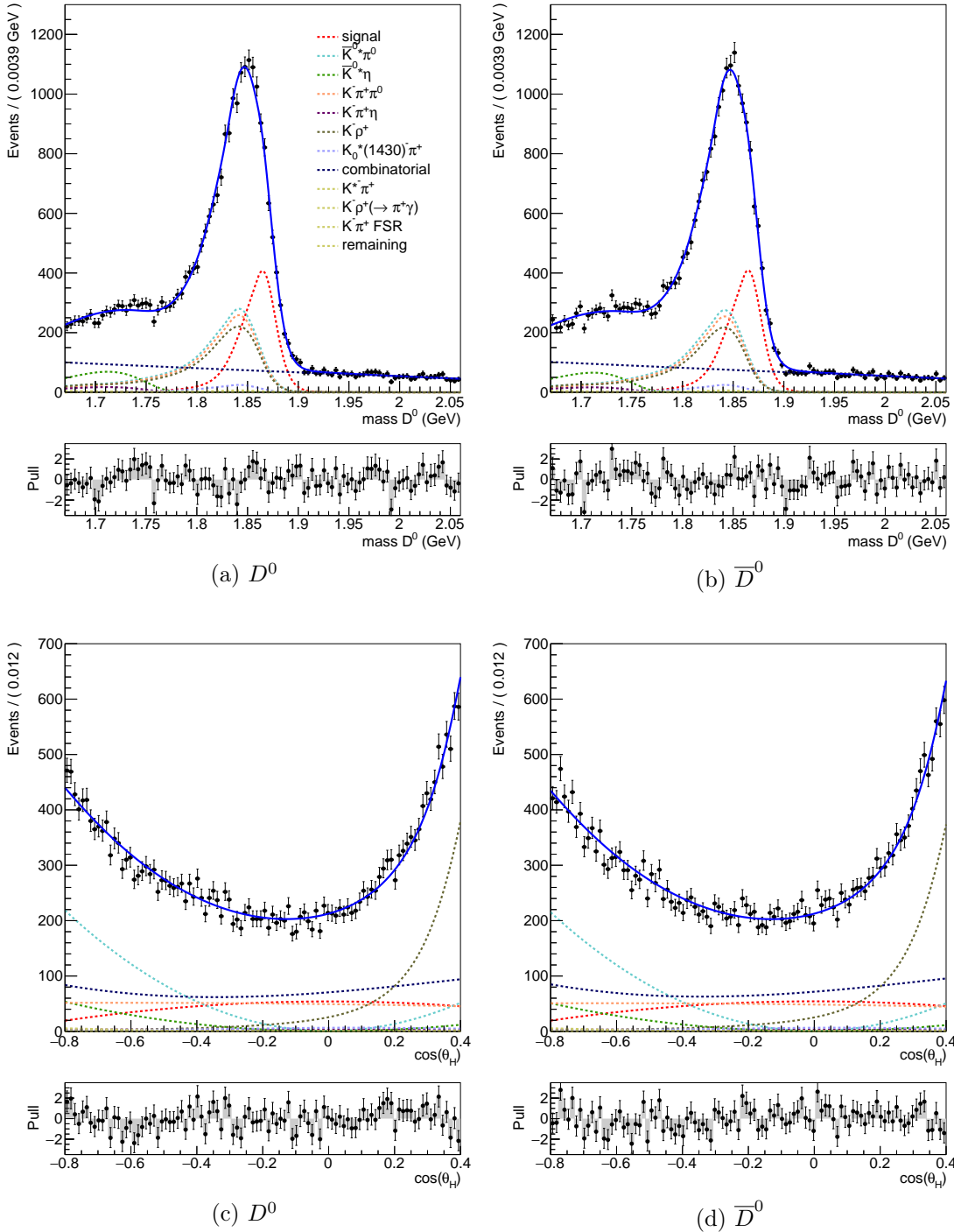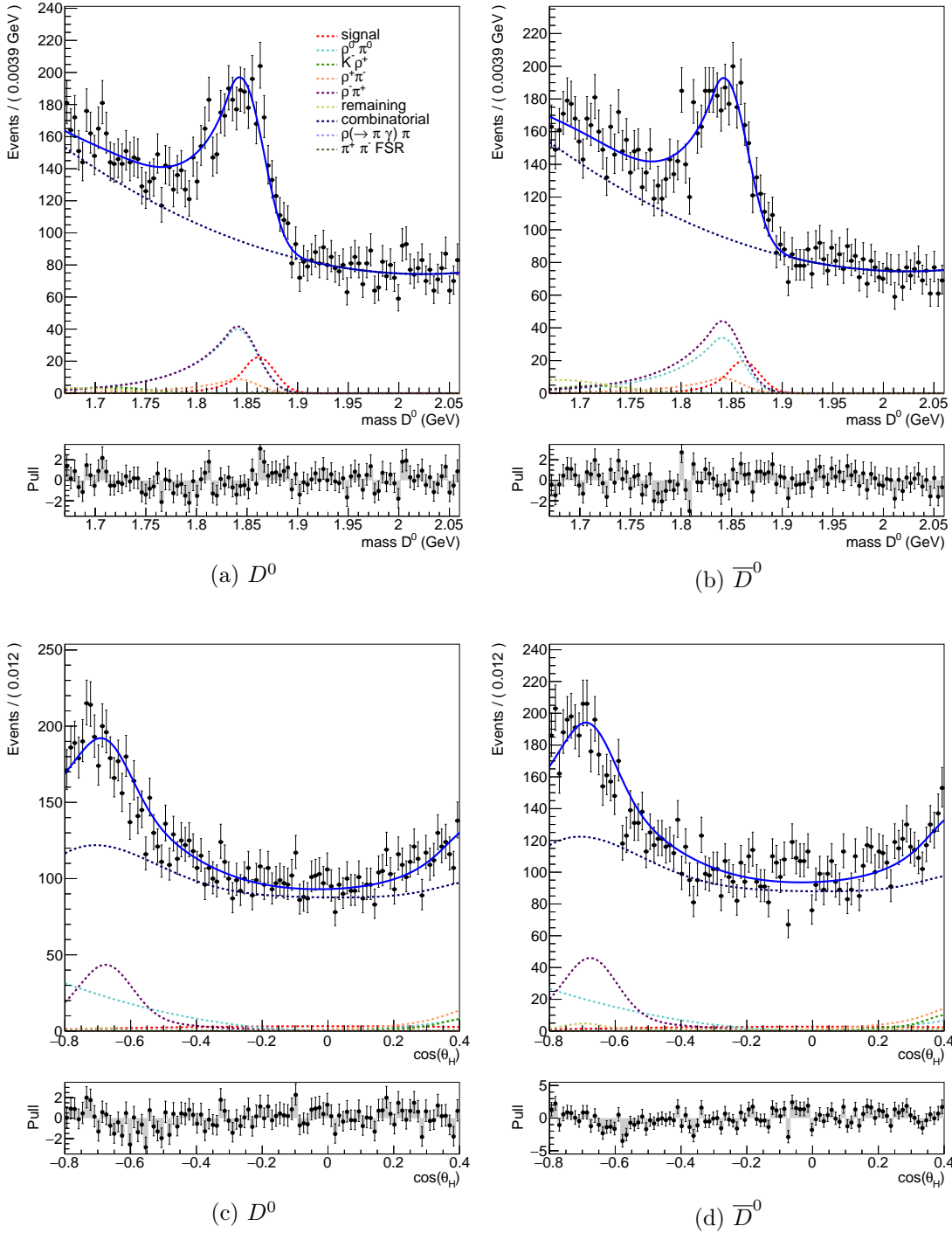
Figure 85: Simultaneous 2-dimensional fit in $m(D^0)$ (top) and $\cos(\theta_H)$ (bottom) of the ρ^0 mode for D^0 (left) and $\overline{D}^0$ (right) in data. The χ^2/NDF of the $m(D^0)$ fit is 1.2 for D^0 and 1.2 for $\overline{D}^0$. The χ^2/NDF of the $\cos(\theta_H)$ fit is 1.2 for D^0 and 1.8 for $\overline{D}^0$.

9.5 CROSS-CHECK FOR THE ω COMPONENT

As discussed in Chapter 5, it is possible that the $D^0 \to \pi^+\pi^-\gamma$ sample contains also a component that decays through the ω resonance, beside the ρ^0 resonance. The ω contribution is expected to be negligible, as the branching fraction for the decay $\rho^0 \to \pi^+\pi^-$ is two order of magnitudes larger than the branching fraction for the decay $\omega \to \pi^+\pi^-$. For the ω decay to constitute a significant contribution, the branching fraction for $D^0 \to \omega\gamma$ would have to be much larger than the branching fraction for $D^0 \to \rho^0\gamma$, which is in contrast with theoretical predictions. A search for an ω component in the $D^0 \to \pi^+\pi^-\gamma$ sample is nevertheless conducted, to verify the assumption that the only relevant component is the decay through the ρ^0 resonance.

As the ρ^0 resonance is much wider than the ω, the signal window in $m(V)$ was chosen accordingly to the width of the ρ^0 resonance. We now perform the 2-dimensional fit in a tighter window around the nominal mass of the ω resonance. The chosen window is ± 2 times the width of the ω. In this window and with all other selection criteria applied, the efficiency of the solely ρ^0 mode is 1.3%. The fit returns a signal yield of 80 ± 29 events. The ratio between the yield and the efficiency, $N_{\mathrm{sig}}/\varepsilon_{\mathrm{sig}}$, is compared for the nominal fit and for the fit in the reduced $m(V)$ range, for the assumption of only the ρ^0 component being present. A significant ω component would cause the ratio to increase in the reduced $m(V)$ window. However, the ratios from the two cases are consistent with each other within the margin of errors. We conclude that no discernible ω component is identified in the $D^0 \to \pi^+\pi^-\gamma$ sample at the present precision level.

9.5.1 *Reconstruction of the $m(\pi^+\pi^-)$ Distribution with ${}_s\mathcal{P}lot$*

An additional test that can be performed is reconstructing the $m(\pi^+\pi^-)$ signal distribution using the ${}_s\mathcal{P}lot$ technique, which is described in detail in Reference [39]. Given a data sample, populated with events belonging to several categories, and knowing the distribution in a set of variables (called discriminating variables) for each category, this statistical technique reconstructs the distribution of an unknown variable (called control variable) for a given category. In our specific case, we reconstruct the background-subtracted $m(\pi^+\pi^-)$ distribution of signal events from the known $m(D^0)$ and $\cos(\theta_H)$ distributions for all categories, signal and background.

First, the 2-dimensional fit is performed and yields are extracted for all categories. For each event of the category n, a weight ${}_s\mathcal{P}$ for each event e can be calculated as

$$
{}_s\mathcal{P}_n(y_e) = \frac{\Sigma_{j=1}^{N_s} \mathrm{V}_{nj} f_j(y_e)}{\Sigma_{k=1}^{N_s} N_k f_k(y_e)} \quad , \tag{55}
$$

where N_s is the total number of categories, N_k is the yield of the kth category, $f_{j(k)}(y_e)$ the value of the PDF of the jth(kth) category in the set of discriminating variables y for the specific event e, and V_{nj} is the covariance matrix. Using this weight, the distribution $\tilde{M}_n$ of the control variable x can be obtained as

$$
N_n \tilde{M}_n(\bar{x})\delta x = \sum_{e \epsilon \delta x} {}_s\mathcal{P}_n(y_e) \quad . \tag{56}
$$
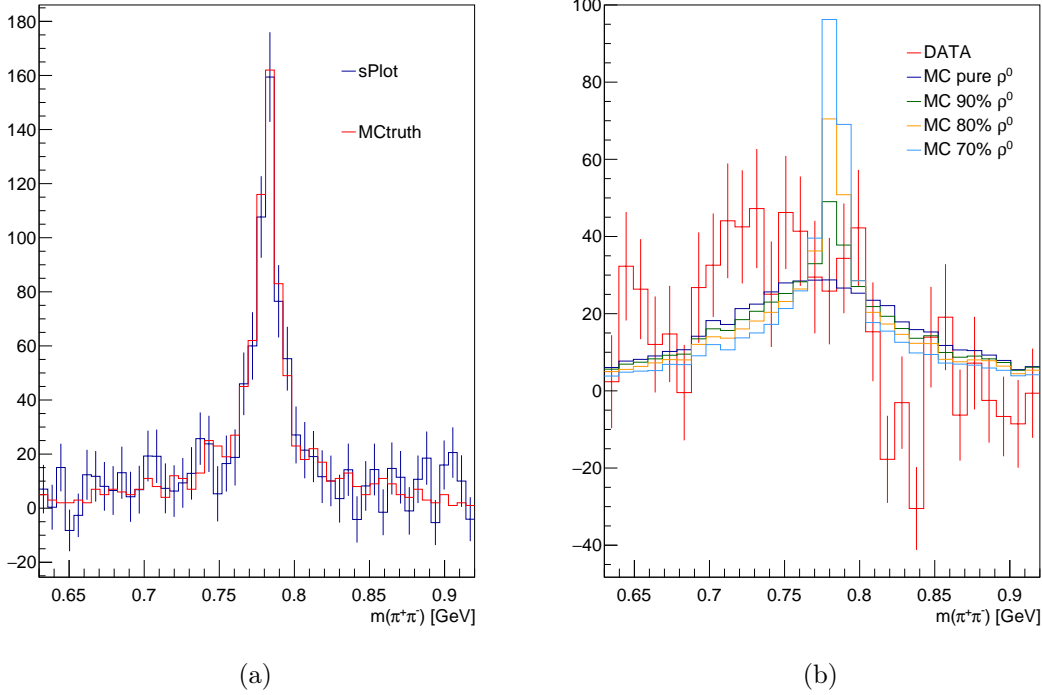
Figure 86: The left plot shows the distribution of $m(\pi^+\pi^-)$ on Monte Carlo, superimposed with the $m(\pi^+\pi^-)$ distribution, obtained with $_s\mathcal{P}lot$. The right plot shows the distribution of $m(\pi^+\pi^-)$ on data, obtained with $_s\mathcal{P}lot$. Superimposed are the $m(\pi^+\pi^-)$ distributions, obtained from Monte Carlo simulations with different admixtures of the ρ^0 and ω components.

On average, this reproduces the true distribution $M_n(x)$:

$$\left\langle N_n \tilde{M}_n(\bar{x}) \right\rangle = N_n M_n(x) \quad . \tag{57}$$

The procedure is first tested on the Monte Carlo simulation. Figure 86a shows the plot of the $m(\pi^+\pi^-)$ distribution, obtained from a signal Monte Carlo simulation, that comprises in equal measure the ρ^0 and ω components, and the $m(\pi^+\pi^-)$ distribution, obtained with the $_s\mathcal{P}lot$ technique. The narrow ω peak and the broad ρ^0 distribution can be clearly distinguished. The distributions from Monte Carlo and $_s\mathcal{P}lot$ show very good agreement, confirming that the $_s\mathcal{P}lot$ technique performs well.

The procedure is then repeated on data. A plot of the $m(\pi^+\pi^-)$ distribution in data, obtained with $_s\mathcal{P}lot$, is shown in Figure 86b. Superimposed are the Monte Carlo distributions for various subsets, composed of different admixtures of the ρ^0 and ω resonances: a pure ρ^0 sample, and samples composed of 90/80/70% ρ^0 and 10/20/30% ω. While the statistics is low, it can be observed that no narrow peak that would belong to the ω resonance seems to be present.

Based on both cross-checks, it is concluded that at the present precision level, no discernible presence of the ω resonance is detected. The $D^0 \to \pi^+\pi^-\gamma$ decay is further considered to arise solely from the ρ^0 resonance.
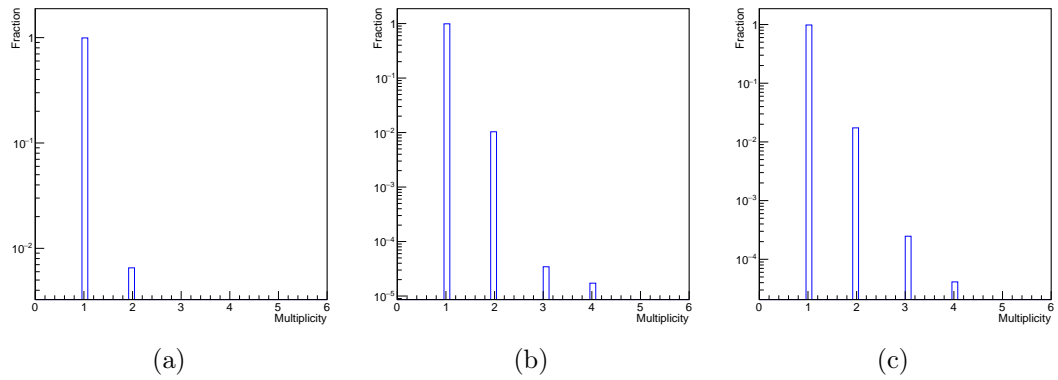
Figure 87: Multiplicity on data for the ϕ (a), $\overline{K}^{*0}$ (b) and ρ^0 (c) mode in the logarithmic scale for the y-axis.

9.6 MULTIPLE CANDIDATES

It was verified on Monte Carlo simulation that double counting does not occur in the analysis. However, the simulation might not represent data perfectly, therefore an additional check is performed on data. The results are presented in Figure 87 for all three signal modes. It can be seen that multiple candidates are present in only a few percent of the cases, and it is confirmed that in all such cases, the D^0 mesons do not come from the same D^{*+} mother. Comparing the results to plots in Figure 26, it can be seen that the generic Monte Carlo simulation describes data well. It is concluded that no double counting occurs during our analysis.

CALCULATION OF $\mathcal{B}R$ AND $\mathcal{A}_{CP}$ ON DATA

Having obtained all necessary values, we can now proceed to calculating the branching fractions and CP asymmetries. The method has already been described in detail in Chapter 5. The branching fraction is calculated from the signal yield and efficiency for the signal and normalisation mode, the branching fraction of the normalisation mode and the branching fraction of the decay of the vector meson into the used final state:

$$\mathcal{B}r(D^0 \to V\gamma) = \frac{\mathcal{B}r(D^0 \to f_1 f_2)}{\mathcal{B}r(V \to f_1 f_2)} \cdot \frac{N_{\text{sig}}}{N_{\text{norm}}} \cdot \frac{\varepsilon_{\text{norm}}}{\varepsilon_{\text{sig}}} \quad . \tag{58}$$

All values that are used for the branching fraction calculations are listed in Table 38. The values of the branching fractions of the normalisation modes and of the vector meson decays are taken from the Particle Data Group [23]. We obtain the following values for the branching fractions of the signal decays:

$$\mathcal{B}r(D^0 \to \phi\gamma) = (2.76 \pm 0.19) \cdot 10^{-5} \quad ,$$
$$\mathcal{B}r(D^0 \to \overline{K}^{*0}\gamma) = (4.66 \pm 0.21) \cdot 10^{-4} \quad ,$$
$$\mathcal{B}r(D^0 \to \rho^0\gamma) = (1.77 \pm 0.30) \cdot 10^{-5} \quad ,$$

where the errors are statistical only. The errors include the statistical error of the signal yield and the statistical error of the yield of the normalisation mode, as well as the statistical error of the efficiencies for both modes. The error of the normalisation modes takes into account the statistical errors of the counted number of events in the signal window and sidebands, as well as the statistical error on the fraction f that is used in the calculation of the yield (see Table 30).

	ϕ	$\overline{K}^{*0}$	ρ^0
signal yield	524 ± 35	9140 ± 396	500 ± 85
yield of normalisation channel	$362\,274 \pm 632$	$4\,018\,940 \pm 2013$	$127\,077 \pm 389$
signal efficiency	9.7%	7.8%	6.8%
efficiency of normalisation channel	22.7%	27.0%	21.4%
$\mathcal{B}r$ of normalisation channel	$(4.01 \pm 0.07)\cdot 10^{-3}$	$(3.93 \pm 0.04)\%$	$(1.42 \pm 0.03)\cdot 10^{-3}$
$\mathcal{B}r$ of vector meson decay	0.489 ± 0.005	0.66 ± 0.00	1.0 ± 0.0

Table 38: All values used in the branching fraction calculations for all three signal modes.

	ϕ	$\overline{K}^{*0}$	ρ^0
signal A_{raw}	-0.0905 ± 0.0657	-0.0018 ± 0.0200	0.0642 ± 0.1515
A_{raw} of normalisation channel	0.0022 ± 0.0017	0.0013 ± 0.0005	0.0082 ± 0.0030
$\mathcal{A}_{CP}$ of normalisation channel	-0.0016 ± 0.0012	0.0	0.0005 ± 0.0015

Table 39: All values used in the $\mathcal{A}_{CP}$ calculations for all three signal modes.

The CP asymmetry is calculated from the raw asymmetries of the signal and normalisation modes and the nominal value of the CP asymmetry of the normalisation modes:

$$\mathcal{A}_{CP}^{\text{sig}} = (A_{\text{raw}}^{\text{sig}} - A_{\text{raw}}^{\text{norm}}) + \mathcal{A}_{CP}^{\text{norm}} \quad .$$

All values that are used in the calculation are listed in Table 39. The values of the CP asymmetries of the normalisation modes are taken from the Heavy Flavor Averaging Group [13]. We obtain the following values for the CP asymmetries of the signal decays:

$$\mathcal{A}_{CP}(D^0 \to \phi\gamma) = -(0.094 \pm 0.066) \quad ,$$
$$\mathcal{A}_{CP}(D^0 \to \overline{K}^{*0}\gamma) = -(0.003 \pm 0.020) \quad ,$$
$$\mathcal{A}_{CP}(D^0 \to \rho^0\gamma) = 0.056 \pm 0.152 \quad ,$$

where the errors are statistical only. The errors include the statistical error of the raw asymmetries of the signal and normalisation modes.

11

SYSTEMATIC UNCERTAINTIES

There are two main sources from which systematic uncertainties arise. One are the differences between the Monte Carlo simulation and real data in terms of reconstruction efficiencies. Since we are not performing an absolute measurement, but instead a relative calculation using normalisation channels for both the branching fraction and the CP asymmetry, many systematic uncertainties due to reconstruction efficiencies, such as tracking and particle identification, can cancel out. This happens if it holds that the ratio of efficiencies between the signal and normalisation channel is the same for Monte Carlo and data, even if the efficiencies for Monte Carlo and data separately are not equal:

$$\Big(\frac{\varepsilon_{\mathrm{sig}}^x}{\varepsilon_{\mathrm{norm}}^x}\Big)_{\mathrm{MC}} = \Big(\frac{\varepsilon_{\mathrm{sig}}^x}{\varepsilon_{\mathrm{norm}}^x}\Big)_{\mathrm{data}} \quad . \tag{59}$$

This is in turn true if ε^x is not a function of x. For variables for which this is known to be true, like charged particle identification, no systematic error needs to be assigned. For variables used in the reconstruction for which it is unclear whether Equation 59 holds, this must be first investigated. Subsequently, a decision is made whether no systematic uncertainty ensues or one needs to be assigned.

Another group of systematic uncertainties arises from the specific analysis, i.e. the method of signal extraction. For the signal channel, these are various attributes of the PDFs used in the fitting procedure, mainly the width and mean, determined on Monte Carlo, that could be slightly different on data. The same possibility is present for the normalisation modes, along with systematic uncertainties due to the specific choice of sidebands and signal window. As for the calculation of $\mathcal{A}_{CP}$, it was already proven in Sections 6.6.3 and 7 that the systematic uncertainty arising from random slow pions is negligible for both the signal and normalisation modes.

Finally, a systematic uncertainty must be attributed to the uncertainty belonging to the external values of the branching fractions and CP asymmetries of any other modes that are used to calculate the final results of the signal modes.

The systematic uncertainties belonging to each group are discussed in detail below. Finally, all systematic uncertainties for all three signal channels are summarised in Tables 47 and 48. For the branching fraction, the systematic uncertainty is reported as the relative error in percentage, whereas for the CP asymmetry, the absolute value is stated.

11.1   SYSTEMATICS DUE TO RECONSTRUCTION EFFICIENCIES

We investigate first the systematic uncertainties related to reconstruction efficiencies. All variables on which a constraint is imposed for the purpose of pre-selection and selection criteria, are a possible source of a systematic error, if the distributions on Monte Carlo and data do not match. All variables featuring in the selection criteria that are connected to the photon are not present in the analysis of the normalisation modes, thus any related systematic uncertainties will not subtract and must be evaluated. Some variables as particle identification for charged particles and vertex fit can be immediately excluded from this investigation, as it has been shown in previous analyses that they do not contribute a significant systematic uncertainty. For other variables, we examine possible systematic uncertainties in the following subchapters.

All systematic uncertainties arising from reconstruction efficiencies are applicable only to the branching fraction. For the raw asymmetry, calculated as in Equation 33, the uncertainties affect both the D^0s and $\overline{D}^0$s and subtract in the calculation of A_{raw}. All systematic uncertainties from sources that are listed below are summarised in Table 40.

11.1.1   *Photon Reconstruction Efficiency*

The uncertainty of the photon reconstruction efficiency is 2.2% [40]. It was estimated on a radiative Bhabha sample, by comparison between Monte Carlo and data.

11.1.2 π^0 *Veto*

The efficiency of the cut on $C(\pi^0)$ for Monte Carlo and data has been examined in Section 4.8. It is clear from the result in Equation 28 that the efficiency of the veto is expected to be the same for Monte Carlo and data, meaning that the full reconstruction efficiencies of the signal modes, obtained from the simulation, should be valid for application on data with regard to this variable within the precision given by Equation 28. The error on the double ratio in Equation 28 thus directly represents the relative systematic uncertainty related to the π^0 veto.

11.1.3 $p_{\mathrm{CMS}}(D^{*+})$

The cut on the CMS momentum of the D^{*+} meson is applied to both the signal and normalisation mode, thus any related systematic uncertainty should cancel, provided that the distributions of $p_{\mathrm{CMS}}(D^{*+})$ for signal and normalisation modes match. Figure 88 shows the $p_{\mathrm{CMS}}(D^{*+})$ distributions for both the signal and normalisation mode, using the respective signal Monte Carlo simulations, for all three signal channels. The χ^2 of the difference of the histogrammed distributions at the statistics, corresponding to the expected signal yield, is 1.0, 1.4 and 0.8 for the ϕ, $\overline{K}^{*0}$ and ρ^0 mode, respectively. It is concluded that systematic uncertainties due to the $p_{\mathrm{CMS}}(D^{*+})$

(a) ϕ channel   (b) $\overline{K}^{*0}$ channel   (c) ρ^0 channel
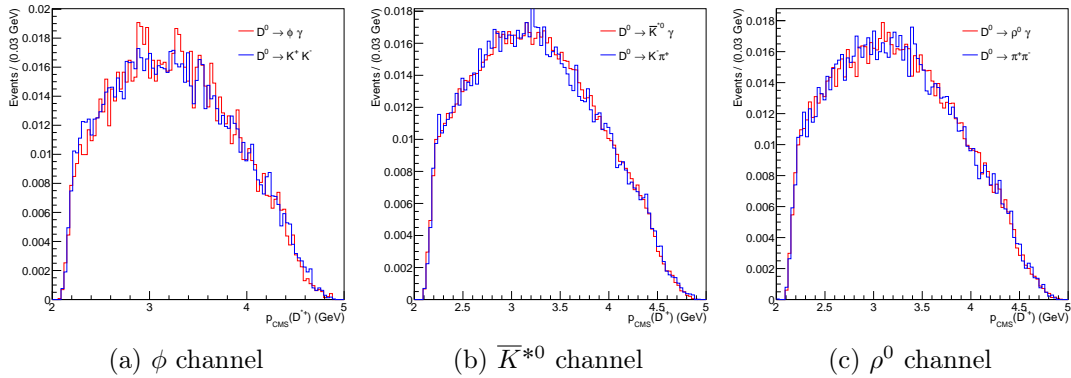
Figure 88: Comparison of the $p_{\text{CMS}}(D^{*+})$ distribution of the signal and normalisation mode for the ϕ (a), $\overline{K}^{*0}$ (b) and ρ^0 channel (c) on respective signal Monte Carlo simulations.

constraint can be expected to cancel between the signal and normalisation modes, thus no remaining systematic uncertainty needs to be assigned.

11.1.4 *Total Energy Released in the Decay q*

The constraint on q is imposed on both the signal and normalisation channels, and any ensuing systematic uncertainties could therefore be subtracted in a relative measurement of the branching fraction, analogously to the $p_{\text{CMS}}(D^{*+})$ criterion. However, the resolution of the mass distributions, and henceforth of the q distribution, is sensitive to the presence of the photon in the final state. The relevant plots are shown in Figure 89, where the Δm distributions of the signal and normalisation modes on the respective signal Monte Carlo simulations are plotted. It is clearly visible that the resolution on the normalisation channels is significantly better than that of the signal distributions. It follows that the systematic uncertainty will not cancel between the signal and normalisation modes and must therefore be estimated separately. We employ the same method as was used to determine the uncertainty of the $C(\pi^0)$ requirement.

The chosen control channel is $D^0 \to \overline{K}^{*0}\pi^0$, which has sufficient statistics, low background level and photons in the final state. We impose a constraint on $p_{\text{CMS}}(D^{*+})$ and define a signal window in $m(D^0)$ and $m(V)$, requiring 1.75 GeV $< m(D^0) < 2.0$ GeV and 0.8 GeV $< m(V) < 1.0$ GeV. The signal yield is extracted via a fit in the $m(D^0)$ distribution for the sample with the nominal q constraint ($q < 0.6$ MeV) and for a sample with a very loose constraint of $q < 2.3$ MeV. The loose constraint is imposed instead of no requirement on q, as no constraint at all on q leaves certain peaking backgrounds. These backgrounds are eliminated with the loose constraint, which still passes over 99% of signal, and is as such valid as an estimate of signal yield with no q requirement. The non-resonant decays to $K^-\pi^+\pi^0$ are allowed to be absorbed in the signal component. To take into account a possible difference in the signal shape between Monte Carlo and data, the signal PDF, determined on simulation, is allowed to have a free offset and width scaling factor, analogously to
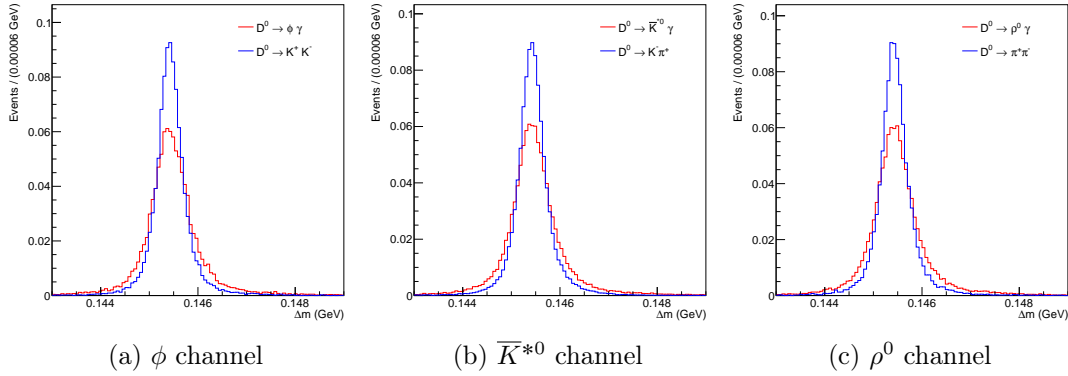
(a) ϕ channel   (b) $\overline{K}^{*0}$ channel   (c) ρ^0 channel

Figure 89: Comparison of the Δm distribution of the signal and normalisation mode for the ϕ (a), $\overline{K}^{*0}$ (b) and ρ^0 channel (c) on respective signal Monte Carlo simulations.

the $\overline{K}^{*0}$ signal PDF in $m(D^0)$ (see Section 6.5.4). It is verified that the full fit on Monte Carlo returns the values of the offset zero and a width scaling factor of 1, within the respective error margins. On data, the offset is negligible, but the width increases for about 6%, which is plausible. Taking the obtained signal yield from the sample with the nominal q requirement and the sample with the loose q requirement, we first calculate the ratio between the two for Monte Carlo and data separately. Then, the double ratio is calculated as

$$\frac{R(\text{MC})}{R(\text{DATA})} = 1.0100 \pm 0.0016 \quad . \tag{60}$$

Since the obtained value is not large, we do not correct the central value of the efficiency, but instead assign a whole systematic uncertainty of 1.16%.

11.1.5 E_9/E_{25}

The systematics due to E_9/E_{25} cannot be determined using the same method of the double ratio calculation as for $C(\pi^0)$ and q, since no suitable control channel with a single photon in the final state is available. Looking at Table 6, it can be seen that the requirement on E_9/E_{25} contributes an additional 10-20% suppression of background (with all other selection criteria applied). The efficiency of the E_9/E_{25} cut is lowest in the $\overline{K}^{*0}$ channel, meaning that by omitting the requirement on E_9/E_{25}, the increase in background will be least impactful. Taking into account also the fact that the $\overline{K}^{*0}$ channel has the largest statistics, we decide to estimate the systematic uncertainty due to the requirement on E_9/E_{25} by repeating the fit of the $\overline{K}^{*0}$ channel without any constraint imposed on said variable. A roughly 10% increase in background is manageable in terms of background fitting and power of signal recognition. The 1-dimensional PDFs of all categories are thus determined for Monte Carlo samples with no constraint imposed on E_9/E_{25}, and used for the final fit in data. The quantity in the branching fraction calculation that changes due to this variation is the fraction of the signal yield over the respective efficiency, $N_{\text{sig}}/\varepsilon$.

The difference between the central value of this quantity, as returned by this fit and the nominal fit, is taken as the systematic error. The obtained uncertainty is 0.23%.

11.1.6 $E(\gamma)$

A difference between the distributions of the energy of the photon on Monte Carlo and data can arise, if the photon energy is a function of the CMS momentum of the D mesons. Momentum distributions are sometimes not completely accurate in the Belle Monte Carlo simulation, with the simulation distributions typically being softer than those of data. Since a constraint on the momentum is imposed, this would influence the efficiency of the cut on $E(\gamma)$, which would in turn differ on Monte Carlo and data. We therefore examine $E(\gamma)$ distributions in different bins of $p_{\text{CMS}}(D^{*+})$. The $p_{\text{CMS}}(D^{*+})$ range from 2.5 to 4.5 GeV is divided into 4 equal bins of 0.5 GeV each and in each bin the $E(\gamma)$ distribution is plotted for both signal, using the signal Monte Carlo, and for all background categories of the π^0 and η type, using generic Monte Carlo. The results are presented in Figure 90. It can be observed that the distribution of $E(\gamma)$ indeed changes as a function of $p_{\text{CMS}}(D^{*+})$. It is plausible to expect that the efficiency of the $E(\gamma)$ constraint will differ between Monte Carlo and data, and a systematic uncertainty must thus be assigned.

An examination of the signal and background rejection values in Table 6 reveals that the efficiency of the $E(\gamma)$ requirement is similar to that of E_9/E_{25}. It is therefore decided to employ the same method for estimating the systematic uncertainty as for E_9/E_{25}. The $\overline{K}^{*0}$ mode is fitted without any constraint imposed on $E(\gamma)$, and the corresponding yield and efficiency are determined. The difference between the central value of the so obtained ratio $N_{\text{sig}}/\varepsilon$, and the value obtained from the nominal fit, is taken as the systematic error. The obtained uncertainty is 1.15%.

11.1.7 *Mass of the Vector Meson $m(V)$*

A systematic uncertainty due to a difference in the efficiency of the constraint on the mass of the vector meson can arise, if the central value or the width of the distribution differ between data and Monte Carlo. To assess a possible difference in these values, we take into account the uncertainties of the nominal mass and width of the vector mesons [23], and a possible difference between these values and the values that are used to generate the Belle Monte Carlo simulation.

The mass distribution of the resonances can be modelled with a relativistic Breit-Wigner function. We calculate the integral of the function in the signal window for the nominal value of the central value and width, and the function, shifted by the maximal error on each of the parameters. In each case, the error is taken to be the uncertainty on the world-average value or the difference between the world-average value and the Belle Monte Carlo value, depending on which is larger. The systematic uncertainty is determined from the ratio of the two integrals. The obtained uncertainties are 0.1% for the ϕ mode, 1.7% for the $\overline{K}^{*0}$ mode and 0.2% for the ρ^0 mode.

(a)   (b)

(c)   (d)
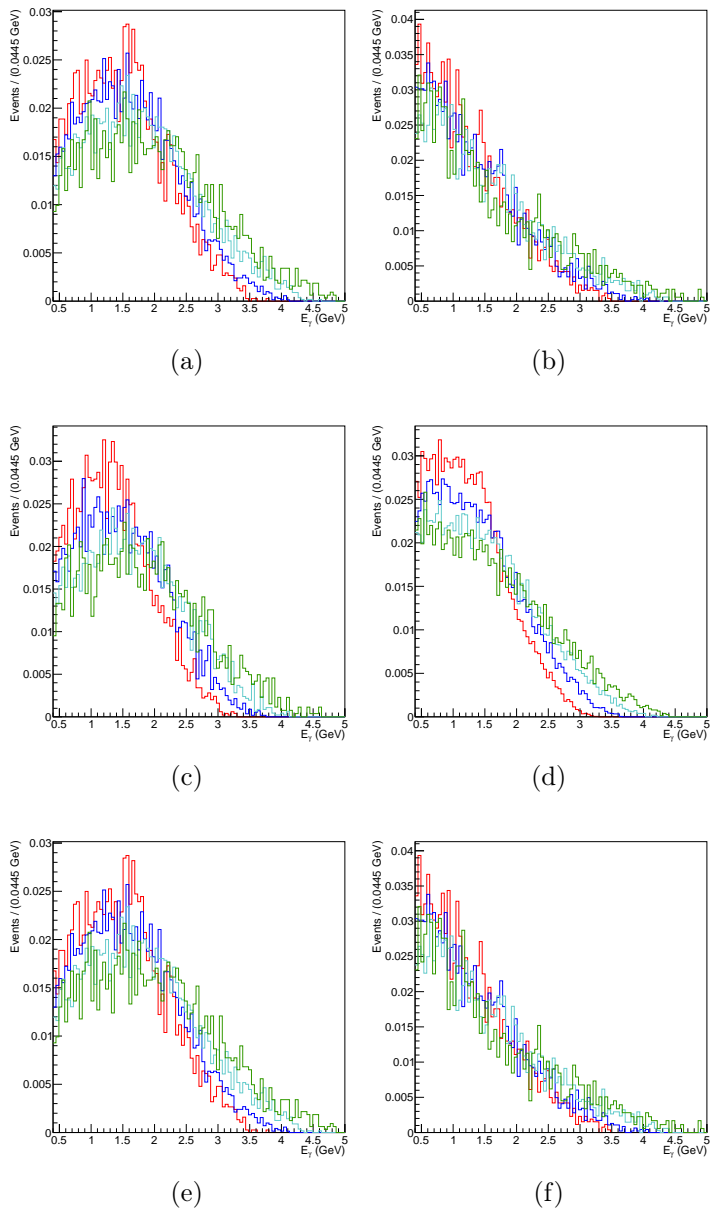
(e)   (f)

Figure 90: Distributions of $E(\gamma)$ in bins of $p_{\mathrm{CMS}}(D^{*+})$ for signal (left) and π^0 and η-type backgrounds (right) of the ϕ (top), $\overline{K}^{*0}$ (middle) and ρ^0 (bottom) modes.

	$\mathcal{B}r[\%]$
γ reconstruction efficiency	2.2
π^0 veto	0.4
q	1.2
E_9/E_{25}	0.2
$E(\gamma)$	1.2
$m(\phi)$	0.1
$m(\overline{K}^{*0})$	1.7
$m(\rho^0)$	0.2

Table 40: Relative systematic uncertainties due to reconstruction efficiencies.

11.2 SYSTEMATICS DUE TO SIGNAL EXTRACTION PROCEDURE

There are various parameters in the fitting procedure that are fixed to values, determined on Monte Carlo simulation. A systematic uncertainty must be assigned whenever it is plausible to expect that the corresponding values on data might differ. As stated on various previous occasions, the fitting procedure is developed so that in many cases parameters are left to float in the fit in data, to reduce reliance on Monte Carlo and avoid systematic uncertainties that would arise from fixing said parameters. Nevertheless, there remain several sources of systematic uncertainties that must be evaluated and assigned to both the branching fraction and the raw asymmetry.

In cases where the parameter that is fixed to a certain value has an own known error or uncertainty, the systematic uncertainty is estimated by varying the parameter by the value of its error and repeating the fit. The greatest difference between the so obtained final result and the nominal result is taken as the systematic uncertainty. The same method is applied also for cases where the parameter in question does not have an own error, with the variation of the parameter being manually selected to represent a reasonable value (this applies to the $m(D^0)$ smearing width of the dominant background, the yield of the "remaining" background category and the category with a FSR photon, and for the normalisation channels, the width of the signal shape and sideband position).

All systematic uncertainties belonging to sources that are listed below are summarised in Tables 41, 42 and 43 for the ϕ, $\overline{K}^{*0}$ and ρ^0 modes, respectively.

11.2.1 Signal $m(D^0)$ PDF

In the $\overline{K}^{*0}$ mode, the signal PDF is allowed to have a free offset and width scaling factor. These parameters, as determined from the fit in data, are subsequently used as fixed values for the fits in the ϕ and ρ^0 modes. To estimate the corresponding systematic uncertainties, the fits in the ϕ and ρ^0 modes are repeated with parameters

varied by their respective statistical errors, as returned from the fit in the $\overline{K}^{*0}$ mode and stated in Section 9.1.2. No uncertainty is assigned to the $\overline{K}^{*0}$ mode results in this regard, as the parameters are left to float in the fit and are thus not dependent on Monte Carlo.

11.2.2 *Calibration of the Dominant Background*

The $m(D^0)$ Monte Carlo distribution of π^0 and η-type backgrounds has been smeared in order to correct for differences between simulation and data, as is extensively described in Section 6.3. The chosen nominal smearing for the fit in data is 7 MeV, corresponding to plot 31e. The corresponding offset that was applied to the relevant PDFs is -1.33 MeV. A systematic uncertainty needs to be applied for both parameters.

In terms of the smearing width, the fit in data is repeated with PDFs for the dominant background categories determined on Monte Carlo samples, obtained with alternative smearings of widths 6 and 8 MeV. The variation values are chosen based on Figure 32, as they cover the broad minimum of the function. The offset, as determined from the smearing procedure, has an own statistical error assigned, 0.25 MeV. The fit is thus repeated with the offset value varied by ± 0.25 MeV.

The source of the systematic uncertainties in signal and dominant background PDFs are discrepancies between Monte Carlo and data. As both signal and dominant background are physical decays with similar characteristics, certain causes for Monte Carlo inaccuracies could affect equally both, causing correlations between the systematic uncertainties, obtained as described in the last two subchapters. Therefore, it stands to reason to obtain a joint systematic uncertainty for the ϕ and ρ^0 channels, meaning that the offsets for the signal and dominant background are varied simultaneously. The same applies for the width of the signal and dominant background PDFs. For the $\overline{K}^{*0}$ mode, where there is no systematic uncertainty due to signal $m(D^0)$ PDF, only the dominant background uncertainties are determined.

11.2.3 *Categories with Fixed Yields*

In the $\overline{K}^{*0}$ and ρ^0 modes, the yields of some of the categories with a low number of events are fixed in the fit. The values for each category are varied in accordance to the respective uncertainty on the nominal branching fraction, as stated in Reference [23]. For the category with the FSR photon, a 20% variation is taken [41]. As the branching fractions contributing to the "remaining" category in the $\overline{K}^{*0}$ mode are not known, we conservatively apply the largest variation from among other categories.

	$\mathcal{B}r[\%]$	$\mathcal{A}_{CP} \ [\cdot 10^{-3}]$
signal and dominant background $m(D^0)$ offset	0.4	0.1
signal and dominant background $m(D^0)$ width	1.0	0.1

Table 41: Systematic uncertainties due to signal extraction procedure for the ϕ mode. The stated uncertainty for the branching fraction is relative, whereas for $\mathcal{A}_{CP}$ the absolute value of the uncertainty is given.

	$\mathcal{B}r[\%]$	$\mathcal{A}_{CP} \ [\cdot 10^{-3}]$
dominant background $m(D^0)$ offset	2.0	0.3
dominant background $m(D^0)$ width	2.0	0.2
$K_0^*(1430)^-\pi^+$ yield	0.2	0.1
$K^{*-}\pi^+$ yield	0.1	0.1
$K^-\rho^+(\to \pi^+\gamma)$ yield	0.2	0.1
$K^-\pi^+$ FSR yield	0.1	0.0
"remaining" yield	0.2	0.1

Table 42: Systematic uncertainties due to signal extraction procedure for the $\overline{K}^{*0}$ mode. The stated uncertainty for the branching fraction is relative, whereas for $\mathcal{A}_{CP}$ the absolute value of the uncertainty is given.

	$\mathcal{B}r[\%]$	$\mathcal{A}_{CP} \ [\cdot 10^{-3}]$
signal and dominant background $m(D^0)$ offset	0.8	0.1
signal and dominant background $m(D^0)$ width	2.2	4.6
$\rho(\to \pi\gamma)\pi$ yield	0.4	0.3
$\pi^+\pi^-$ FSR yield	0.4	0.4

Table 43: Systematic uncertainties due to signal extraction procedure for the ρ^0 mode. The stated uncertainty for the branching fraction is relative, whereas for $\mathcal{A}_{CP}$ the absolute value of the uncertainty is given.

11.3   SYSTEMATICS RELATED TO THE NORMALISATION MODES

The statistical uncertainty of the fraction that is used to calculate the signal yield is already taken into account in the statistical error of the final branching fraction of the signal modes, and the statistical error of the raw asymmetry of the normalisation modes. The remaining sources of systematic uncertainties are discussed below. All uncertainties are summarised in Table 44.

11.3.1   *Sideband Position*

Taking guidance from the previous Belle analysis of the normalisation modes [33], the sidebands are selected in an alternative position, starting at ± 25 MeV from the nominal D^0 mass. The signal yield an raw asymmetry are extracted using the so obtained alternative fraction.

11.3.2   *Background Shape*

It has been verified that in the $K^-\pi^+$ and $\pi^+\pi^-$ modes, the ratio of events between the lower and upper sideband is not equal in Monte Carlo and data, implying that there can be a difference in background shape, which would in turn result in a different fraction f on data than on Monte Carlo. A relative uncertainty of 5.4% (6.5%) is assigned to the fraction of the $K^-\pi^+$ ($\pi^+\pi^-$) mode and propagated to the uncertainty of the yield of the corresponding modes, which is in turn propagated to the uncertainty of the branching fraction of the signal modes. This feature can be expected to affect equally decays of both flavours of the D^0, thus the uncertainties will subtract in the calculation of the raw asymmetry.

11.3.3   *Uncertainty in Determination of the Yield*

It has been tested on Monte Carlo that the yield, as extracted by the utilised procedure, differs from the true value by a relative 0.5%, 0.3% and 0.4%, for the K^+K^-, $K^-\pi^+$ and $\pi^+\pi^-$ modes, respectively (see Section 7.1). These uncertainties are directly attributed to the uncertainty on the branching fraction, as the errors on the yields directly translate into the errors for the branching fraction. This feature can be expected to affect equally decays of both flavours of the D^0, thus the uncertainties will subtract in the calculation of the raw asymmetry.

11.3.4   *Signal Shape*

As it was shown that for both signal and dominant background, the $m(D^0)$ distribution is slightly wider on data than it is on Monte Carlo, it can be expected that a similar situation might occur in the normalisation channels. Since the tails of the signal distribution extend slightly also into the sidebands, a certain number of signal events is present in the counted total number of events in the sidebands.

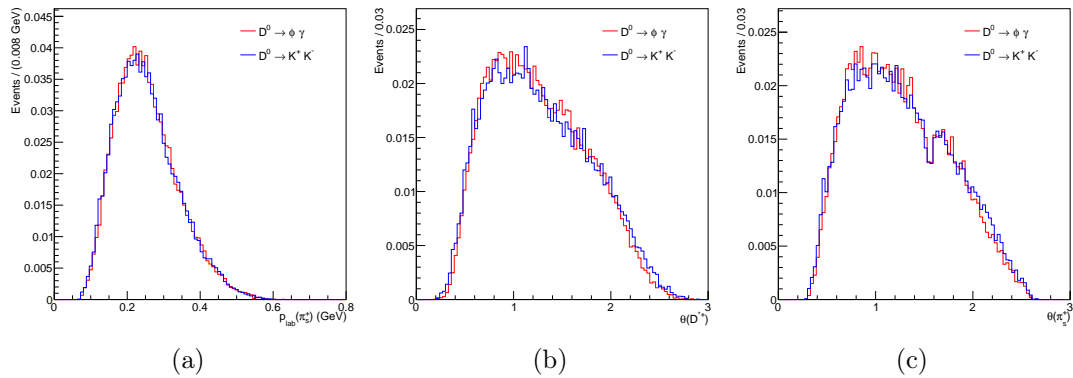(a)   (b)   (c)

Figure 91: Comparison of the $p_{\text{lab}}(\pi_s)$ (a), $\theta(D^{*+})$ (b) and $\theta(\pi_s)$ (c) distribution of the signal and normalisation modes for the ϕ channel, on respective signal Monte Carlo simulations.

A wider signal distribution on data would increase the number of signal events in the sidebands, affecting the fraction that is then used to extract the signal yield. To estimate the related systematic uncertainty, a similar method as for the calibration of the dominant background is employed. The Monte Carlo distribution is gradually smeared with a Gaussian of an increasing width, and for each step histogrammed PDFs determined on Monte Carlo are used to fit the data distribution. For all three normalisation channels, it is proven that the χ^2 of the fit is smallest with a smearing of 1.6 MeV. Therefore, the Monte Carlo distributions are smeared with a Gaussian of 1.6 MeV width. The corresponding fraction is calculated, followed by the extraction of the signal yield and raw asymmetry. The systematics uncertainty is again estimated by the difference in the final results.

11.3.5 A_{FB} and $A_\varepsilon^{\pi_s}$ Subtraction

We have assumed in Chapter 5 that A_{FB} and $A_\varepsilon^{\pi_s}$ completely cancel between the signal and normalisation modes. While in general, the kinematics of signal and normalisation modes is not the same, this will still hold, if the kinematics of the two decays match in the aspects that affect these asymmetries. It has already been investigated that the distributions of CMS momentum of the D^{*+} show good agreement. We further investigate also the laboratory momentum of the slow pion from the $D^{*+} \to D^0 \pi_s$ decay, and the polar angle of both the D^{*+} and π_s. The corresponding distributions are shown in Figure 91 for the ϕ mode. All distributions exhibit fairly good matching, based on which it is concluded, that the asymmetries in question should cancel between signal and normalisation modes and no correction needs to be assigned.

	ϕ		$\overline{K}^{*0}$		ρ^0	
	$\mathcal{B}r[\%]$	$\mathcal{A}_{CP}\ [\cdot10^{-3}]$	$\mathcal{B}r[\%]$	$\mathcal{A}_{CP}\ [\cdot10^{-3}]$	$\mathcal{B}r[\%]$	$\mathcal{A}_{CP}\ [\cdot10^{-3}]$
sideband position	0.0	0.5	0.0	0.0	0.1	0.3
background shape	0.3		0.0			
uncertainty of yield extraction	0.5		0.3		0.4	
signal shape width	0.0	0.0	0.0	0.0	0.1	0.0

Table 44: Systematic uncertainties due to signal extraction procedure in the normalisation modes. The stated uncertainty for the branching fraction is relative, whereas for $\mathcal{A}_{CP}$ the absolute value of the uncertainty is given.

11.4 SYSTEMATICS DUE TO EXTERNAL $\mathcal{B}r$ AND $\mathcal{A}_{CP}$ VALUES

In the calculations of the branching fraction and CP asymmetry of the signal modes, we use values of branching fractions and CP asymmetries of other modes, which are taken from Reference [23] and Reference [13]. Since these values are known only to a certain precision level, the related uncertainties must be propagated to the uncertainty of our final result. The values in question are the branching fraction and CP asymmetry of the normalisation modes, and the branching fractions for the decays of the vector mesons. In the calculation of the final results for the signal modes, these values are varied by their respective errors and the difference between the so obtained final results and the nominal final results are taken as the systematic uncertainty.

All related systematic uncertainties are summarised in Tables 45 and 46.

	ϕ	$\overline{K}^{*0}$	ρ^0
	$\mathcal{B}r[\%]$	$\mathcal{B}r[\%]$	$\mathcal{B}r[\%]$
$\mathcal{B}r$ of normalisation channel	1.8	1.0	1.8
$\mathcal{B}r$ of vector meson decay	1.0	0.0	0.0

Table 45: Relative systematic uncertainties due to uncertainties on external branching fractions that are used in the calculation.

| | ϕ | $\overline{K}^{*0}$ | ρ^0 |
	$\mathcal{A}_{CP}$ [$\cdot 10^{-3}$]	$\mathcal{A}_{CP}$ [$\cdot 10^{-3}$]	$\mathcal{A}_{CP}$ [$\cdot 10^{-3}$]
$\mathcal{A}_{CP}$ of normalisation channel	1.2	0.0	1.5

Table 46: Absolute values of the systematic uncertainties due to uncertainties on the external CP asymmetries that are used in the calculation.

11.5 SUMMARY OF SYSTEMATIC UNCERTAINTIES

The systematic uncertainties for the branching fractions are summarised in Table 47, and the systematic uncertainties for the CP asymmetries are summarised in Table 48. The contributions are summed in quadrature to one joint value of the systematic uncertainty for each channel.

	ϕ $\mathcal{B}r[\%]$	$\overline{K}^{*0}$ $\mathcal{B}r[\%]$	ρ^0 $\mathcal{B}r[\%]$
reconstruction efficiencies	2.8	3.3	2.8
signal and dominant background parametrisation	1.0		2.3
dominant background parametrisation		2.8	
fixed background yields		0.3	0.6
normalisation modes systematics	0.5	0.3	0.2
$\mathcal{B}r$ and $\mathcal{A}_{CP}$ values of other modes	2.0	1.0	1.8
total	3.6	4.4	4.1

Table 47: Summary of all systematic uncertainties (relative values) on the branching fractions for all three signal modes.

	ϕ $\mathcal{A}_{CP}$ [$\cdot 10^{-3}$]	$\overline{K}^{*0}$ $\mathcal{A}_{CP}$ [$\cdot 10^{-3}$]	ρ^0 $\mathcal{A}_{CP}$ [$\cdot 10^{-3}$]
signal and dominant background parametrisation	0.1		5.3
dominant background parametrisation		0.4	
fixed background yields		0.2	0.5
normalisation modes systematics	0.5	0.0	0.3
$\mathcal{B}r$ and $\mathcal{A}_{CP}$ values of other modes	1.2		1.5
total	1.3	0.4	5.5

Table 48: Summary of all systematic uncertainties (absolute values) on $\mathcal{A}_{CP}$ for all three signal modes.

FINAL RESULTS AND CONCLUSIONS

We have measured the branching fractions and CP asymmetries in the decays $D^0 \rightarrow V\gamma$, where $V = \phi, \overline{K}^{*0}, \rho^0$, on the full data set, collected by the Belle experiment. The final results, as obtained in Chapter 10, are presented here by including the systematic uncertainties, estimated in the previous chapter.

12.1 BRANCHING FRACTIONS

Including the total systematic uncertainties from Table 47 in the result, we obtain the following branching fractions for the radiative D^0 decays:

$$\mathcal{B}r(D^0 \rightarrow \phi\gamma) = (2.76 \pm 0.19 \pm 0.10) \cdot 10^{-5} \quad ,$$
$$\mathcal{B}r(D^0 \rightarrow \overline{K}^{*0}\gamma) = (4.66 \pm 0.21 \pm 0.21) \cdot 10^{-4} \quad ,$$
$$\mathcal{B}r(D^0 \rightarrow \rho^0\gamma) = (1.77 \pm 0.30 \pm 0.07) \cdot 10^{-5} \quad ,$$

where the first error is statistical and the second systematic.

The branching fraction of the ϕ mode is consistent with the current world average value of $(2.70 \pm 0.35) \cdot 10^{-5}$, obtained from the combined measurements by the Belle and BaBar collaborations. The previous Belle analysis [21] reported a value of $(2.60^{+0.70}_{-0.61}{}^{+0.15}_{-0.17}) \cdot 10^{-5}$, and BaBar reported a value of $(2.73 \pm 0.30 \pm 0.26) \cdot 10^{-5}$ [22]. In can be seen that our present result constitutes a significant improvement in terms of precision. The precision of the present result exceeds the precision of the current world-average by around 50%.

The only previous measurement of the branching fraction of the $\overline{K}^{*0}$ mode was performed by BaBar, with the result of $(3.22 \pm 0.20 \pm 0.27) \cdot 10^{-4}$. Our result has around twice better relative precision, and the central value is higher than the one from BaBar [22] by 3.2σ, where σ is the combined uncertainty of both measurements.

The ρ^0 mode has not been observed previously and the present result represents the first observation of this decay mode. The significance of the observation is evaluated from the negative log likelihood curve. We perform repeated fits with the signal yield fixed to values from zero to 900 with a step of 50. For each fit, the likelihood is calculated. Figure 92a shows the distribution of $(\mathcal{L}_{max}/\mathcal{L})^2$, where $\mathcal{L}_{max}$ is the likelihood of the nominal fit. To incorporate the systematic uncertainties, a convolution with a Gaussian with mean zero and width, corresponding to the
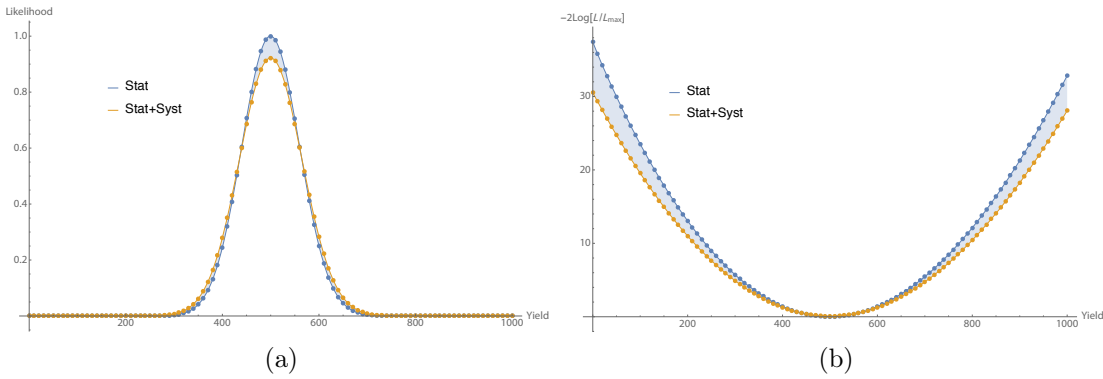
(a)   (b)

Figure 92: Distrbutions of the likelihood value (a) and $-2 \ln \mathcal{L}/\mathcal{L}_{max}$ (b) with respect to the signal yield for the ρ^0 mode, for the statistical uncertainty only and for the combined statistical and systematic uncertainties.

systematic uncertainty on the yield, is applied to the distribution. The resulting distribution is presented in Figure 92a. From the likelihood values, the negative log likelihood is computed as

$$ -2 \ln \mathcal{L}/\mathcal{L}_{max} \quad . \tag{61} $$

The result is shown in Figure 92b. The significance is given as $\sqrt{-2 \ln \mathcal{L}_0/\mathcal{L}_{max}}$, where $\mathcal{L}_0$ is the likelihood value when the signal yield is fixed to zero. We obtain a significance of 5.5σ for the observation of the decay $D^0 \rightarrow \rho^0 \gamma$.

The value of the obtained branching fraction of the ρ^0 mode is somewhat larger than the theoretical predictions (see Table 2), all lying in the range from 10^{-6} to 10^{-5}.

12.2 CP ASYMMETRY

Including the total systematic uncertainties from Table 48 to the result, we obtain the following CP asymmetries for the radiative D^0 decays:

$$
\begin{aligned}
\mathcal{A}_{CP}(D^0 \rightarrow \phi\gamma) &= -(0.094 \pm 0.066 \pm 0.001) \quad , \\
\mathcal{A}_{CP}(D^0 \rightarrow \overline{K}^{*0}\gamma) &= -(0.003 \pm 0.020 \pm 0.000) \quad , \\
\mathcal{A}_{CP}(D^0 \rightarrow \rho^0\gamma) &= 0.056 \pm 0.152 \pm 0.005 \quad ,
\end{aligned}
$$

where the first error is statistical and the second systematic. The results are consistent with no CP asymmetry in any of the decay modes. It can be observed that the statistical error is by far the dominant uncertainty. Only in the $\overline{K}^{*0}$ mode the sensitivity reaches the percent level, at which the effects of New Physics could become observable. Taking into account the dominance of the statistical uncertainty, the sensitivity of the measurement can be greatly improved at the upgrade of the Belle Experiment, the Belle II detector [42], which aims to collect 50 times more data than the Belle detector.

POVZETEK DOKTORSKEGA DELA

13.1 UVOD

Standardni model je relativistična kvantna teorija polja, ki opisuje osnovne delce in interakcije med njimi. Desetletja eksperimentov v fiziki osnovnih delcev so preverjala napovedi in izračune Standardnega modela z visoko natančnostjo, in razen redkih izjem, je ujemanje med eksperimentalnimi rezultati in teoretičnimi izračuni zelo dobro, celo izjemno. Kljub vsem uspehom Standardnega modela pa obstaja več indicev, ki nakazujejo, da Standardni model ni dokončna teorija, temveč bolj verjetno le nizkoenergijska limita bolj splošne teorije. Poglavitne pomanjkljivosti Standardnega modela so: dejstvo, da ne vključuje gravitacije; predvideva, da so nevtrini brezmasni, medtem ko eksperimentalno potrjen mehanizem nevtrinskih oscilacij dokazuje, da imajo maso; ne razloži temne energije in ne predvideva kandidata za temno snov; da je stopnja kršitve simetrije CP v Standardnem modelu prenizka, da bi lahko razložila opaženo asimetrijo med snovjo in antisnovjo v vesolju. Tako vemo, da morajo obstajati dodatni fizikalni procesi in delci izven Standardnega modela, ki jih s skupnim imenom imenujemo Nova fizika. Iskanje teh je glavno gonilo trenutnih eksperimentov v fiziki osnovnih delcev.

Eno izmed pomembnih področij iskanja Nove fizike je kršitev simetrije CP, t.j. simetrije ob konjugaciji naboja in transformaciji parnosti. Cilj eksperimentov je izmeriti stopnjo kršitve, ki bi bila občutno večja od napovedi Standardnega modela, in je lahko razložena s teorijo Nove fizike, vendar dosedaj izmerjene vrednosti v nobenem procesu ne kažejo statistično signifikantnega odstopanja od Standardnega modela. Z naraščanjem natančnosti eksperimentalnih meritev lahko merimo vedno redkejše procese iz vidika Standardnega modela, kjer bi lahko bili prispevki Nove fizike znatni. Tako področje je na primer fizika čarobnih hadronov, t.j. hadronov, ki vsebujejo kvark c (vendar ne težjih kvarkov). Zanje velja, da je kršitev simetrije CP po mehanizmu Standardnega modela zelo majhna, saj pri procesih sodelujeta v prvem približku le prvi dve generaciji kvarkov. Pripadajoči elementi matrike CKM, v kateri nastopa kompleksna faza, ki generira kršitev simetrije CP v Standardnem modelu, so skoraj realni, in napovedana kršitev simetrije CP je reda velikosti 10^{-3}. Do danes kršitev simetrije CP v sistemu čarobnih hadronov še ni bila izmerjena.

Primeren proces za iskanje prispevkov Nove fizike so radiativni razpadi mezonov D^0 v vektorski mezon in foton, $D^0 \to V\gamma$. Teoretični izračuni razširitve Standardnega modela s prispevkom kromomagnetnih dipolnih operatorjev predvidevajo, da lahko v primeru, kjer je $V = \phi$ ali ρ^0, kršitev simetrije CP doseže tudi za red velikosti višjo

	$\mathcal{B}r[10^{-5}]$
$\phi\gamma$	2.70 ± 0.35
$\overline{K}^{*0}\gamma$	$32.7\ \pm 3.4$
$\rho^0\gamma$	< 24 pri 90% stopnji zanesljivosti

Tabela 49: Vrednosti razvejitvenih razmerij razpadov $D^0 \to V\gamma$ [23].

vrednost od prispevka Standardnega modela [15]. Razpadi $D^0 \to V\gamma$ so zanimivi tudi iz vidika izračuna razvejitvenega razmerja. Pri teh razpadih prevladujejo prispevki dolgega dosega, ki ne omogočajo perturbativnega računanja, in so zato zelo zahtevni s teoretičnega vidika izračuna razvejitvenih razmerij. Eksperimentalne meritve teh vrednosti so tako dobrodošle kot test teoretičnih izračunov.

Razpadi $D^0 \to V\gamma$ so bili prvič opaženi leta 2003 v primeru, kjer je vektorski mezon $V = \phi$ [21], s strani kolaboracije Belle. Ponovno je te razpade izmerila kolaboracija Babar leta 2008, skupaj z razpadi, kjer je $V = \overline{K}^{*0}$ [22]. Od takrat ni bila izvedena nobena ponovna analiza razpadov $D^0 \to V\gamma$, kar tudi pomeni, da meritev kršitve simetrije CP v teh razpadih ni bila nikoli izvedena. Za razpade, kjer je $V = \rho^0$, ki še niso bili opaženi, je kolaboracija CLEO II postavila zgornjo mejo razvejitvenega razmerja [20]. Trenutne izmerjene vrednosti razvejitvenih razmerij so povzete v tabeli 49. V pričujočem doktorskem delu je predstavljena analiza razpadov $D^0 \to V\gamma$, kjer $V = \phi, \overline{K}^{*0}, \rho^0$; tako meritev razvejitvenega razmerja kot tudi prva meritev asimetrije CP v teh razpadih. Uporabljena je konvencija $\hbar = c = 1$.

13.2   EKSPERIMENTALNA POSTAVITEV

Analiza je opravljena na celotnem vzorcu podatkov, zajetim s spektrometrom Belle na trkalniku elektronov in pozitronov KEKB v Tsukubi na Japonskem, kar znese 943 fb^{-1}. Podrobnejši opis trkalnika se nahaja v referenci [24], opis detektorja Belle pa v referenci [25].

13.2.1   *Trkalnik KEKB*

Trkalnik KEKB je asimetrični trkalnik elektronov z energijo 8.5 GeV in pozitronov z energijo 3 GeV. Težiščna energija žarkov je tako 10.58 GeV, kar ustreza masi resonance $\Upsilon(4S)$. Ta resonanca, ki je vezano stanje kvarkov $b\bar{b}$, dominantno razpada v par mezonov B, možni pa so tudi drugi procesi, na primer vezano stanje kvarkov $c\bar{c}$, iz katerih lahko dobimo par čarobnih mezonov.

13.2.2 *Detektor Belle*

Detektor Belle je postavljen v interakcijski točki, kjer se križata žarka elektronov in pozitronov. Predstavljen je na sliki 93. Od središča navzven je sestavljen iz sledečih komponent:

SILICIJEV DETEKTOR VERTEKSOV: izmeri točko razpada kratkoživih delcev z ločljivostjo približno 100 μm.

OSREDNJA POTOVALNA KOMORA: izmeri sledi nabitih delcev v magnetnem polju 1.5 T. Iz njihove ukrivljenosti lahko določimo gibalno količino delca. Poleg tega omogoča identifikacijo delcev pri nizkih gibalnih količinah, pod 0.8 GeV, prek meritve specifične ionizacije.

PRAGOVNI ŠTEVEC SEVANJA ČERENKOVA: omogoča ločevanje med kaoni in pioni v območju visokih gibalnih količin, med 1.5 in 3.5 GeV. Sestavljen je iz aerogela, katerega lomni količnik omogoča, da pioni v izbranem energijskem območju pri preletu sevajo svetlobo Čerenkova, kaoni pa ne.

MERILEC ČASA PRELETA: izmeri čas, ki ga delec potrebuje za prelet od interakcijske točke do merilca. Skupaj z informacijo o gibalni količini delca, dobljeno iz potovalne komore, omogoča identifikacijo delcev v območju srednjih gibalnih količin, med 0.8 in 1.2 GeV.

ELEKTROMAGNETNI KALORIMETER: izmeri energijo fotonov z ločljivostjo približno 1.7%.

DETEKTOR MEZONOV K_L IN MIONOV: omogoča identifikacijo mezonov K_L in mionov prek meritve vdorne globine.

Za pričujočo analizo so predvsem pomembni pod-detektorji za identifikacijo delcev in elektromagnetni kalorimeter, ki izmeri energijo fotonov. Skupna informacija o verjetnosti za identiteto delca je podana kot zmnožek verjetnosti, dobljenimi z vsemi tremi pod-detektorji. Skupno dobimo ločevanje med kaoni in pioni z natančnostjo 3σ, za gibalne količine do 3.5 GeV.
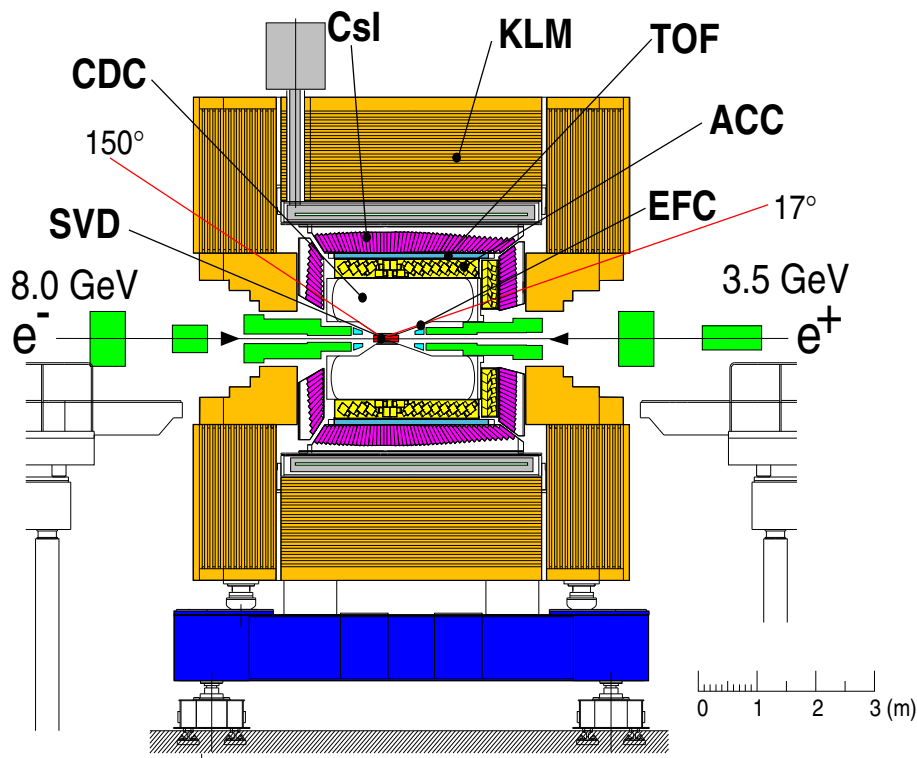
Slika 93: Detektor Belle [25].

13.3   ANALIZNI POSTOPEK

Postopek analize je bil razvit na podlagi simulacije Monte Carlo. Tako razvejitveno razmerje kot asimetrijo CP bomo izmerili relativno glede na normalizacijski kanal, ki je za vsak signalni kanal izbran tako, da vsebuje enake nabite delce v končnem stanju. Za ϕ kanal je to razpad $D^0 \to K^+K^-$, za $\overline{K}^{*0}$ kanal $D^0 \to K^-\pi^+$ in za ρ^0 kanal $D^0 \to \pi^+\pi^-$. Razvejitveno razmerje dobimo iz izmerjenega števila dogodkov signalnega in normalizacijskega razpada, N_{sig} in N_{norm}, iz pripadajočih izkoristkov ϵ_{sig} in ϵ_{norm}, ter iz znanega razvejitvenega razmerja za normalizacijski kanal [23]:

$$\mathcal{B}r_{\mathrm{sig}} = \mathcal{B}r_{\mathrm{norm}} \times \frac{N_{\mathrm{sig}}}{N_{\mathrm{norm}}} \times \frac{\varepsilon_{\mathrm{norm}}}{\varepsilon_{\mathrm{sig}}} \quad . \tag{62}$$

Rekonstrukcijska asimetrija $A_{\mathrm{rek}} = \frac{N(D^0) - N(\overline{D}^0)}{N(D^0) + N(\overline{D}^0)}$, dobljena iz števila signalnih dogodkov za mezone D^0 in $\overline{D}^0$, vsebuje poleg asimetrije CP $\mathcal{A}_{CP}$ tudi asimetrijo iz naslova produkcije čarobnih mezonov, A_{FB}, in detektorskih izkoristkov, $A_{\varepsilon}^{\pm}$: $A_{\mathrm{rek}} = \mathcal{A}_{CP} + A_{\mathrm{FB}} + A_{\varepsilon}^{\pm}$. Relativna meritev $\mathcal{A}_{CP}$ z uporabo normalizacijskih kanalov omogoča, da se slednji dve asimetriji odštejeta, pri čemer dobimo

$$\mathcal{A}_{CP}^{\mathrm{sig}} = A_{\mathrm{rek}}^{\mathrm{sig}} - A_{\mathrm{rek}}^{\mathrm{norm}} + \mathcal{A}_{CP}^{\mathrm{norm}} \quad , \tag{63}$$

kjer sta $A_{\mathrm{rek}}^{\mathrm{sig}}$ in $A_{\mathrm{rek}}^{\mathrm{norm}}$ rekonstrukcijski asimetriji signalnega in normalizacijskega kanala, $\mathcal{A}_{CP}^{\mathrm{norm}}$ pa znana vrednost asimetrije CP normalizacijskega kanala [13].

13.3.1 *Rekonstrukcija*

Iz celotnega vzorca podatkov so kandidati za signalne dogodke izbrani z aplikacijo izbirnih kriterijev, ki so izbrani tako, da je signifikanca vzorca maksimalna:

$$N_{\text{sig}}/\sqrt{N_{\text{sig}} + N_{\text{oz}}} = \text{maks.} \quad , \tag{64}$$

kjer N_{sig} in N_{oz} predstavljata število signalnih dogodkov oz. ozadja. Ker razvejitveno razmerje za razpade $D^0 \to \rho^0 \gamma$ ni znano, uporabimo za oceno količine signalnih dogodkov v vzorcu, dobljenem po aplikaciji izbirnih kriterijev, vrednost $\mathcal{B}r\,(D^0 \to \rho^0 \gamma)$ = 3×10^{-5}. Zanesljivost postopka določitve signalnih dogodkov v vzorcu tudi ob drugačnih vrednostih razvejitvenega razmerja je preverjena s testom linearnost.

Za določitev okusa mezona D^0 postavimo zahtevo, da kandidati izvirajo iz razpada $D^{*+} \to D^0 \pi^+$, kjer okus določimo na podlagi naboja piona. Takšen pogoj omogoča tudi rez na masni razliki $m(D^{*+}) - m(D^0)$, kar bistveno zmanjša količino kombinatoričnega ozadja. Signalni dogodki so rekonstruirani v sledečih razpadnih kanalih vektorskih mezonov: $\phi \to K^+ K^-$, $\overline{K}^{*0} \to K^- \pi^+$ in $\rho^0 \to \pi^+ \pi^-$. Sprejmemo kandidate, katerih masa leži v izbranem intervalu okoli nominalne mase [23] vektorskih mezonov: 11 MeV za ϕ, 60 MeV za $\overline{K}^{*0}$ in 150 MeV za ρ^0. Za fotone zahtevamo, da njihova energija presega 540 MeV. Postavimo tudi rez na razmerje energije, deponirane v 3×3 mreži kristalov kalorimetra, ter energije, deponirane v 5×5 mreži, ki zajema prejšnjo, in sicer zahtevamo, da to razmerje, E_9/E_{25}, presega vrednost 0.94. S to zahtevo zmanjšamo količino dogodkov, kjer visokoenergijski pion razpade v dva fotona, ki zadeneta kalorimeter pod majhnim kotom in sta zato zaznana kot en sam foton.

Pri rekonstrukciji obeh čarobnih mezonov (D^{*+} in D^0) prilagajamo sledi hčerinskih delcev v skupno točko in zahtevamo, da p-vrednost ujemanja presega 10^{-3}. V primeru D^{*+} zahtevamo tudi, da oba hčerinska delca prihajata iz interakcijske točke. Za zmanjšanje prispevka kombinatoričnega ozadja zahtevamo, da celotna energija, sproščena v razpadu D^{*+}, $q = m(D^{*+}) - m(D^0) - m(\pi^+)$, ne odstopa za več kot 0.6 MeV od nominalne vrednosti [23]. Omejimo tudi gibalno količino mezona D^{*+} v težiščnem sistemu, $p_{\text{CMS}}(D^{*+})$, in sicer mora presegati 2.42 GeV za ϕ kanal, 2.17 GeV za $\overline{K}^{*0}$ kanal in 2.72 GeV za ρ^0 kanal.

Največji prispevek k ozadju predstavljajo razpadi mezona D^0, ki vsebujejo enake nabite delce v končnem stanju, vendar namesto fotona nevtralen pion, ki razpade v dva fotona. Pri tem se pri rekonstrukciji en foton izgubi, kar povzroči, da je porazdelitev dogodkov po masi rekonstruiranega mezona D^0 za take razpade premaknjena k nižjim vrednostim v primerjavi s porazdelitvijo pravih signalnih dogodkov, vendar se vrhova še vedno prekrivata. Za dobro prepoznavanje signalih dogodkov je torej ključnega pomena čim bolj zmanjšati prispevek tega ozadja. V ta namen smo razvili veto π^0, dobljen z uporabo programa nevronske mreže `NeuroBayes` [32]. Kandidata za signalni foton povežemo z vsemi ostalimi fotoni v dogodku, katerih energija presega izbrano mejno vrednost, ter mu dodelimo tisto di-fotonsko maso, ki leži najbližje nominalni masi π^0. Dve tako dobljeni spremljivki, eno, kjer zahtevamo minimalno enegijo drugega fotona 75 MeV, ter eno, kjer zahtevamo minimalno energijo drugega fotona 30 MeV, uporabimo v programu `NeuroBayes`, s čemer dobimo eno končno

spremenljivko. Rez na tej spremeljivki zavrne 60% ozadja, pri čemer ohrani 85% signala.

13.3.2 *Določitev števila signalnih dogodkov*

Število signalnih dogodkov v vzorcu določimo s prilagajanjem funkcij, ki opisujejo signalne dogodke oz. različna ozadja, v dveh spremeljivkah: masi rekonstruiranega mezona D^0 in $\cos(\theta_H)$. Kot θ_H je kot med materjo in hčerinskim delcem vektorskega mezona v njegovem lastnem mirovnem sistemu. Porazdelitev signalnih dogodkov v tej spremeljivki je sorazmerna $1 - \cos^2(\theta_H)$, nobena vrsta ozadja pa nima podobne porazdelitve. Za $\overline{K}^{*0}$ in ρ^0 kanal dodatno omejimo interval spremenljivke $\cos(\theta_H)$ na $-0.8 < \cos(\theta_H) < 0.4$, pri čemer pomembno zmanjšamo prispevek ozadij, ki zavzemajo maksimalne vrednosti pri ± 1, ter izločimo območje, kjer simulacija Monte Carlo ne opiše dobro porazdelitve na fizikalnih podatkih. Prilagajanje je simultano izvedeno na vzorcu D^0 in $\overline{D}^0$. Izkoristki, določeni kot razmerje pravilno rekonstruiranih dogodkov po aplikaciji izbirnih kriterijev, ter številom vseh dogodkov, so 9.7% za ϕ kanal, 7.8% za $\overline{K}^{*0}$ kanal in 6.8% za ρ^0 kanal.

Porazdelitev signalnih dogodkov po masi mezona D^0 opišemo s funkcijo Crystal-Ball [35] za ϕ in ρ^0 kanal, ter kombinacijo funkcije Crystal-Ball in dveh Gaussovih funkcij v primeru $\overline{K}^{*0}$. Zaradi možnih razlik med simulacijo in podatki dovolimo pri $\overline{K}^{*0}$ kanalu dva prosta parametra: premik srednje vrednosti in faktor razširitve širine. Vrednosti, dobljeni na podatkih, uporabimo pri funkcijah za ϕ in ρ^0 kanala.

Porazdelitve dogodkov po masi mezona D^0 ozadij, kjer nastopata π^0 ali η, ki razpadeta v dva fotona, opišemo s kombinacijami funkcij Crystal-Ball, logaritmične Gaussove funkcije [36] ter dodatkom do dveh Gaussovih funkcij, s katerima opišemo repe porazdelitev. Edino ozadje tega tipa, ki nastopa pri ϕ kanalu, je $D^0 \to \phi\pi^0$. V $\overline{K}^{*0}$ kanalu so ozadja tega tipa $D^0 \to \overline{K}^{*0}\pi^0$, $K^-\rho^+$, $K_0^*(1430)^-\pi^+$, $K^{*-}\pi^+$, neresonančni razpad $K^-\pi^+\pi^0$, $\overline{K}^{*0}\eta$ in neresonančni razpad $K^-\pi^+\eta$. V ρ^0 kanalu so ozadja tega tipa $\rho^0\pi^0$, razpad v nabita $\rho\pi$ in $K^-\rho^+$, kjer je kaon napačno identificiran kot pion. V vseh treh signalnih razpadih definiramo dodatno ozadje "remaining", ki vsebuje vse ostale razpade, kjer je D^0 rekonstruiran iz večine svojih hčerinskih delcev. V $\overline{K}^{*0}$ in ρ^0 kanalu se pojavita še dve dodatni ozadji: neresonančni razpad v $K^-\pi^+$ ($\overline{K}^{*0}$) oz. $\pi^+\pi^-$ (ρ^0), kjer je foton izsevan v končnem stanju, in razpad v $K^-\rho^+$, kjer ρ razpade radiativno v pion in foton. Ker so v tem primeru ne izgubimo nobenega delca v končnem stanju, je porazdelitev takih dogodkov po masi D^0 enaka kot signalna porazdelitev. Število teh dogodkov pa je izredno majhno, zato ga fiksiramo na vrednosti, dobljene iz simulacije Monte Carlo ter prilagojene glede na znana razvejitvena razmerja. Ostane še kombinatorično ozadje, ki ga parametriziramo z eksponentno funkcijo v ϕ kanalu in s Čebiševim polinomom druge stopnje v $\overline{K}^{*0}$ in ρ^0 kanalih. Vsi parametri teh funkcij ostanejo prosti.

Za kalibracijo porazdelitve dogodkov po masi mezona D^0 ozadij s mezonoma π^0 ali η tako na simulaciji kot pravih podatkih rekonstruiramo razpad $D^0 \to K_S^0\gamma$. Ta razpad je prepovedan, zato dobljeni dogodki večinoma prihajajo iz razpadov $D^0 \to K_S^0\pi^0$ in $D^0 \to K_S^0\eta$. Pri rekonstrukciji uporabimo enake kriterije za identifikacijo delcev ter rez na q kot pri signalnih kanalih, in rez na $p_{\mathrm{CMS}}(D^{*+})$ kot pri ϕ kanalu. Masa kandidatov

za K_S^0 mora ležati v intervalu ± 9 MeV od nominalne vrednosti. Porazdelitev na simuliranih dogodkih numerično konvoluiramo z Gaussovo funkcijo širine (7 ± 1) MeV in zamika srednje vrednosti (-1.33 ± 0.25) MeV, da dosežemo ujemanje s podatki.

Porazdelitev signalnih dogodkov po $\cos(\theta_H)$ opišemo kot $1 - \cos^2(\theta_H)$ brez prostih parametrov za vse tri kanale. Porazdelitev dogodkov razpadov $D^0 \to V\pi^0$ in $V\eta$, kjer je V enak vektorski mezon kot pri signalnih dogodkih, je blizu funkciji $\cos^2(\theta_H)$ in jo opišemo s Čebiševim polinomom druge (ϕ in ρ^0 kanal) oz. tretje stopnje ($\overline{K}^{*0}$ kanal). V ϕ kanalu dovolimo prost linearen parameter, ki opiše možne interference med resonančnimi in neresonančnimi amplitudami. Za ostale ozadja, ki ne vsebujejo vektorskega mezona, so porazdelitve po $\cos(\theta_H)$ netrivialne in jih parametriziramo, kot je potrebno.

V $\overline{K}^{*0}$ kanalu poleg prej omenjenih kategorij, katerim fiksiramo število dogodkov, enako storimo še za nekatera druga ozadja: $K_0^*(1430)^-\pi^+$, $K^{*-}\pi^+$ in ozadje "remaining". Pri vseh kategorijah, kjer je število dogodkov fiksirano, fiksiramo tudi vrednost rekonstrukcijske asimetrije. Pri $\overline{K}^{*0}$ kanalu dodatno dodelimo en sam parameter rekonstrukcijske asimetrije za vsa ozadja s π^0, ter enako za vsa ozadja z η.

13.3.3   Rezultati prilagajanja

Rezultati prilagajanja funkcij so prikazani na slikah 94, 95 in 96 za ϕ, $\overline{K}^{*0}$ in ρ^0 kanale. Signalna komponenta je označena s črtkasto rdečo črto. Dobljeno število signalnih dogodkov je 524 ± 35 (ϕ kanal), 9104 ± 396 ($\overline{K}^{*0}$ kanal) in 500 ± 85 (ρ^0 kanal). Dobljene rekonstrukcijske asimetrije so -0.091 ± 0.066 (ϕ kanal), -0.002 ± 0.020 ($\overline{K}^{*0}$ kanal) in 0.056 ± 0.151 (ρ^0 kanal). Negotovosti so statistične.

13.3.4   Analiza normalizacijskih kanalov

Pri analizi normalizacijskih kanalov se zgledujemo po predhodni analizi teh istih kanalov kolaboracije Belle [33]. Uporabimo enake kriterije za identifikacijo delcev, prilagajanje sledi v skupno točko in reze na q in $p_{\mathrm{CMS}}(D^{*+})$, kot pri signalnih kanalih. Število dogodkov je dobljeno z metodo štetja. Na simuliranih dogodkih določimo razmerje dogodkov ozadja v signalnem oknu $N_{\mathrm{sigO}}^{\mathrm{oz}}$, in vseh dogodkov v dveh simetričnih stranskih oknih na obeh straneh signalnega okna, N_{strO}: $f = (N_{\mathrm{sigO}}^{\mathrm{oz}}/N_{\mathrm{strO}})_{\mathrm{sim}}$. Da dobljeno razmerje velja tudi na podatkih, preverimo s primerjavo porazdelitve ozadja v stranskem oknu q med simuliranimi in pravimi podatki. Prav tako preverimo, da enako razmerje velja za D^0 in $\overline{D}^0$ vzorca. Na podatkih nato s štetjem dogodkov v stranskih oknih in uporabo zgornjega razmerja dobimo število dogodkov ozadja v signalnem oknu: $(N_{\mathrm{sigO}}^{\mathrm{oz}})_{\mathrm{podatki}} = f \times (N_{\mathrm{strO}})_{\mathrm{podatki}}$. Število signalnih dogodkov v normalizacijskih kanalih dobimo tako, da v signalnem oknu od celotnega števila dogodkov odštejemo dobljeno število dogodkov ozadja.

Signalno okno za K^+K^- kanal je interval ± 14 MeV od nominalne vrednosti, stranski okni pa $\pm(31-41)$ MeV. Za $K^-\pi^+$ kanal je signalno okno ± 16.2 MeV, stranski okni pa $\pm(28.8-45)$ MeV. Za $\pi^+\pi^-$ kanal je signalno okno ± 15 MeV, stranski okni pa $\pm(20-35)$ MeV. Izkoristki, določeni na simuliranih dogodkih, so 22.7%, 27.0%
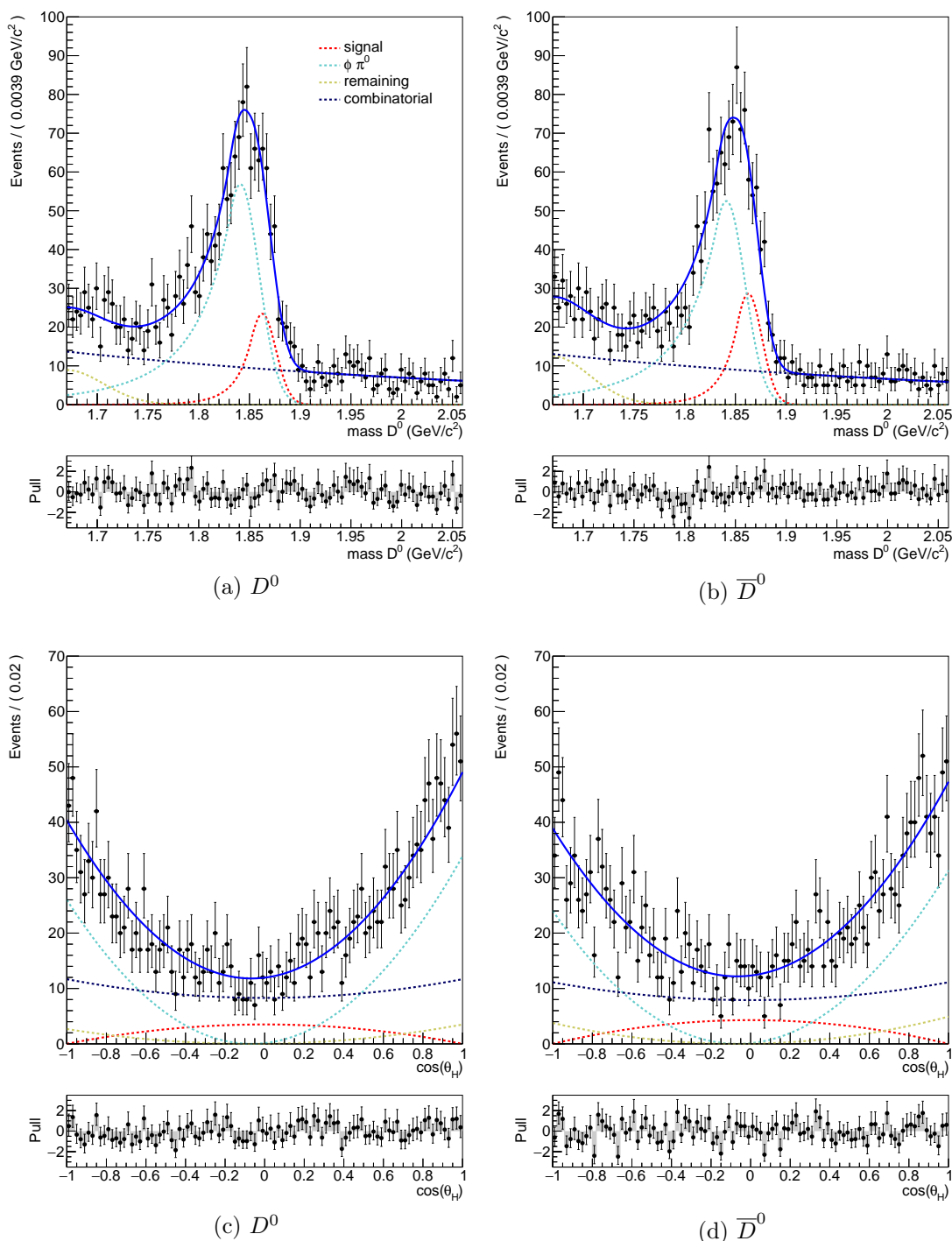
Slika 94: Simultano 2-dimenzionalno prilagajanje krivulj na porazdelitve $m(D^0)$ (zgoraj) in $\cos(\theta_H)$ (spodaj) ϕ kanala za D^0 (levo) in $\overline{D}^0$ (desno). Vrednosti χ^2/NDF (NDF je število prostorskih stopenj) so 0.9 za D^0 in 0.8 za $\overline{D}^0$. Vrednosti χ^2/NDF prilagajanja krivulj na porazdelitev po $\cos(\theta_H)$ so 0.8 za D^0 in 1.1 za $\overline{D}^0$.
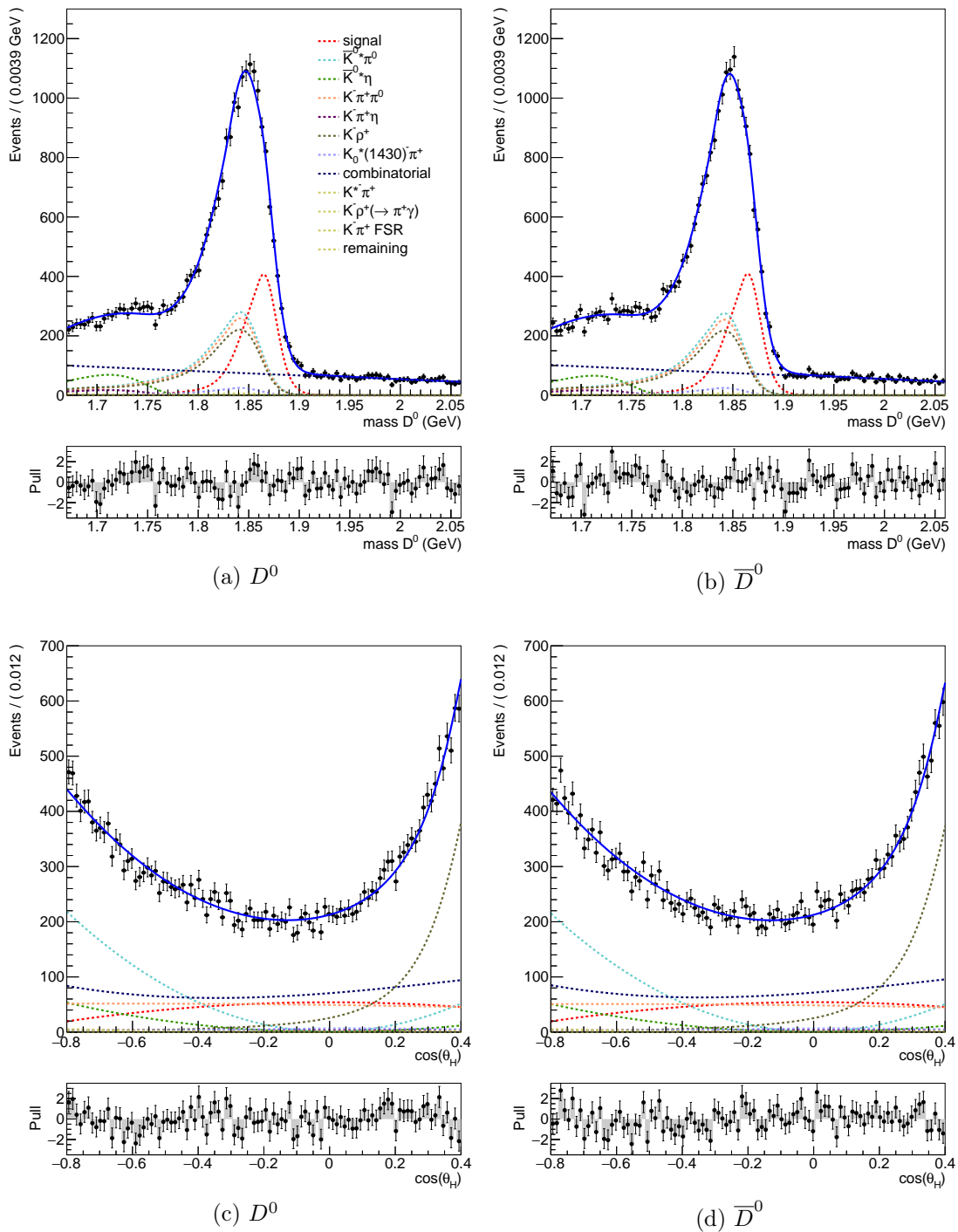
Slika 95: Simultano 2-dimenzionalno prilagajanje krivulj na porazdelitve $m(D^0)$ (zgoraj) in $\cos(\theta_H)$ (spodaj) $\overline{K}^{*0}$ kanala za D^0 (levo) in $\overline{D}^0$ (desno). Vrednosti χ^2/NDF (NDF je število prostorskih stopenj) so 1.2 za D^0 in 1.4 za $\overline{D}^0$. Vrednosti χ^2/NDF prilagajanja krivulj na porazdelitev po $\cos(\theta_H)$ so 1.4 za D^0 in 1.4 za $\overline{D}^0$.

(a) D^0

(b) $\overline{D}^0$

(c) D^0

(d) $\overline{D}^0$
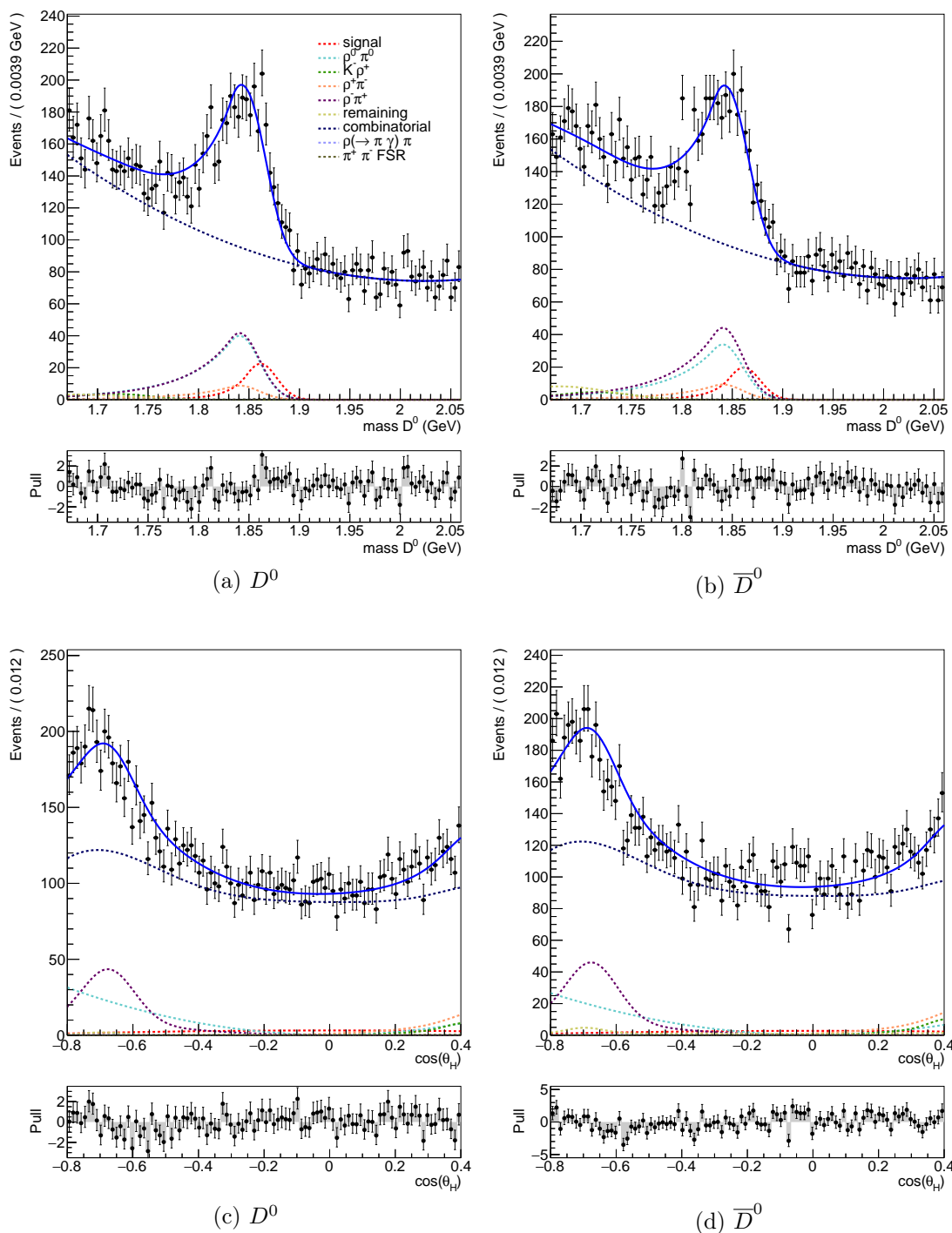
Slika 96: Simultano 2-dimenzionalno prilagajanje krivulj na porazdelitve $m(D^0)$ (zgoraj) in $\cos(\theta_H)$ (spodaj) ρ^0 kanala za D^0 (levo) in $\overline{D}^0$ (desno). Vrednosti χ^2/NDF (NDF je število prostorskih stopenj) so 1.2 za D^0 in 1.2 za $\overline{D}^0$. Vrednosti χ^2/NDF prilagajanja krivulj na porazdelitev po $\cos(\theta_H)$ so 1.2 za D^0 in 1.8 za $\overline{D}^0$.

in 21.4% za K^+K^-, $K^-\pi^+$ in $\pi^+\pi^-$ kanal. Dobljeno število dogodkov je 362274, 4.02×10^6 in 127683 za K^+K^-, $K^-\pi^+$ in $\pi^+\pi^-$ kanal. Dobljene rekonstrukcijske asimetrije so $(2.2\pm1.7)\times10^{-3}$ (K^+K^-), $(1.3\pm0.5)\times10^{-3}$ $(K^-\pi^+)$ in $(8.1\pm3.0)\times10^{-3}$ $(\pi^+\pi^-)$.

13.4 SISTEMATSKE NEGOTOVOSTI

Nekatere sistematske negotovosti, ki izhajajo iz rezov na posameznih spremeljivkah, se v končnem rezultatu odštejejo, če so enake za signalni in normalizacijski kanal. Te so: negotovosti, povezane z identifikacijo delcev, prilagajanjem sledi v skupno točko, in rez na $p_{\mathrm{CMS}}(D^{*+})$. Prisotnost fotona v signalnih kanalih poslabša resolucijo porazdelitve q, zato se ta negotovost ne odšteje, čeprav je enak rez uporabljen pri signalnih in normalizacijskih kanalih. Ocenimo jo na kontrolnem razpadu $D^0 \to \overline{K}^{*0}\pi^0$. Tako na simuliranih kot na pravih podatkih izračunamo razmerje R med dobljenim številom signalnih dogodkov pri uporabi reza na q, ter brez reza. Nato izračunamo dvojno razmerje $R_{\mathrm{sim}}/R_{\mathrm{podatki}}$. Dobljena vrednost je 1.0100 ± 0.0016. Iz tega naslova tako pripišemo sistematsko napako 1.16%.

Izkoristku pri rekonstrukciji fotonov pripišemo napako 2.2% [40]. Za oceno negotovosti zaradi reza na spremeljivki veta π^0 uporabimo metodo dvojnega razmerja, podobno kot na primeru q, na kontrolnem kanalu $D^0 \to K_S^0\pi^0$. Hčerinski foton mezona π^0, ki ima višjo enegijo, združimo z vsakim ostalim fotonom razen pravega drugega hčerinska fotona π^0, ter za simulirane in prave podatke izračunamo razmerje R med dogodki pri uporabi reza, ter brez. Dobimo dvojno razmerje $R_{\mathrm{sim}}/R_{\mathrm{podatki}} = 1.002 \pm 0.005$, iz česar pripišemo sistematsko napako 0.5%.

Sistematski negotovosti zaradi rezov na razmerju E_9/E_{25} in $E(\gamma)$ ocenimo na $\overline{K}^{*0}$ kanalu tako, da ponovimo postopek prilagajanja krivulj na vzorcu brez rezov na omenjenih spremeljivkah. Sistematsko negotovost dobimo kot razliko med razmerjem števila dogodkov in izkoristka v tem primeru, ter originalnem rezultatu, kjer je bil rez uporabljen. Dobljeni negotovosti sta 0.23% za E_9/E_{25} in 1.15% za $E(\gamma)$. Negotovosti zaradi reza na masi vektorskega mezona ocenimo na masni porazdelitvi, ki jo opišemo z relativistično Breit-Wignerjevo funkcijo. V signalnem oknu primerjamo integrala znotraj uporabljenih rezov za nominalno funkcijo, ter funkcijo, modificirano glede na znane nezanesljivosti srednje vrednosti in širine. Dobljene negotovosti so so 0.1%, 1.7% in 0.2% za ϕ, $\overline{K}^{*0}$ in ρ^0 kanal. Vse sistematske negotovosti iz naslova rezov na spremeljivkah vplivajo samo na razvejitveno razmerje, saj se pri izračunu asimetrije odštejejo med vzorcema D^0 in $\overline{D}^0$. Združena vrednost za naštete negotovosti, sešteta v kvadratu, je predstavljena v tabeli 50 pod "Izkoristek".

Sistematske negotovosti, ki izhajajo iz parametrizacije signala in ozadja, določimo za parametre, ki so fiksirani na vrednosti, dobljene iz simulacije: zamik srednje vrednosti in faktor širine funkcije, ki opisuje porazdelitev po $m(D^0)$ dogodkih ozadij s π^0 in η, ter zamik srednje vrednosti in faktor širine funkcije, ki opisuje porazdelitev signalnih dogodkov po $m(D^0)$ (določen na $\overline{K}^{*0}$ kanalu) za ϕ in ρ^0 kanala. Združena vrednost negotovosti je predstavljena v tabeli 50 pod "Parametrizacija".

Konstantne vrednosti števila dogodkov variiramo glede na negotovosti znanih vrednosti razvejitvenih razmerij. Za kategorijo s fotonom, izsevanim v končnem stanju,

	$\sigma(\mathcal{B}r)/\mathcal{B}r$ [%]			$\mathcal{A}_{CP}$ [$\times 10^{-3}$]		
	ϕ	$\overline{K}^{*0}$	ρ^0	ϕ	$\overline{K}^{*0}$	ρ^0
Izkoristek	2.8	3.3	2.8	–	–	–
Parametrizacija	1.0	2.8	2.3	0.1	0.4	5.3
Normalizacija ozadja	–	0.3	0.6	–	0.2	0.5
Normalizacijski kanali	0.0	0.0	0.1	0.5	0.0	0.3
Zunanji $\mathcal{B}r$ and $\mathcal{A}_{CP}$	2.0	1.0	1.8	1.2	0.0	1.5
Skupno	3.6	4.5	4.1	1.3	0.4	5.5

Tabela 50: Sistematske negotovosti.

uporabimo negotovost 20% [41]. Ker je to največja negotovosti v primerjavi z ostalimi, jo uporabimo tudi za kategorijo "remaining", kjer ne poznamo razvejitvenega razmerja. Združena vrednost negotovosti je predstavljena v tabeli 50 pod "Normalizacija ozadja".

Analizo normalizacijskih kanalov ponovimo pri drugače izbranih stranskih oknih, ki začnejo pri ± 25 MeV stran od nominalne vrednosti $m(D^0)$. Razliko pri končnem rezultati upoštevamo kot sistematsko napako. Zaradi morebitnih razlik v porazdelitvi po $m(D^0)$ med simuliranimi in pravimi podatki, uporabimo enak postopek kalibracije kot za ozadja s π^0 in η, ter pripišemo sistematsko napako za primer, kjer je simulirana porazdelitev numerično konvoluirana z Gaussovo funkcijo širine 1.6 MeV. Združena vrednost negotovosti je predstavljena v tabeli 50 pod "Normalizacijski kanali".

Negotovost pripišemo tudi zaradi negotovosti na vrednostih zunanjih razvejitvenih razmerij in asimetrij CP, ki so bile uporabljene za izračun končnega rezultata.

Vse sistematske negotovosti so povzete v tabeli 50.

13.5   končni rezultat

Končni rezultat za razvejitvena razmerja in asimetrije CP dobimo po enačbah 62 oz. 63. Pripišemo še sistematske napake, opisane zgoraj. Dobljene vrednosti razvejitvenih razmerij so

$$\mathcal{B}r\left(D^0 \to \rho^0\gamma\right) = (1.77 \pm 0.30 \pm 0.07) \times 10^{-5},$$
$$\mathcal{B}r\left(D^0 \to \phi\gamma\right) = (2.76 \pm 0.19 \pm 0.10) \times 10^{-5},$$
$$\mathcal{B}r\left(D^0 \to \overline{K}^{*0}\gamma\right) = (4.66 \pm 0.21 \pm 0.21) \times 10^{-4}.$$

Razpadi $D^0 \to \rho^0\gamma$ so prvič opaženi. Signifikanca je, ob upoštevanju tako statistične kot sistematske negotovosti, 5.5σ. Dobljeno razvejitveno razmerje za razpade $D^0 \to \phi\gamma$ je v skladu s prejšnjimi meritvami, a z višjo natančnostjo. Relativna natančnost je višja tudi v primeru razvejitvenega razmerja za razpad $D^0 \to \overline{K}^{*0}\gamma$, centralna vrednost je v okviru teoretičnih napovedi, vendar odstopa za 3.2σ v primerjavi z rezultatom kolaboracije BaBar, kjer je σ združena negotovost obeh meritev.

Opravili smo tudi prvo meritev asimetrije CP v danih razpadih. Dobljene vrednosti so

$$\mathcal{A}_{CP}\left(D^0 \to \rho^0 \gamma\right) = +0.056 \pm 0.152 \pm 0.006,$$
$$\mathcal{A}_{CP}\left(D^0 \to \phi\gamma\right) = -0.094 \pm 0.066 \pm 0.001,$$
$$\mathcal{A}_{CP}\left(D^0 \to \overline{K}^{*0}\gamma\right) = -0.003 \pm 0.020 \pm 0.000,$$

in so skladne z ohranitvijo simetrije CP v okviru napake. Glede na to, da je prevladujoča napaka statistična, lahko pričakujemo znatno izboljšanje natančnosti pri prihodnji nadgradnji eksperimenta Belle, Belle II.

BIBLIOGRAPHY

[1] E. Noether. Invariant Variation Problems. *Gott.Nachr.*, 1918:235–257, 1918. (Cited on page 3.)

[2] C. S. Wu, E. Ambler, R. W. Hayward, D. D. Hoppes, and R. P. Hudson. Experimental Test of Parity Conservation in Beta Decay. *Phys. Rev.*, 105: 1413–1414, 1957. doi: 10.1103/PhysRev.105.1413. (Cited on page 3.)

[3] R. L. Garwin, L. M. Lederman, and Marcel Weinrich. Observations of the Failure of Conservation of Parity and Charge Conjugation in Meson Decays: The Magnetic Moment of the Free Muon. *Phys. Rev.*, 105:1415–1417, 1957. doi: 10.1103/PhysRev.105.1415. (Cited on page 3.)

[4] J. H. Christenson, J. W. Cronin, V. L. Fitch, and R. Turlay. Evidence for the 2 pi Decay of the k(2)0 Meson. *Phys. Rev. Lett.*, 13:138–140, 1964. doi: 10.1103/PhysRevLett.13.138. (Cited on page 3.)

[5] Kazuo Abe et al. Observation of large CP violation in the neutral B meson system. *Phys. Rev. Lett.*, 87:091802, 2001. doi: 10.1103/PhysRevLett.87.091802. (Cited on page 3.)

[6] Bernard Aubert et al. Observation of CP violation in the B^0 meson system. *Phys. Rev. Lett.*, 87:091801, 2001. doi: 10.1103/PhysRevLett.87.091801. (Cited on page 3.)

[7] Makoto Kobayashi and Toshihide Maskawa. CP Violation in the Renormalizable Theory of Weak Interaction. *Prog. Theor. Phys.*, 49:652–657, 1973. doi: 10.1143/ PTP.49.652. (Cited on page 3.)

[8] S. L. Glashow, J. Iliopoulos, and L. Maiani. Weak Interactions with Lepton-Hadron Symmetry. *Phys. Rev.*, D2:1285–1292, 1970. doi: 10.1103/PhysRevD.2. 1285. (Cited on page 4.)

[9] Y. Amhis et al. Averages of b-hadron, c-hadron, and τ-lepton properties as of summer 2016. 2016. (Cited on page 8.)

[10] J. E. Augustin et al. Discovery of a Narrow Resonance in e+ e- Annihilation. *Phys. Rev. Lett.*, 33:1406–1408, 1974. doi: 10.1103/PhysRevLett.33.1406. [Adv. Exp. Phys.5,141(1976)]. (Cited on page 8.)

[11] J. J. Aubert et al. Experimental Observation of a Heavy Particle J. *Phys. Rev. Lett.*, 33:1404–1406, 1974. doi: 10.1103/PhysRevLett.33.1404. (Cited on page 8.)

[12] R Aaij et al. Observation of $D^0 - \overline{D}^0$ oscillations. *Phys. Rev. Lett.*, 110(10): 101802, 2013. doi: 10.1103/PhysRevLett.110.101802. (Cited on page 8.)

[13] Y. Amhis et al. Averages of b-hadron, c-hadron, and τ-lepton properties as of summer 2014. 2014. (Cited on pages 10, 115, 144, 156, and 164.)

[14] Gustavo Burdman and Ian Shipsey. D^0 - $\bar{D}^0$ mixing and rare charm decays. *Ann. Rev. Nucl. Part. Sci.*, 53:431–499, 2003. doi: 10.1146/annurev.nucl.53. 041002.110348. (Cited on page 9.)

[15] Gino Isidori and Jernej F. Kamenik. Shedding light on CP violation in the charm system via D to V gamma decays. *Phys. Rev. Lett.*, 109:171801, 2012. doi: 10.1103/PhysRevLett.109.171801. (Cited on pages 11 and 162.)

[16] James Lyon and Roman Zwicky. Anomalously large $\mathcal{O}_8$ and long-distance chirality from $A_{\mathrm{CP}}[D^0 \to (\rho^0, \omega)\gamma](t)$. 2012. (Cited on page 11.)

[17] Gustavo Burdman, Eugene Golowich, JoAnne L. Hewett, and Sandip Pakvasa. Radiative weak decays of charm mesons. *Phys. Rev. D*, 52:6383–6399, 1995. doi: 10.1103/PhysRevD.52.6383. (Cited on page 11.)

[18] S. Fajfer, Sasa Prelovsek, and P. Singer. Long distance contributions in D —> V gamma decays. *Eur. Phys. J. C*, 6:471–476, 1999. doi: 10.1007/s100529800914. (Cited on page 11.)

[19] Svjetlana Fajfer. Theoretical perspective on rare and radiative charm decays. In Alexey A Petrov et al., editors, *Proceedings of CHARM-2015*. SLAC Electronic Proceedings, 2015. URL http://arxiv.org/pdf/1509.01997v1.pdf. (Cited on page 11.)

[20] D. M. Asner et al. Radiative decay modes of the D0 meson. *Phys. Rev. D*, 58: 092001, 1998. doi: 10.1103/PhysRevD.58.092001. (Cited on pages 11 and 162.)

[21] O. Tajima et al. Observation of the radiative decay $D^0 \to \phi\gamma$. *Phys. Rev. Lett.*, 92:101803, Mar 2004. doi: 10.1103/PhysRevLett.92.101803. URL http://link.aps.org/doi/10.1103/PhysRevLett.92.101803. (Cited on pages 11, 159, and 162.)

[22] Bernard Aubert et al. Measurement of the Branching Fractions of the Radiative Charm Decays D0 —> anti-K*0 gamma and D0 —> phi gamma. *Phys. Rev. D*, 78:071101(R), 2008. doi: 10.1103/PhysRevD.78.071101. (Cited on pages 11, 159, and 162.)

[23] K. A. Olive et al. Review of Particle Physics. *Chin. Phys. C*, 38:090001, 2014. doi: 10.1088/1674-1137/38/9/090001. (Cited on pages 12, 28, 53, 117, 143, 149, 152, 156, 162, 164, and 165.)

[24] S. Kurokawa and E. Kikutani. Overview of the KEKB accelerators. *Nucl. Instrum. Method Phys. Res., Sect. A*, 499:1–7, 2003. (Cited on pages 13 and 162.)

[25] A. Abashian et al. The Belle Detector. *Nucl. Instrum. Method Phys. Res., Sect. A*, 479:117–232, 2002. doi: 10.1016/S0168-9002(01)02013-7. (Cited on pages 13, 16, 17, 18, 20, 21, 22, 23, 162, and 164.)

[26] R. Seuster et al. Charm hadrons from fragmentation and B decays in e^+e^- annihilation at $\sqrt{s} = 10.6$ GeV. *Phys. Rev.*, D73:032002, 2006. doi: 10.1103/ PhysRevD.73.032002. (Cited on page 25.)

[27] S. Fajfer, Sasa Prelovsek, P. Singer, and D. Wyler. A Possible arena for searching new physics: The $\Gamma(D^0 \to \rho^0\gamma)/\Gamma(D^0 \to \omega\gamma)$ ratio. *Phys. Lett.*, B487:81–86, 2000. doi: 10.1016/S0370-2693(00)00731-0. (Cited on page 26.)

[28] D. J. Lange. The EvtGen particle decay simulation package. *Nucl. Instrum. Method Phys. Res., Sect. A*, 462:152–155, 2001. doi: 10.1016/S0168-9002(01) 00089-4. (Cited on page 26.)

[29] R. Brun, F. Bruyant, M. Maire, A. C. McPherson, and P. Zanarini. GEANT3. *CERN Report No. DD/EE/84-1*, 1987. (Cited on page 26.)

[30] Piotr Golonka and Zbigniew Was. PHOTOS Monte Carlo: A Precision tool for QED corrections in Z and W decays. *Eur. Phys. J. C*, 45:97–107, 2006. doi: 10.1140/epjc/s2005-02396-4. (Cited on page 26.)

[31] P. Koppenburg et al. An Inclusive measurement of the photon energy spectrum in b —> s gamma decays. *Phys. Rev. Lett.*, 93:061803, 2004. doi: 10.1103/ PhysRevLett.93.061803. (Cited on page 34.)

[32] M. Feindt and U. Kerzel. The NeuroBayes neural network package . *Nucl. Instrum. Method Phys. Res., Sect. A*, 559(1):190 – 194, 2006. doi: http://dx. doi.org/10.1016/j.nima.2005.11.166. URL `http://www.sciencedirect.com/ science/article/pii/S0168900205022679`. (Cited on pages 34 and 165.)

[33] M. Staric et al. Measurement of CP asymmetry in Cabibbo suppressed D^0 decays. *Phys. Lett. B*, 670:190–195, 2008. doi: 10.1016/j.physletb.2008.10.052. (Cited on pages 54, 107, 108, 154, and 167.)

[34] H. Mendez et al. Measurements of D Meson Decays to Two Pseudoscalar Mesons. *Phys. Rev.*, D81:052013, 2010. doi: 10.1103/PhysRevD.81.052013. (Cited on page 54.)

[35] Tomasz Skwarnicki. PhD thesis, Cracow, INP, 1986. URL `http://lss. fnal.gov/cgi-bin/find_paper.pl?other/thesis/skwarnicki.pdf`. (Cited on pages 65 and 166.)

[36] H. Ikeda et al. A detailed test of the CsI(Tl) calorimeter for BELLE with photon beams of energy between 20-MeV and 5.4-GeV. *Nucl. Instrum. Method Phys. Res., Sect. A*, 441:401–426, 2000. doi: 10.1016/S0168-9002(99)00992-4. (Cited on pages 65 and 166.)

[37] Michael Feindt and Michael Prim. An algorithm for quantifying dependence in multivariate data sets. *Nucl. Instrum. Meth.*, A698:84–89, 2013. doi: 10.1016/j. nima.2012.09.043. (Cited on page 78.)

[38] M. Staric et al. Search for CP Violation in $D^{\pm}$ Meson Decays to $\phi\pi^{\pm}$. *Phys. Rev. Lett.*, 108:071801, 2012. doi: 10.1103/PhysRevLett.108.071801. (Cited on page 125.)

[39] Muriel Pivk and Francois R. Le Diberder. SPlot: A Statistical tool to unfold data distributions. *Nucl. Instrum. Meth.*, A555:356–369, 2005. doi: 10.1016/j.nima.2005.08.106. (Cited on page 139.)

[40] N. K. Nisar et al. Search for the rare decay $D^0 \rightarrow \gamma\gamma$ at Belle. *Phys. Rev. D*, 93 (5):051102(R), 2016. doi: 10.1103/PhysRevD.93.051102. (Cited on pages 146 and 171.)

[41] Maurice Benayoun, S. I. Eidelman, V. N. Ivanchenko, and Z. K. Silagadze. Spectroscopy at B factories using hard photon emission. *Mod. Phys. Lett. A*, 14:2605–2614, 1999. doi: 10.1142/S021773239900273X. (Cited on pages 152 and 172.)

[42] T. Abe et al. Belle II Technical Design Report. 2010. (Cited on page 160.)